Stereotactic Atlas of the Human Thalamus and Basal Ganglia

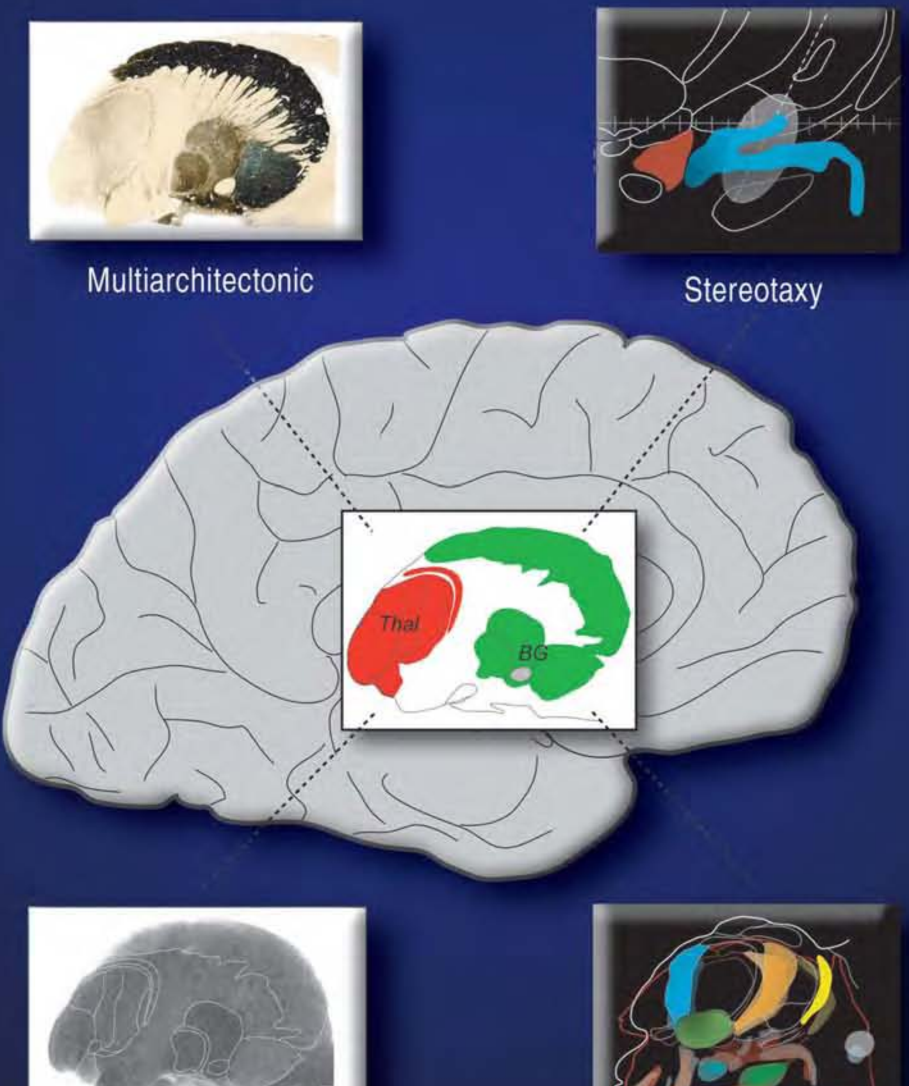

Anne Morel

Stereotactic Atlas of the Human Thalamus and Basal Ganglia

Stereotactic Atlas of the Human Thalamus and Basal Ganglia

Anne Morel
University Hospital Zurich
Zurich, Switzerland

informa
healthcare

New York London

Informa Healthcare USA, Inc.
270 Madison Avenue
New York, NY 10016

© 2007 by Informa Healthcare USA, Inc.
Informa Healthcare is an Informa business

No claim to original U.S. Government works
Printed in the United States of America on acid-free paper
10 9 8 7 6 5 4 3 2 1

International Standard Book Number-10: 0-8247-2894-7 (Hardcover)
International Standard Book Number-13: 978-0-8247-2894-6 (Hardcover)

This book contains information obtained from authentic and highly regarded sources. Reprinted material is quoted with permission, and sources are indicated. A wide variety of references are listed. Reasonable efforts have been made to publish reliable data and information, but the author and the publisher cannot assume responsibility for the validity of all materials or for the consequences of their use.

No part of this book may be reprinted, reproduced, transmitted, or utilized in any form by any electronic, mechanical, or other means, now known or hereafter invented, including photocopying, microfilming, and recording, or in any information storage or retrieval system, without written permission from the publishers.

For permission to photocopy or use material electronically from this work, please access www.copyright.com (http://www.copyright.com/) or contact the Copyright Clearance Center, Inc. (CCC) 222 Rosewood Drive, Danvers, MA 01923, 978-750-8400. CCC is a not-for-profit organization that provides licenses and registration for a variety of users. For organizations that have been granted a photocopy license by the CCC, a separate system of payment has been arranged.

Trademark Notice: Product or corporate names may be trademarks or registered trademarks, and are used only for identification and explanation without intent to infringe.

Library of Congress Cataloging-in-Publication Data

Morel, Anne.
Stereotactic atlas of the human thalamus and basal ganglia / Anne Morel.
p. ; cm.
Includes bibliographical references and index.
ISBN-13: 978-0-8247-2894-6 (hb : alk. paper)
ISBN-10: 0-8247-2894-7 (hb : alk. paper)
1. Thalamus--Anatomy--Atlases. 2. Basal ganglia--Anatomy--Atlases. 3. Stereotaxic techniques--Atlases. I. Title.
[DNLM: 1. Thalamus--anatomy & histology--Atlases. 2. Thalamus--anatomy & histology--Handbooks. 3. Basal Ganglia--anatomy & histology--Atlases. 4. Basal Ganglia--anatomy & histology--Handbooks. 5. Stereotaxic Techniques--Atlases. 6. Stereotaxic Techniques--Handbooks. WL 17 M839s 2007]

QM455.M686 2007
611'.81--dc22 2007004928

Visit the Informa Web site at
www.informa.com

and the Informa Healthcare Web site at
www.informahealthcare.com

Preface

The field of stereotactic functional neurosurgery for the treatment of patients with chronic therapy-resistant functional brain disorders has made significant progress due to better knowledge of the anatomy and physiology of brain networks implicated in the different pathologies. The surgical approaches, whether through chronic stimulations or therapeutic lesions, are directed at retuning dysfunctional brain systems, with targets aimed mostly at pallidal, prethalamic, or thalamic levels.

For all surgical interventions, the identification of the target and its precise anatomical localization are most important to obtain durable and consistent results, with low risks for side-effects. Accurate anatomical localization is even more mandatory in case of neuroradiologically guided surgery where there is no physiological verification of the target (e.g., radiosurgery).

In spite of the progress in magnetic resonance image (MRI) resolution for guiding stereotactic neurosurgery, the precision of the targeting, in particular in the thalamus and subthalamic area, still depends on the quality of the anatomical atlas used to determine the three-dimensional target coordinates. The necessity to develop a new atlas based on multiarchitectonic parcellation and integrating high spatial resolution and stereotactic precision motivated our work for the last fifteen years.

The first atlas focused on the thalamus was published in 1997 and was the first step toward our goal. The present book is an extension of the atlas to the basal ganglia, with complementary information related to fiber tracts, interindividual variability and MRI correlations, which we hope will contribute significantly to the establishment of the anatomical framework indispensable for stereotactic neurosurgery and neuroimaging.

Anne Morel

Acknowledgments

This atlas work was undertaken fifteen years ago under the intiative of Prof. D. Jeanmonod, head of the Department of Functional Neurosurgery, to provide an anatomical basis for selective and precise targeting in stereotactic neurosurgery. The task was made very stimulating by his constant support and enthusiasm, and above all by his dedicated efforts to integrate neuroanatomy and physiology in day-to-day discussions on surgical planning and in the operating room. This very tight team work seems quite unique in the field of functional neurosurgery and has been a high motivation for this atlas project.

As successive heads of the Department of Neurosurgery, Prof. G. Yasargil and Y. Yonekawa gave essential support for the research and clinical developments of our functional neurosurgical approach.

For the basis of the atlas, I am particularly indebted to V. Streit, S. Richter, and H. Rayvedera for their skillful histological work. The contributions at different phases of the work of Drs. J. Liu, M. Gallay, F. Loup, K. Jetzer, M. Magnin, and Prof. J.-M. Fritschy were essential to the success of the project. Other members of the team, from clinical assistants to physiologists, were all important for day-to-day discussions about operations. The collaboration with Dr. K. Niemann, Germany, has been particularly fruitful in providing the first three-dimensional model of the thalamic atlas and its registration to MRI. I am very grateful to a number of colleagues at the University who gave support for the project: Prof. P. Kleihues, A. Aguzzi (Department of Neuropathology), and H.-P. Lipp (Institute of Anatomy) for providing autopsy material; Prof. S. Kollias, Dr. D. Meier (Neuroradiology), and M. Wyss (Philips) for MRI acquisitions; J. Schindlerholz and W. Bollinger for building the guillotine; P. Roth, R. Stillhard, and H. Job for graphical and photographical help; V. Bügler and V. Cucci for secretarial and administrative support.

I also owe special gratitude to Profs. J. H. Kaas, J. Bullier, and T. J. Imig for the very rich and valuable experience I acquired during my postdoctoral years in the field of neuroanatomy, which allowed me to successfully conduct this project. I am also indebted to Prof. F. de Ribaupierre for my learning experience in the field of neuroscience during my postgraduate years.

I also thank all my friends and my family for their encouragement during the preparation of this book.

Finally, I would like to take the opportunity to acknowledge the influential role of the zoologist Arnold Lang, my great grandfather, in the foundation of the Department of Zoology at the University of Zurich and, as Dean of the University from 1898 to 1900, in the construction of the University Center that is still the place for young professors' inaugural lectures.

This work has been continuously supported by grants of the Swiss National Science Foundation (grants Nrs. 31-36330.92; 31-47238.96; 31-54179.98; 31-68248.02) and is partially supported by the National Centre of Competence in Research on "Computer Aided and Image Guided Medical Interventions" (NCCR CO-ME).

Contents

Preface iii

Acknowledgments v

1. A New Anatomical Framework for Stereotactic Functional Neurosurgery and Neuroimaging *1*

2. Material and Methods *3*

3. Thalamus *13*

4. Basal Ganglia *53*

5. Subthalamic Fiber Tracts *111*

6. Interindividual Anatomical Variability *119*

7. Atlas Applications *129*

References 137

List of Abbreviations 143

Index 145

1 A New Anatomical Framework for Stereotactic Functional Neurosurgery and Neuroimaging[a]

The importance of the thalamus, basal ganglia and related cortical networks in sensory, motor, cognitive and emotional experiences is well recognized. The complexity of the circuitry is far from being fully comprehended, although great progress has already been made through recent developments in all fields of neuroscience, whether experimental or clinical. In the clinical environment, the increasing number and accuracy of noninvasive methods for exploring the human brain provide insights into normal as well as pathological conditions. Knowledge of the location of the cerebral insult and/or the system affected is of prime importance not only to determine the cause of the disorder, but also for surgical interventions aimed at removing or modulating abnormally functioning brain structures. In surgical treatment of chronic functional disorders [e.g., Parkinson's disease (PD), neurogenic pain], deep brain structures such as the thalamus and basal ganglia are reached stereotactically, with procedures allowing the surgeon to selectively target an anatomically defined nuclear or fiber system (**Fig. 1** in chap. 7). Today, stereotactic surgery is generally guided by magnetic resonance imaging (MRI) to plane electrode trajectory and transfer target coordinates defined on an anatomical atlas onto individual patients brain images, using a common 3D stereotactic reference system. Recent progress in MRI resolution allows better visualization of some structures of interest as well as anatomical landmarks in the vicinity of the target. In particular, visualization of major subdivisions of the basal ganglia (striatum and pallidum) and more recently, of the subthalamic nucleus (STh) in specific MRI sequences has lead more neurosurgeons to rely on these images to directly target the internal pallidum or STh in patients undergoing stereotactic surgery for PD (1–4). MRI measurements (automated or manual) also are useful to study large samples of the whole thalamus or particular nuclei (e.g., pulvinar and mediodorsal nuclei) in controls as well as in pathological cases, such as in schizophrenic subjects (5–7). Nevertheless, these images give only approximate contours of some of these structures, such as for the ventral limit of the STh with adjacent substantia nigra (SN). Furthermore, fine histological structures such as precise delimitation of individual nuclei in the thalamus or anatomo-functional territories in the basal ganglia are still beyond MR image resolution. One has still to rely on indirect targeting, that is, by transfer of detailed histological maps obtained from 3D anatomical atlas onto individual patients' brain images. Accurate anatomical localization in the field of stereotactic surgery reduces operative time and, thus, the hazard of complication by minimizing the tissue volume to be explored physiologically for final identification of the target site. Anatomical and stereotactic precision is even more critical in cases of radiosurgery [e.g., gamma knife radiosurgery (8–11)] or other neuradiological approaches where there is no electrophysiological verification of the target. These interventions also require evaluation of the degree of interindividual anatomical variability of subcortical structures, which can be adequately performed only when the different brains are cut stereotactically, thus minimizing the risk of under- or overestimating interindividual anatomical variations. Stereotactic atlases are needed not only for precise targeting in functional neurosurgery, but also for accurate projections of peroperative physiological data (stimulations, microelectrode recordings) (12–17), localization of therapeutic lesions or high frequency

---

[a] Parts of this study were published elsewhere in Refs. 39 and 44.

stimulation (HFS) sites (18–20), localization of vascular damages (21–22), or diffusion tensor imaging (DTI) data (23–24).

There have been a number of anatomical atlases of the human brain devoted to the thalamus and neighboring structures, from early morphometric analyses of nuclear boundaries to topometric presentations in relation to brain sizes and measurements (25–28). These are reviewed in a recent chapter on the human thalamus (29). In modern stereotaxy, the atlas of the human thalamus by Schaltenbrand and Wahren (26) has been, and still is, widely used for deep brain mapping and surgical targeting. It is focused on the thalamus and subthalamic areas, but also contains partial maps of the basal ganglia. The atlas is based on three series of maps drawn on the basis of the cytoarchitecture and transferred onto photomicrographs of myelin stained sections, with more than 120 delimited nuclei and abbreviations derived from Hassler's terminology (30). The Schaltenbrand and Wahren atlas, however, has limitations in stereotactic precision (the three series are not orthogonal to each other) and anatomical resolution (uneven and coarse spacing between the slides) (31). The nomenclature is difficult to relate to the terminology used in nonhuman primates where large amounts of data provide the anatomo-functional framework for understanding many aspects of human brain function and dysfunction. In the more recent atlas of the human brain by Mai et al. (32), series of drawings from the thalamus and basal ganglia are presented only in the coronal plane and illustrated, as in the Schaltenbrand and Wahren atlas, by the myeloarchitecture.

Because of the drawbacks of existing atlases and to take advantage of new staining procedures for the refinement of thalamic and basal ganglia parcellations, we developed a new atlas of the human thalamus and basal ganglia with the main objective of combining both high anatomical resolution and stereotactic precision. To this aim, the following steps were taken:

1. Use of multiple architectonic criteria to define nuclear thalamic boundaries and anatomo-functional basal ganglia subterritories similar to those in nonhuman primates (33–43), thus providing indirect information on anatomo-functional pathways in the human brain.
2. Apply a nomenclature close to that used in nonhuman primates in order to ease comparisons with the rich amount of data amassed in the last decades. The importance of a unifying terminology has been first proposed by Jones et al. (44–46) on the basis of multiarchitectonic equivalent definition of thalamic nuclei in the two species.
3. Provide high spatial resolution and stereotactic precision by presenting series of maps at close and regular intervals, in planes orthogonal to each other with the intercommissural plane as stereotactic reference plane.
4. Correlate atlas maps to postmortem MRIs to provide a basis for recognizing structures of interest and landmarks in "in vivo" MRIs.
5. Evaluate interindividual anatomical variability "in vitro" by comparing atlas maps from different brains and "in vivo" by overall thalamic or basal ganglia MRI measurements.

With these objectives, we hope to provide the neuroscience community with a new anatomical basis for research and clinical applications.

2 Material and Methods

AUTOPSY MATERIAL

This study is based on postmortem examination of seven autopsy brains provided by the Department of Neuropathology at the University Hospital Zurich. All brains were from normal subjects, with no history of neurological disease or pathological signs at autopsy. Ages of subjects ranged between 46 and 74 years and postmortem delays were between 4 and 24 hours (Table 2.1). Six of the brains had already been used for another atlas study (47) and neurochemical compartmentalization of the human basal ganglia (48). In one case (Hb7, Table 2.1; **Fig. 2.3**), stereotactic 3D magnetic resonance images (MRIs) were acquired with a 3-Tesla scanner (Philips Corp.) (see protocol below). An additional brain provided by the Department of Anatomy was used for correlation with high resolution proton density 3-Tesla MRI (see protocol below). However, because of the lack of informations on the history of the subject (age, gender, cause of death and postmortem delay), this case was not included in the atlas study per se.

BLOCK PREPARATION AND SECTIONING

After excision, whole brains were first immersed in a fixative solution containing either 4% paraformaldehyde (PAF) in 0.1 *M* phosphate buffer (PB) at pH 7.4 for 7 to 15 days (four brains, Table 2.1) or in 10% neutral formalin for few weeks to several months (three brains, Table 2.1). In two cases (including Hb7, Table 2.1), a series of MRIs of the whole brain in stereotactic planes were obtained from a Philips 3-Tesla at the University Hospital Department of Neuroradiology after 10 days of PAF fixation (Hb7) or after one year fixation in formalin 4%. Before blocking, the brain was cleaned by gently removing the arachnoida, then placed on a Plexiglas plate with the interhemispheric plane aligned on the axis of the guillotine knife (**Fig. 2.1**). This guillotine was manufactured at the University Hospital. The following steps were taken for cutting the brain into blocks containing the thalamus and the basal ganglia:

1. Interhemispheric section.
2. Each hemisphere was placed on its interhemispheric face on the plexiglas plate and a mirror was used to align the centers of the posterior (pc) and anterior (ac) commissures on a line engraved on the plate (**Fig. 2.1A,B**). The centers of the commissures, instead of the superior edge of the ac and of the lower edge of the pc as used by some others (26,49), were chosen as less variable between individuals.
3. Two cuts were made orthogonal to this axis in coronal planes by moving the knife 8 to 15 mm posterior to the pc and 5 to 10 (for thalamic blocks) to 30 mm (for thalamic and basal ganglia blocks) anterior to the ac.
4. A similar procedure was used to make cuts in the horizontal plane, one 25 mm dorsal and the other 10 to 15 mm ventral to the ac–pc plane.
5. The last cut was made by aligning the block along the midsagittal plane and moving the knife 40 mm lateral.

The blocks thus obtained varied in size, from ~55 cm^3 for the thalamic atlas, to ~95 cm^3 for the thalamus and basal ganglia atlas (**Figs. 2.1–2.2**). Each block contained the two commissures (ac and pc), the thalamus, subthalamic nucleus and for the basal ganglia atlas, also the striatum,

TABLE 2.1

Case Nr	Age (yr)/ Gender	PM delay (hr)	Cause of death	Brain weight (g)	ac–pc[a] (mm)	Fixation	Structures[b]	Hemisphere/Plane of section	Histology[c]
Hb1	70/female	<24	Coronary infarct	980	25	Formalin	Thalamus (and part of BG)	L/SAG[e] R/HOR[e]	CaBP
Hb2	70/male	<24	Lung carcinoma	1188	30	Formalin	Thalamus (and part of BG)	L/FRO R/HOR	CaBP
Hb3	57/female	<24	Lung carcinoma	1260	30	Formalin	Thalamus and BG	R/FRO L/HOR	CaBP / TH
Hb4	51/male	11	Heart disease	1463	27	PAF	Thalamus (and part of BG)	R/HOR	CaBP / AChE
Hb5	46/male	15	Heart disease	1440	28	PAF	Thalamus and BG	R/FRO L/HOR	CaBP / AChE
Hb6	74/female	4	Lung carcinoma	1133	24	PAF	Thalamus and BG	R/HOR L/SAG	CaBP / SMI / AChE / TH
Hb7[d]	59/female	16	Anal carcinoma	1314	26	PAF	Thalamus and BG	R/SAG[e] L/FRO[e]	CaBP / SMI / AChE

[a] Intercommissural (ac–pc) distances are indicated in millimeters “in vivo.”

[b] Cases Hb1, Hb2, and Hb4 were focused on the thalamus (and subthalamic area), but also comprise part of the striatum and pallidum. Cases Hb3 and Hb5 to Hb7 comprise the whole thalamus and basal ganglia.

[c] Staining procedures additional to standard Nissl and myelin stains that were done in all cases.

[d] The whole brain was scanned through 3-Tesla MRI before blocking and histology.

[e] Hemispheres used for the atlas maps.

pallidum, and part of the substantia nigra. The blocks were postfixed in PAF 4% for one to three days (seven blocks) or in 10% formalin (six blocks), then transferred in progressively increasing sucrose concentrations (10%, 20%, and 30%) in 0.1 *M* PB over two to three weeks for cryoprotection. All but four blocks were then frozen by immersion in isopentane (–30°C) and then stored at –75°C. The blocks were sectioned in a cryostat, with section thicknesses varying between 40 and 50 µm. Six to nine adjacent series were collected in 0.1 *M* PB; some series were transferred in a cryoprotectant solution and stored at –20°C for later processing. In all cases, two adjacent series were stained for Nissl with cresyl violet and for myelin with a modified Heidenhain procedure applied to free-floating or mounted sections (50,51). Three additional series were immunostained with antibodies directed against the calcium-binding proteins (CaBP) parvalbumin (PV), calbindin D-28K (CB), and calretinin (CR), and in few cases also with antibodies against tyrosine hydroxylase (TH) (Table 2.1). In the cases with relatively short PAF fixation, additional series were processed for acetylcholinesterase (AChE) with a modified Koelle–Friedenwald method (52,53) or immunoreacted against the nonphosphorylated neurofilament protein (with SMI-32).

IMMUNOCYTOCHEMISTRY

Immunocytochemical procedures were similar to those described previously (47,48). Prior to exposure to antibodies, some series were pretreated 10 min in a microwave in a 4% aluminium chloride solution (54) to improve antigen retrieval in formalin stored sections. All series for immunocytochemistry were preincubated 10 min in 1.5% H_2O_2 to remove endogenous peroxidase activity. After several rinses in phosphate buffered saline (pH 7.4), sections were incubated 48 hours at 4°C or 24 hours at room temperature in primary antibodies (dilutions 1:1000 to 1:5000, depending on the antibody and tissue fixation), 2% normal horse or goat serum, and 0.2% triton-X-100. The antibodies used were mouse monoclonal directed against PV or CB (SWant, Bellinzona, Switzerland; or Sigma, St. Louis, Missouri, U.S.A.), rabbit polyclonal against CR (SWant), mouse monoclonal against the nonphosphoneurofilament protein (SMI-32, Sternberger Monoclonals Inc., Lutherville, Maryland, U.S.A.) and mouse monoclonal against TH (Boehringer, Mannheim, Germany). After several rinses, sections were then incubated 30 to 60 minutes at room temperature in biotinylated secondary antibodies (1:200, Vector Laboratories, Burlingame, California, U.S.A.) and stained with the avidin-biotin complex (ABC) immunoperoxidase method (Vectastain Elite kits, Vector Laboratories). The reaction was visualized with 3,3′-diaminobenzidine tetrahydrochloride as chromogen, diluted 0.05% in 0.05 *M* Tris-saline (pH 7.7) and 0.001% H_2O_2. For TH immunostaining, the reaction was enhanced with 0.1% nickel ammonium sulfate. Sections were then washed thoroughly and immediately mounted on gelatin-coated slides, dehydrated, and coverslipped. As controls, the primary antibody was omitted while the rest of the procedure remained the same.

DATA ANALYSIS

Contours of Nissl stained sections were drawn with a Wild stereomicroscope (Leica) equipped with a camera lucida, or traced on scanned images of the sections using Adobe Photoshop and Illustrator. Then, adjacent sections were superimposed using contours and blood vessels. Myelin stained sections were most helpful to delimit pallidal segments (GPe and the two subdivisions of GPi) and delineate prethalamic fiber tracts, particularly the pallidothalamic tract [comprised of the ansa lenticularis (al), the fasciculus thalamicus (ft) and lenticularis (fl)], the cerebellothalamic tract [fasciculus cerebellothalamicus (fct)], and the medial lemniscus/spinothalamic tracts (ml/stt). Besides Nissl and myelin stains, the distribution of AChE, CaBP, SMI-32 and to some extent also TH, served for the subcompartmentalization of the basal ganglia and refined thalamic nuclear delimitation. A more detailed analysis of the distribution of different markers was obtained at higher magnification with a computerized plotting system (Neurolucida, MicroBrightField Inc., Colchester, Connecticut, U.S.A.). Camera lucida drawings of the sections were digitized on a graphic tablet (with the Lotus Freelance program) or scanned and processed with a vector program (Adobe Illustrator). For illustrations, scan images or photomicrographs captured from a Leica microscope (Leica MZ 16) and digital camera (Leica DC 300) were adjusted for contrast and brightness with Adobe Photoshop and transferred as computer files to the software Adobe Illustrator for production of the final montage.

Multiarchitectonic Parcellation

Different stains were used to help define thalamic nuclei, basal ganglia subdivisions and striatopallidal compartmentalization, as well as fiber pathways. In previous studies from our group (47,48), the cytoarchitecture and differential distribution of calcium-binding proteins were described in detail for the thalamic nuclei, while additional criteria were used for the compartmentalization of the basal ganglia, such as the distribution of the nonphosphorylated epitope of neurofilament protein with antibody SMI-32 and that of acetylcholinesterase (AChE). This atlas is an extension of these studies, with additional architectonic criteria for both the thalamus and basal ganglia, as well as a description of fiber pathways that are of significance in the context of stereotactic surgery. The graphic maps represented in **Figures 3.1** to **3.25** focus on the thalamus and include only part of the basal ganglia, while the basal ganglia are more completely represented in **Figures 4.1** to **4.47**. Altogether this atlas is comprised of a series of maps from two different brains: two in the sagittal plane (Hb1 and Hb7, **Figs. 3.14** to **3.25** and **4.23** to **4.47**), one series in the horizontal plane (Hb1, **Figs. 3.1** to **3.13**) and one frontal series (Hb7, **Figs. 4.1** to **4.22**) (Table 2.1). The latter series has replaced the previously published series (47) as more complete and based on MRI for accurate alignment with the stereotactic plane. Nevertheless, the frontal series from the earlier atlas (Hb2, Table 2.1) has been revised by adding intermediate sections (intervals 0.9 between maps), part of the putamen, pallidum and SN, as well as subthalamic fiber tracts. This series is used for evaluation of the anatomical variability and is compared with sections from brain Hb7 in Chapter 6. Compared with the previously published atlas (47), the series of maps presented here include additional ventral maps in the horizontal series and lateral maps in the sagittal series, as well as complementary drawings of basal ganglia and fiber tracts.

The description is first directed at the thalamus and subthalamic area, and second at the basal ganglia (striatum, pallidal segments, subthalamic nucleus, substantia nigra). The two are discussed together in terms of anatomical variability in Chapter 6.

Nomenclature

For the thalamus, the terminology follows closely that proposed by Jones et al. for humans and nonhuman primates (44–46), introduced initially by Walker (55) in the monkey thalamus. Few modifications were proposed to account for subdivisions not delimited in the human thalamus previously (47). The choice of nomenclature was based on using similar criteria for thalamic parcellation in the two species, thus easing comparison with extensive knowledge accumulated in the last two decades on nonhuman primate thalamus, as well as of the pathophysiological data derived from primate models of functional disorders such as Parkinson's disease. [For equivalence with Hassler terminology, we refer to Table 1 on p. 16 in Hirai and Jones (46)]. For fiber tracts innervating the thalamus, we used a nomenclature derived from early anatomical descriptions to depict the pallido- and cerebellothalamic tracts (56,57). In the basal ganglia and adjacent structures, the nomenclature follows in part that of Heimer et al. in the human brain (58,59) and of Parent et al. (60,61) in the monkey brain.

GRAPHIC REPRESENTATIONS

In the atlas maps presented in **Figures 3.1** to **3.25** and **4.1** to **4.47**, the grids indicate millimeters "in vivo" that is, after correction for shrinkage. A shrinkage factor was evaluated in one case from a patient suffering from neurogenic pain and operated with a medial thalamotomy, who died from his cancer 18 months after the operation. His brain, under provision of his will, was donated to us and processed for Nauta degeneration to analyze thalamocortical projections from the lesions located in the medial thalamus. From the values of the intercommissural distances (i.e., the distance between the centers of ac and pc) measured on axial peroperative MRI and after formalin fixation and sectioning, this factor was evaluated to be 1.04. A slightly smaller factor (1.02) was estimated by the distance measured on postmortem MRI and after sectioning in case Hb7. Together, these measurements indicate only minimal deformation within the plane of section. A more variable factor was evaluated for distances measured across sections and includes a possible deformation caused by pressure of the knife during sectioning. In case Hb7 (**Figs. 4.1** to **4.47**), the levels of maps first evaluated by the distances between sections (50 μm thickness) were then only slightly adjusted to fit with the corresponding MRIs. In case Hb1 (**Figs. 3.1** to **3.25**), the correction factor applied for distances between sections (1.12) proved to be adequate since close correlations were found for distances measured between sagittal and horizontal sections and a high consistency between the two hemispheres was demonstrated in a 3D digital model (62). In terms of histological processing, sections stained for myelin were the most affected by shrinkage due to alcohol processing and had to be enlarged by average of 112% for overlay with Nissl sections. The recent use of a myelin staining procedure (50) applied on mounted rather than free-floating sections improved the fitting greatly.

On every map, a millimeter grid is adjusted to the positions of the posterior commissure (AP0) and interhemispheric planes in horizontal sections, to AP0 and the intercommissural plane DV0 in sagittal sections, and to the intercommissural and interhemispheric planes in frontal sections. In sagittal and horizontal sections, the midcommissural (mcl) and anterior commissural (ac) levels are also indicated.

REFERENCE COORDINATE SYSTEM

The ac–pc reference plane is defined by the axis passing through the centers of the two commissures, as also used by Mai et al. (32). We estimate this measurement as more accurate in terms of identification and correlation with the variations in forms and thickness of the ac and pc, particularly in MRIs . The coordinates in the atlas maps are given in millimeters relative to the position of the pc, for frontal sections (P–, for posterior, A–, for anterior, and AP0, for pc level; **Figs. 4.1** to **4.22**), to the ac-pc plane (D–, for dorsal, V–, for ventral, and DV0 for ac–pc plane; **Figs. 3.1** to **3.13**) for horizontal sections, and to the thalamo-ventricular border or interhemispheric plane (L0 or L–, respectively) for sagittal sections (**Figs. 3.14** to **3.25**; **Figs. 4.23** to **4.47**). The terms horizontal and frontal correspond to axial and coronal, respectively, in MRI domain.

MAGNETIC RESONANCE IMAGES

The MRIs in this book are from two principal sources: *i*) per- and postoperative examinations from patients undergoing stereotactic surgery for the treatment of functional disorders (e.g., Parkinson’s disease, essential tremor, neurogenic pain), and *ii*) autopsy brain two weeks to several months after fixation.

For postoperative examinations, 17 stereotactic axial and 15 sagittal T1-weighted MRIs were acquired on a 1.5-Tesla scanner (Philips) with following parameters: slice thickness 2 mm/0.2 mm gap; FOV 30 mm; matrix 256 × 256; TE 20 ms; TR 500 ms. For lesion reconstructions, the coordinates of the center of the lesions were measured on horizontal [for anteroposterior (AP) and mediolateral (ML) coordinates] and sagittal [for dorsoventral (DV) and AP coordinates] MRIs using the eFilm (Merge e-Film, Milwaukee, Wisconsin, U.S.A.) program. These coordinates (“*effective*” lesion) were then transferred onto the atlas, where they were compared with the 3D coordinates of the “*intended*” lesion. The lesion reconstructions serve for mapping physiological data (stimulations, microrecordings) and correlation analyses with clinical outcomes. Peroperative 3D inversion recovery (IR) series (FOV 90 mm; matrix 256 × 256; 100 slices, thickness 1.6 or 2 mm; TSE factor 9; TE 13 ms; TR 2000 ms; acquisition voxel: 0.9/1.45/1.60 mm) were also obtained from a group of patients for atlas-to-MR registration (62). With the 3D reconstruction eFilm module, these images provide “in vivo” measurements of overall thalamic variations across individuals to compare with postmortem interindividual variability evaluation (**Fig. 6.5**).

In two autopsy brains, MRIs were acquired with a 3-Tesla scanner (Philips). Whole brains were placed in a plastic bag filled with 4% PAF or formalin and fixed in the scanner with foam pieces. For the first case (Hb7; Table 2.1), T1-weighted MRIs were acquired with the following parameters: FOV 220 mm; 400 × 400; TSE factor 15; TR 3000 ms; TE 80; thickness 2 mm/0 overlap; acquisition voxel: 0.55/0.56/2.0 mm: scan time three hours). For the second case, a protocol for high resolution proton density MRI was used: 2D multislice acquisition; FOV: 160 mm; matrix: 528 × 528; 52 coronal and 32 axial slices; 1.25 thickness/0 gap; TR 3000; TE 24; acquisition voxel size: 0.30 × 0.30 mm (coronal) and 0.31 × 0.31 (axial); scan time five hours for each series.

FIGURE 2.1 Guillotine procedure and bloc preparation for the thalamic atlas. (**A**) and (**B**) show a soft rubber brain model of a right hemisphere placed on a Plexiglas plate (**A**) and aligned on the intercommissural plane (Hor DV0) using a mirror (**B**). The guillotine knife in (**A**) is oriented orthogonal to this line for a section in the frontal plane (the line intercepting pc level is indicated by Fro AP 0). The bloc obtained by this procedure is shown in (**C**) for case Hb1 (Table 2.1), with the two axes DV 0 and AP 0 indicated by dotted lines in the diagram. Sections in case Hb1 were cut in the horizontal (right hemisphere) and sagittal planes (left hemisphere) and the two drawings in (**D**) illustrate the horizontal level 4.5 mm dorsal to intercommissural plane (D4.5) and sagittal level 7.2 mm lateral to thalamo-ventricular border (L7.2). *Scale bars*: 2 cm, (**A**) and (**B**); 5 mm, (**C**); 2 mm, (**D**).

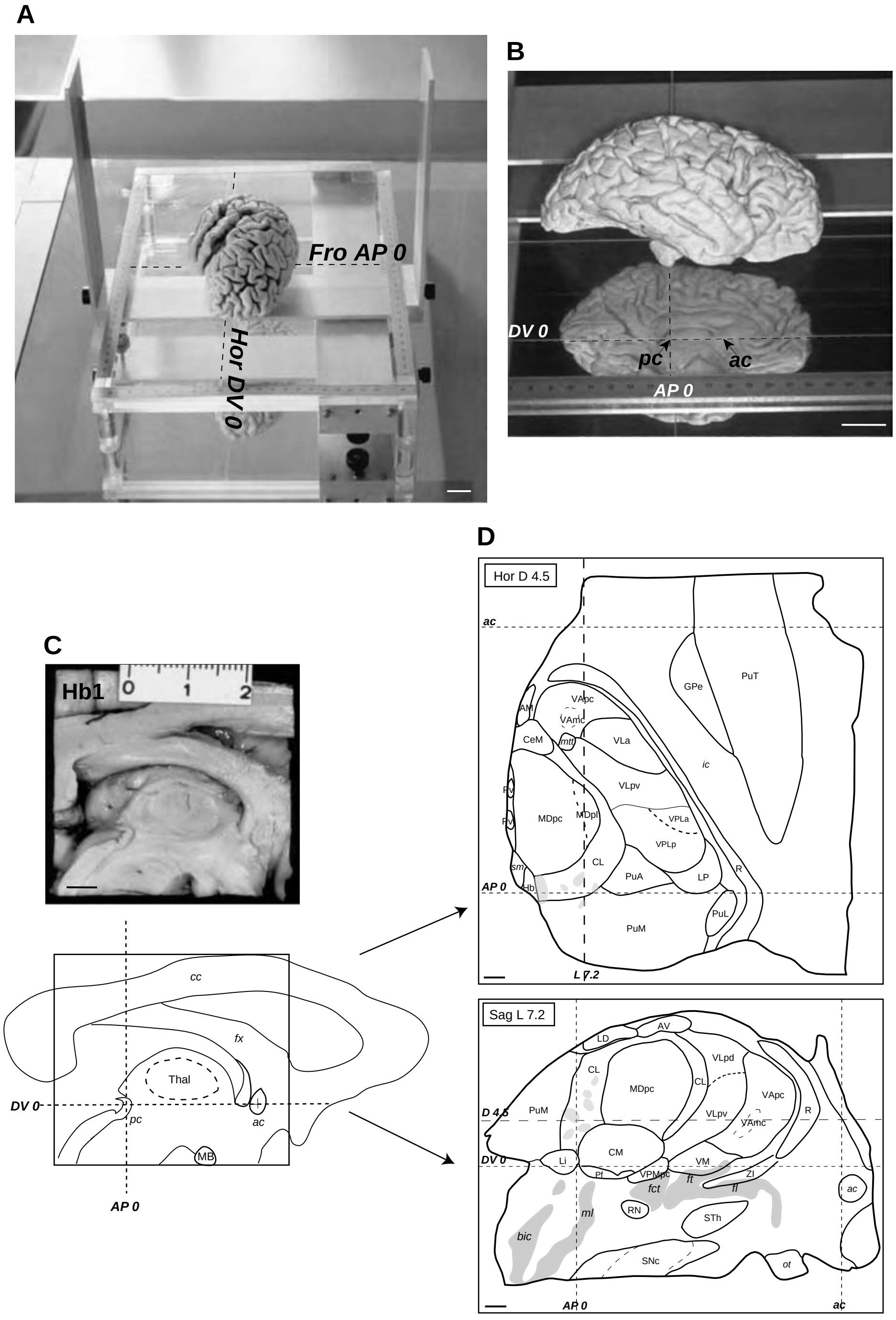

FIGURE 2.2 Block preparation for the basal ganglia atlas (case Hb7; Table 2.1). The two hemispheres are shown in (**A**) and (**B**) and the resulting guillotine blocs illustrated in (**C**) and (**D**). In the right hemisphere (**D**), the most medial part of the thalamus cut during interhemispheric section was placed again on the bloc to assess the positions of the two commissures. Examples of sections stained for AChE and cut in the frontal plane 17 mm anterior to pc and in the sagittal plane 14 mm lateral to interhemispheric plane (12 mm from thalamo-ventricular border) are illustrated in (**E**) and (**F**), respectively. *Scale bars*: 10 mm, (**A**) and (**B**); 5 mm, (**C–F**).

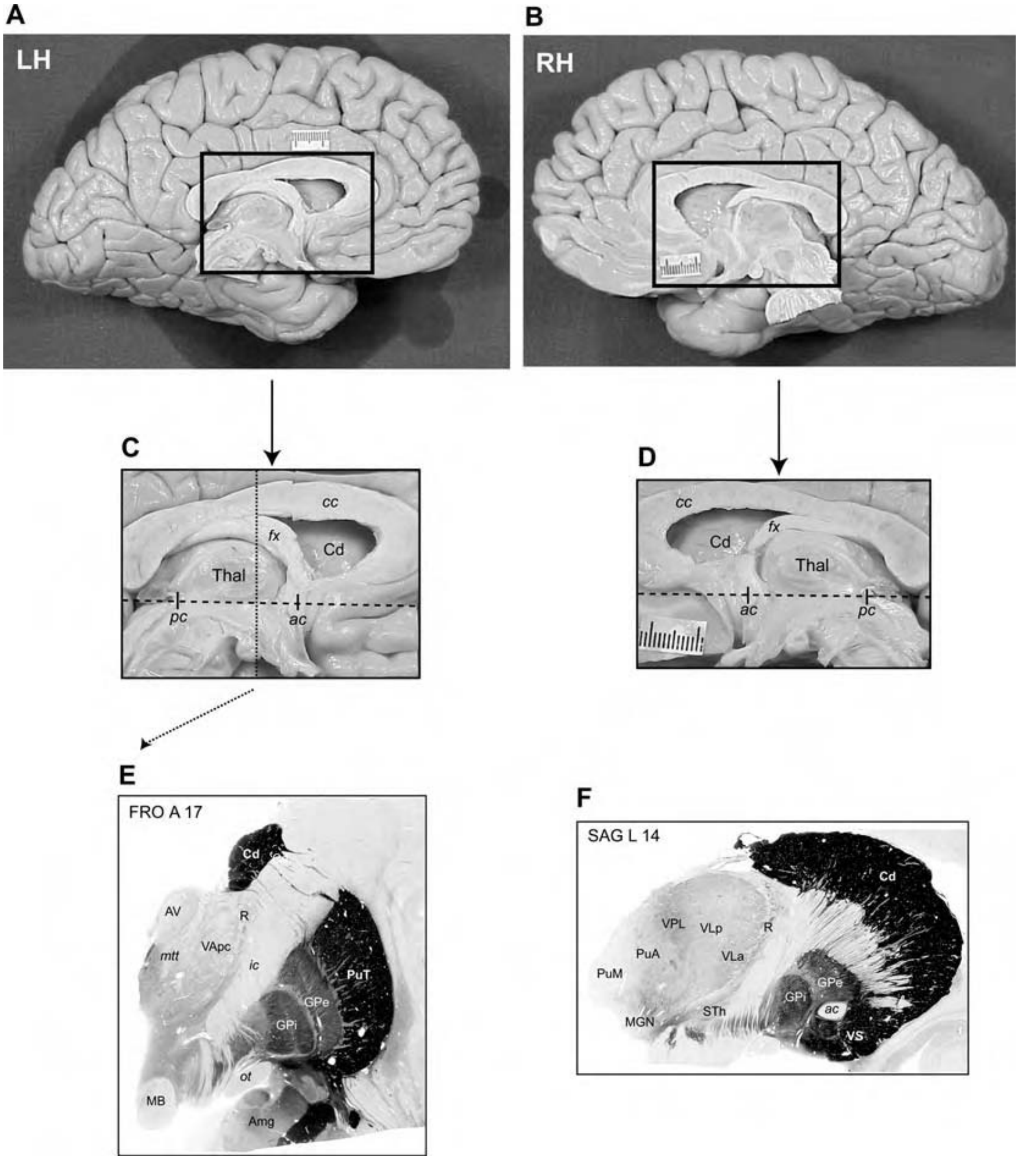

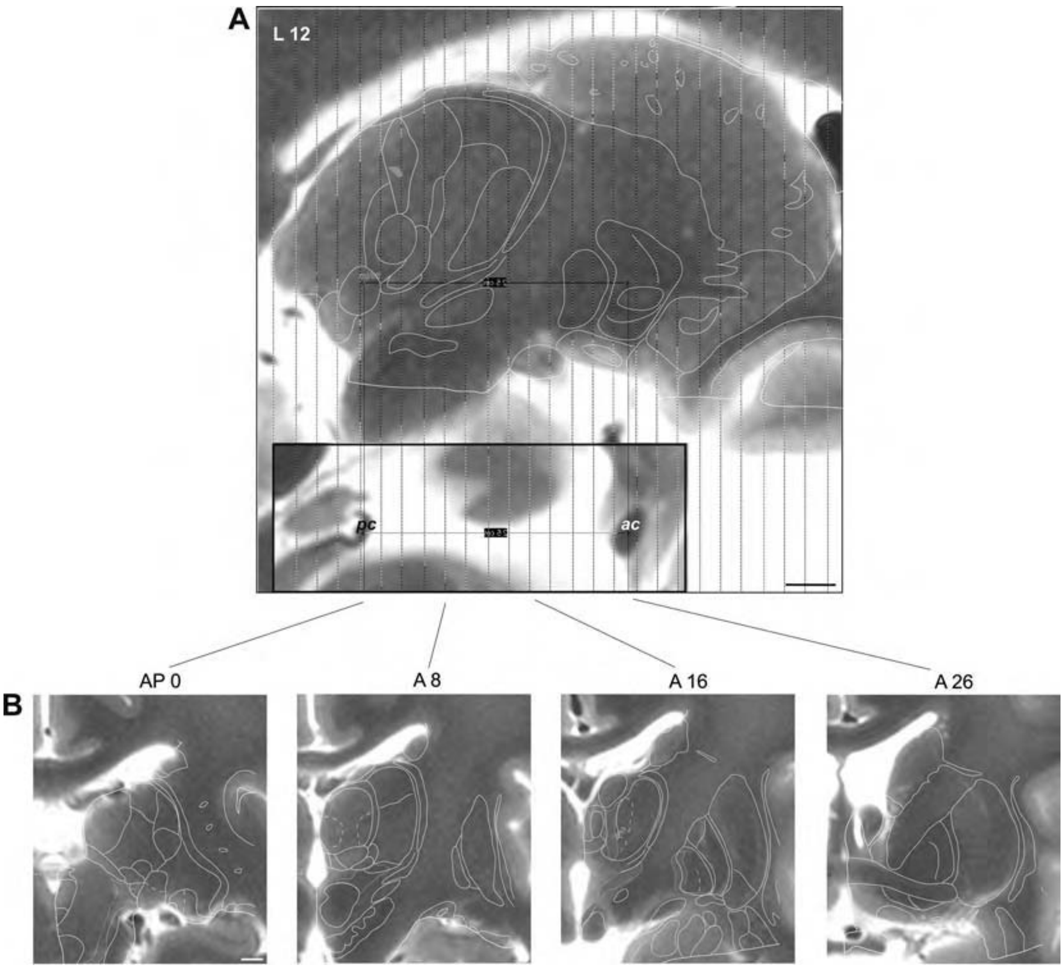

FIGURE 2.3 3-Tesla T1-weighted MRIs acquired from case Hb7 (Table 2.1) in (**A**) sagittal (12 mm lateral to inter-hemispheric plane) and (**B**) frontal stereotactic planes. The positions of the two commissures on midsagittal plane are shown in lower inset in (**A**). Anteroposterior levels of the frontal sections are indicated in millimeters anterior to pc (AP 0) level. Drawings of the thalamic and basal ganglia structures are superimposed onto the MRIs. The ac–pc distance is 25 mm postmortem corresponding to 26 mm "in vivo." *Scale bars*: 5 mm.

3 Thalamus

Atlas maps of the human thalamus in the horizontal and sagittal planes which were published earlier (47) are complemented in the present version (**Figs. 3.1–3.25**) with additional informations:

1. Ventral sections through basal ganglia (levels V2.7–V8.1) were added in the horizontal series (**Figs. 3.10–3.13**),
2. More lateral sections (up to level L23) were added in the sagittal maps (**Figs. 3.23–3.25**) to cover the whole thalamus,
3. Additional structures were included, such as part of the striatum, pallidum, and subthalamic fiber tracts, and some delimitations were refined (e.g., for the subdivisions of the substantia nigra). In more recent cases (Table 2.1), staining for AChE provided better delineation of some subdivisions [e.g., in CM (**Fig. 3.33**)].

A summary diagram of the compartmentalization of CaBP in the thalamus/subthalamic area and a histogram of the thalamic distribution of CaBP in terms of relative intensity of neuropil staining is given in **Figure 3.36**.

MAJOR GROUPS OF THALAMIC NUCLEI

The following classification of thalamic nuclei into five major groups is based on their location relative to the internal medullary lamina and on anatomo-functional criteria defined in non-human primates. In this classification, the MGN and LGN nuclei are included in the posterior group in spite of their functional and connectional characteristics closer to those of the lateral group, and the MD is integrated in the medial group, in spite of its more restricted and more specific connections than intralaminar and midline nuclei. The zona incerta (ZI) in the ventral thalamus is described in Chapter 5 together with the subthalamic pallidothalamic tract.

Lateral Group

Ventroposterior complex (VPL, VPM, VPI)
Ventral lateral posterior (VLp) and ventral lateral anterior (VLa)
Ventral anterior (VA)
Ventral medial (VM)

Medial Group

Mediodorsal (MD)
Intralaminar:
    Centre médian (CM)
    Parafascicular (Pf), subparafascicular (sPf)
    Central lateral (CL)
Midline:
    Central medial (CeM)
    Paraventricular (Pv)
    Medioventral (MV)
Habenula (Hb)

Posterior Group

Medial geniculate nucleus (MGN)
Lateral geniculate nucleus (LGN)

Posterior nucleus (Po)
Suprageniculate/limitans (SG/Li)
Lateral posterior (LP)
Pulvinar nuclei (PuM, PuI, PuL, PuA)

Anterior Group

Anteroventral (AV)
Anteromedial (AM)
Anterodorsal (AD)
Lateral dorsal (LD)

Reticular Nucleus (R)

MULTIARCHITECTONIC CHARACTERISTICS

The cytoarchitectonic criteria in terms of size and density of neurons have been described previously (47) and correspond closely to those reported in the human thalamus by others (30,46,63). These criteria for the major nuclei are described below and relative intensity of immunostaining for the calcium-binding proteins (CaBP) also summarized in **Figure 3.36**. The myeloarchitecture [described in more detail here than in our previous study (47) for its importance in defining fiber tracts that are of significance in stereotactic surgery], is described separately in Chapter 5.

Following the same grouping of nuclei (lateral, medial, posterior, and anterior groups), the present study, which is based on a larger number of cases and additional stainings (e.g., AChE, SMI-32), provides a more thorough description of the multiarchitectonic organization of the human thalamus. Histochemical staining for AChE, in particular, was very useful for thalamic and basal ganglia delimitations, although with some uneven distributions not necessarily respecting thalamic nuclear boundaries. Whole thalamus or specific areas are illustrated by photomicrographs in **Figures 3.26** to **3.35**.

Several conventions were adopted to represent thalamic subdivisions in the graphical maps (**Figs. 3.1–3.25**): continuous lines represent outlines for major nuclei and interrupted lines for subdivisions within a major nucleus (e.g., between MD or VLp subdivisions). While the borders were first delineated on the basis of cytoarchitectonic criteria, they were also adapted in some areas to account for specific staining to one or more other markers. Also, sub-structures, which were considered as particularly significant for the delineation of a given nucleus, are indicated. This is the case in the thalamus for islands of dense and darkly stained cells in the posterior part of the central lateral nucleus, which are represented by light grey areas (e.g., **Figs. 3.14–3.17**). Although other parts of the CL nucleus also present AChE-, CB-, or CR-rich patches, these are composed of smaller cells and more homogeneously distributed than in posterior CL.

Calcium-Binding Proteins

The differential distribution of calcium-binding proteins PV, CB and CR in the human thalamus has previously been described in detail (47,64–66) and is briefly reviewed here. Few additional thalamic subdivisions were added to the previous published version and the density of staining reupdated to account for more recent cases. In general, areas of dense cellular immunostaining coregister with those containing fiber staining and therefore the two are not separately described here. We refer to other reports (64–66) for more specific cellular versus axonal distributions in the human thalamus. The overall distribution shown in **Figure 3.36** is similar to that described previously (Fig. 5 in Ref. 47): the expression of PV immunoreactivity (-ir) is present in most thalamic nuclei, but with clear dominance in primary sensory (VPL/VPM, MGN, LGN) and motor (VLp) nuclei, as well as in the reticular nucleus (R). Immunoreactivity to CB is enhanced in the VA/VLa nuclei, the posterior complex (SG-Li, Po), VPI, VPMpc, sPf, and intralaminar CL nuclei. Some of the same regions characterized by dense CB-ir are also enriched in CR-ir (i.e., posterior complex, CL, sPf) but CR-ir is more strongly expressed in more limbic thalamic regions [anterior group, midline and paraventricular nuclei] and in R. The distribution of CaBP allows better definition of some subnuclear borders, such as in the MGN between the large central portion of the nucleus enhanced in PV-ir, and the smaller ventral part (e.g., MGv, **Fig. 3.34**) characterized by enhanced CB-ir. In the LGN, both the parvo- and magnocellular divisions exhibit enhanced PV-ir, but the magno- more than the parvocellular division expresses additional CR-ir (**Fig. 3.33**). PV-ir is also relatively dense in the AV nucleus and lateral part of CM (CMl) (**Figs. 3.26** and **3.27**). In the VA nucleus, there is a gradient for higher CB-ir in the parvocellular (VApc) and higher PV-ir in the magnocellular division (VAmc).

The histograms in **Figure 3.36** summarize the results:

1. PV- and CB-ir densest areas are largely complementary in the thalamus, though light CB-ir is also expressed in PV-ir dense ventral nuclei (particularly VPL), and conversely, PV-ir is expressed in CB-ir dense nuclei (e.g., VLa/VA).
2. CR-ir is dominantly expressed in nuclei associated with the limbic system (midline, Pv, AV), but is also present in primary sensory and motor nuclei enhanced in PV-ir, as well as in R.
3. Intralaminar CL, posterior complex (Po, SG, Li), and VPMpc express similar high levels of CB- and CR-ir.
4. Only few areas express relatively low levels of CaBP-ir, that is, MD, PuM and medial CM/parafascicular (Pf) nuclei. Interestingly, MD and PuM which are the largest in the human thalamus share many characteristics, from morphological (similar cytoarchitecture) to connectional (few peripheral afferents and involved in a large thalamocorticothalamic network including most, if not all, associative and paralimbic areas of cortex).

Acetylcholinesterase

Histochemical staining for acetylcholinesterase (AChE) was particularly useful to delimit medial thalamic regions. In particular, in the centre médian-parafascicular complex (CM-Pf), the border between lateral and medial parts of CM, and between CM and Pf is clearly identified by an increasing gradient of AChE staining (e.g., **Figs. 3.33** and **3.35**). This distinction is not seen or not very clearly with the CaBP. In the CL nucleus (which corresponds for the most part to the internal medullary lamina as defined by others, except that it extends posteriorly to include a region comprised between the PuM and MDpc), dense cellular patches are strongly stained for AChE and correspond to clusters immunostained for CB and CR. This is particularly marked in the posterior part of the nucleus (**Fig. 3.33**) that was already included by Jones and colleagues (46,67) in the CL according to cyto- and histochemical criteria. Similar to the CL patches, the limitans nucleus (Li) exhibits strong AChE (**Figs. 3.33** and **3.34**). In the MD nucleus, the magnocellular (MDmc) tends to show more intense AChE than MDpc, although in the latter subdivision, there are small cell clusters that express enhanced AChE, and CB- and CR-ir, as in the CL nucleus (**Figs. 3.26** to **3.28**).

In the lateral thalamus, the limit between VLa/VA nuclei expressing strong AChE and VLp, which is relatively lightly stained, is particularly obvious in sagittal and horizontal sections (**Figs. 3.29** and **3.32**), and corresponds also to differences in CB-ir, as described above. Posteriorly, the boundary between LP and PuM, which is not very sharp in Nissl or CaBP-ir, corresponds to a clear transition from high to low AChE staining (e.g., **Figs. 3.32** and **4.48**). Overall, the pattern of AChE staining is similar to that described by Hirai and Jones (46) in the human thalamus, and to that reported in the nonhuman primate (34,68).

FUNCTIONAL CONSIDERATIONS

The relation between neurochemical compartmentalization of the thalamus and functionally distinct systems has been demonstrated in the monkey where tracing of connections was related to CaBP territories. A similar neurochemical organization in the human thalamus has been discussed at length previously (47) and will be only briefly reviewed here to account for recent data obtained in the monkey brain.

In the somatosensory system, spinothalamic afferents (for nociceptive pathways) to the thalamus were directly related to areas of dense immunostaining to the calcium-binding protein calbindin (CB) in the monkey (43,69–71) and indirectly to similar CB territories in the human thalamus (47,72,73). Our results are in favor of a larger thalamic territory involved in pain processing than that proposed by Craig et al. (72,73), comprising VPI, VPMpc, Po, sPf, Li and dense cellular islands of the posterior CL. This complies with earlier observations on spinothalamic pathways in human (74,75). As will be discussed in Chapter 5, we were not able to clearly separate spinothalamic fibers on the basis of CaBP, except in some instances where immunostaining to CB was expressed by fibers that are directed to thalamic nuclei known as spinothalamic recipients (e.g., **Figs. 3.26** and **3.34**). The other subdivisions of the VP complex [i.e., VPL (p and a) and VPM, which receive primary afferents from the medial lemniscus and trigeminal tract, respectively] express high PV-ir (**Figs. 3.31** and **3.33**) and only low levels of CB-ir. The presence of CB-ir in the VPL-VPM complex, as well as in other "primary" sensory nuclei, has been proposed to represent a "matrix" of smaller cells projecting more diffusely to superficial cortical layers than PV-ir neurons projecting to layer IV (37,76–77).

In the auditory system, subdivisions characterized by CB- and PV-ir were related to lemniscal and nonlemniscal pathways in nonhuman primates (78,79). In the present study, a large part of the MGN expresses high PV-ir, while a small ventral part shows particularly dense CB-ir (**Fig. 3.34**). These two regions seem to correspond to the "ventral divison" projecting to primary auditory cortex and to the posterior part of the ventral division projecting mainly to nonprimary auditory cortex, respectively, in monkeys (79–81). The medial division (MGm) contains both PV- and CB-ir neuropil. In the visual system, the parvo- and magnocellular layers of the LGN associated with functionally distinct pathways can be differentiated by higher CR-ir in LGNm, and stronger PV-ir in LGNp (**Fig. 3.33**), while interlaminar neurons express CB-ir [see also (82)].

In the motor system, chemically distinct thalamic territories were associated with the two major afferent motor pathways in the monkey (i.e., the cerebello- and pallidothalamic tracts) and to their projections to frontal cortex (33,83–84). Indirect evidence suggests a similar relation in the human thalamus (47). The VLp is clearly differentiated from more anterior motor thalamic nuclei by light AChE, enhanced PV-ir, and little or no CB-ir (**Figs. 3.27–3.32**). The association between CB-ir negative territory and cerebellar afferents has been recently demonstrated in the monkey (33). As will be shown in Chapter 5, the cerebellothalamic afferents to VLp also present some enhanced PV-ir. More anterior parts of the motor thalamus (VLa, VA, VM) express progressively more CB-ir and relatively moderate PV-ir in comparison to VLp (**Figs. 3.28, 3.29,** and **3.32**). There is thus a complementary compartmentalization of the motor nuclei based on CB-ir which corresponds to CB-ir negative territory associated primarily with cerebellar inputs and CB-ir positive territory associated with dominant pallidal afferents (33,47,83,85). This complementary distribution is not only related to the afferents, since the CM, which expresses PV-ir (lateral part) and no CB-ir, receives presumably also pallidal afferents (85,86).

FIGURES 3.1 to 3.13 These figures present a series of drawings of horizontal sections of the human thalamus and basal ganglia (right hemisphere of case Hb1; Table 2.1) oriented parallel to the intercommissural stereotactic plane (DV 0, shown in **Fig. 3.9**) and represented in a dorsal to ventral sequence. In each drawing the posterior commissure (*AP 0*), midcommissural (*mcl*), and anterior commissure (*ac*) levels (*dotted horizontal lines*) are indicated. Dorsoventral levels are given in millimeters dorsal (D) or ventral (V) to intercommissural plane DV 0 in the lower right hand-side of each drawing (see the text section on "Methods" for the coordinate system). The interhemispheric plane corresponds to the vertical line intersecting the mediolateral axis at 0. Each division on the grid corresponds to 1 mm "in vivo" and the intercommissural distance is 25 mm. Light grey areas in the CL nucleus correspond to dense cellular clusters. Moderate grey areas indicate subthalamic fiber tracts.

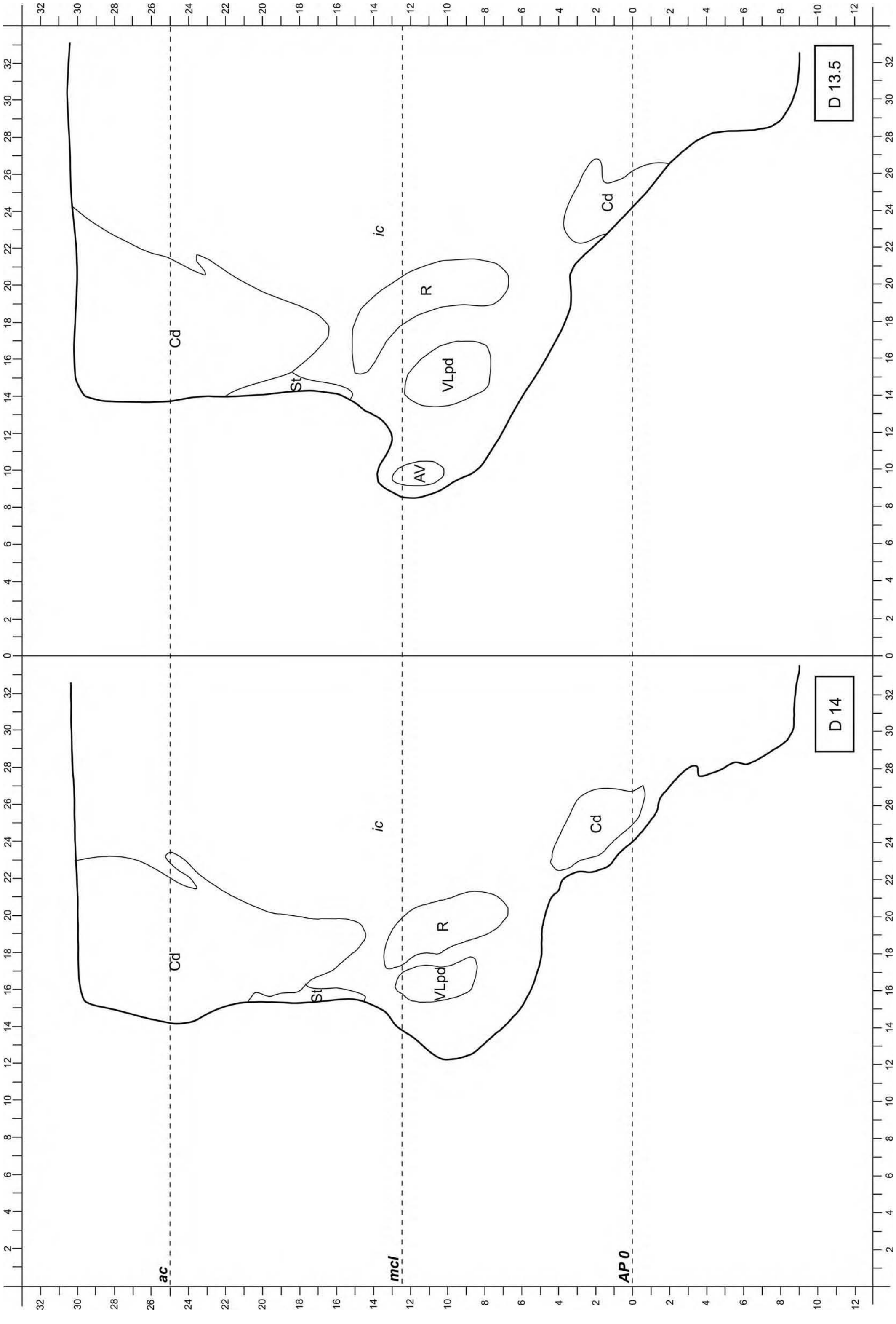
D 13.5
D 14
Cd
Cd
Cd
Cd
ic
ic
R
R
VLpd
VLpd
St
St
AV
ac
mcl
AP 0
32 30 28 26 24 22 20 18 16 14 12 10 8 6 4 2 0 2 4 6 8 10 12
32 30 28 26 24 22 20 18 16 14 12 10 8 6 4 2 0 2 4 6 8 10 12 14 16 18 20 22 24 26 28 30 32

FIGURE 3.1

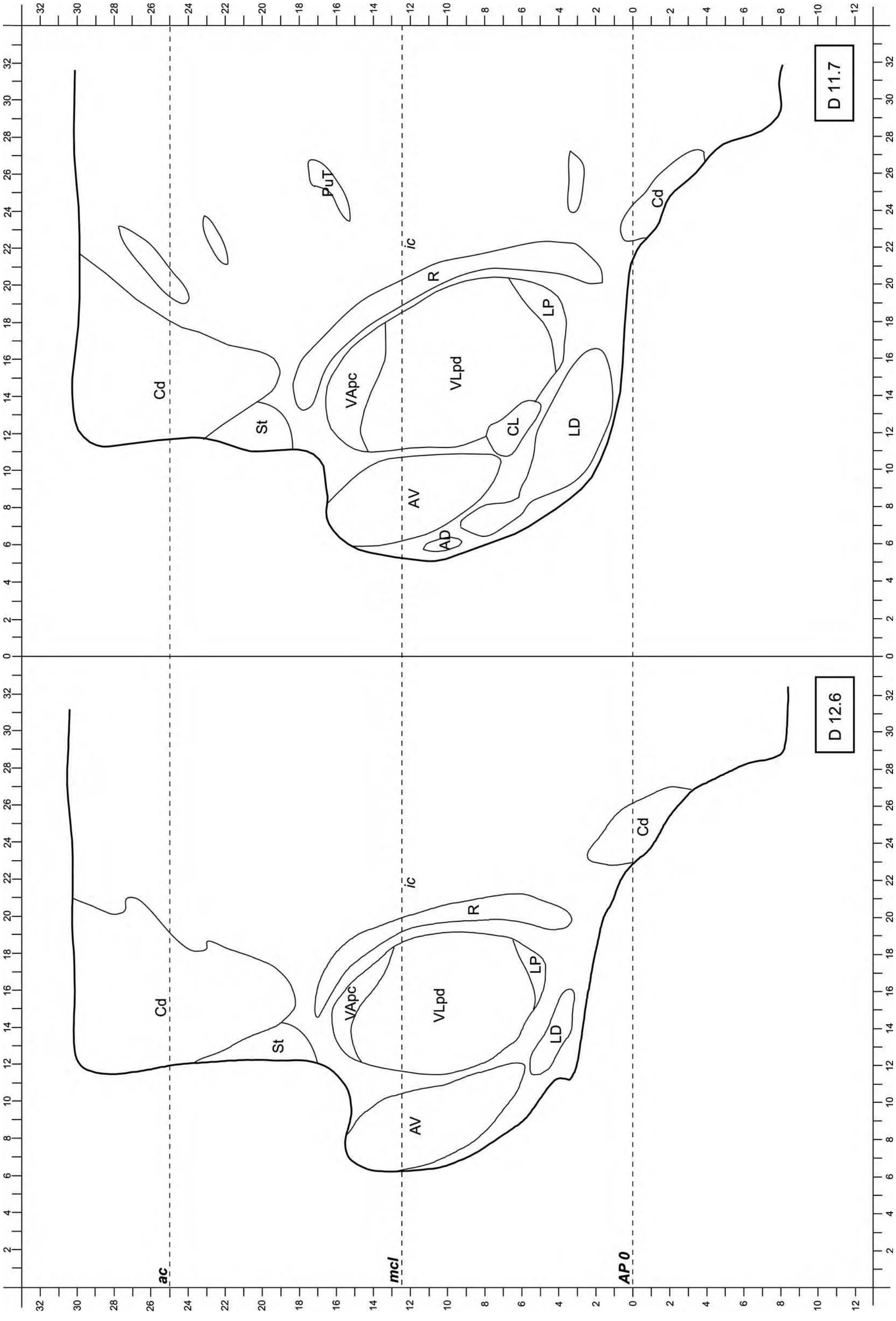
D 11.7
D 12.6
Cd
St
VApc
VLpd
LP
LD
CL
AV
AD
R
ic
PuT
ac
mcl
AP 0
32
30
28
26
24
22
20
18
16
14
12
10
8
6
4
2
0

FIGURE 3.2

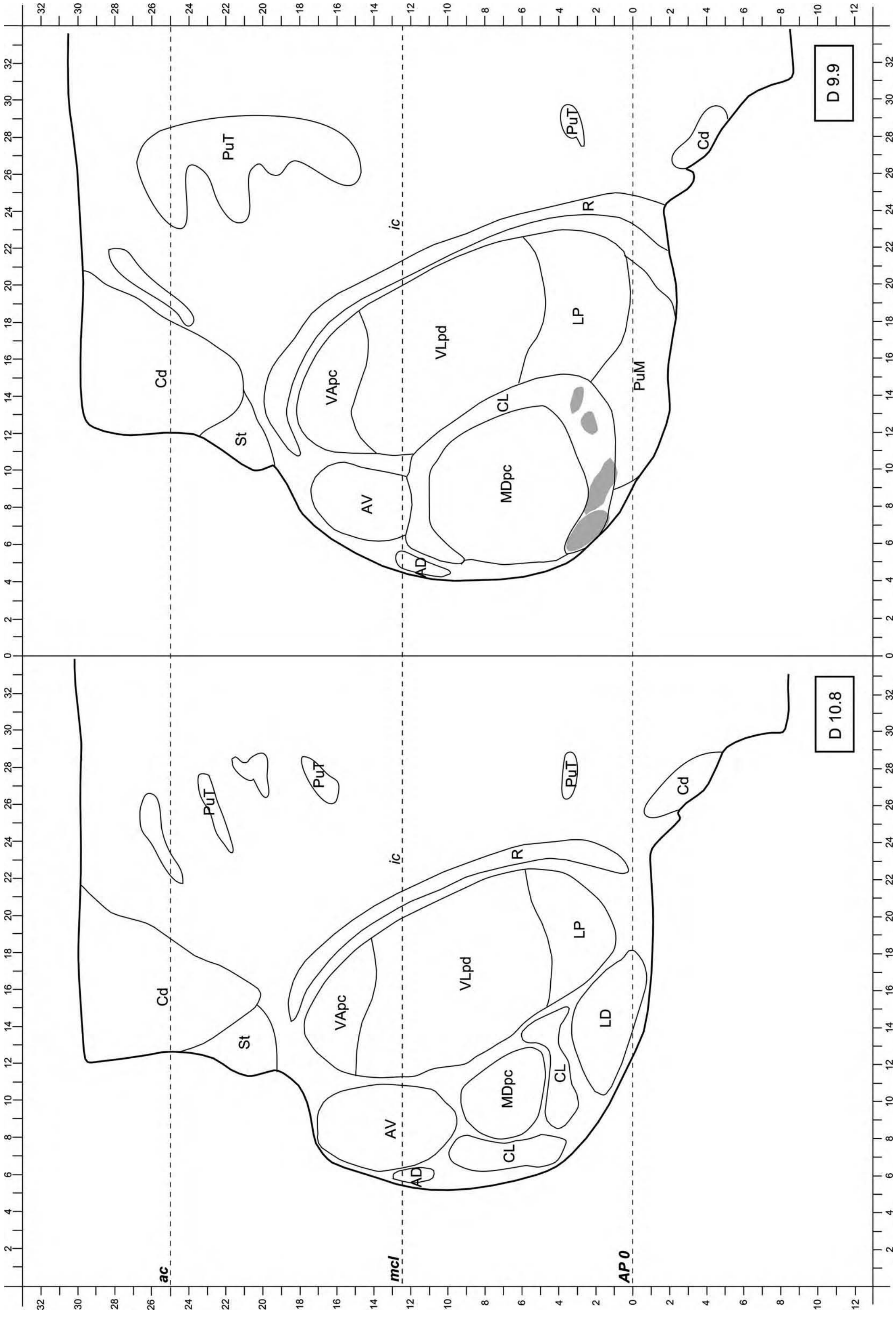
D 9.9
D 10.8
ac
mcl
AP 0
ic
PuT
Cd
St
VApc
VLpd
LP
PuM
CL
MDpc
AV
AD
R
LD
32
30
28
26
24
22
20
18
16
14
12
10
8
6
4
2
0
2
4
6
8
10
12

FIGURE 3.3

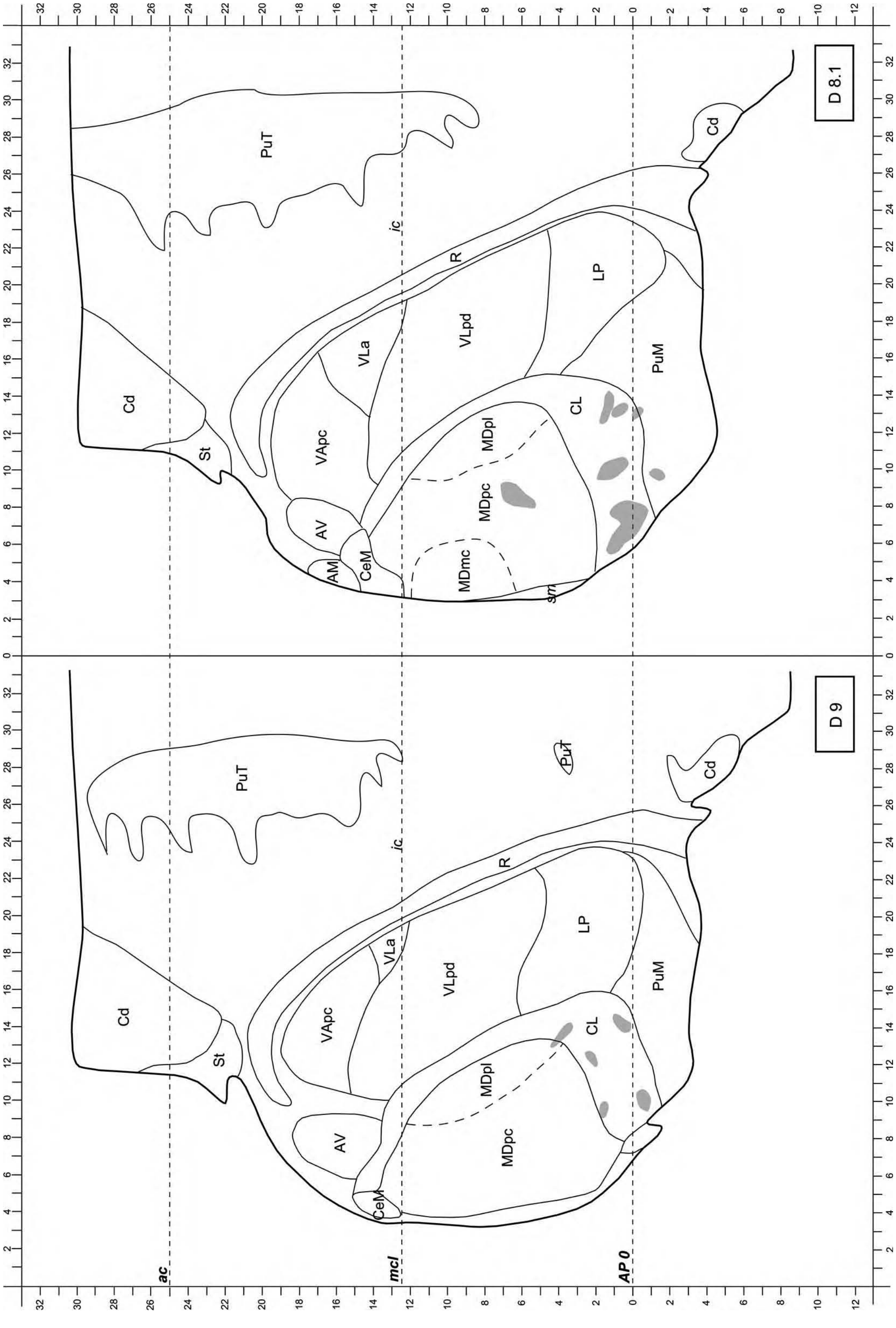
D 8.1
D 9
PuT
Cd
St
ic
R
VApc
VLa
VLpd
LP
PuM
CL
MDpl
MDpc
MDmc
AV
AM
CeM
sm
ac
mcl
AP 0

FIGURE 3.4

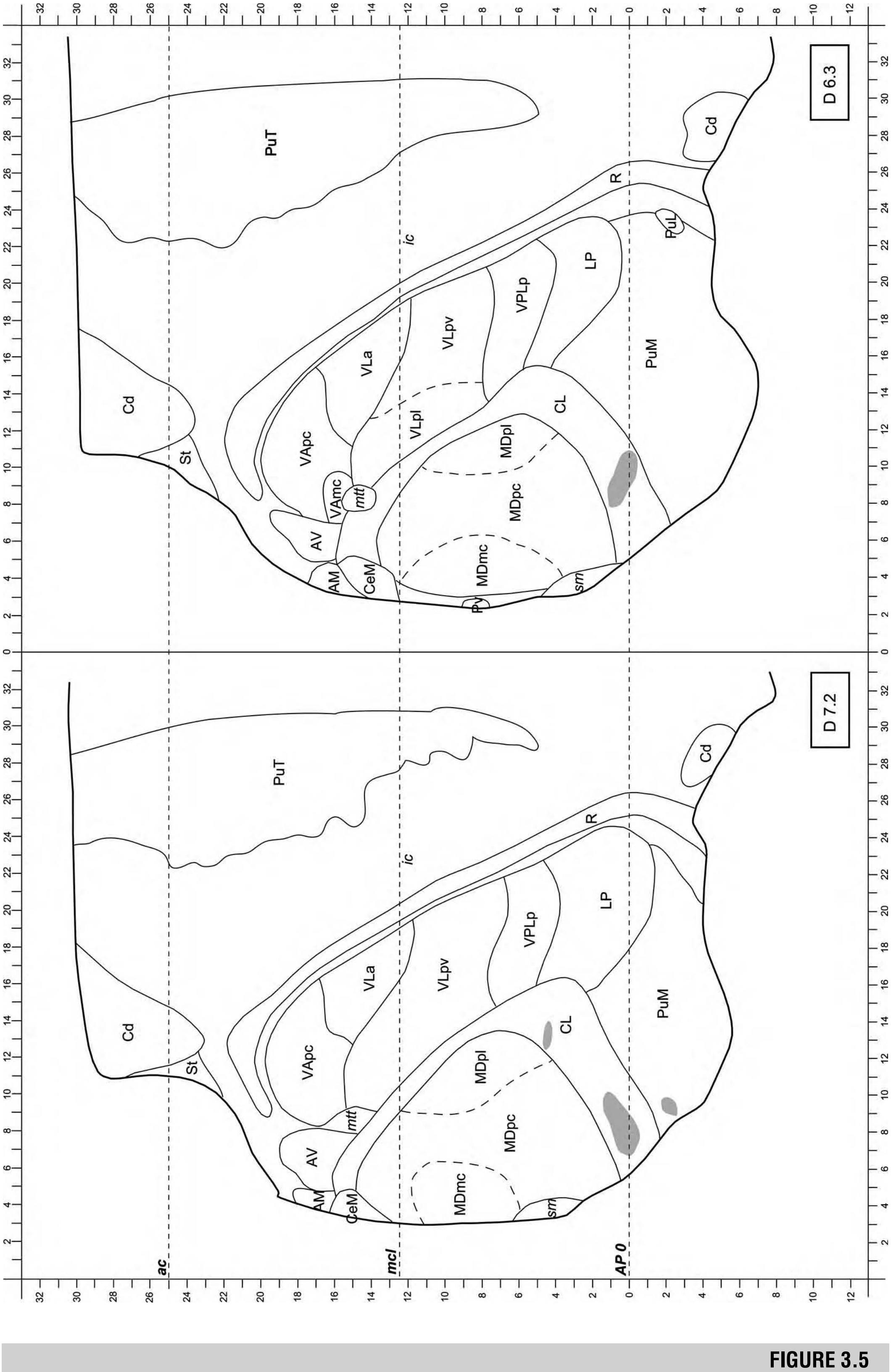
D 6.3
PuT
Cd
St
R
ic
PuL
LP
VPLp
VLpv
VLa
VApc
VAmc
mtt
VLpl
MDpl
CL
PuM
MDpc
MDmc
AV
AM
CeM
Pv
sm
D 7.2
ac
mcl
AP 0
32
30
28
26
24
22
20
18
16
14
12
10
8
6
4
2
0

FIGURE 3.5

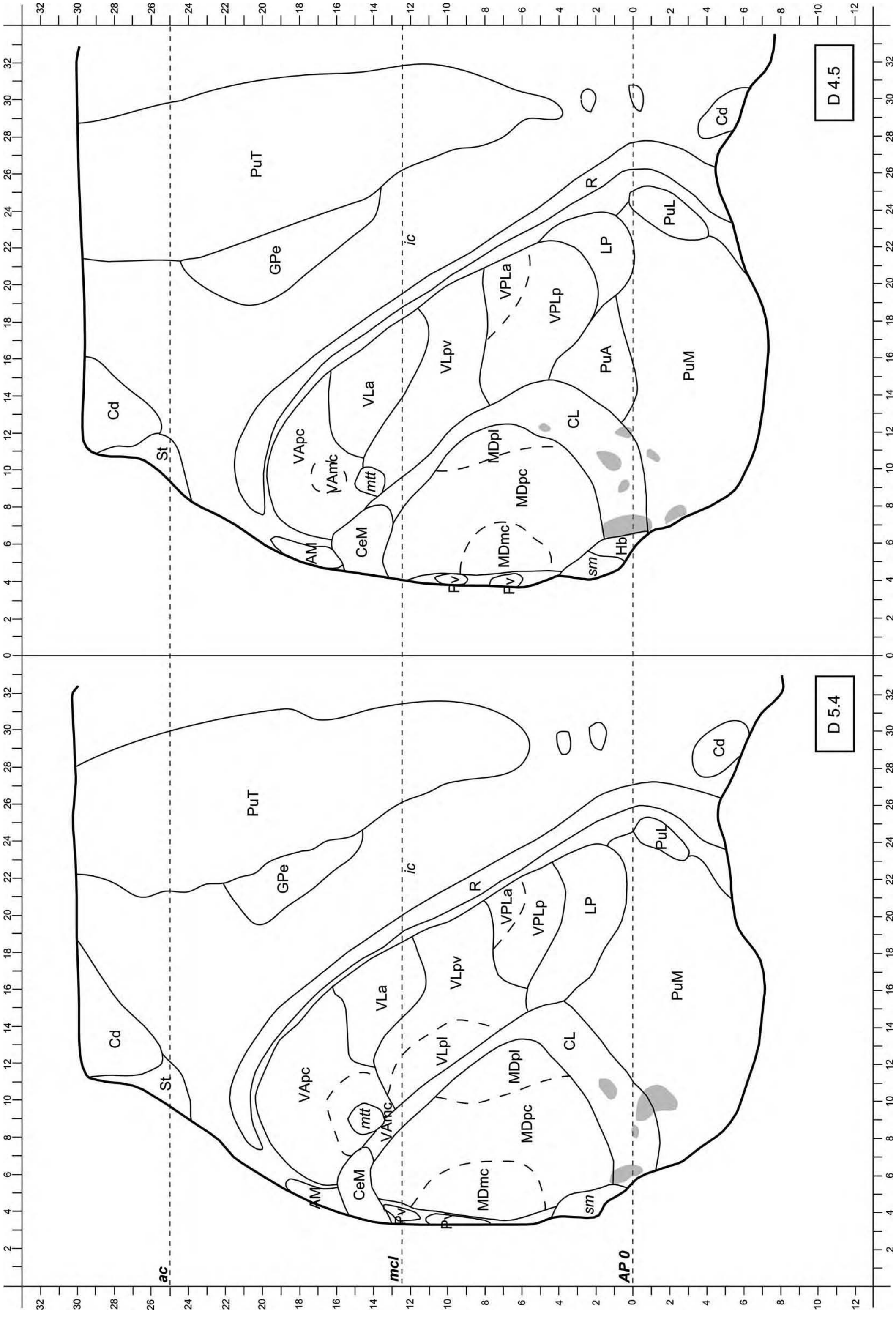
D 4.5
PuT
GPe
Cd
St
ic
R
PuL
LP
VPLa
VPLp
PuA
PuM
VLpv
VLa
VApc
VAmc
mtt
CL
MDpl
MDpc
MDmc
CeM
AM
Pv
sm
Hb
D 5.4
VLpl
ac
mcl
AP 0
32
30
28
26
24
22
20
18
16
14
12
10
8
6
4
2
0

FIGURE 3.6

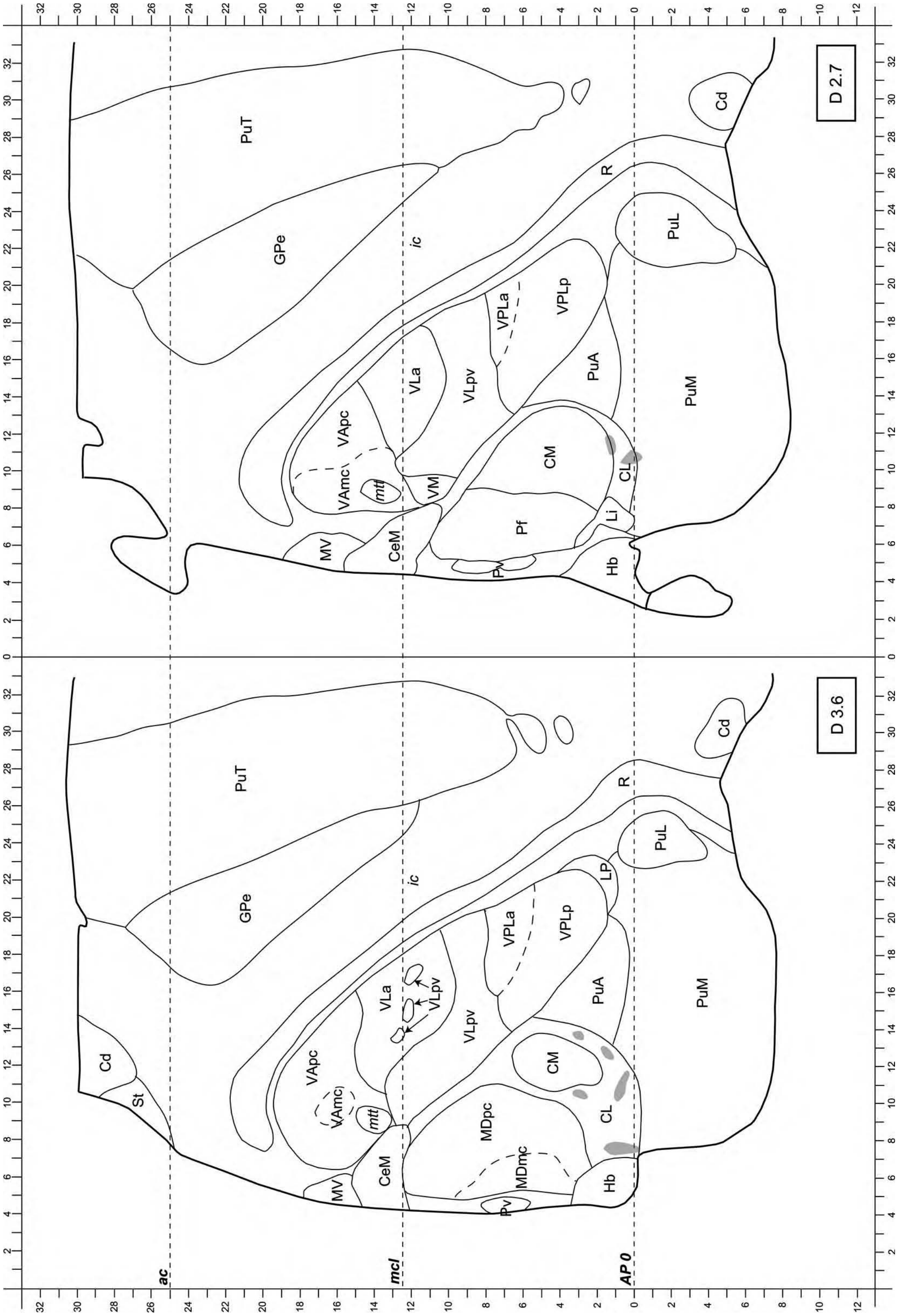
D 2.7
PuT
GPe
ic
R
Cd
PuL
VPLa
VPLp
VLa
VLpv
PuA
PuM
VApc
VAmc
mtt
VM
CM
CL
Li
Pf
CeM
MV
Pv
Hb
D 3.6
Cd
St
PuT
GPe
ic
R
Cd
PuL
LP
VPLa
VPLp
VLa
VLpv
VLpv
PuA
PuM
VApc
VAmc
mtt
CM
CL
MDpc
MDmc
CeM
MV
Pv
Hb
ac
mcl
AP 0
32 30 28 26 24 22 20 18 16 14 12 10 8 6 4 2 0 2 4 6 8 10 12
2 4 6 8 10 12 14 16 18 20 22 24 26 28 30 32

FIGURE 3.7

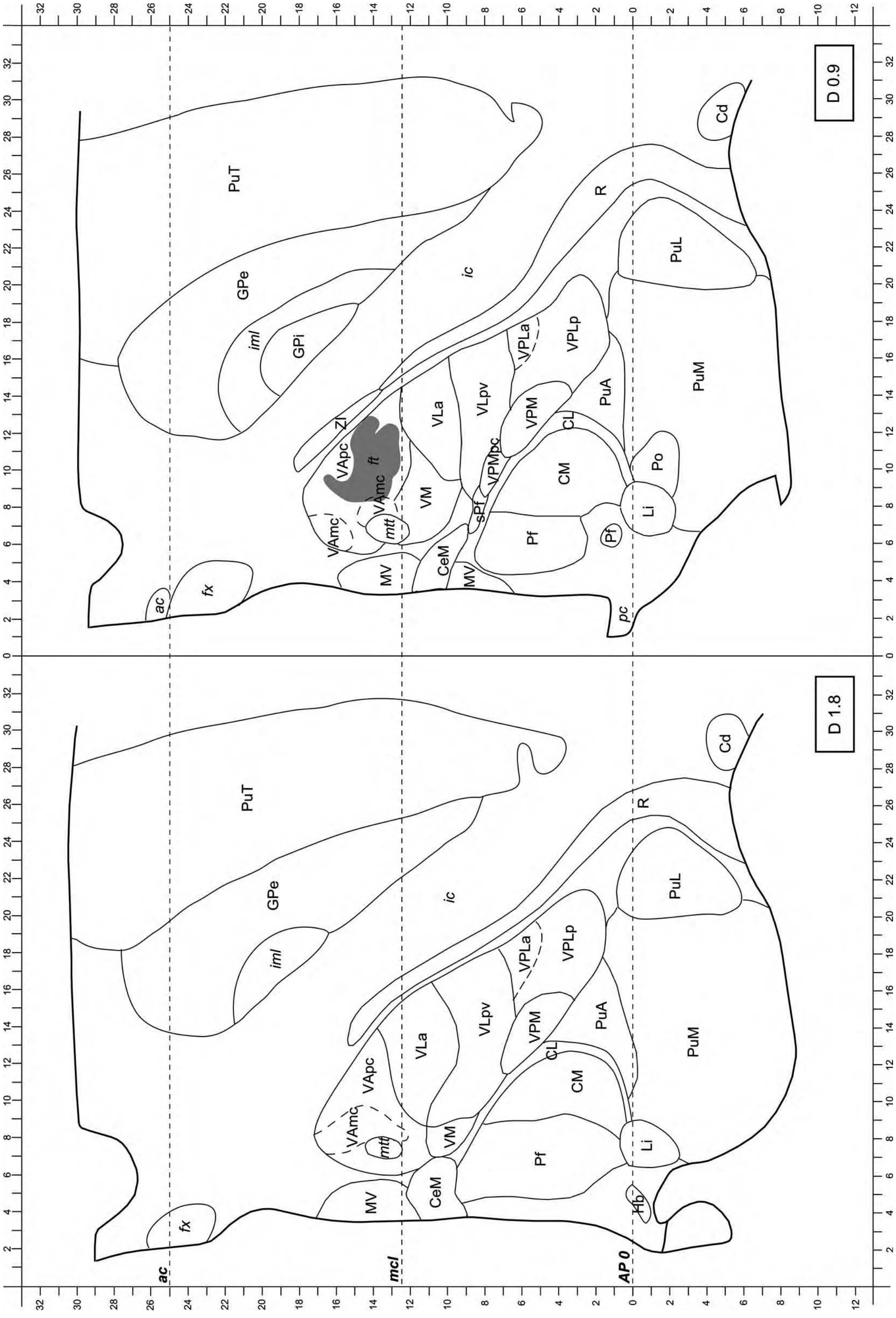
D 0.9
PuT
GPe
GPi
iml
ic
R
Cd
PuL
PuM
VPLa
VPLp
VLpv
VLa
VPM
PuA
CL
ZI
VApc
ft
VAmc
VPMpc
CM
Po
Li
VM
sPf
mtt
Pf
CeM
MV
fx
ac
pc
D 1.8
PuT
GPe
iml
ic
R
Cd
PuL
PuM
VPLa
VPLp
VLpv
VLa
VPM
PuA
CL
VApc
VAmc
mtt
CM
VM
Pf
Li
CeM
MV
Hb
fx
ac
mcl
AP 0
32
30
28
26
24
22
20
18
16
14
12
10
8
6
4
2
0
2
4
6
8
10
12

FIGURE 3.8

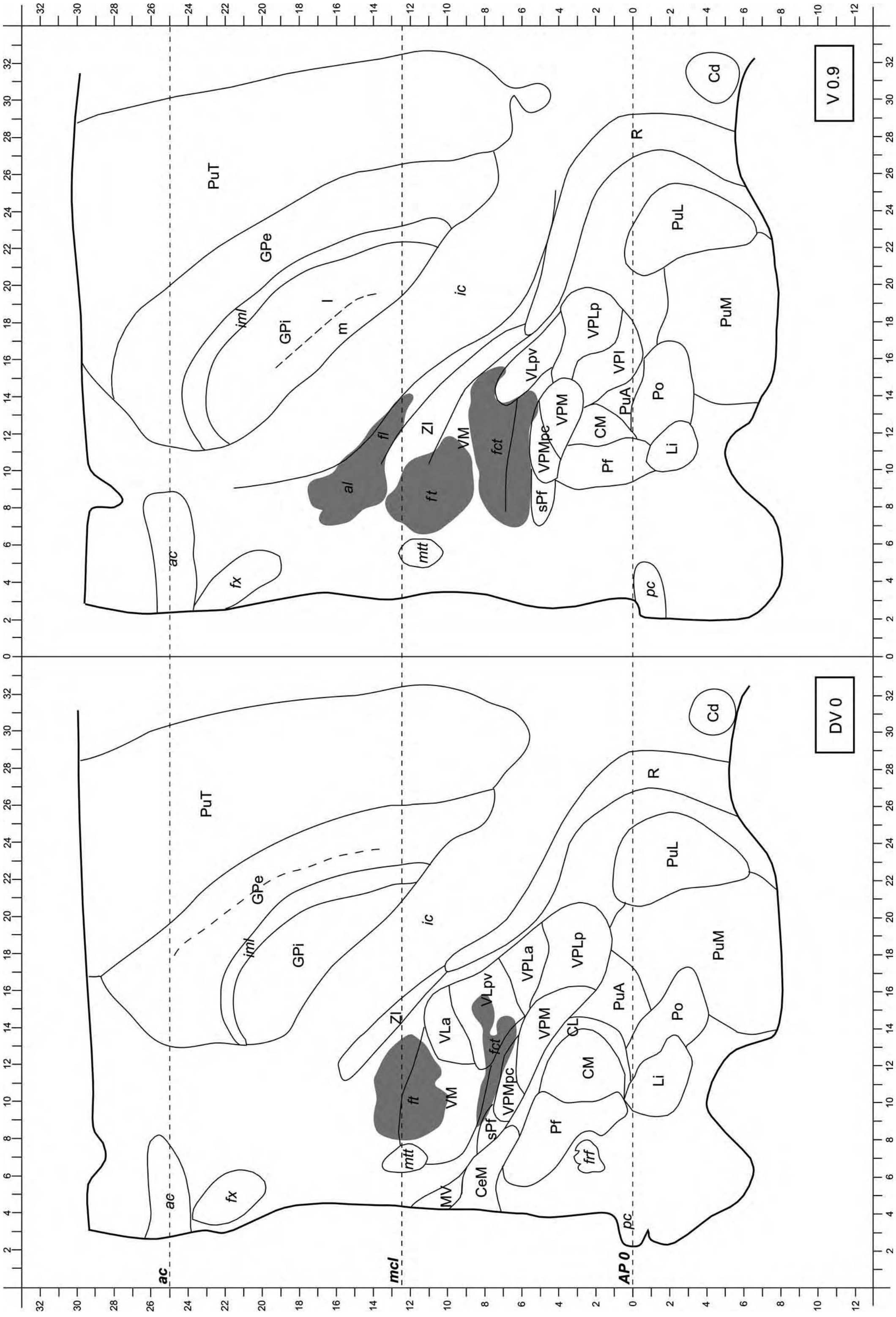
DV 0
PuT
GPe
iml
GPi
ic
ZI
VLa
VLpv
VPLa
VPLp
VPM
CL
PuA
PuL
PuM
Po
Li
CM
Pf
frf
ft
VM
fct
VPMpc
sPf
mtt
CeM
MV
fx
ae
pc
R
Cd
ac
mcl
AP 0
V 0.9
PuT
GPe
iml
GPi
l
m
ic
ZI
fl
al
ft
VM
fct
VLpv
VPLp
VPl
VPM
VPMpc
sPf
CM
Pf
PuA
Po
Li
PuL
PuM
R
Cd
mtt
ac
fx
pc

FIGURE 3.9

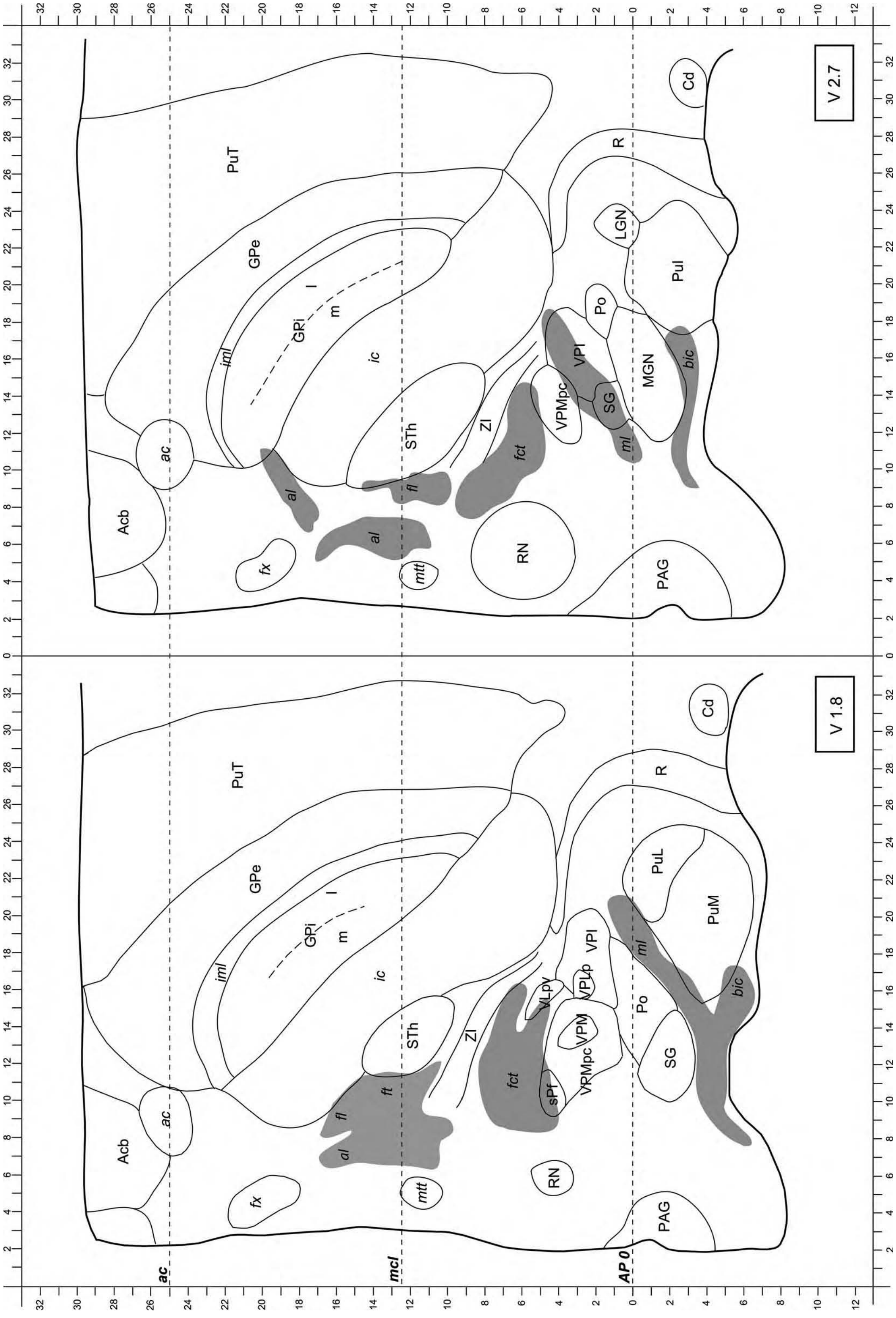
V 2.7
PuT
GPe
GPi
iml
l
m
ic
STh
ZI
fct
fl
al
ac
Acb
fx
mtt
RN
PAG
VPMpc
VPl
SG
ml
MGN
bic
Po
Pul
LGN
R
Cd
V 1.8
PuT
GPe
GPi
iml
l
m
ic
STh
ZI
fct
ft
fl
al
ac
Acb
fx
mtt
RN
PAG
VLpv
VPLp
VPl
VPM
VPMpc
sPf
Po
SG
ml
bic
PuL
PuM
R
Cd
ac
mcl
AP 0
32
30
28
26
24
22
20
18
16
14
12
10
8
6
4
2
0
2
4
6
8
10
12

FIGURE 3.10

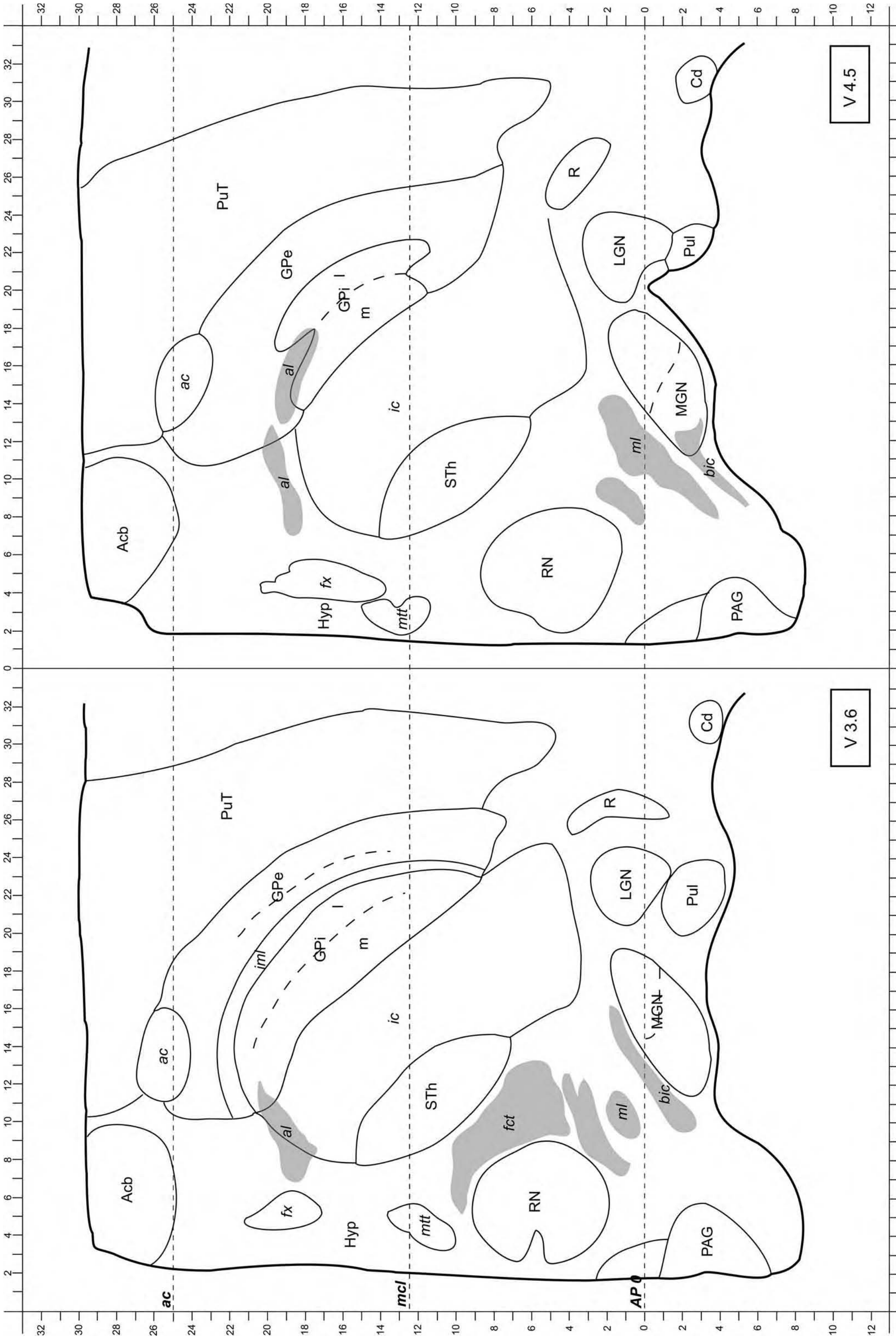
V 4.5
V 3.6
PuT
GPe
GPi
l
m
iml
ac
al
ic
STh
fct
ml
bic
R
LGN
Pul
MGN
Cd
Acb
fx
Hyp
mtt
RN
PAG
ac
mcl
AP 0
32
30
28
26
24
22
20
18
16
14
12
10
8
6
4
2
0
2
4
6
8
10
12

FIGURE 3.11

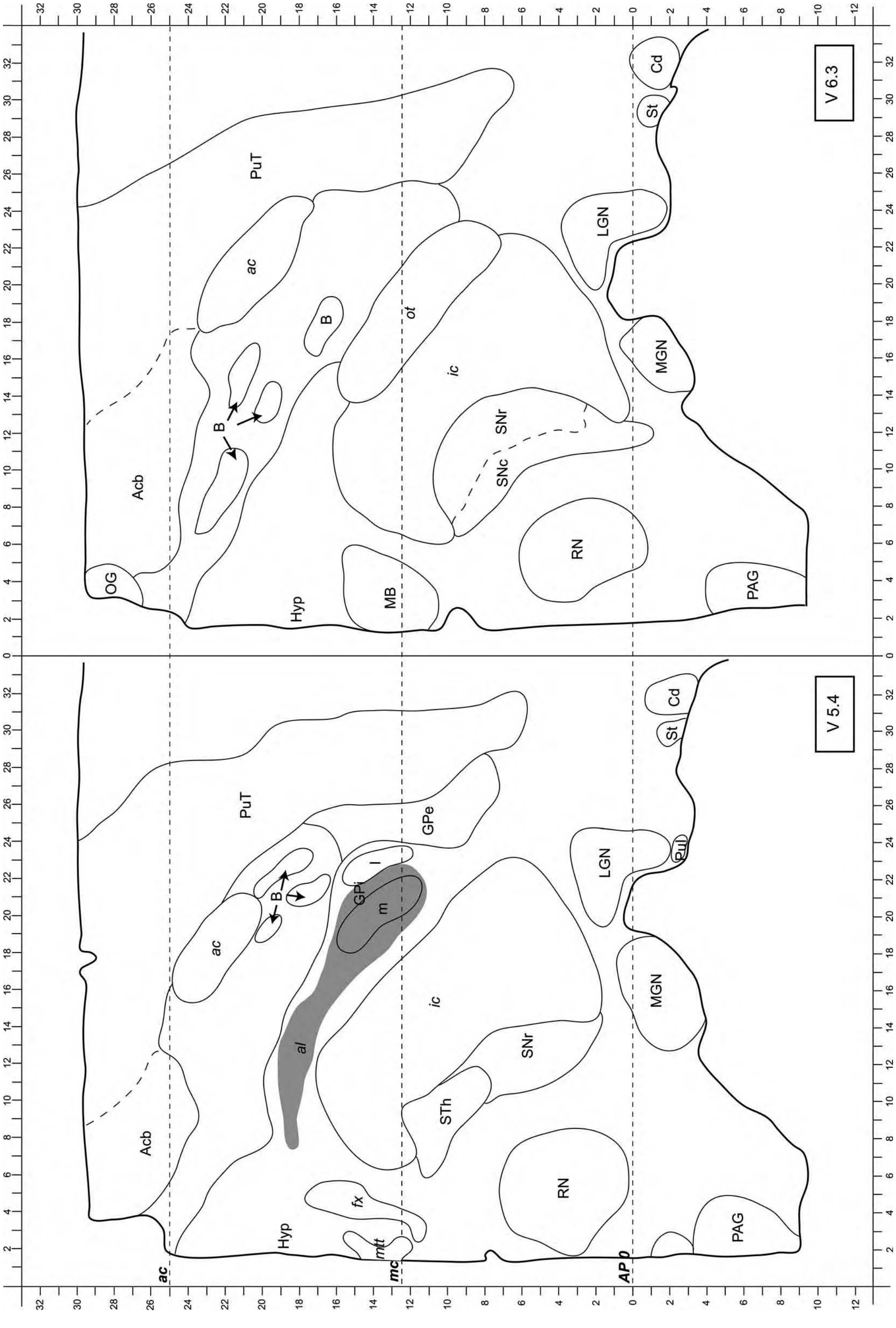
V 6.3
PuT
ac
B
B
ot
ic
SNr
SNc
Acb
OG
Hyp
MB
RN
LGN
MGN
PAG
St
Cd
V 5.4
PuT
GPe
I
GPi
m
ac
B
al
ic
SNr
STh
Acb
fx
mtt
Hyp
RN
LGN
Pul
MGN
PAG
St
Cd
ac
mc
AP 0
32
30
28
26
24
22
20
18
16
14
12
10
8
6
4
2
0
2
4
6
8
10
12

FIGURE 3.12

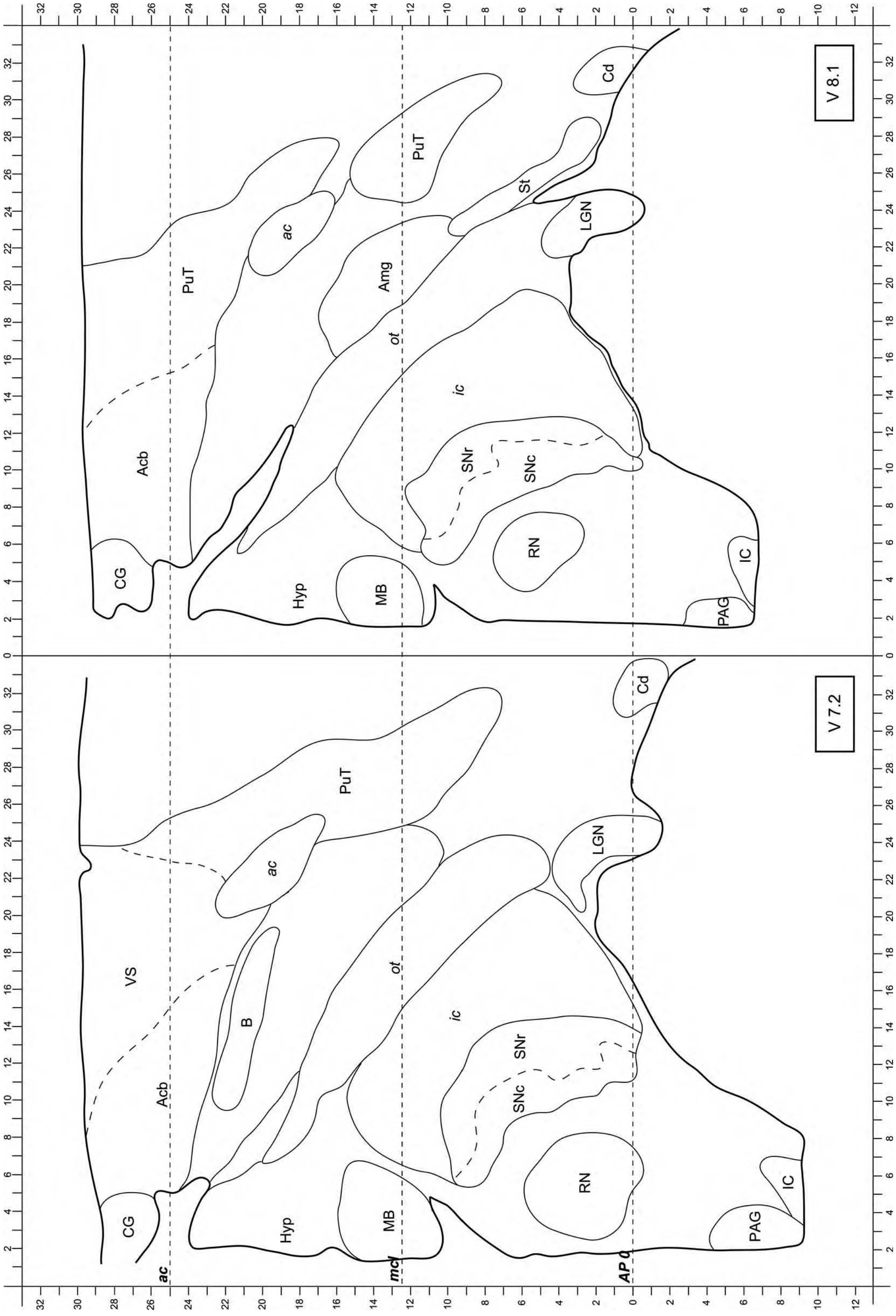
V 8.1
Cd
PuT
St
LGN
ac
PuT
Amg
ot
ic
SNr
SNc
RN
IC
PAG
Hyp
MB
CG
Acb
V 7.2
Cd
PuT
LGN
ac
VS
B
ot
ic
SNr
SNc
RN
IC
PAG
Hyp
MB
CG
Acb
ac
mcl
AP 0

FIGURE 3.13

FIGURES 3.14 to 3.25 Series of drawings of sagittal sections of the human thalamus and basal ganglia (left hemisphere of case Hb1; Table 2.1) arranged in a medial to lateral sequence. Mediolateral levels (in millimeters) relative to

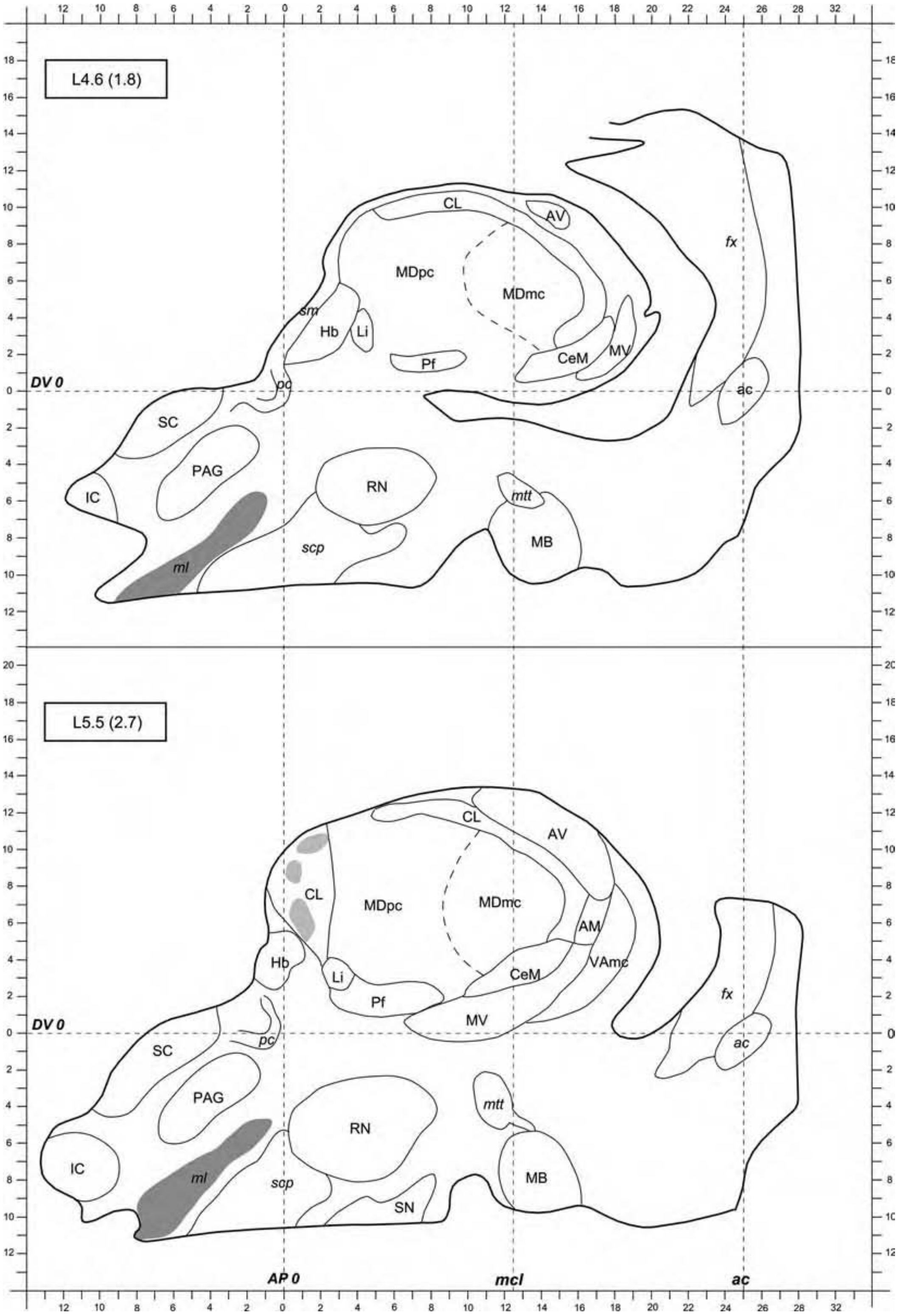

FIGURE 3.14

interhemispheric plane or estimated thalamo-ventricular border (in parentheses) are indicated in upper left of each drawing. *Vertical dotted lines* indicate the posterior commissure (*AP 0*), midcommissural (*mcl*) and anterior commissure (*ac*) levels. For other conventions, see legend of Figures 3.1 to 3.13.

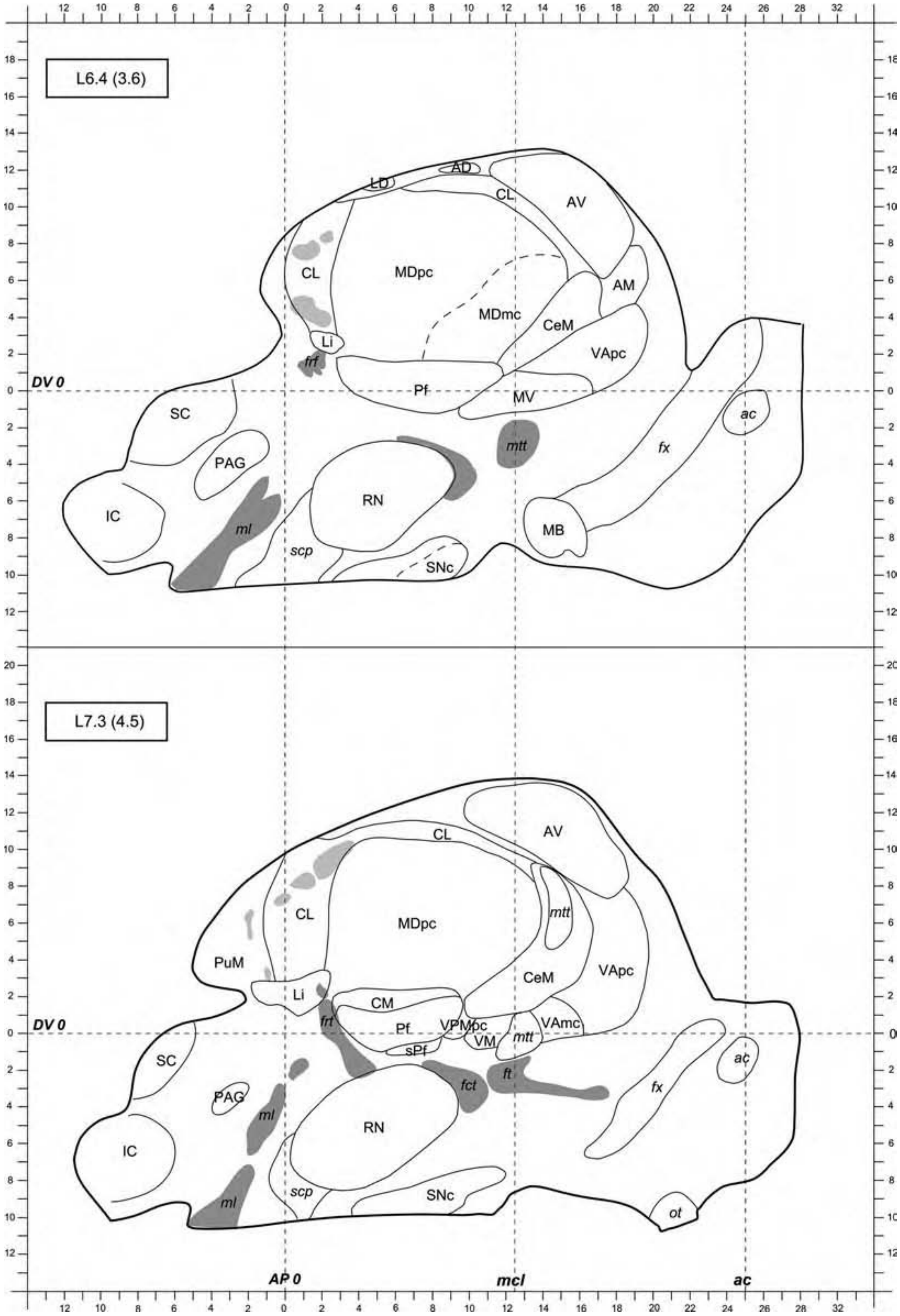

FIGURE 3.15

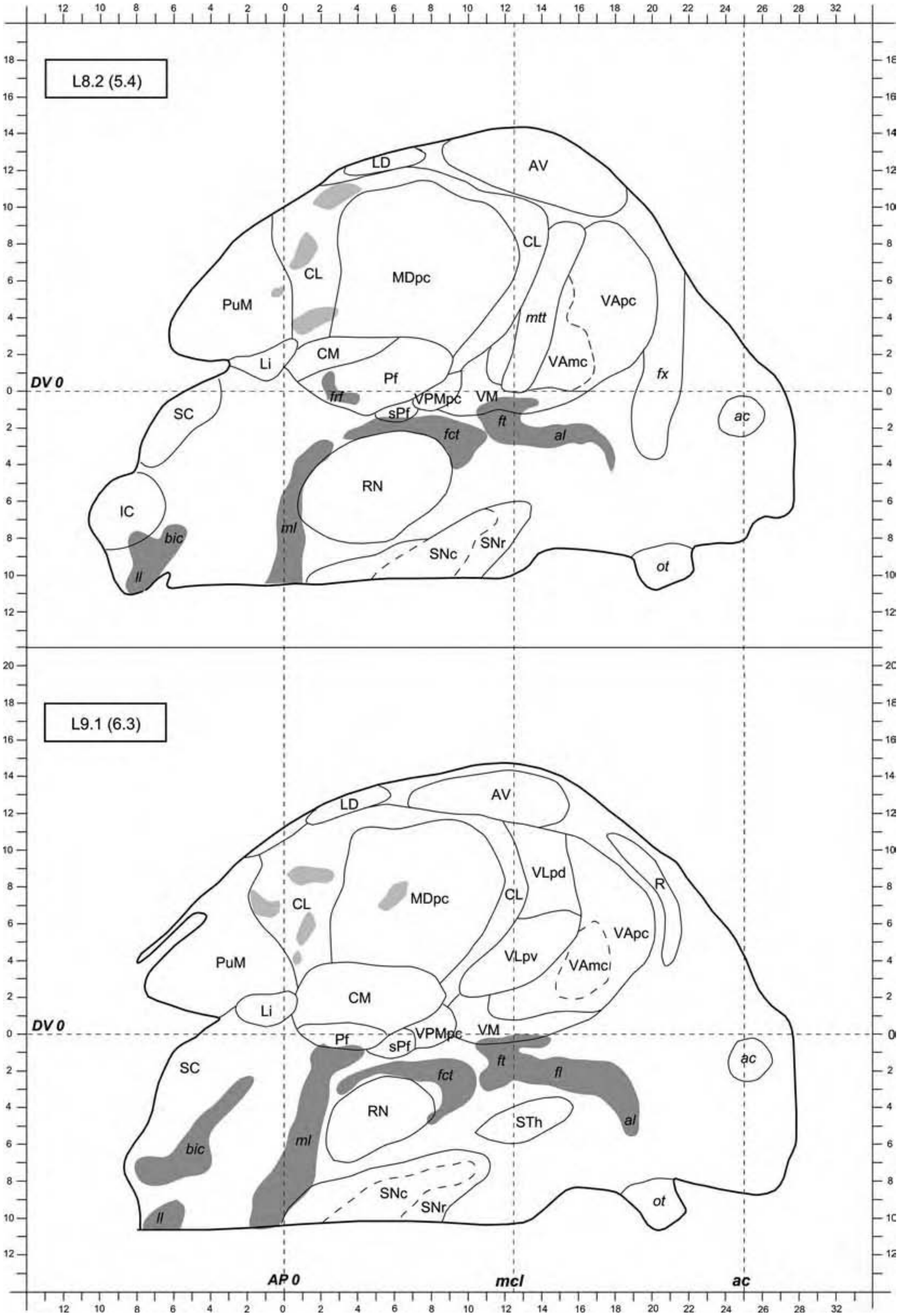
L8.2 (5.4)
LD
AV
CL
MDpc
PuM
mtt
VApc
VAmc
fx
Li
CM
Pf
DV 0
frf
sPf
VPMpc
VM
ft
al
SC
fct
ac
RN
IC
bic
ml
SNc
SNr
ll
ot
L9.1 (6.3)
LD
AV
VLpd
R
CL
MDpc
VApc
PuM
VLpv
VAmc
CM
Li
DV 0
Pf
sPf
VPMpc
VM
SC
ft
fl
ac
fct
RN
STh
al
bic
ml
SNc
SNr
ot
ll
AP 0
mcl
ac
12 10 8 6 4 2 0 2 4 6 8 10 12 14 16 18 20 22 24 26 28 32
18 16 14 12 10 8 6 4 2 0 2 4 6 8 10 12
20 18 16 14 12 10 8 6 4 2 0 2 4 6 8 10 12

FIGURE 3.16

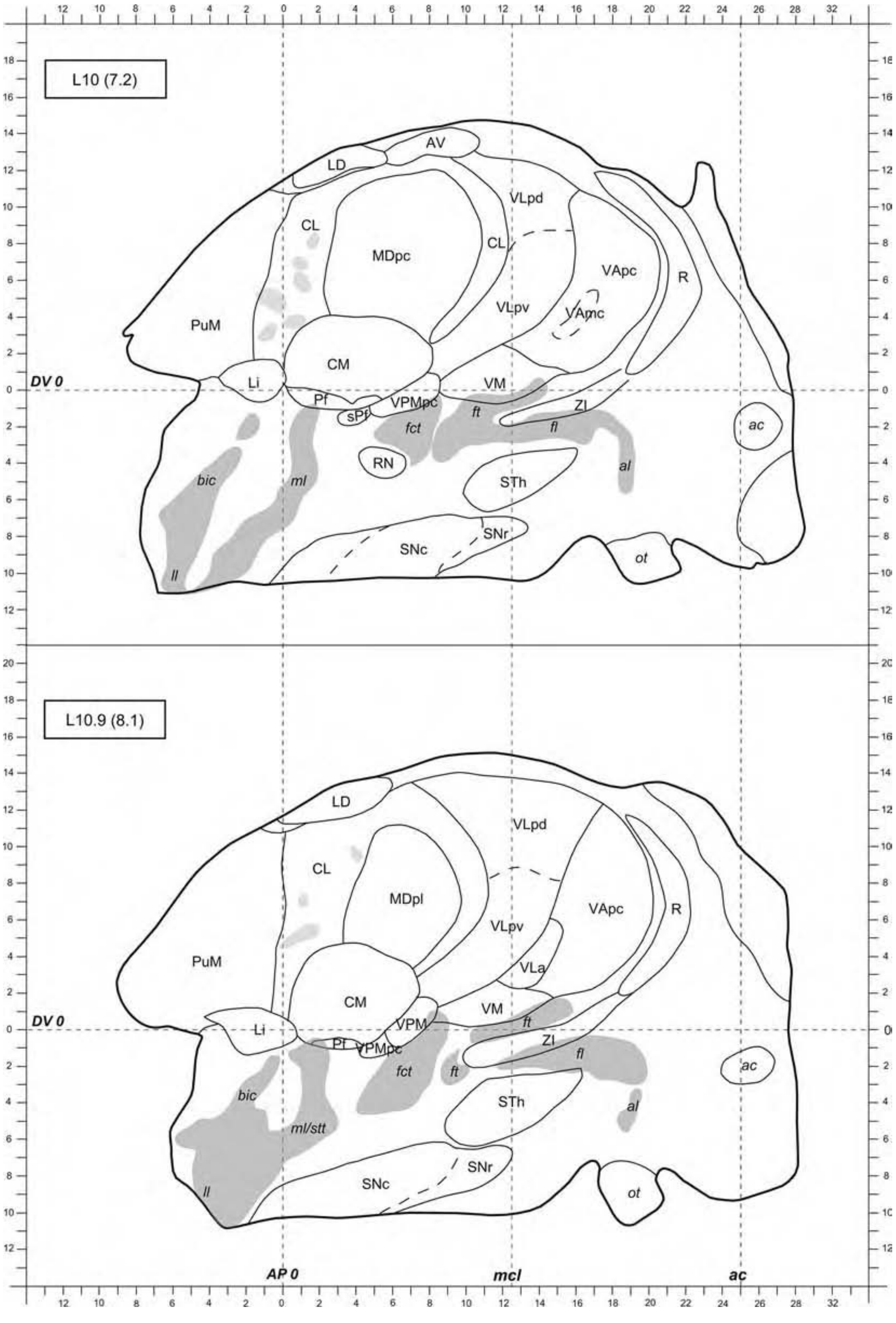
L10 (7.2)
AV
LD
VLpd
CL
MDpc
CL
VApc
R
VLpv
VAmc
PuM
CM
Li
VM
DV 0
Pf
sPf
VPMpc
ft
ZI
fct
fl
ac
RN
al
bic
ml
STh
SNr
SNc
ot
ll
L10.9 (8.1)
LD
VLpd
CL
MDpl
VApc
R
VLpv
VLa
PuM
CM
VM
VPM
ft
DV 0
Li
Pf
VPMpc
ZI
fl
fct
ft
ac
bic
STh
al
ml/stt
SNr
SNc
ot
ll
AP 0
mcl
ac
12
10
8
6
4
2
0
2
4
6
8
10
12
14
16
18
20
22
24
26
28
32

FIGURE 3.17

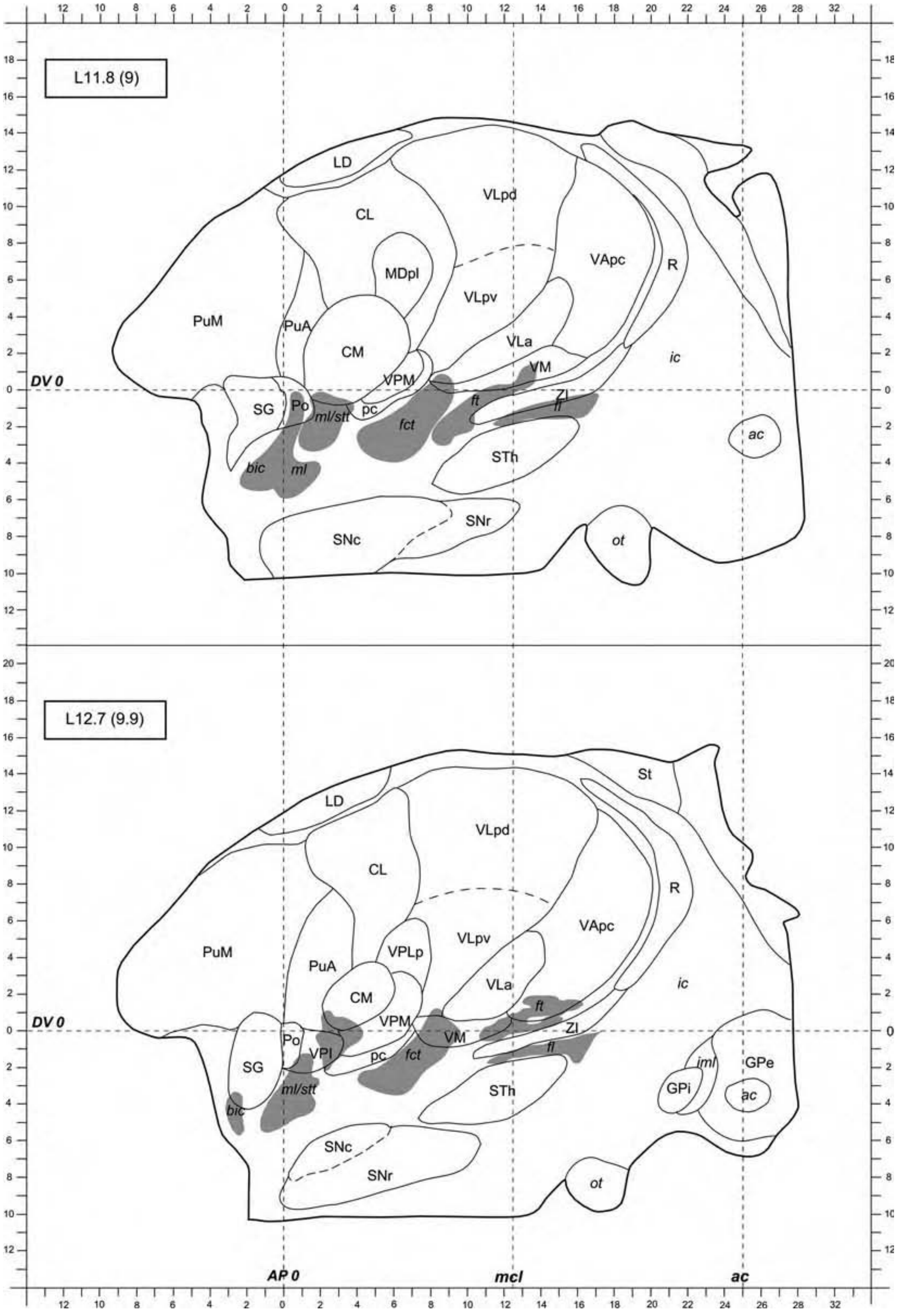
L11.8 (9)
LD
CL
VLpd
MDpl
VApc
R
VLpv
PuM
PuA
CM
VLa
ic
VM
VPM
DV 0
SG
Po
pc
ft
ZI
fl
ml/stt
fct
ac
STh
bic
ml
SNr
SNc
ot
L12.7 (9.9)
St
LD
VLpd
CL
R
VApc
PuM
PuA
VPLp
VLpv
ic
CM
VLa
ft
VPM
DV 0
Po
VM
ZI
VPl
fl
SG
pc
fct
iml
GPe
ml/stt
GPi
ac
STh
bic
SNc
SNr
ot
AP 0
mcl
ac

FIGURE 3.18

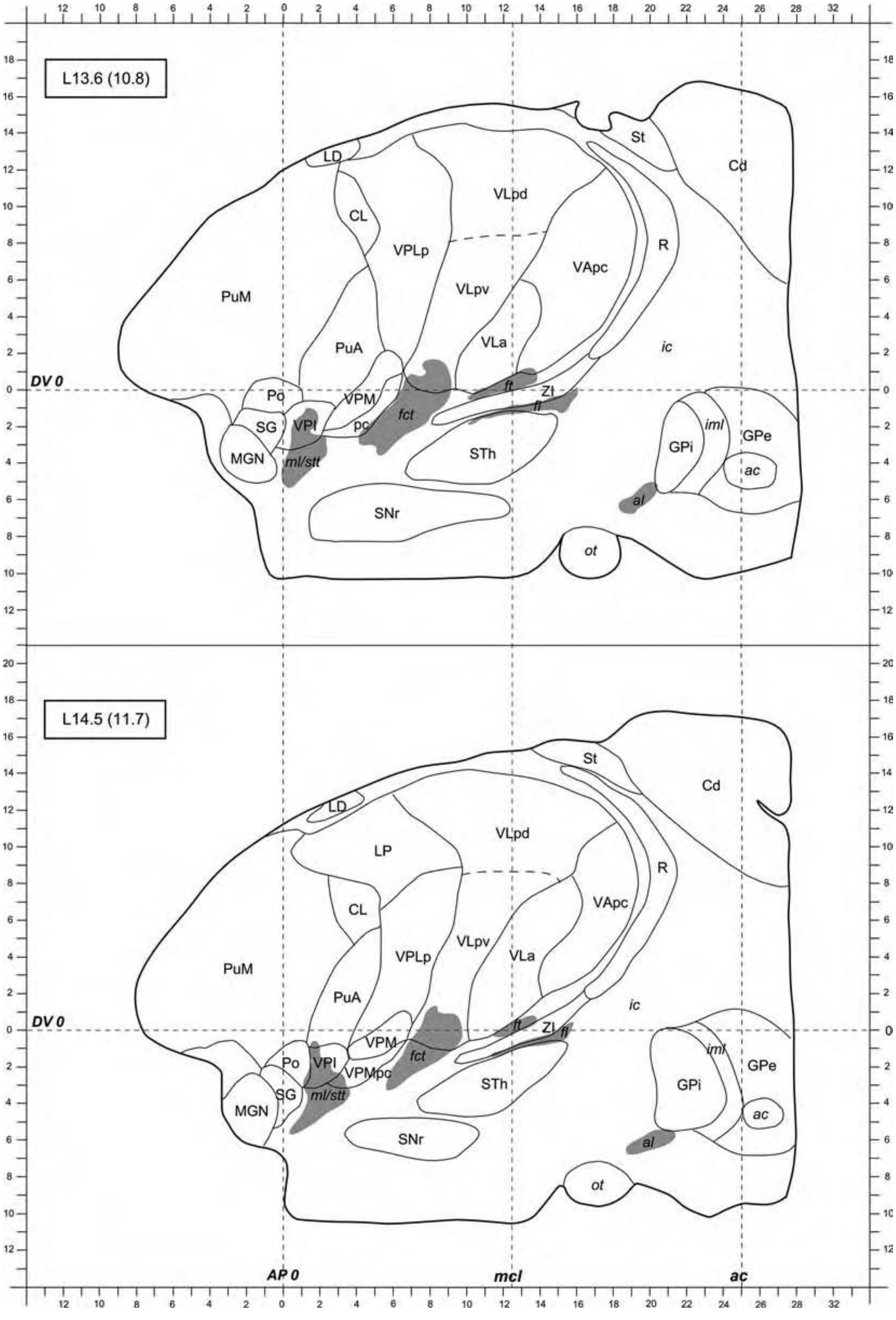
L13.6 (10.8)
LD
CL
VLpd
VPLp
VLpv
VApc
R
St
Cd
PuM
PuA
VLa
ic
Po
VPM
ft
ZI
fl
SG
VPI
pc
fct
STh
GPi
iml
GPe
ac
MGN
ml/stt
al
SNr
ot
DV 0
L14.5 (11.7)
LD
LP
VLpd
CL
VLpv
VPLp
VLa
VApc
R
St
Cd
PuM
PuA
VPM
VPMpc
Po
VPI
SG
MGN
ml/stt
fct
ft
ZI
fl
STh
GPi
iml
GPe
ac
al
SNr
ot
ic
DV 0
AP 0
mcl
ac

FIGURE 3.19

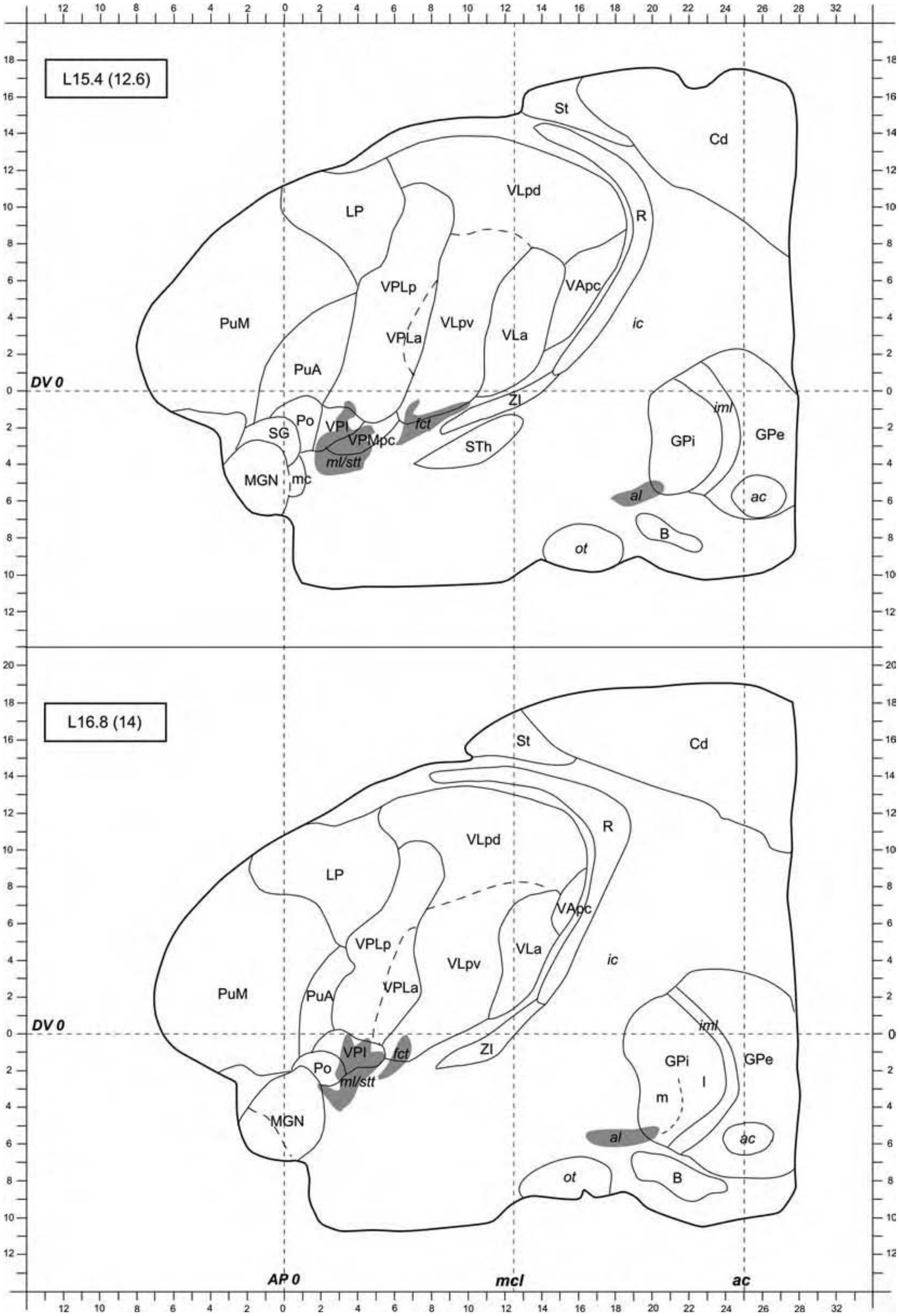
L15.4 (12.6)
St
Cd
VLpd
LP
R
VPLp
VApc
PuM
VPLa
VLpv
VLa
ic
PuA
DV 0
ZI
Po
VPI
fct
iml
SG
VPMpc
STh
GPi
GPe
ml/stt
MGN
mc
al
ac
B
ot
L16.8 (14)
St
Cd
R
VLpd
LP
VApc
VPLp
VLa
ic
VLpv
PuM
PuA
VPLa
DV 0
iml
VPI
fct
ZI
GPi
GPe
Po
ml/stt
l
m
MGN
al
ac
ot
B
AP 0
mcl
ac

FIGURE 3.20

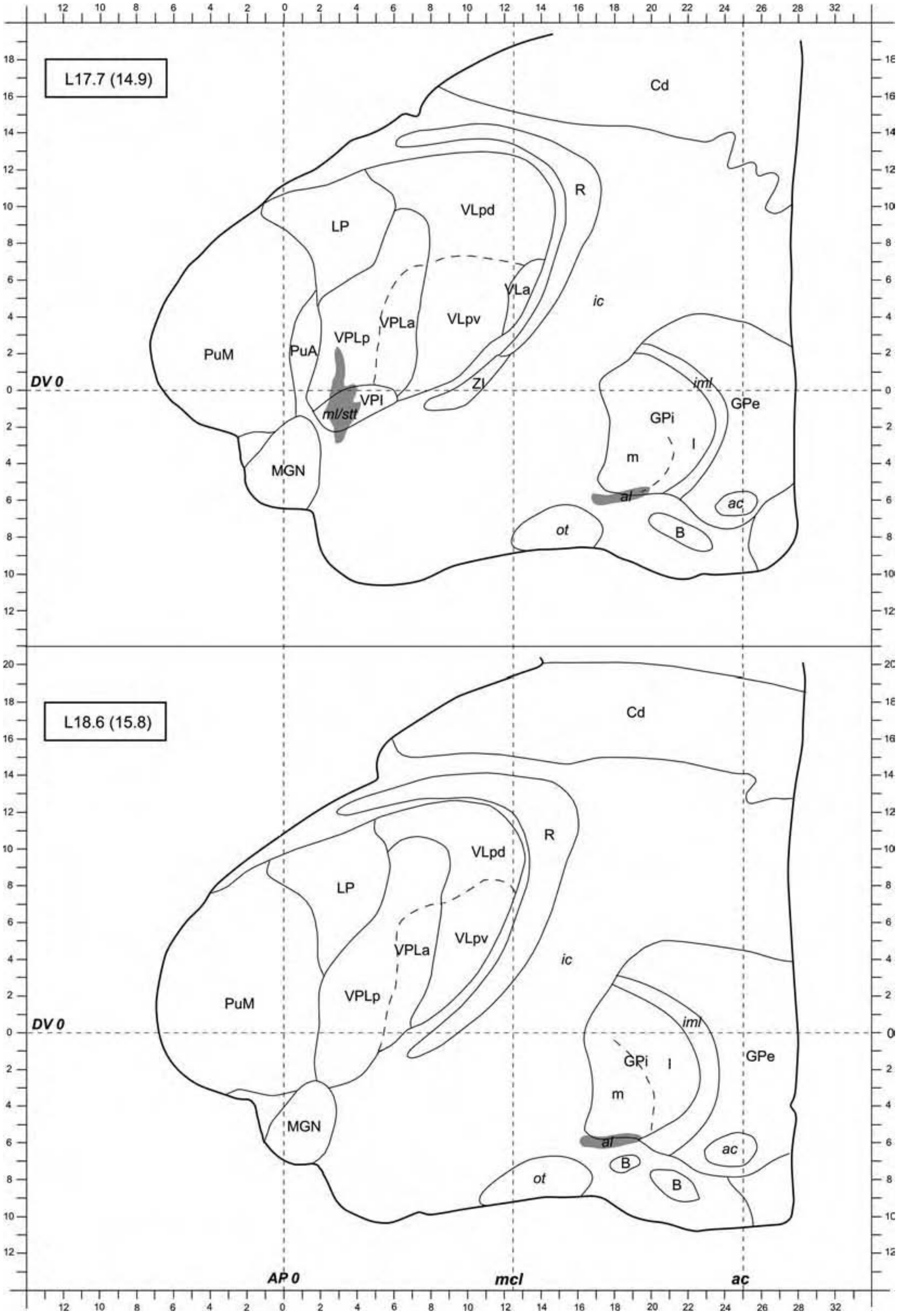
12 10 8 6 4 2 0 2 4 6 8 10 12 14 16 18 20 22 24 26 28 32
18 16 14 12 10 8 6 4 2 0 2 4 6 8 10 12
L17.7 (14.9)
Cd
R
VLpd
LP
VLa
ic
VPLa
VLpv
VPLp
PuM
PuA
iml
DV 0
VPl
ZI
GPe
GPi
ml/stt
I
m
MGN
al
ac
ot
B
20 18 16 14 12 10 8 6 4 2 0 2 4 6 8 10 12
L18.6 (15.8)
Cd
R
VLpd
LP
VLpv
VPLa
ic
PuM
VPLp
iml
DV 0
GPi
I
GPe
m
MGN
al
ac
B
ot
B
AP 0
mcl
ac
12 10 8 6 4 2 0 2 4 6 8 10 12 14 16 18 20 22 24 26 28 32

FIGURE 3.21

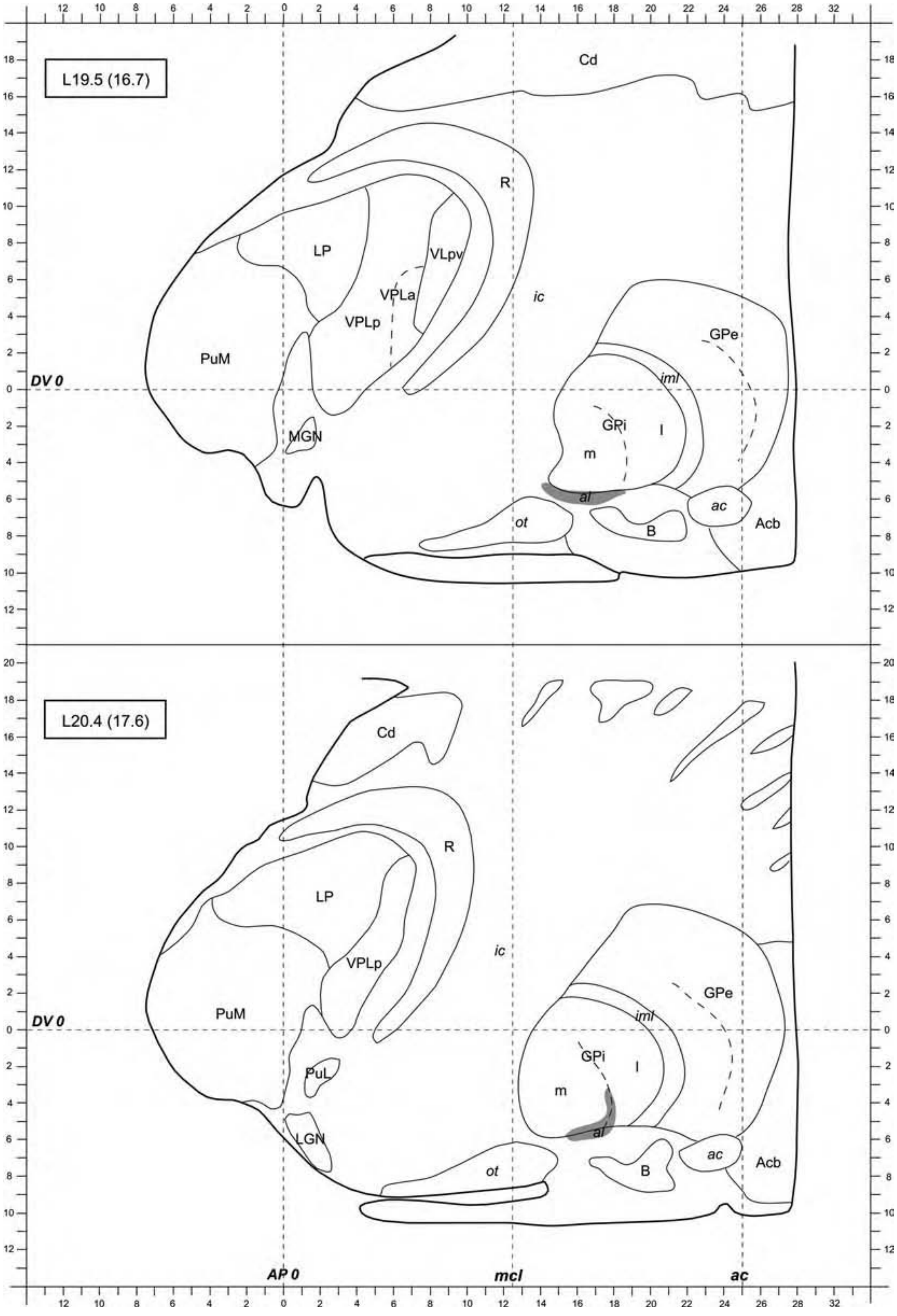
12 10 8 6 4 2 0 2 4 6 8 10 12 14 16 18 20 22 24 26 28 32
L19.5 (16.7)
Cd
R
LP
VLpv
VPLa
VPLp
ic
PuM
DV 0
GPe
iml
GPi
l
m
MGN
al
ac
ot
B
Acb
18 16 14 12 10 8 6 4 2 0 2 4 6 8 10 12
L20.4 (17.6)
Cd
R
LP
ic
VPLp
PuM
DV 0
GPe
iml
GPi
l
m
PuL
LGN
al
ac
ot
B
Acb
20 18 16 14 12 10 8 6 4 2 0 2 4 6 8 10 12
AP 0
mcl
ac

FIGURE 3.22

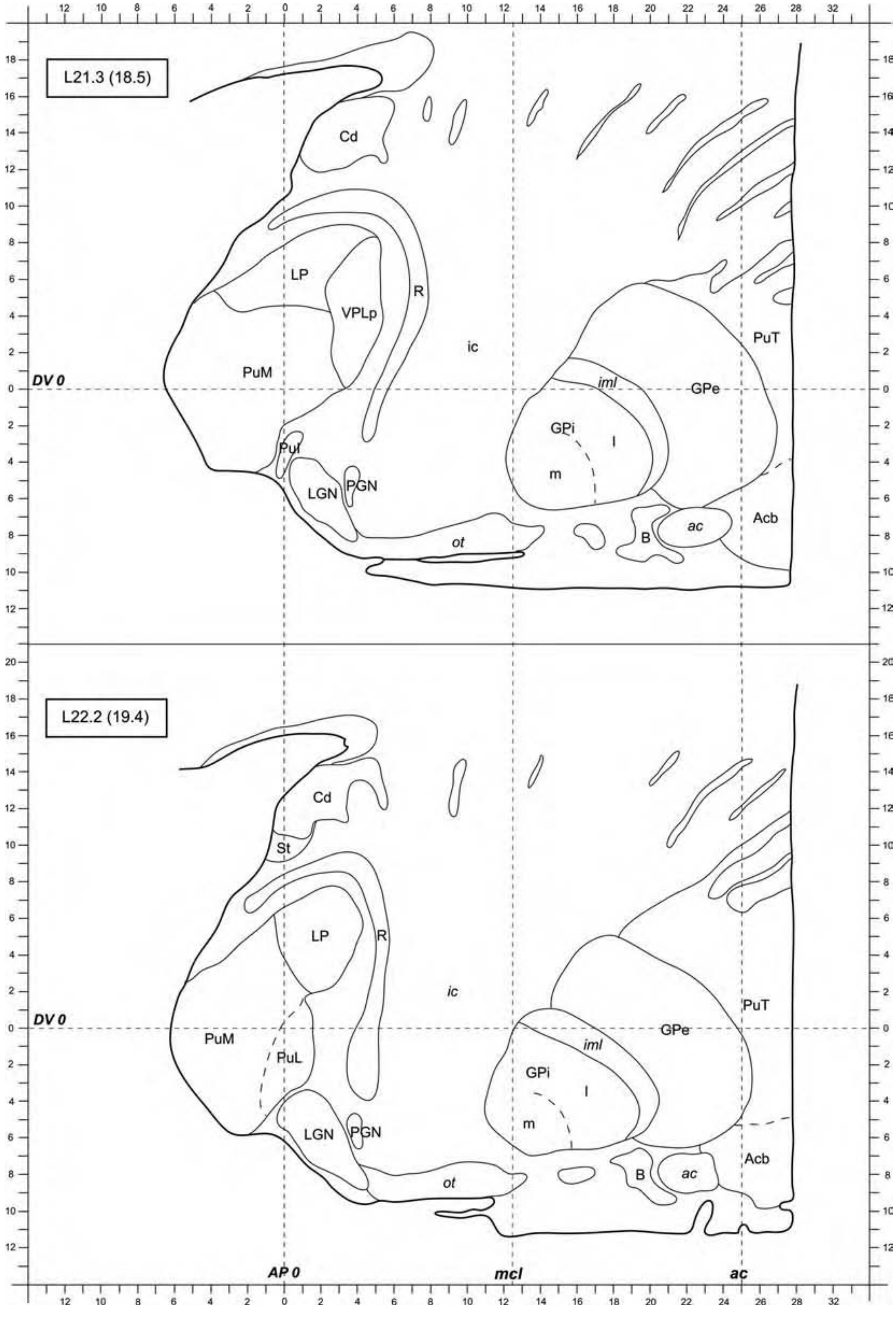
L21.3 (18.5)
Cd
LP
VPLp
R
PuM
ic
DV 0
iml
GPe
PuT
GPi
l
m
PuI
LGN
PGN
ot
ac
B
Acb
L22.2 (19.4)
Cd
St
LP
R
ic
PuT
DV 0
PuM
iml
GPe
PuL
GPi
l
m
LGN
PGN
ot
B
ac
Acb
AP 0
mcl
ac
12
10
8
6
4
2
0
2
4
6
8
10
12
14
16
18
20
22
24
26
28
32
18
16
14
12
10
8
6
4
2
0
2
4
6
8
10
12
20

FIGURE 3.23

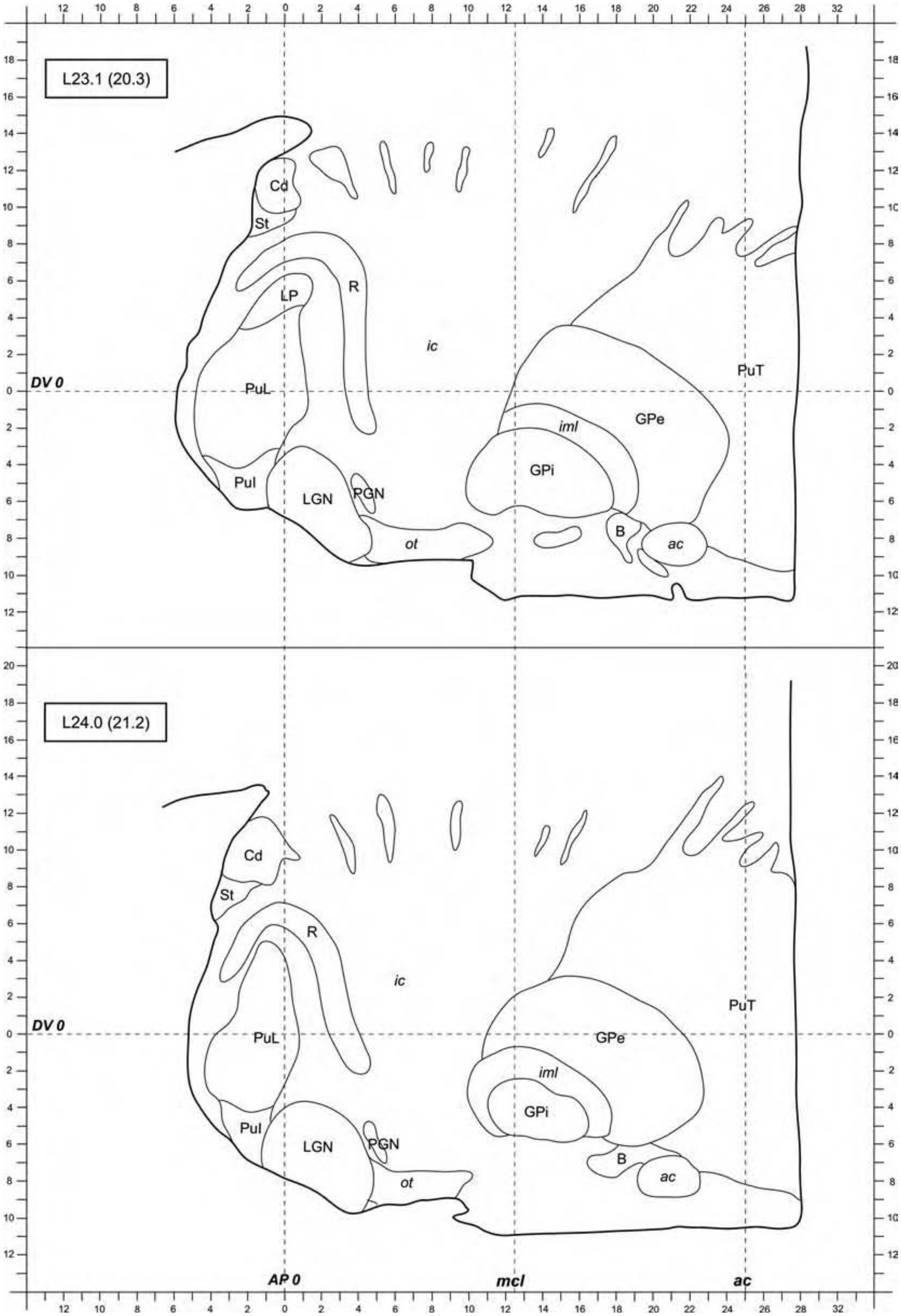
L23.1 (20.3)
Cd
St
LP
R
ic
PuL
PuI
LGN
PGN
ot
iml
GPe
GPi
B
ac
PuT
DV 0
L24.0 (21.2)
Cd
St
R
ic
PuL
PuI
LGN
PGN
ot
iml
GPe
GPi
B
ac
PuT
DV 0
AP 0
mcl
ac
12 10 8 6 4 2 0 2 4 6 8 10 12 14 16 18 20 22 24 26 28 32
18 16 14 12 10 8 6 4 2 0 2 4 6 8 10 12
20 18 16 14 12 10 8 6 4 2 0 2 4 6 8 10 12

FIGURE 3.24

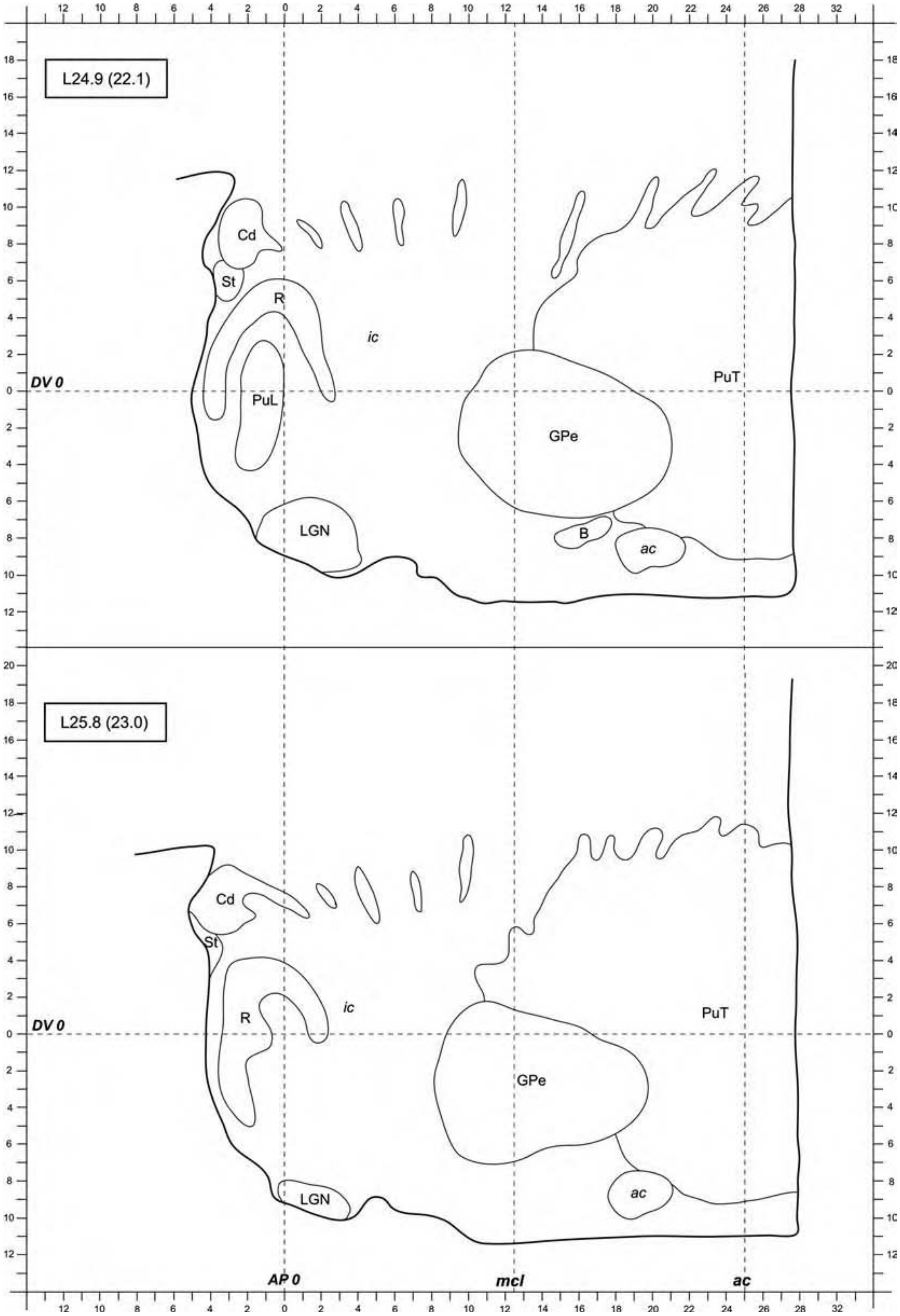
L24.9 (22.1)
Cd
St
R
ic
PuL
PuT
GPe
LGN
B
ac
DV 0
L25.8 (23.0)
Cd
St
R
ic
PuT
GPe
LGN
ac
DV 0
AP 0
mcl
ac

FIGURE 3.25

FIGURE 3.26 Photomicrographs of myelin (**B**) and Nissl (**D**) stainings, and of the immunoreactivity to the calcium-binding proteins CB (**C**), CR (**E**) and PV (**F**) in sagittal sections the human thalamus (case Hb1; Table 2.1) at levels adjacent to the map shown in (**A**). Notice the similar distributions of CB and CR in the CL and Li, but complementary distributions in other areas such as VApc, VM, the inferior colliculus (IC), and substantia nigra, pars reticulata (SNr). They are both complementary to PV in the red nucleus (RN). The *arrow* in (**C**) indicates position of the presumed spinothalamic tract (*stt*). *Scale bar* (***A***): 5 mm.

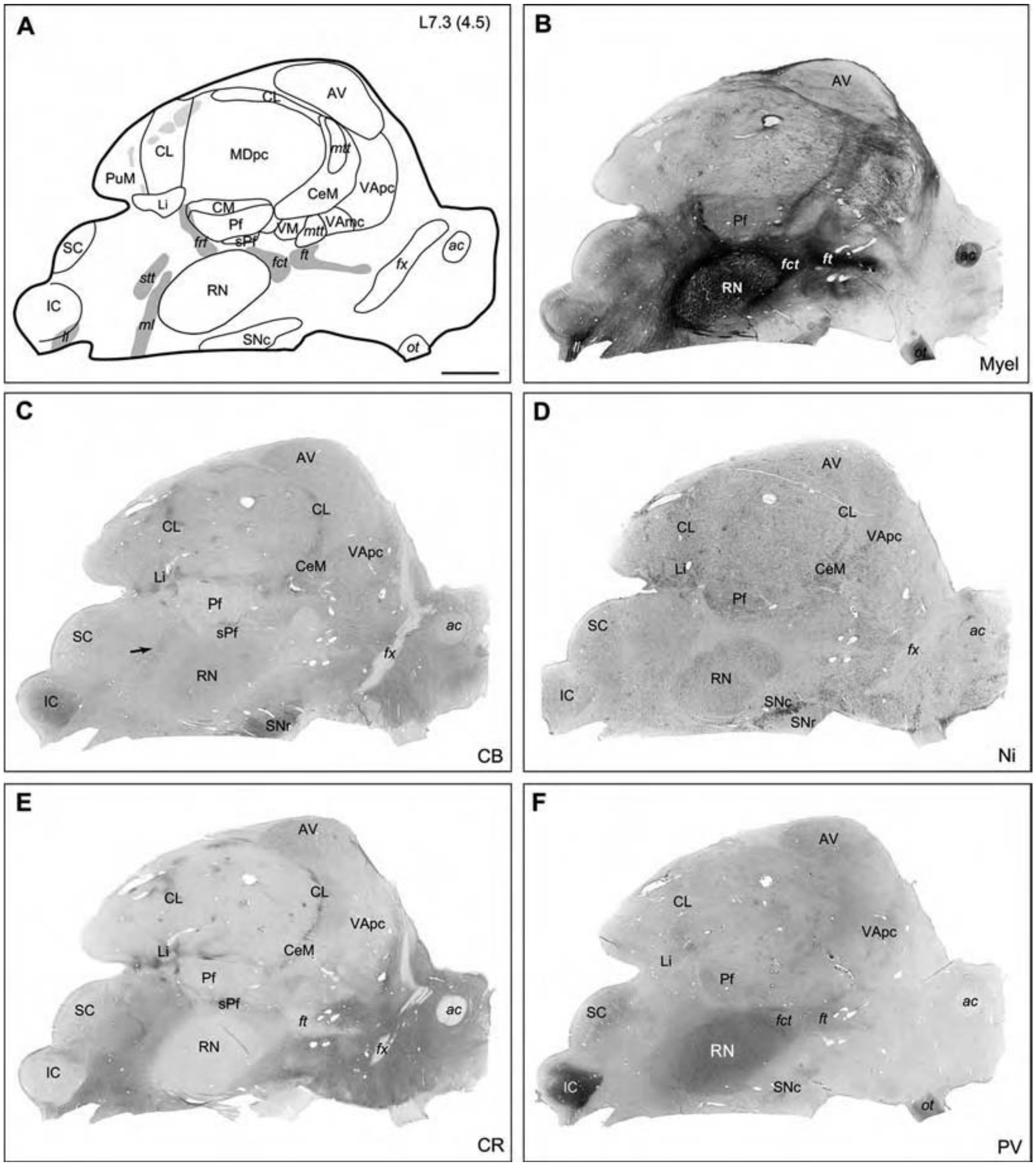

FIGURE 3.27 Photomicrographs of Nissl (**B**) and myelin (**D**) stainings, and of the immunoreactivity to the calcium-binding proteins CR (**C**) and PV (**E**) in sagittal sections of the human thalamus (case Hb1; Table 2.1) adjacent to the map shown in (**A**) and 2.7-mm lateral to level shown in Figure 3.26. Notice the complementary distributions of CR and PV in the thalamic and subthalamic areas (e.g., in VLp, CM and STh nuclei) and the strong immunostaining to CR in posterior part of the CL nucleus, in register with darkly stained cell clusters visible also in Nissl. Among the fiber tracts seen in myelin section and represented in grey areas in the map, the fasciculus cerebellothalamic (*fct*) and, to a lesser extent, the fasciculus thalamicus (*ft*) are enhanced in PV immunostaining. *Scale bar* (***A***): 5 mm.

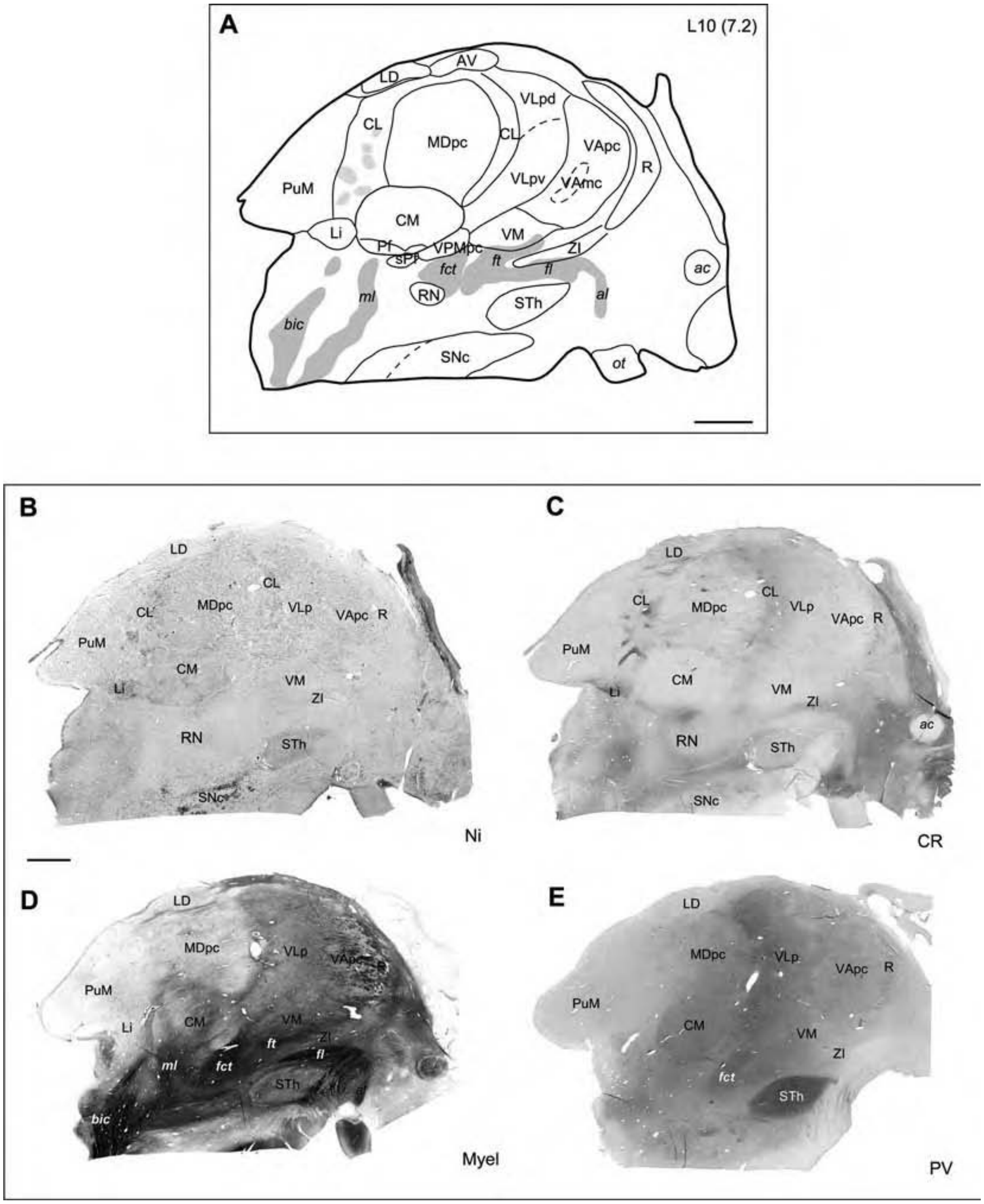

FIGURE 3.28 Postmortem MRI (**A**) and photomicrographs of multiple stainings (**B–F**) in sagittal sections 7 mm lateral to interhemispheric plane (brain Hb7; Table 2.1). Notice the clear delineation of the CL nucleus on the basis of the distributions of AChE, CB- and CR-ir, and the strong AChE staining in medial CM/Pf and in STh nucleus, except for its ventral portion (**B**). *Scale bar* (***A***): 5 mm.

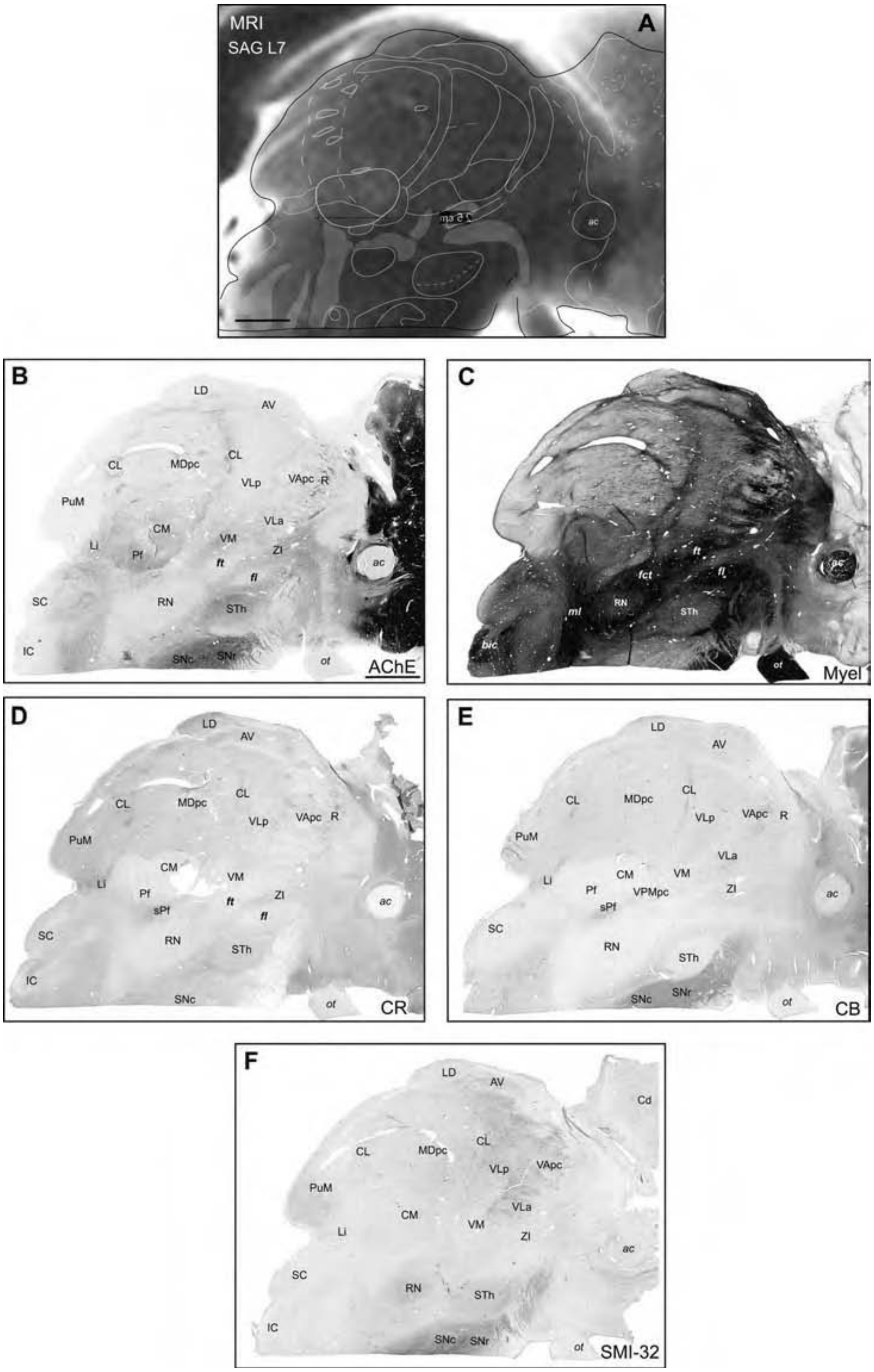

FIGURE 3.29 Photomicrographs of multiple stainings (AChE, myelin, CB- and SMI-32-ir, **A–D**) in sagittal sections of brain Hb6 (Table 2.1) at a similar level to the sections illustrated in Figure 3.27 for case Hb1, or in Figure 3.28 for case Hb7. Notice the similar patterns presented in the different cases, although with some differences in staining intensities. *Scale bar* (***A***): 5 mm.

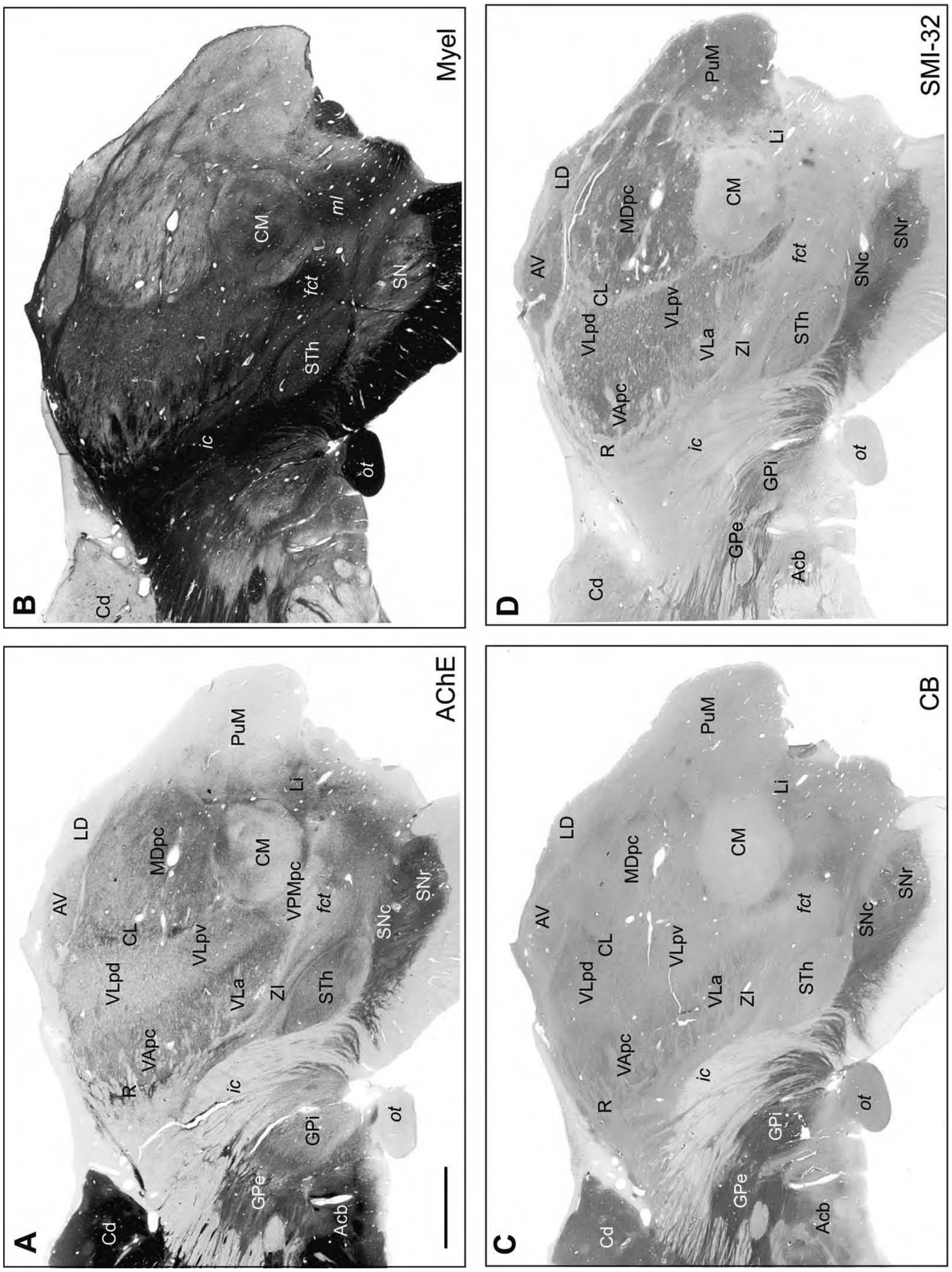

FIGURE 3.30 Photomicrographs of Nissl staining (**B**) and immunoreactivity to the calcium-binding proteins PV (**C**) and CR (**D**) in horizontal sections of the dorsal thalamus (10.8 mm dorsal to intercommissural plane, case Hb1, Table 2.1), at a level corresponding closely to the map shown in (**A**). The two CaBPs have largely complementary distributions except in VLpd and the reticular nucleus (R). *Scale bar* (***A***): 5 mm.

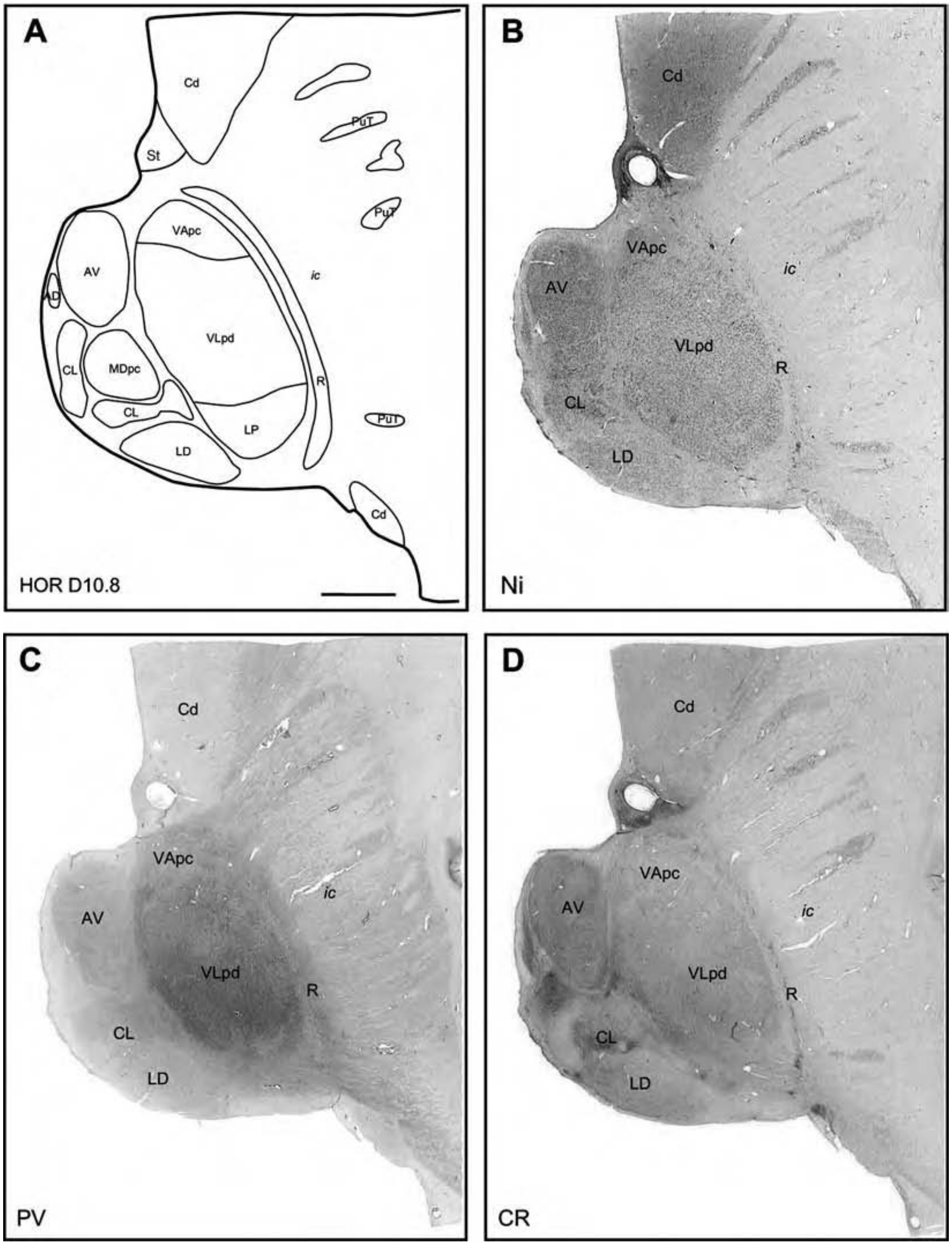

FIGURE 3.30

FIGURE 3.31 Photomicrographs of Nissl staining (**A**) and immunoreactivity to the calcium-binding proteins PV (**B**), CB (**C**) and CR (**D**) in horizontal sections of the dorsal thalamus (case Hb3, Table 2.1). *Scale bar* (***A***): 5 mm.

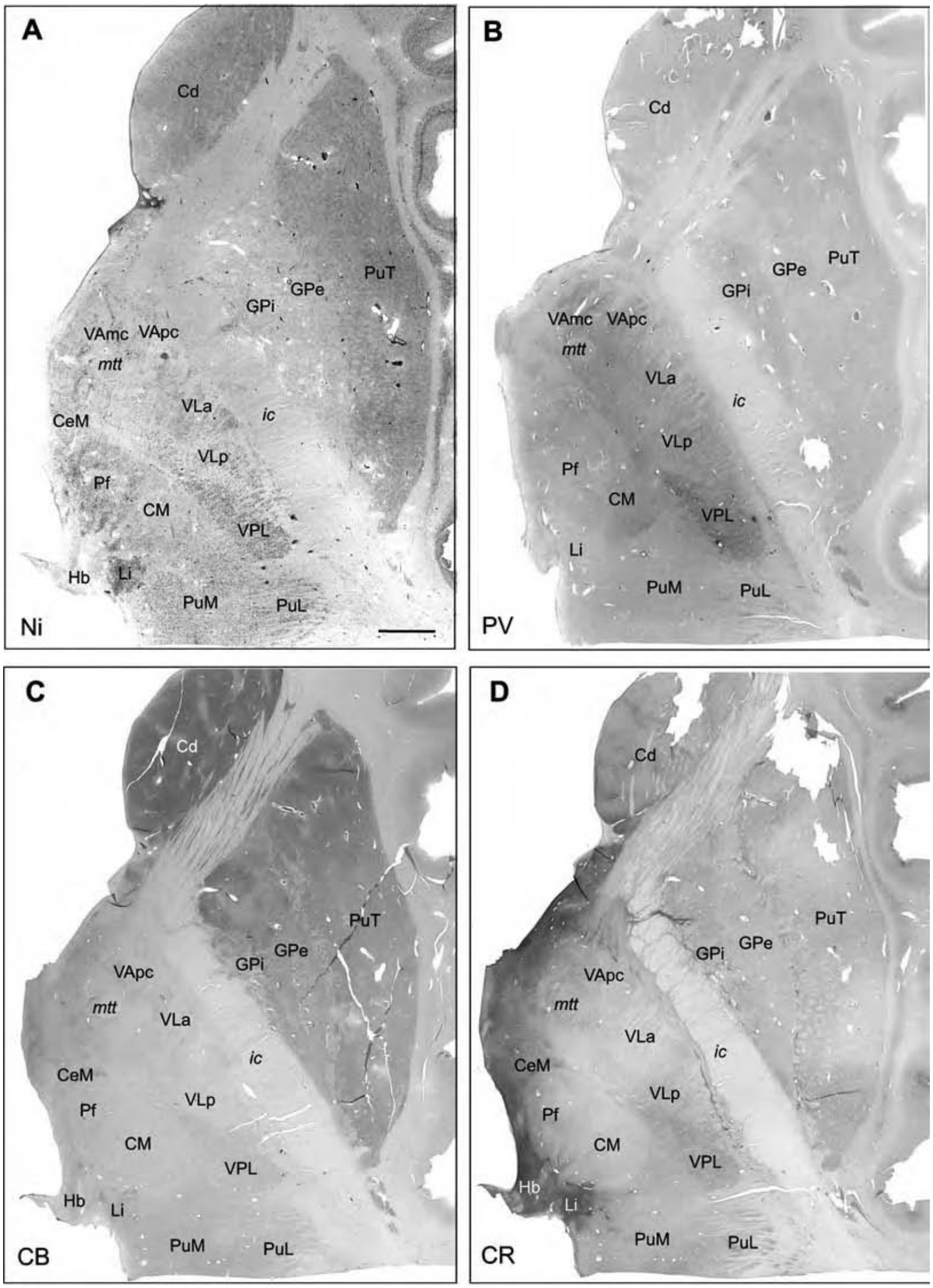

FIGURE 3.32 Photomicrographs of myelin (**A**) and AChE (**B**) stainings, and immunoreactivity to SMI-32 (**C**) and the calcium-binding proteins CB (**D**) in horizontal sections of the dorsal thalamus (case Hb6, Table 2.1), at level comparable to sections shown in Figure 3.31. VApc and VLa nuclei contain dense CB-ir, in contrast to VLpv which is enhanced in PV-ir, as seen in Figure 3.31B. *Scale bar* (***B***): 5 mm.

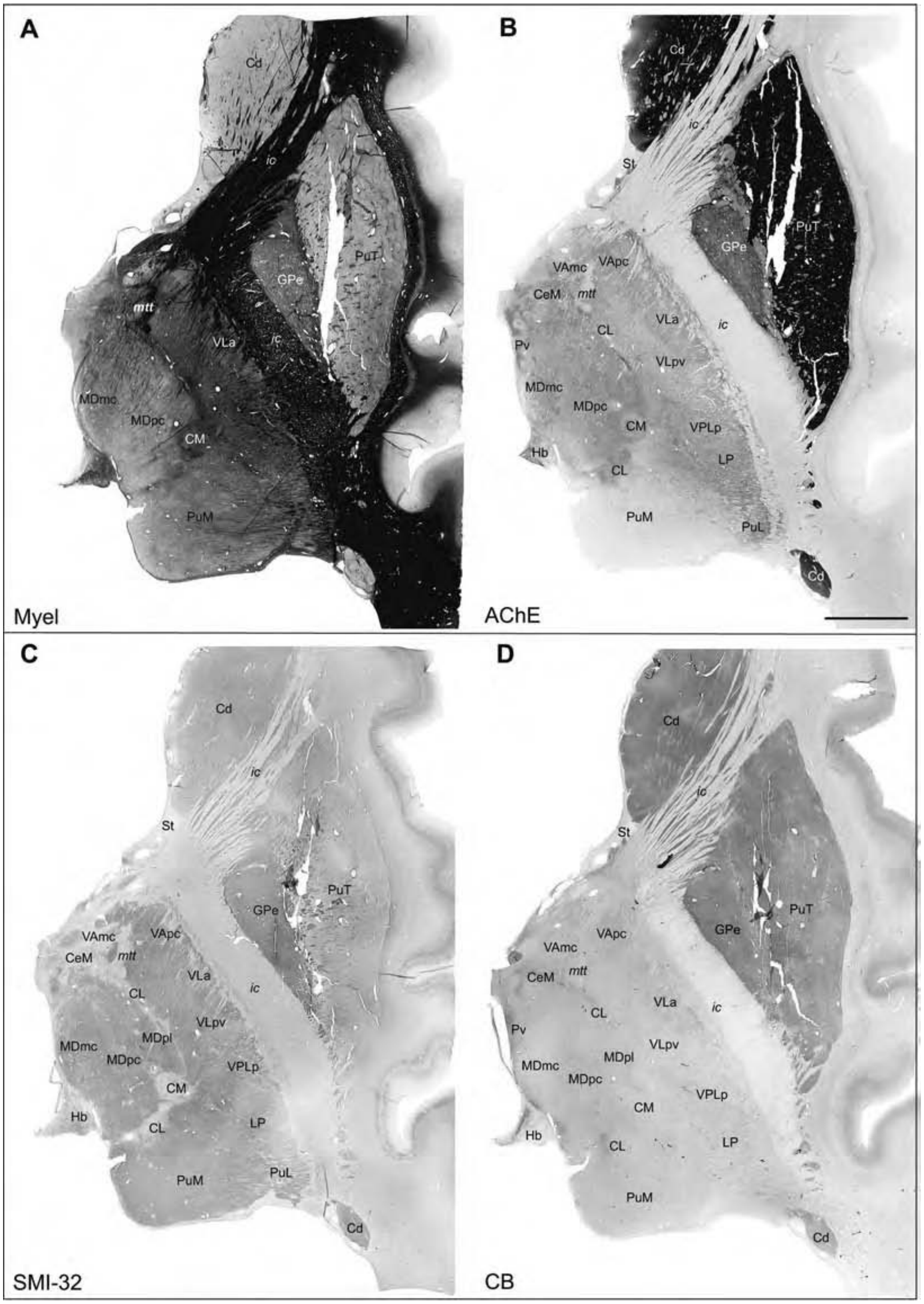

FIGURE 3.32

FIGURE 3.33 Postmortem MRI and photomicrographs of multiple stainings (myelin, AChE, PV-, CB-, and CR-ir) at frontal level 2 mm anterior to pc (A 2) (case Hb7, Table 2.1). The clusters in the posterior part of the CL nucleus are particularly marked by enhanced CB- and CR-ir, and AChE staining. *Scale bar* (MRI): 5 mm.

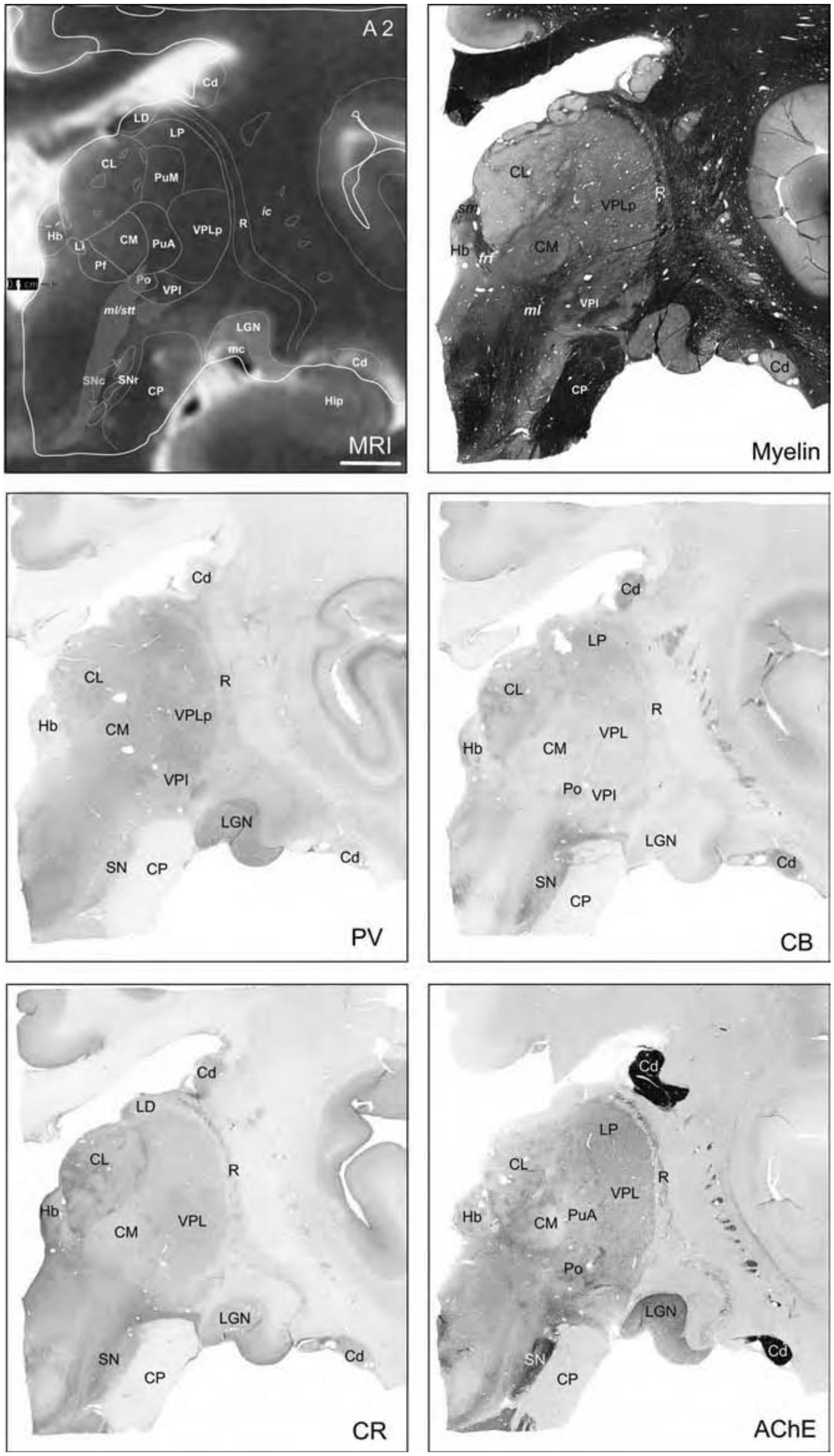

FIGURE 3.34 Photomicrographs of stainings for Nissl, myelin, AChE and immunostainings for CB, CR and PV in the area comprised in *dotted square* on frontal map of the posterior human thalamus (posterior commissure level, AP 0, left hand-side of the Figure) (case Hb7, Table 2.1). Notice the complementary distributions of CB and PV in the CL, Po, MGN and VPL nuclei, and the presence of CB-ir fibers (*arrow*) running toward Po and probably corresponding to spinothalamic fibers (*stt*). *Scale bars*: 5 mm (*left panel*) and 2 mm (*right panels*).

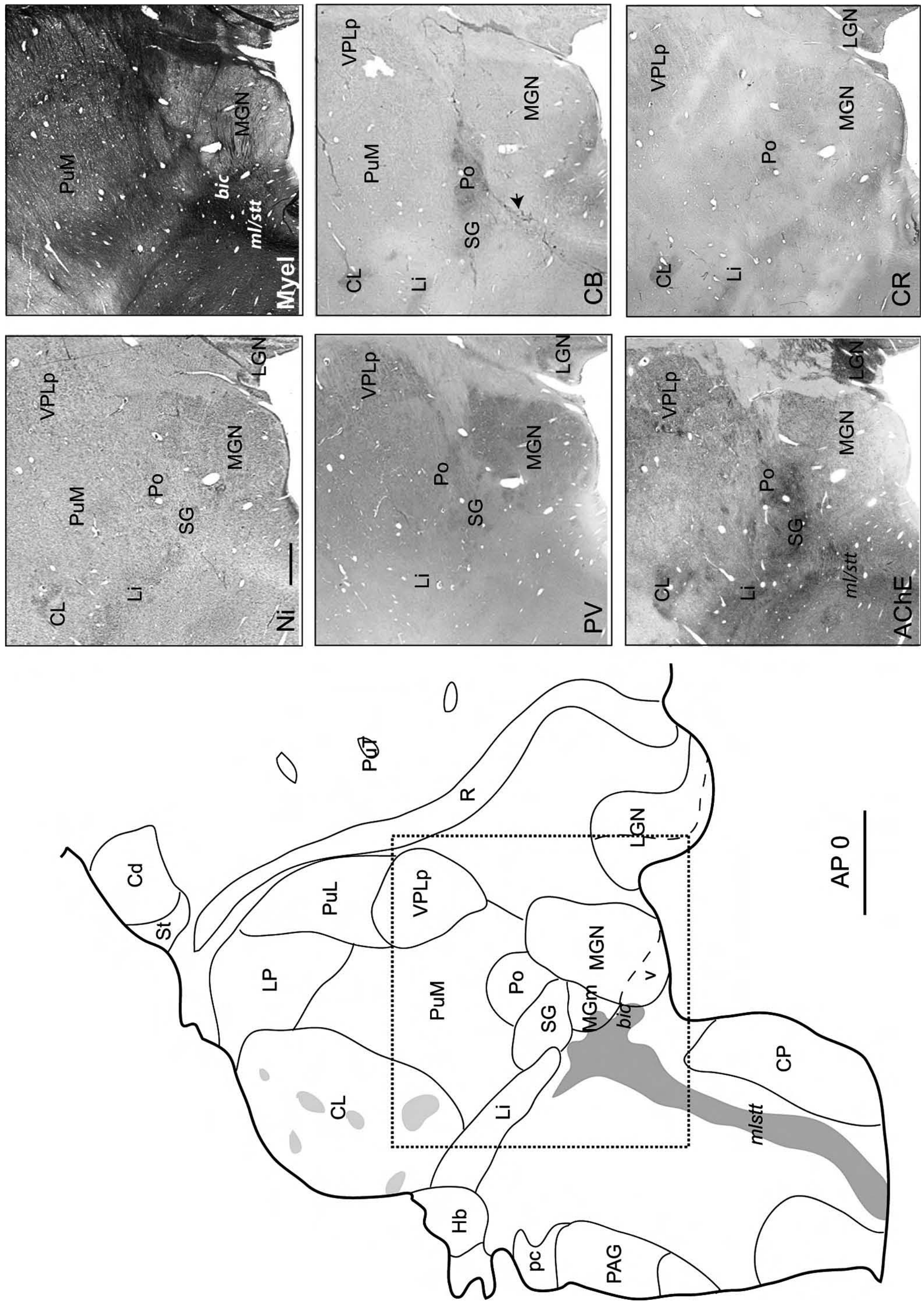

FIGURE 3.35 Photomicrographs of stainings for Nissl, myelin, AChE and immunostainings for CB, CR and SMI-32 in the area comprised in *dotted square* on frontal map of the human thalamus (left of the figure), 6-mm anterior to pc (A 6) and to level shown in Figure 3.34. Notice the gradients of AChE in the CM and Pf nuclei, enhanced CB-ir in VLa and VPMpc, and high CB- and CR-ir in sPf (case Hb7, Table 2.1). *Scale bars*: 5 mm (*left panel*); 2 mm (*right panels*).

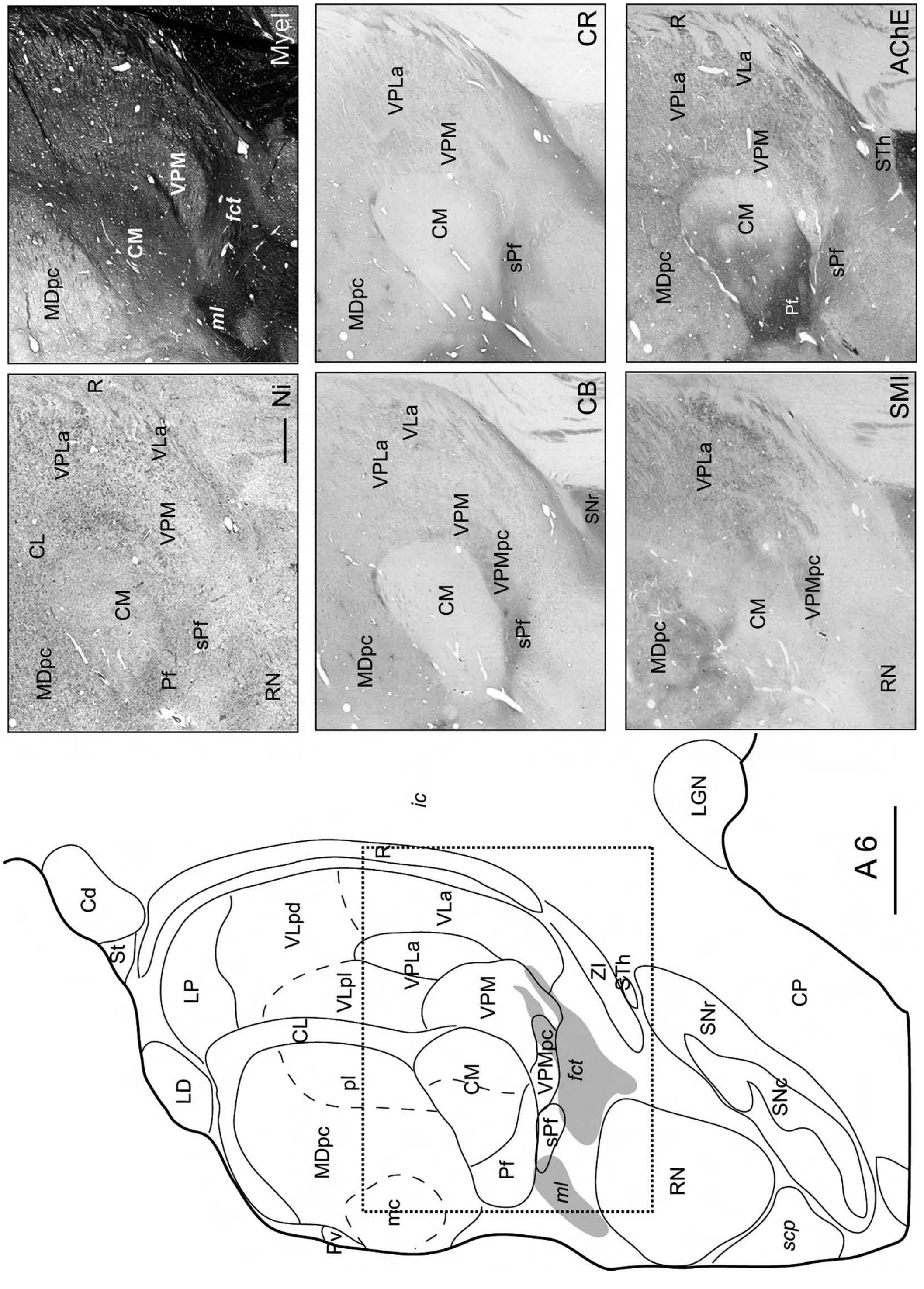

FIGURE 3.36 ***(See color insert.)*** Summary diagram of the distribution of CaBP in horizontal and sagittal sections of the human thalamus and subthalamic area (*upper panels*) and histograms of the relative densities of CaBP neuropil immunoreactivity (graded from 1 to 4) in the thalamus (*lower panels*).

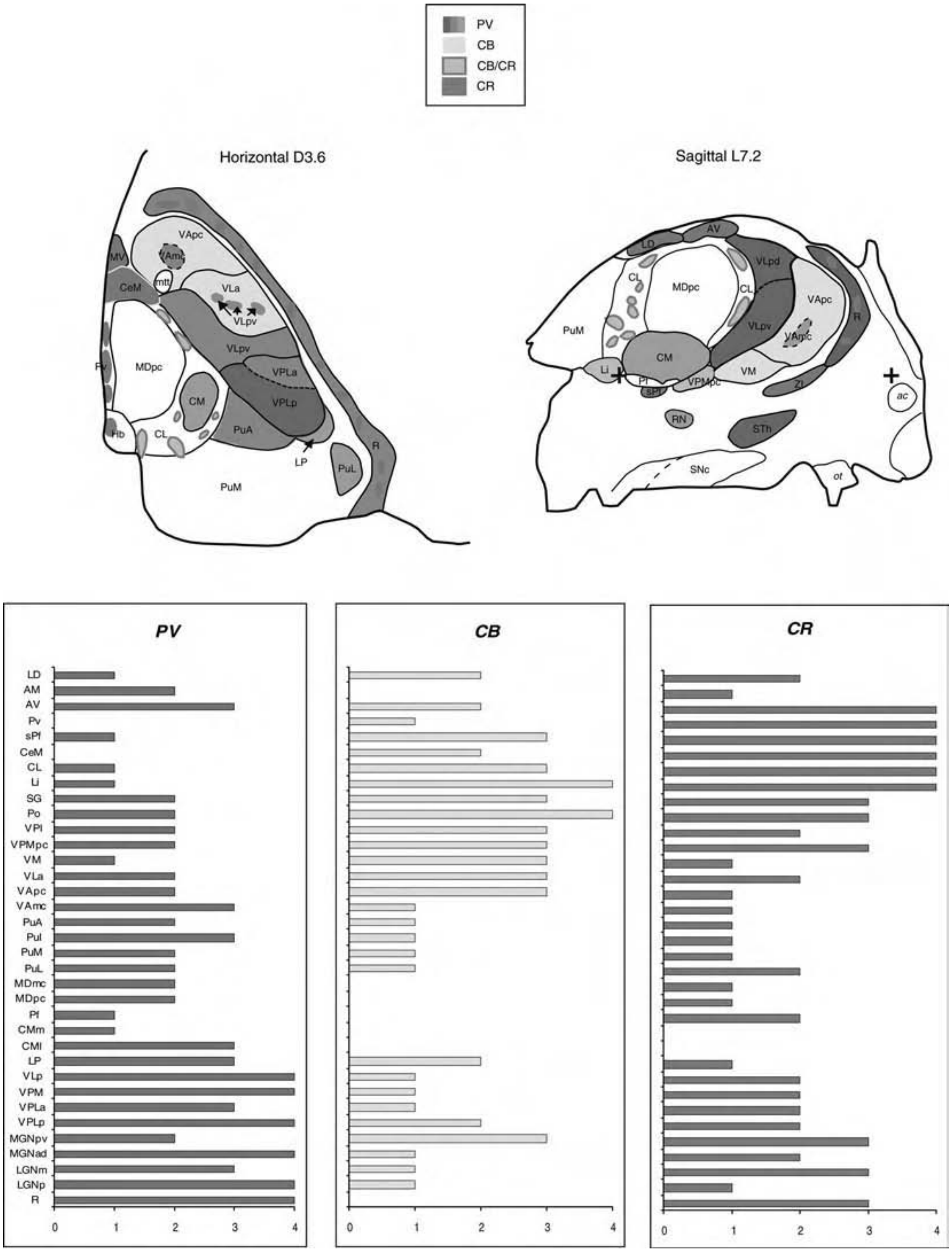

FIGURE 3.36

4 Basal Ganglia

Interest in the basal ganglia has grown particularly since the development of new surgical targets for pharmacotherapy-resistant parkinsonian patients and of animal models of the disease. This has led to a great number of investigations directed at the anatomical and functional (physiological and pathophysiological) organization of the basal ganglia (41,42,58–61,87). Because of this, the extension of this atlas to include the basal ganglia appeared necessary to cover major domains of stereotactic functional neurosurgery. In a previous study, we presented a neurochemical organizational scheme of the human basal ganglia that were subdivided into anatomo-functional territories on the basis of the distribution of CaBP and SMI-32 (48). This multiarchitectonic compartmentalization, as summarized in **Figure 4.54** for the striatum and pallidum, was not presented in a stereotactic atlas framework and is thus updated and added to the current atlas.

ATLAS MAPS

The series of maps presented in **Figures 4.1** to **4.47** were derived from case Hb7 where sections from the left and right hemispheres were cut in the frontal and sagittal planes, respectively. The distance between maps are given in millimeters "in vivo" in each drawing. Similar conventions to those described in Chapter 3 for the thalamic atlas were applied here, with additional areas indicated in many maps by dotted lines that represent the patch/matrix organization of the striatum, as well as differential staining in the pallidum and subthalamic nucleus. Whole pallidum, STh, and part of the striatum and SN are also represented in the maps of the thalamic atlas in Chapter 3 (**Figs. 3.1–3.13** and **3.18–3.25**). Structures outside the basal ganglia, such as parts of the hypothalamus, amygdala, and adjoining cortex, are not delimited in detail.

ANATOMO-FUNCTIONAL COMPARTMENTALIZATION

In the basal ganglia, compartmentalization of the human striatum and pallidum into distinct anatomofunctional territories was proposed on the basis of similar chemically defined compartments that receive projections from known cortical territories in the monkey. The distribution of calcium-binding proteins and SMI-32 was most helpful to identify anatomo-functional compartments of the striatum and pallidum and modular patterns of CaBP were related to AChE patch/matrix organization in the striatum. This anatomo-functional organization has been described extensively (48) and will be briefly reported here, with additional histological illustrations. The same stainings helped to demarcate subdivisions of the substantia nigra (SNc, SNr, and the VTA) and subthalamic nucleus. The pedunculopontine nucleus (PPN), another output structure of the basal ganglia, is not represented in this atlas and we refer to others (89,94,98–100) for an overview of its anatomy, functional organization, and role in movements disorders.

Striatum

Based on connections with the cortex, the striatum (caudate nucleus and putamen) has been subdivided into at least two compartments: the dorsal and ventral striatum. The first is related to sensorimotor and associative domains (postcommissural putamen and most of caudate nucleus), and the second (rostro-ventral parts of the caudate and putamen and the accumbens nucleus) to limbic cortical domains (59,60,90,101,102). As presented previously (48) and summarized in **Figure 4.54**, we divided the striatum and pallidum into four territories: sensorimotor (*T1*), associative (*T2*), paralimbic (*T3*), and limbic (*T4*) on the basis of CaBP and SMI-32. These are also illustrated by photomicrographs in **Figures 4.48** to **4.54**.

All but the rostral and ventral half of the putamen is characterized by enhanced neuropil immunostaining to PV and SMI-32, with relatively low CB-ir and CR-ir (*T1;* **Figs. 4.51, 4.52,** and **4.54**). The decrease of PV and SMI-32 immunostainings in the rostral and ventral half of the putamen demarcates the limit with a territory that also includes the caudate nucleus (Cd) and is characterized by progressive enhanced matriceal but low in the patches CB-ir (*T2,* **Figs. 3.31, 4.51,** and **4.54**). An approximate boundary between *T1* and *T2* territories in rostroventral PuT is shown in **Figure 4.54** (middle diagram), to cross a zone of progressively lower PV-/SMI-32-ir, and higher matriceal CB-ir. The territory of enhanced matriceal CB-ir extends into the rostral striatum where it is limited dorsolaterally by an area of relatively low CB-ir and conversely higher PV-ir, and ventromedially, by a complementary pattern of CB- and CR-ir patches. This complementary pattern is bordered ventrally and medially by the accumbens nucleus (Acb, **Figs. 4.49, 4.52,** and **4.54**). This is further divided into a core and shell on the basis of CB- and CR-ir, as demonstrated previously (48). The transitions from *T2* (with enhanced matriceal CB-ir) to *T3* (with apparition of CR-ir within or around low-CB patches) and *T4* (with enhanced CR-ir in a more complex mosaic pattern in the Acb) are best seen in frontal sections of the anterior striatum in **Figure 4.54** (*left panels*). In the maps, we considered a limit between the ventral striatum (VS) and the Acb as corresponding to different patterns of AChE and CaBP staining. The transitions between territories are also shown in horizontal sections of the striatum, in **Figure 4.54**. These transitions, though more subtle, correspond to changes in the expression of SMI-32-ir, with progressive lower densities in *T2* to *T4* (**Fig. 4.49**). The patterns seen in Acb extend posteriorly to the level of the subcommissural pallidum and subpallidal area (sPal). The boundary with the more posterior part of the basal forebrain is not clearly defined but can be estimated by the transition to more uniform CR-ir in sublenticular fibers (e.g., **Figs. 4.48** and **4.49**) and the appearance of the basal nucleus of Meynert (B). This region corresponds closely to the extended amygdala described by others (59,87,97,103) and also comprising the ansa peduncularis (*ap*), linking the amygdala to the hypothalamus and to the rostral parts of MD and R through the inferior thalamic peduncle (94). The ventral striatum, particularly the accumbens, has been subject to many investigations because of its connections with the limbic system, role in mediating motivated behavior and implications in several disorders (59,91,103,104). It is important to note that the neurochemical compartments described above are not of segregated territories, but rather of gradients, as is the case with cortical projections (see Ref. 90 for a review).

Pallidum

The separation between internal (GPi) and external (GPe) subdivisions of the pallidum are clearly identified with all stainings, but particularly well defined with AChE and myelin stains. The GPi is further partitioned along its caudal two-thirds by the internal accessory lamina into laterodorsal (l) and medioventral (m) portions. Interestingly, a thin lamina also divides the GPe (e.g., **Fig. 4.50**) but is less obvious and, to our knowledge, has not been related to any particular functional subdivision, as has been done for the GPi. The anatomo-functional compartmentalization of the pallidum was described in detail before (48), and is illustrated by the photomicrographs in **Figures 4.48** to **4.54** and the summary diagram in **Figure 4.54**.

Parallel to the striatum, the pallidum (GPi and GPe) is organized into four compartments on the basis of neurochemical gradients: enhanced PV and SMI-32 neuropil immunostaining in the caudal half to two-thirds of the GPe and GPi (*T1* territory), and, conversely, increased CB-ir in the rostral part of both divisions (*T2* territory). At the most rostral, precommissural level, dense neuropil CB-ir encompasses both portions of the pallidum situated above and just beneath the anterior commissure, with the latter corresponding to the so-called ventral pallidum (GPv) (**Figs. 4.49, 4.52,** and **4.54**). Further ventrally, the decrease of CB-ir delimits the ventral pallidal border with underlying sPal (**Figs. 4.53–4.54**). On the basis of differences in intensity and patterns of CB- and CR-ir, we consider the anteroventral, subcommissural extension of the pallidum and sPal as two separate territories (*T3* and *T4*; **Fig. 4.54**). More posteriorly, sPal is continuous with the intense but more uniform staining of CR-ir fibers running underneath the pallidum and ansa lenticularis and corresponding to the extended amygdala and including the ansa peduncularis (*ap*) (e.g., **Fig. 4.50**).

In both pallidal segments and traversing the capsula, fiber bundles express high AChE, SMI-32- and CB-ir and can be traced up to the level of the SN (**Figs. 3.29; 4.48–4.49** and **5.3–5.4**). Fibers immunostained for PV appear to reach the STh, as seen in **Figures 4.51** and **5.4**. These are part of the "comb" system (94) that includes striato-nigral and pallido-subthalamic fibers (see also Chapter 5).

Subthalamic Nucleus

The nucleus has a typical elongated shape oriented obliquely in a lateral, dorsal and anterior to medial, ventral and posterior direction. It is well delimited between the zona incerta dorsally, and the internal capsule and the substantia nigra ventro-posteriorly. The nucleus has an homogeneous dense cell population and is characterized by strong PV-ir and AChE staining, except for a small ventral portion of the nucleus (**Figs. 3.28** and **5.3A**). The nucleus appears negative in sections immunostained for CB and contains moderate levels of CR-ir, except for some densely stained fibers at the most posterior and medial tip of the nucleus (e.g., **Fig. 3.28**).

Substantia Nigra

As in our previous study (48), we consider the two major divisions of the SN: pars compacta (SNc) and pars reticulata (SNr). The SNc comprises the large TH-positive cells organized in a dorsal layer (densocellular ventral tier) and cell columns extending into SNr (**Fig. 4.53**). The SNr extends further ventrally, caudally, but also dorsolaterally to adjoin the ventral STh (also identified as dorsolateral SN). The delimitation of the two divisions of the SN have been introduced in this new atlas, including the maps from Hb1, which were previously published (chap. 3). In **Figure 3.29**, immunostaining in the SN can be seen together with that in the thalamus, STh, and medial striato-pallidal divisions, as well as in fiber bundles traversing the internal capsule. Neuropil CB-ir is most dense in the SNr and largely spares SNc cell columns in the ventral tier (**Fig. 4.53C**), similar to the pattern described by other (105). This high CB-ir in SNr is continuous with that seen in the fibers coursing from the striatum through the two pallidal divisions and the internal capsule (**Figs. 3.29C** and **4.52**). In contrast, neuropil CR-ir is concentrated in the SNc, including the dorsal division and part of the cell columns of the ventral tier (**Fig. 4.53D**) as well as in VTA, thus in complementary pattern to that of the CB-ir. Immunostaining to PV is generally low in the neuropil of both SN and VTA, except for the more lateral and dorsal part of the SN, which shows some moderate staining (**Fig. 3.26F**). We refer to others for more specific neuronal distributions of the CaBP in the substantia nigra (35,106–108).

FIGURES 4.1 to 4.22 A series of drawings of frontal sections of the human thalamus and basal ganglia (case Hb7; Table 2.1) oriented orthogonal to the intercommissural stereotactic plane (DV 0, indicated by a horizontal interrupted line intersecting the dorsoventral grid axis at 0) and represented in a posterior to anterior sequence. Anteroposterior levels relative to the pc level (AP 0, represented in **Fig. 4.2**) are indicated in lower right of each drawing (see the section entitled Methods for explanation of the coordinate system). The interhemispheric plane is represented by a vertical interrupted line intersecting the grid at mediolateral point 0. Intervals between sections are 1 mm, except for the most rostral, precommissural part of the striatum where the intervals can reach 1.5 mm. Each division on the grid corresponds to 1 mm "in vivo" and the intercommissural distance is 26 mm. The same conventions are used as in Figures 3.1 to 3.25.

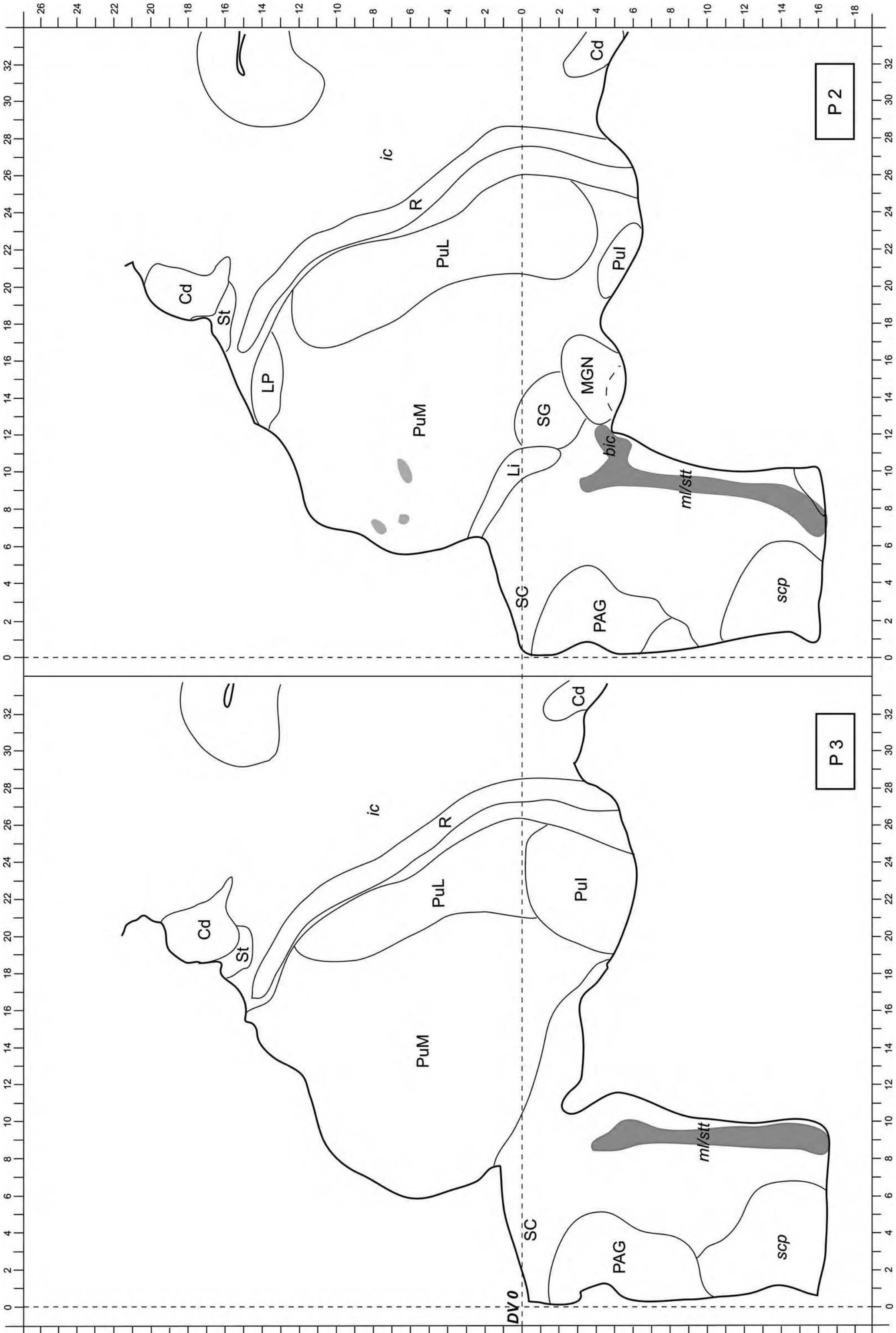
P 2
Cd
Cd
St
ic
R
PuL
Pul
LP
PuM
SG
MGN
Li
bic
ml/stt
SG
PAG
scp
P 3
Cd
Cd
St
ic
R
PuL
Pul
PuM
ml/stt
SC
PAG
scp
DV 0
26
24
22
20
18
16
14
12
10
8
6
4
2
0
2
4
6
8
10
12
14
16
18
0
2
4
6
8
10
12
14
16
18
20
22
24
26
28
30
32

FIGURE 4.1

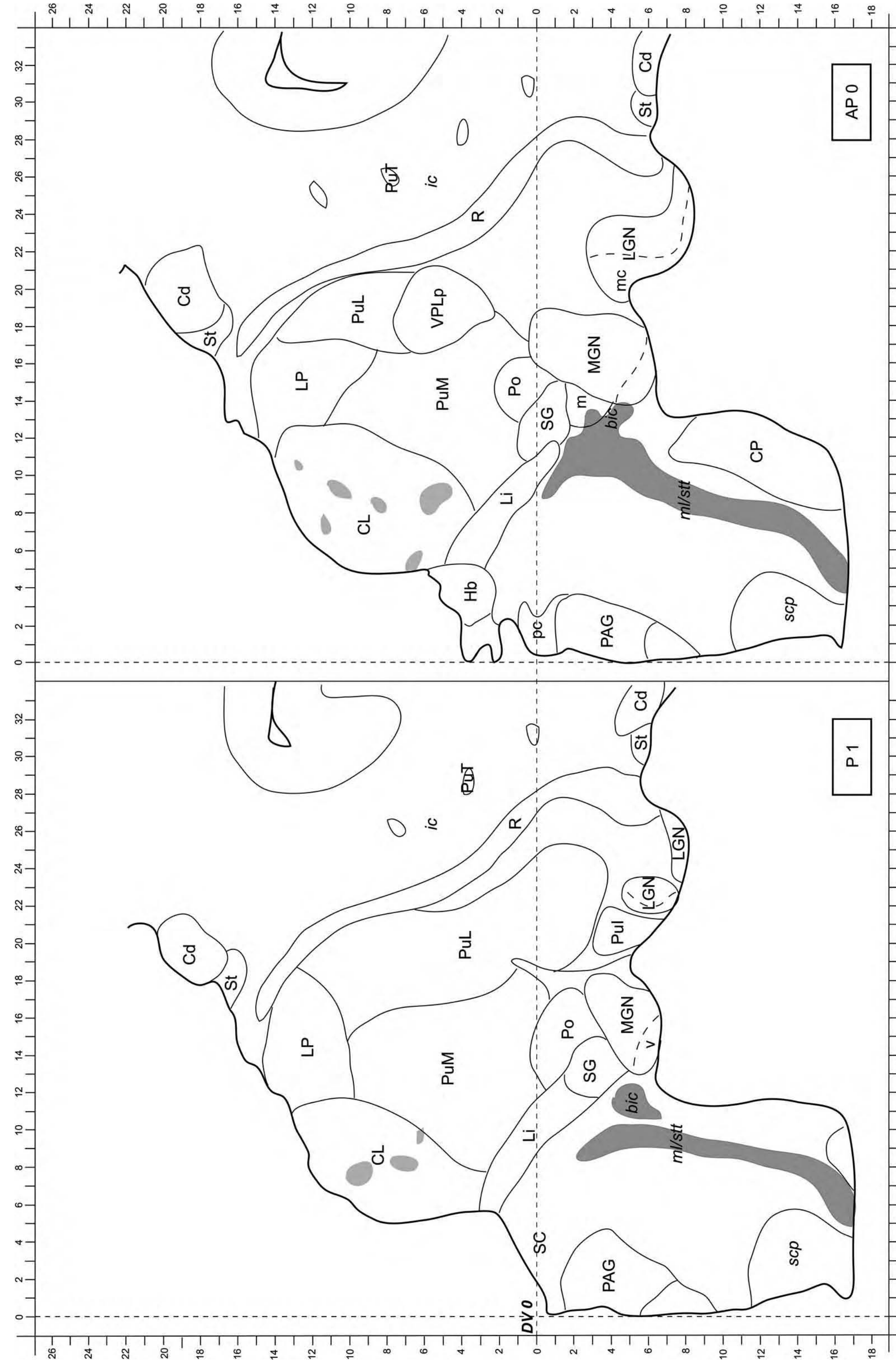
AP 0
Cd
St
PuT
ic
R
LGN
mc
Cd
St
PuL
VPLp
LP
PuM
Po
MGN
SG
m
bic
CL
Li
ml/stt
CP
Hb
pc
PAG
scp
P 1
Cd
St
PuT
ic
R
LGN
LGN
Pul
Cd
St
PuL
LP
PuM
Po
MGN
v
SG
bic
CL
Li
ml/stt
SC
PAG
scp
DV 0
26 24 22 20 18 16 14 12 10 8 6 4 2 0 2 4 6 8 10 12 14 16 18
0 2 4 6 8 10 12 14 16 18 20 22 24 26 28 30 32

FIGURE 4.2

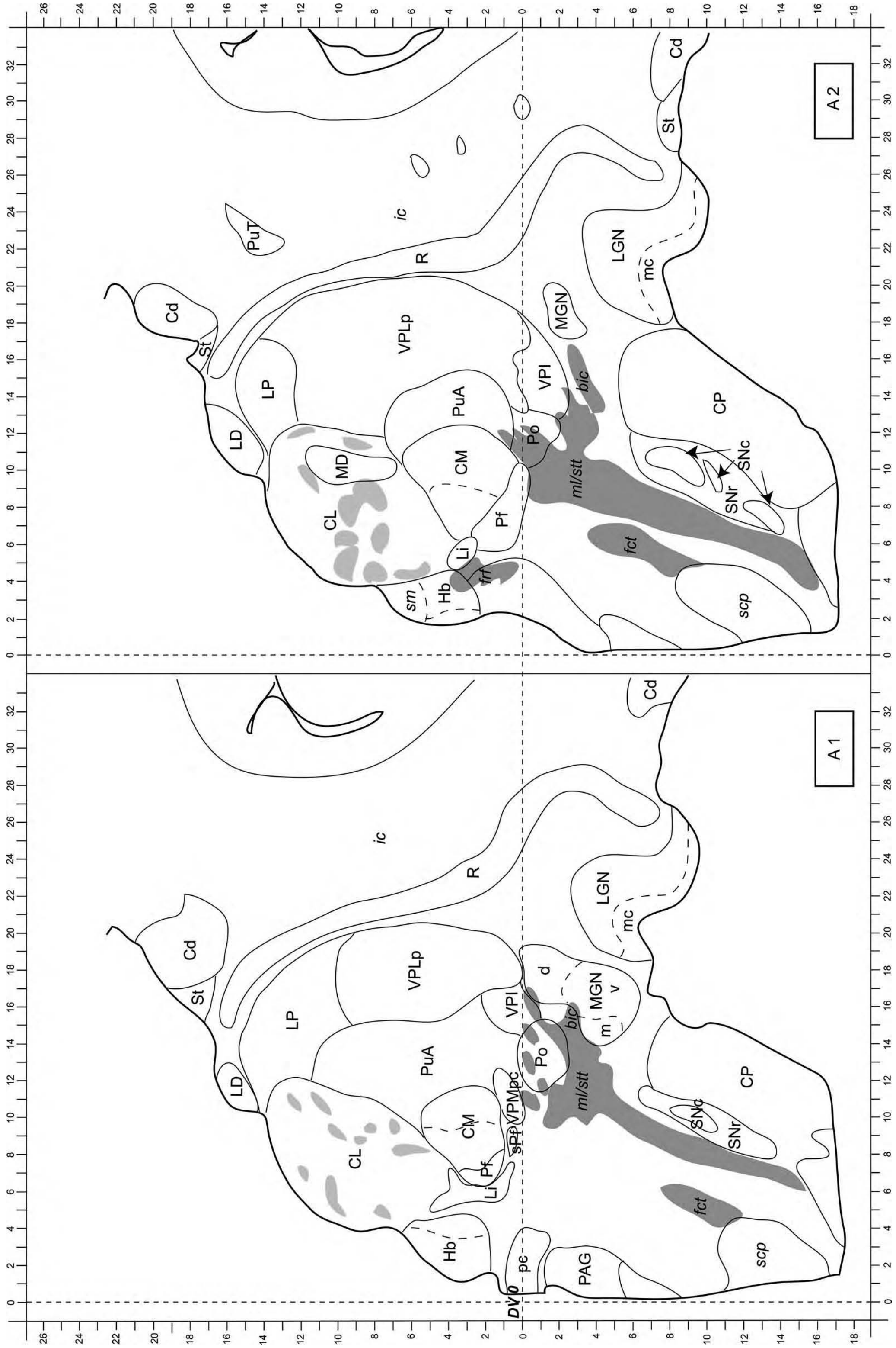
A 2
Cd
St
PuT
ic
R
LD
LP
VPLp
MD
CL
PuA
CM
Pf
Li
Hb
sm
fr
Po
VPI
MGN
bic
ml/stt
fct
LGN
mc
CP
SNc
SNr
scp
Cd
St
A 1
Cd
St
LD
LP
VPLp
PuA
ic
R
CL
CM
Pf
Li
SPf
VPMpc
Hb
pe
PAG
DV 0
Po
VPI
d
MGN
v
m
bic
ml/stt
LGN
mc
CP
SNc
SNr
fct
scp
Cd
0
2
4
6
8
10
12
14
16
18
20
22
24
26
28
30
32
26
24
22
20
18
16
14
12
10
8
6
4
2
0
2
4
6
8
10
12
14
16
18

FIGURE 4.3

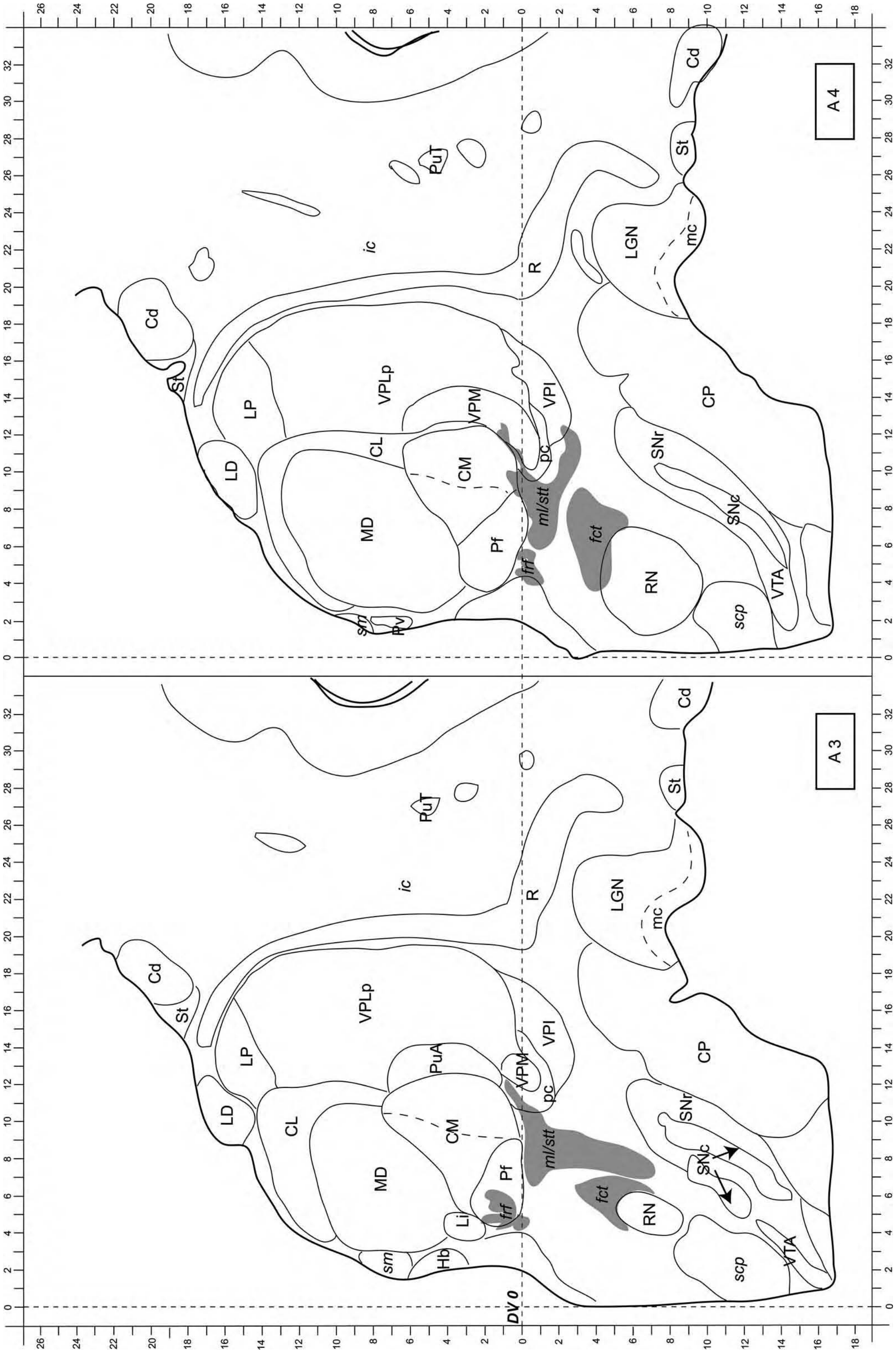
A 4
A 3
DV 0
Cd
St
LD
LP
CL
MD
VPLp
VPM
VPl
CM
Pf
pc
ml/stt
frf
fct
RN
scp
VTA
SNr
SNc
CP
LGN
mc
R
ic
PuT
PuA
sm
Pv
Hb
Li

FIGURE 4.4

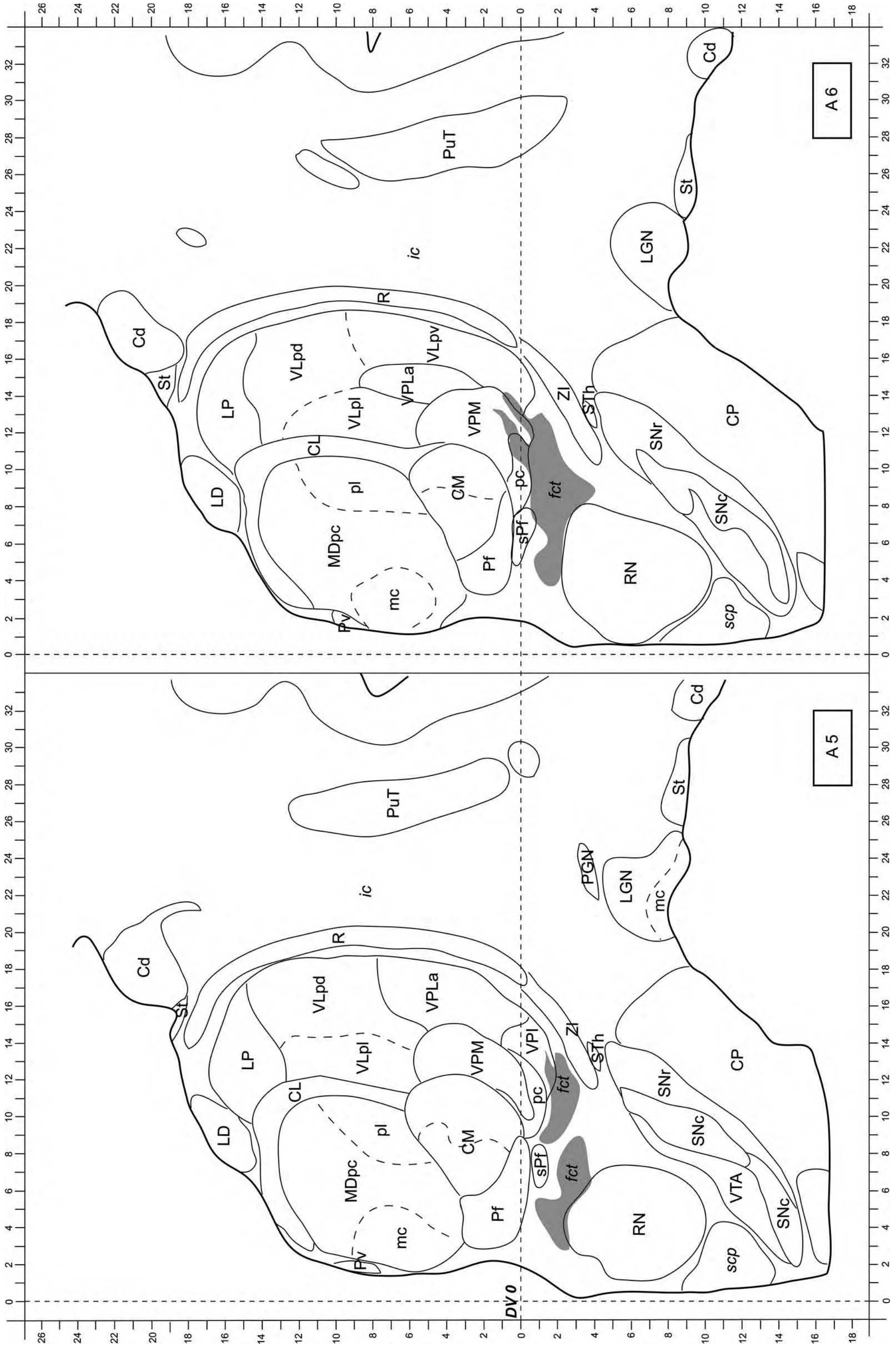
A 6
Cd
PuT
ic
R
VLpd
VLpv
VPLa
LP
St
VLpl
CL
VPM
ZI
STh
LD
pl
CM
pc
fct
sPf
MDpc
Pf
mc
Pv
RN
SNr
SNc
CP
scp
LGN
St
Cd
A 5
Cd
St
R
ic
PuT
VLpd
VPLa
LP
VLpl
CL
VPM
VPl
ZI
STh
fct
pc
LD
pl
CM
sPf
fct
MDpc
mc
Pv
Pf
RN
SNr
SNc
VTA
SNc
scp
CP
PGN
LGN
mc
St
Cd
DV 0
26
24
22
20
18
16
14
12
10
8
6
4
2
0
2
4
6
8
10
12
14
16
18
32
30
28
26
24
22
20
18
16
14
12
10
8
6
4
2
0

FIGURE 4.5

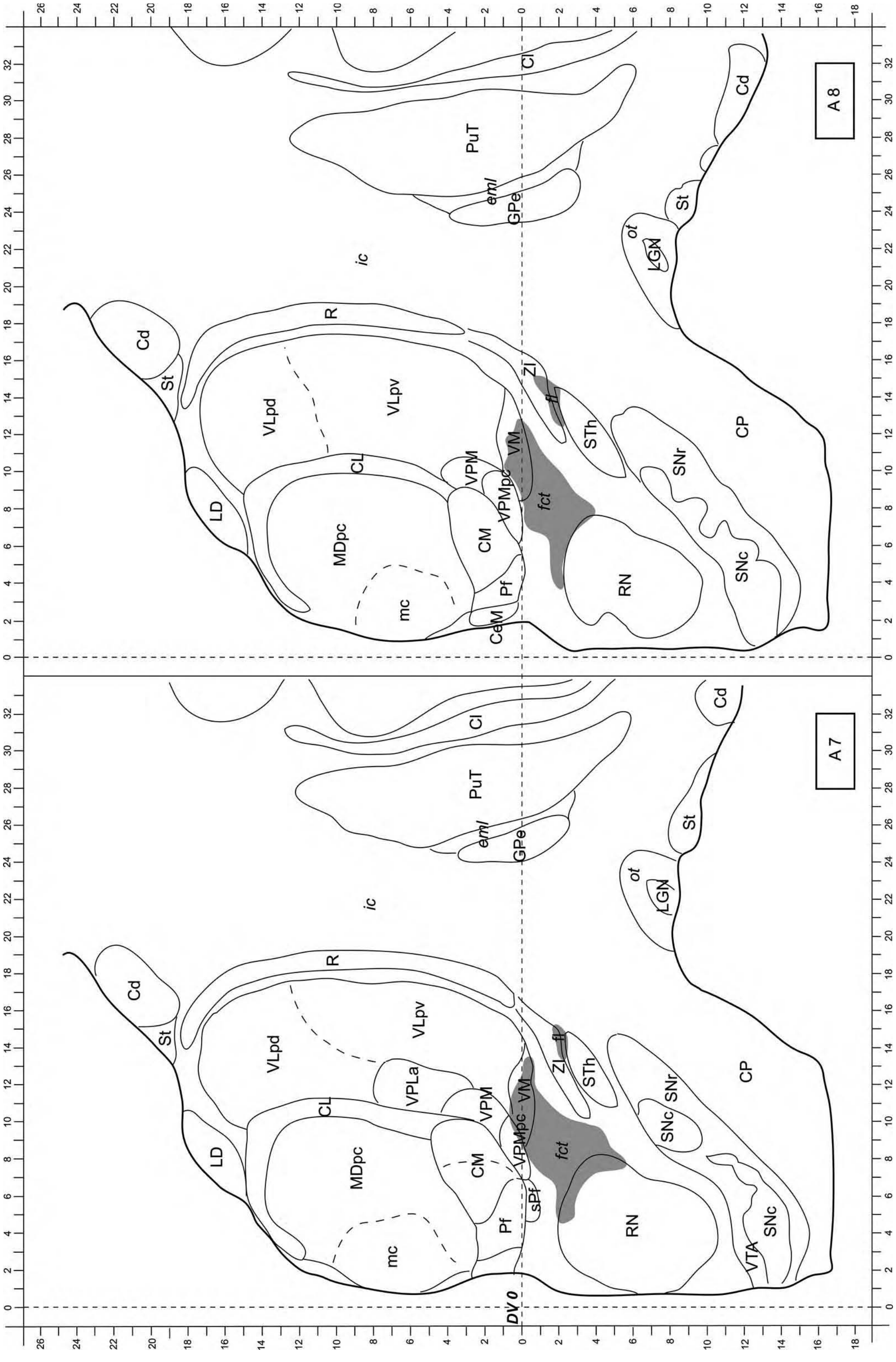
A 8
A 7
DV 0
Cd
St
Cl
PuT
eml
GPe
ic
ot
LGN
R
VLpd
VLpv
VLPa
CL
LD
MDpc
mc
VPM
VPMpc
VM
CM
Pf
sPf
CeM
ZI
fl
fct
STh
SNr
SNc
RN
VTA
CP
0
2
4
6
8
10
12
14
16
18
20
22
24
26
28
30
32

FIGURE 4.6

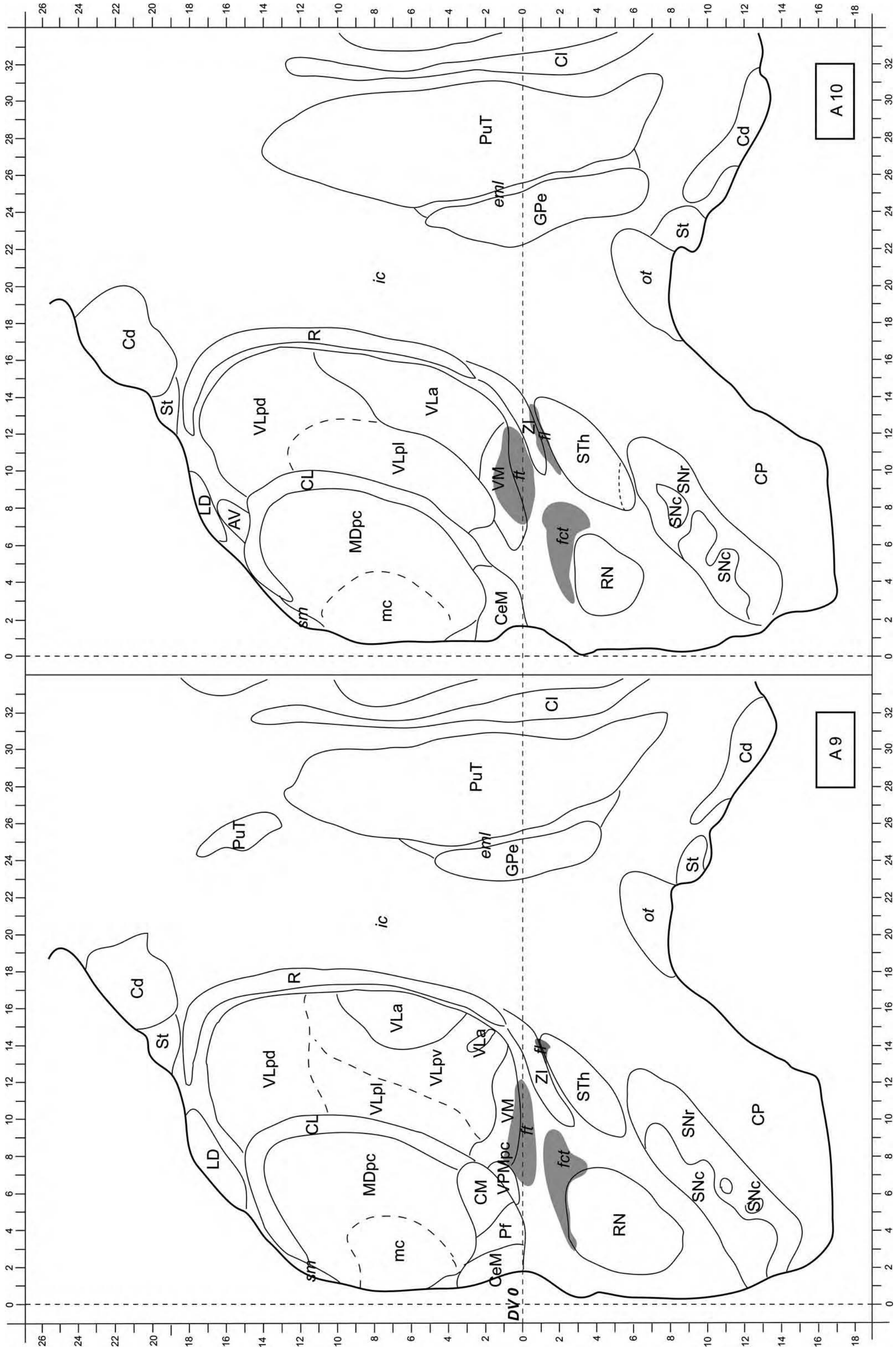
A 10
Cd
St
R
VLpd
VLa
VLpl
CL
LD
AV
MDpc
mc
sm
CeM
VM
ft
ZI
fl
STh
fct
RN
SNc
SNr
SNc
CP
ot
St
Cd
GPe
eml
PuT
Cl
ic
A 9
Cd
St
R
VLa
VLpd
VLpl
VLpv
VLa
LD
CL
MDpc
mc
sm
CeM
Pf
CM
VPMpc
VM
ft
ZI
fl
STh
fct
RN
SNr
SNc
SNc
CP
ot
St
Cd
GPe
eml
PuT
PuT
Cl
ic
DV 0
26
24
22
20
18
16
14
12
10
8
6
4
2
0
2
4
6
8
10
12
14
16
18
0
2
4
6
8
10
12
14
16
18
20
22
24
26
28
30
32

FIGURE 4.7

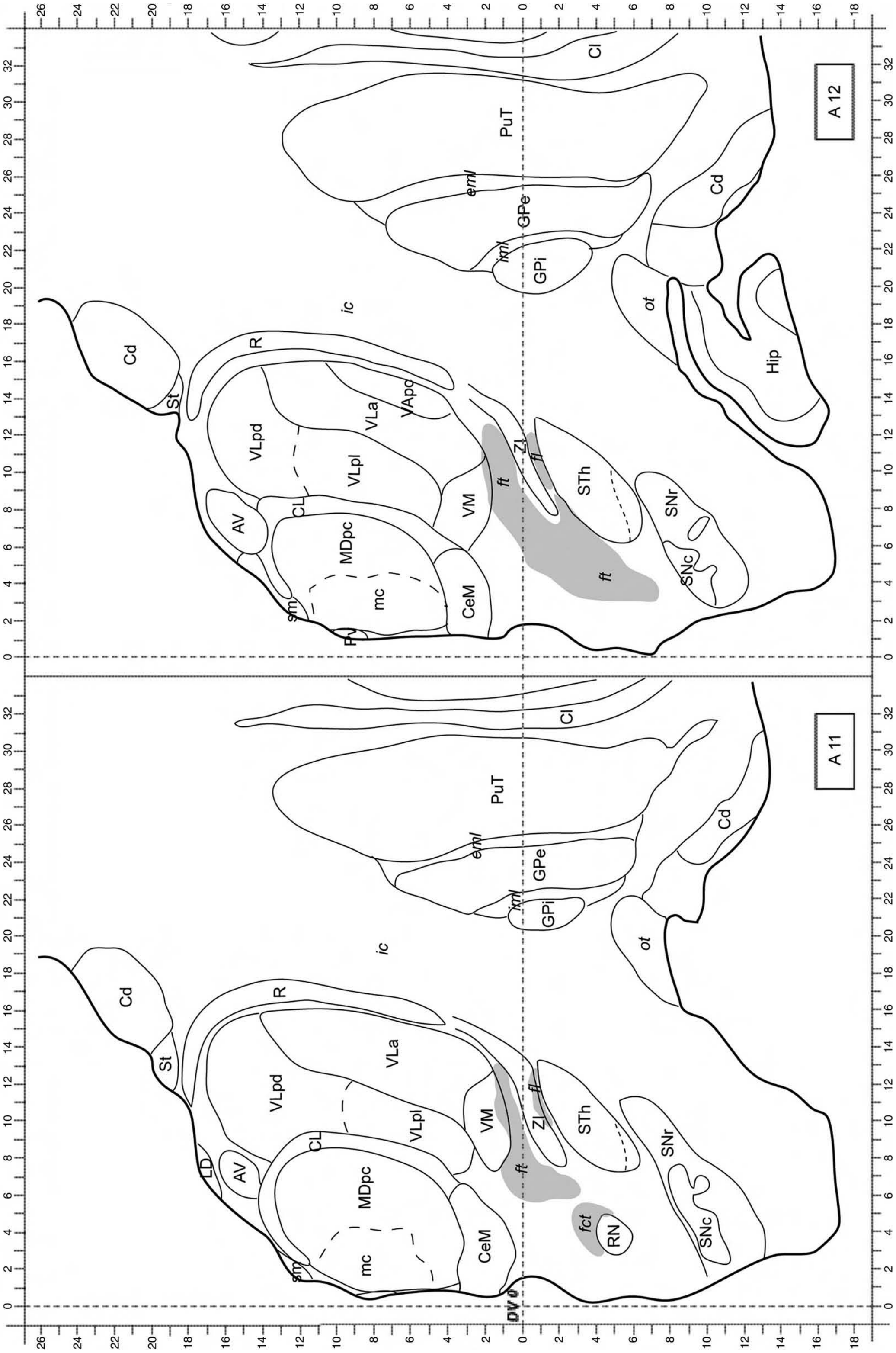
A 12
Cd
St
R
ic
VLpd
VLa
VApc
VLpl
AV
CL
MDpc
mc
sm
Pv
CeM
VM
ZI
fl
ft
STh
SNr
SNc
PuT
eml
GPe
iml
GPi
Cl
ot
Hip
A 11
Cd
St
R
ic
LD
AV
CL
VLpd
VLa
VLpl
VM
MDpc
mc
sm
CeM
ft
ZI
fl
fct
RN
STh
SNr
SNc
PuT
eml
GPe
iml
GPi
Cl
ot
DV 0

FIGURE 4.8

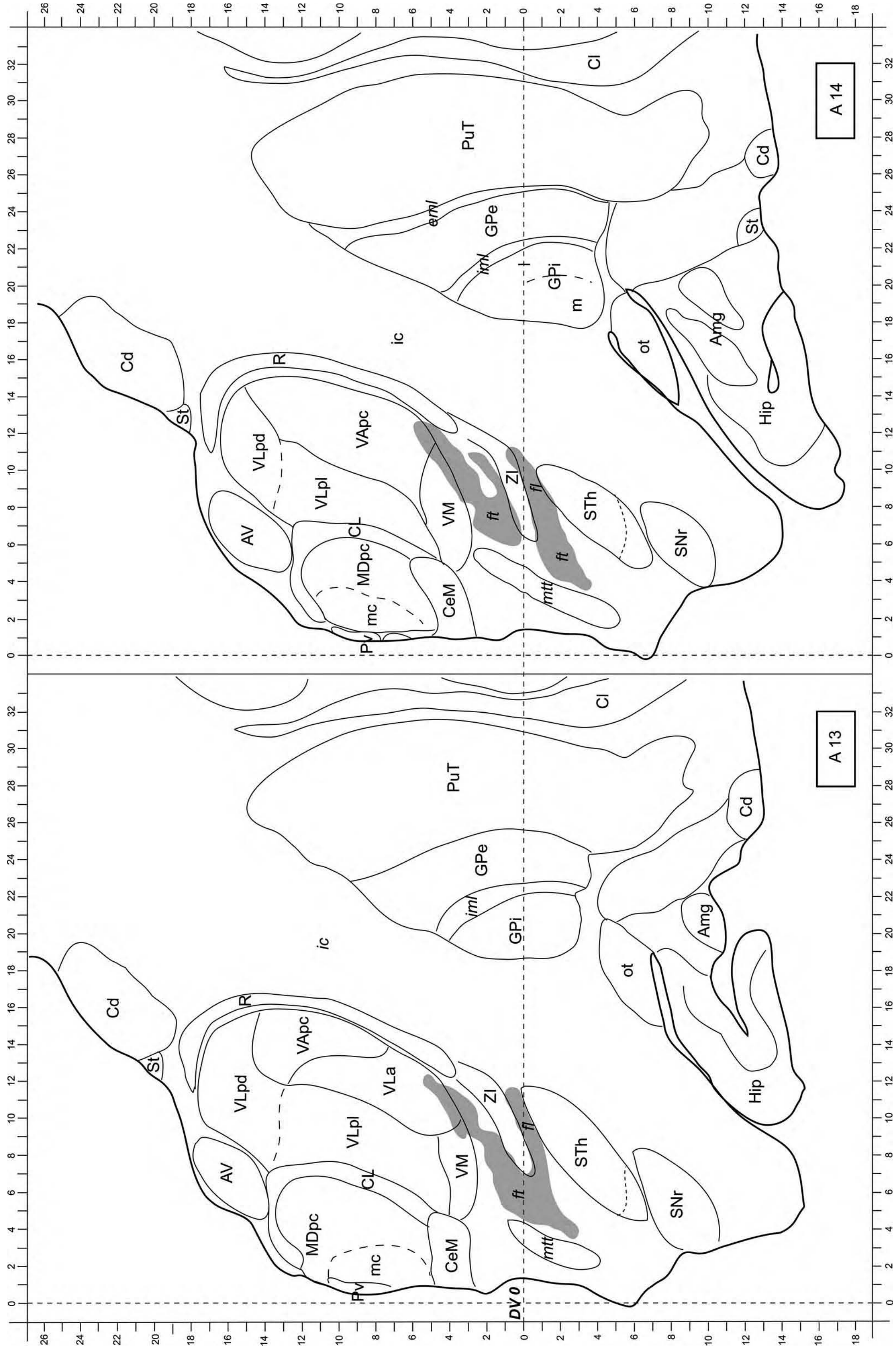
A 14
Cl
PuT
Cd
St
eml
GPe
iml
l
GPi
m
ic
Cd
St
R
VApc
VLpd
VLpl
AV
CL
MDpc
mc
Pv
CeM
VM
ft
ZI
fl
STh
SNr
mtt
ot
Amg
Hip
A 13
Cl
PuT
Cd
GPe
iml
GPi
ic
Cd
St
R
VApc
VLa
VLpd
VLpl
AV
CL
MDpc
mc
Pv
CeM
VM
ZI
fl
ft
STh
SNr
mtt
ot
Amg
Hip
DV 0

FIGURE 4.9

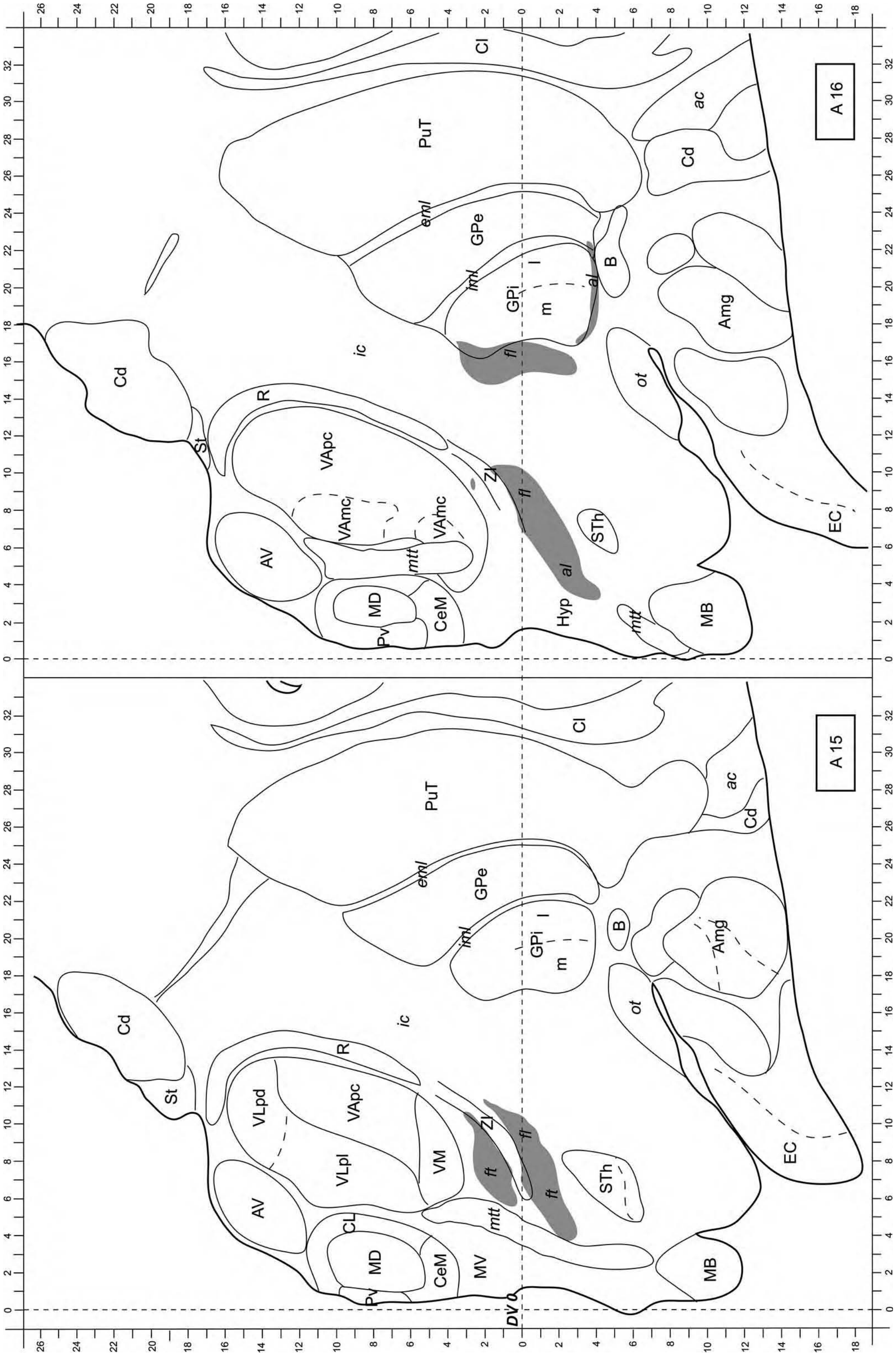
A 16
Cl
PuT
ac
Cd
eml
GPe
iml
l
GPi
m
al
B
Amg
ic
fl
ot
Cd
R
St
VApc
ZI
VAmc
VAmc
fl
STh
AV
mtt
al
MD
CeM
Pv
Hyp
mtt
MB
EC
A 15
Cl
PuT
ac
Cd
eml
GPe
iml
l
GPi
m
B
Amg
ic
ot
Cd
R
St
VLpd
VApc
VLpl
VM
ZI
fl
ft
ft
STh
AV
CL
mtt
MD
CeM
MV
Pv
MB
EC
DV 0

FIGURE 4.10

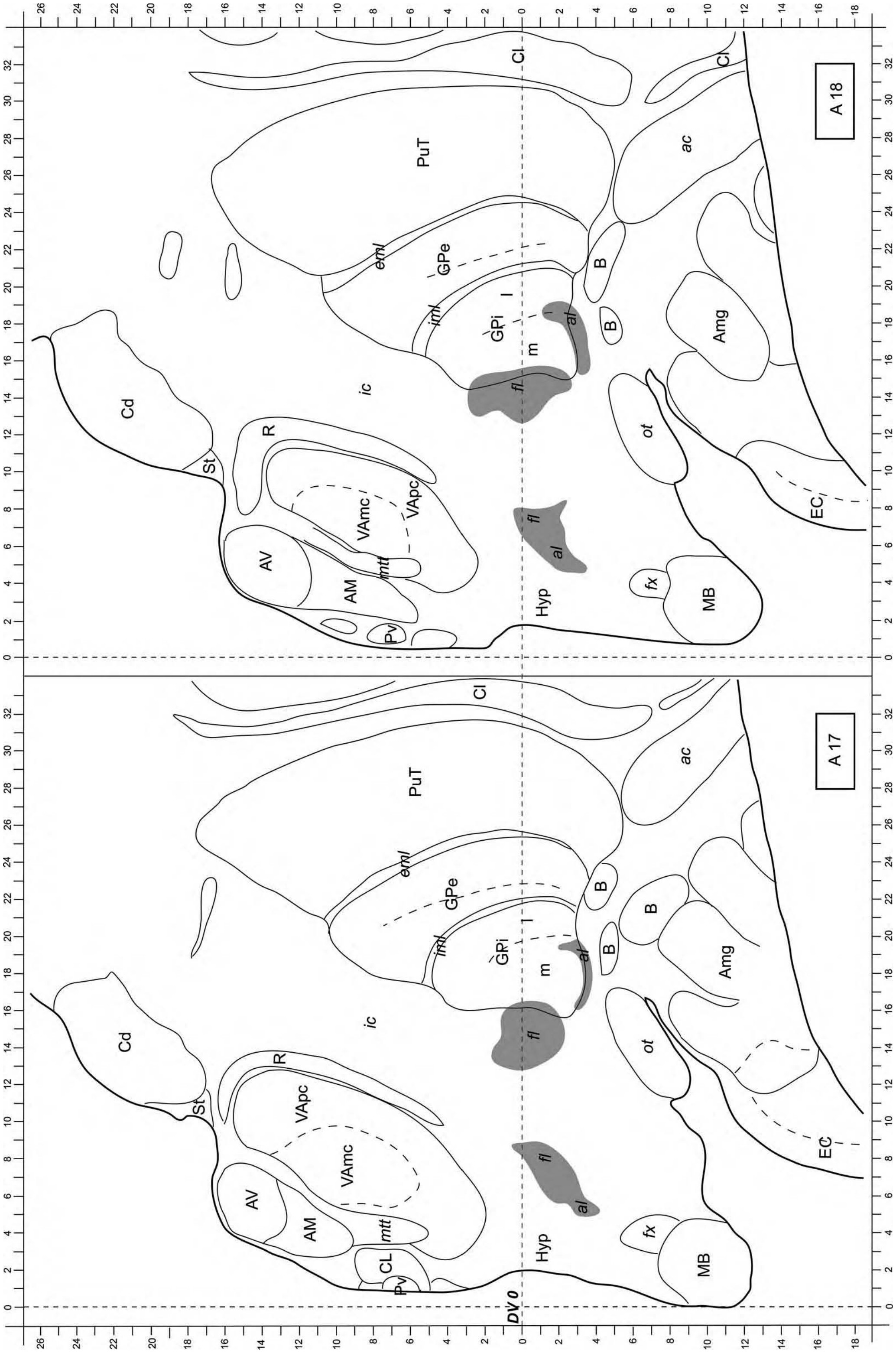
A 18
Cl
PuT
ac
eml
GPe
GPi
iml
l
m
al
fl
B
Amg
ot
EC
Cd
St
R
ic
VAmc
VApc
AV
AM
mtt
Pv
Hyp
fx
MB
A 17
CL
DV 0
26
24
22
20
18
16
14
12
10
8
6
4
2
0
32
30
28

FIGURE 4.11

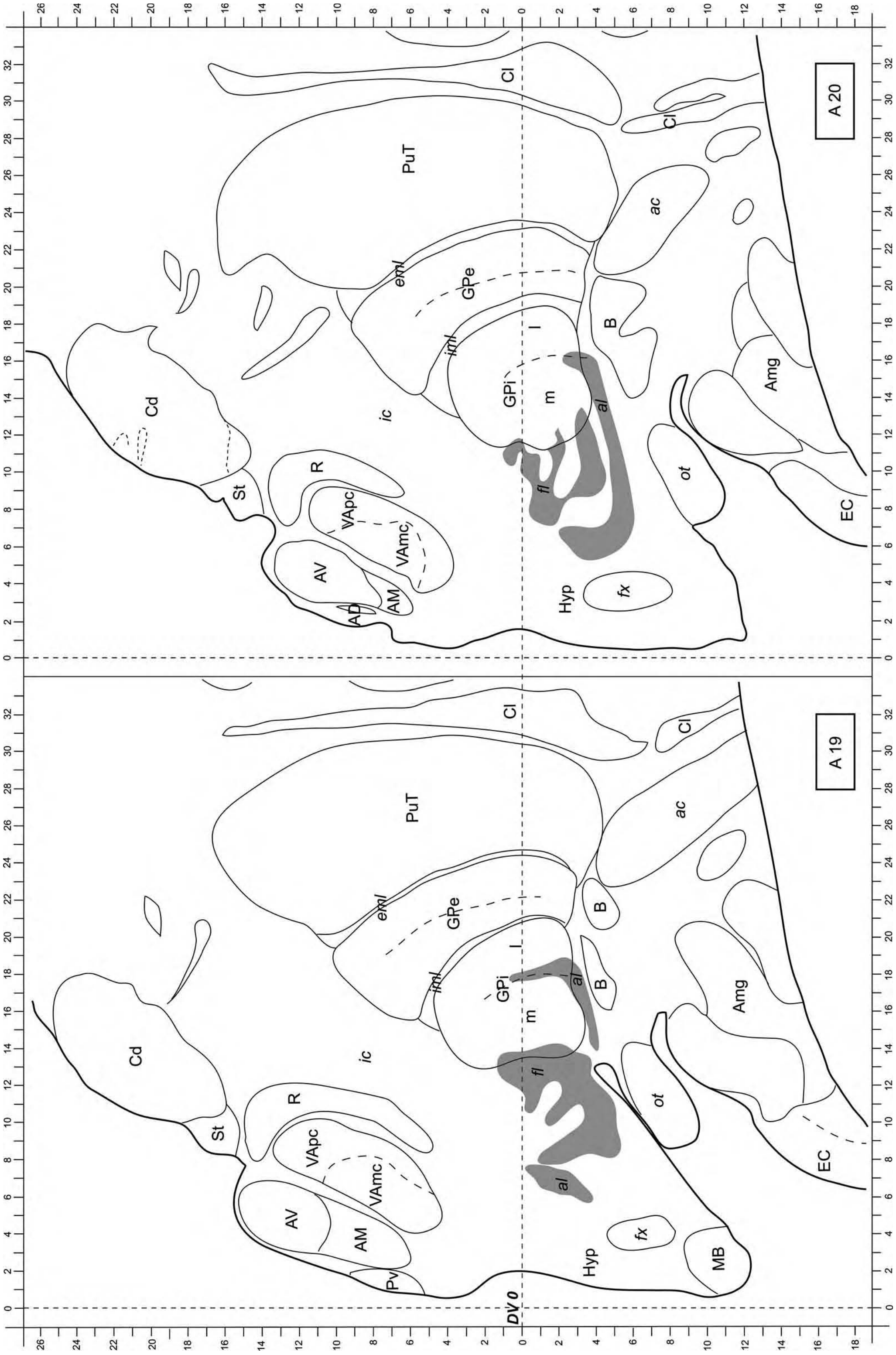
A 20
Cl
PuT
Cl
ac
eml
GPe
iml
l
B
GPi
m
al
Amg
Cd
ic
R
St
VApc
VAmc
fl
ot
EC
AV
AM
AD
Hyp
fx
A 19
Cl
Cl
PuT
ac
eml
GPe
iml
l
B
GPi
al
B
m
Amg
Cd
ic
R
St
VApc
VAmc
fl
ot
EC
al
AV
AM
Pv
Hyp
fx
MB
DV 0
26
24
22
20
18
16
14
12
10
8
6
4
2
0
2
4
6
8
10
12
14
16
18
32
30
28
26
24
22
20
18
16
14
12
10
8
6
4
2
0

FIGURE 4.12

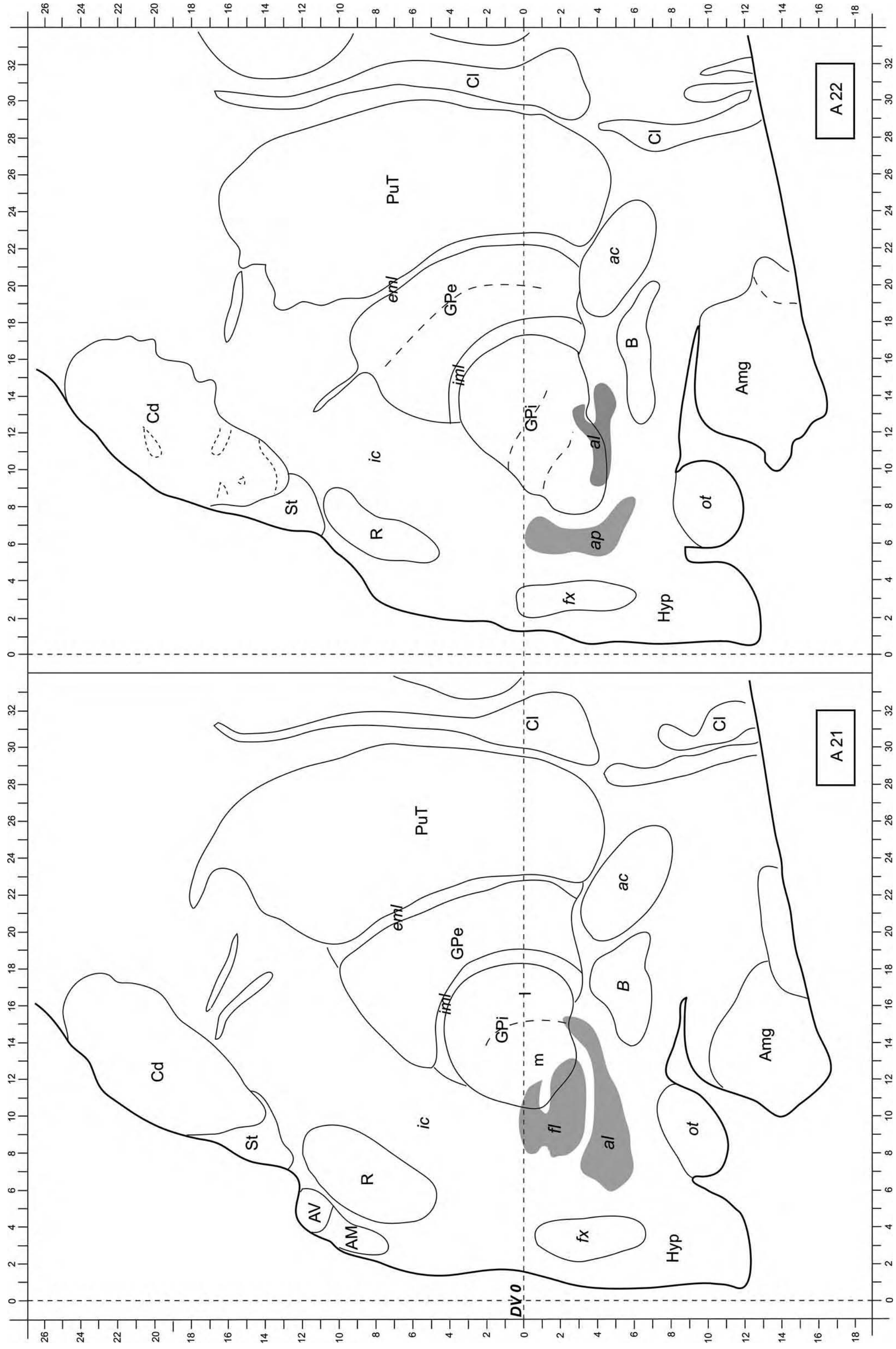
A 22
Cl
Cl
PuT
ac
eml
GPe
B
iml
Amg
Cd
GPi
al
ic
St
ot
R
ap
fx
Hyp
A 21
Cl
Cl
PuT
ac
eml
GPe
B
iml
l
GPi
m
Amg
Cd
ic
fl
al
ot
St
R
AV
AM
fx
Hyp
DV 0
26 24 22 20 18 16 14 12 10 8 6 4 2 0 2 4 6 8 10 12 14 16 18
32 30 28 26 24 22 20 18 16 14 12 10 8 6 4 2 0

FIGURE 4.13

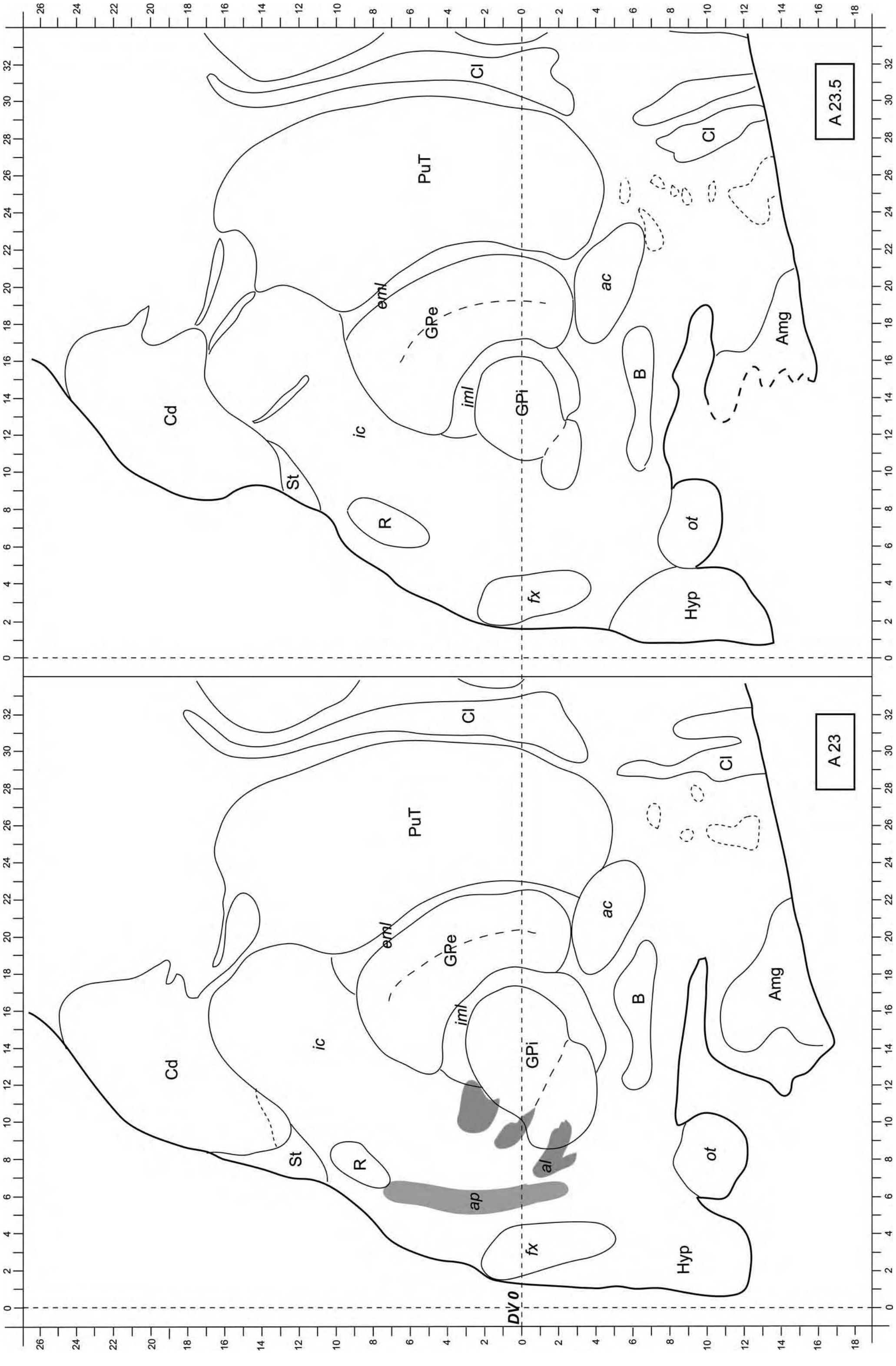
A 23.5
Cl
PuT
Cl
eml
GRe
ac
GPi
iml
Cd
ic
St
B
Amg
R
ot
fx
Hyp
A 23
Cl
PuT
Cl
eml
GRe
ac
B
Amg
Cd
ic
iml
GPi
St
R
al
ap
ot
fx
Hyp
DV 0
26 24 22 20 18 16 14 12 10 8 6 4 2 0 2 4 6 8 10 12 14 16 18
32 30 28 26 24 22 20 18 16 14 12 10 8 6 4 2 0

FIGURE 4.14

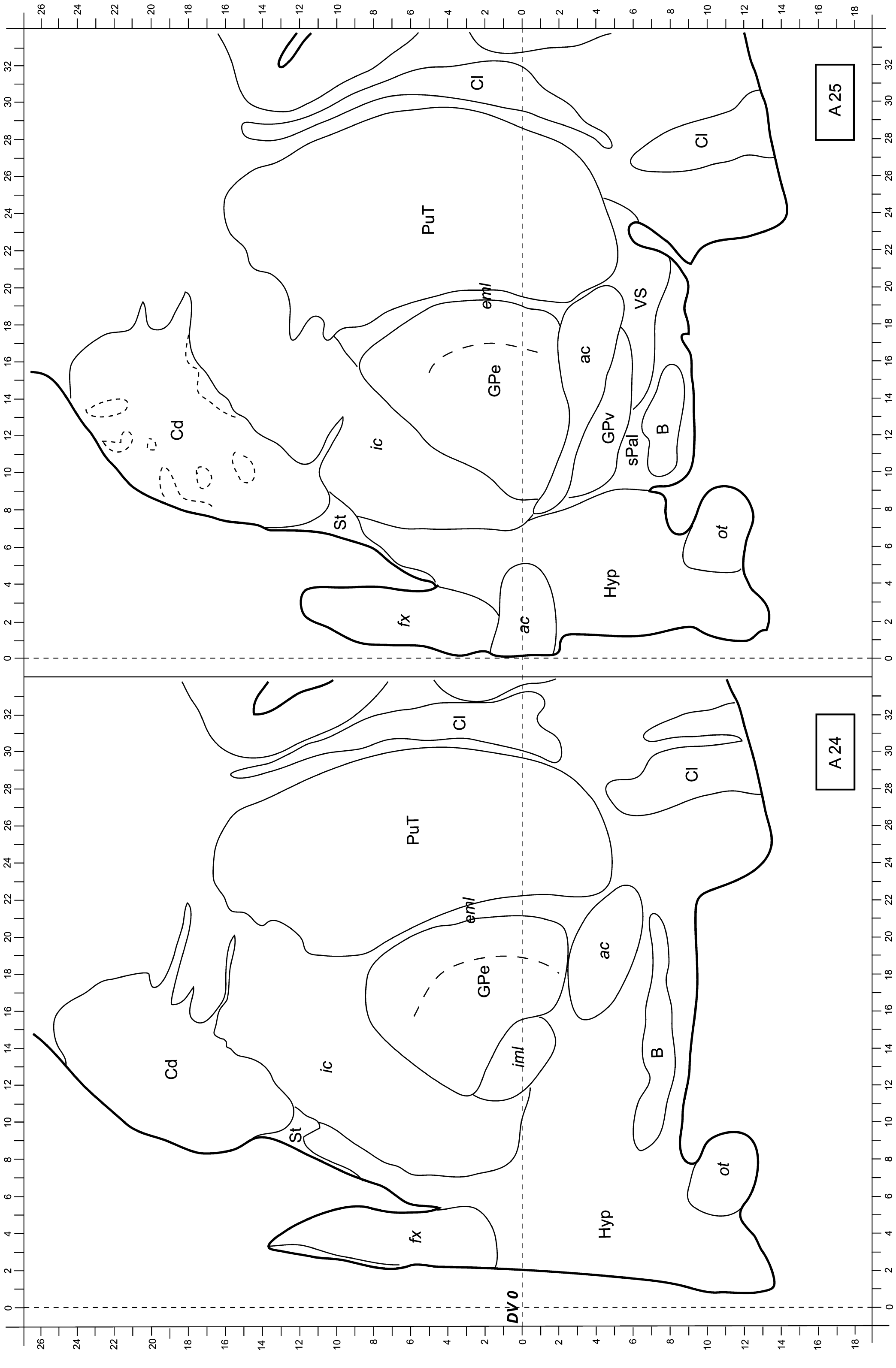
A 25
Cl
PuT
eml
GPe
ac
VS
GPv
sPal
B
Cd
ic
St
fx
ac
Hyp
ot
Cl
A 24
Cl
PuT
eml
GPe
iml
ac
B
Cd
ic
St
fx
Hyp
ot
Cl
DV 0
26 24 22 20 18 16 14 12 10 8 6 4 2 0 2 4 6 8 10 12 14 16 18
32 30 28 26 24 22 20 18 16 14 12 10 8 6 4 2 0

FIGURE 4.15

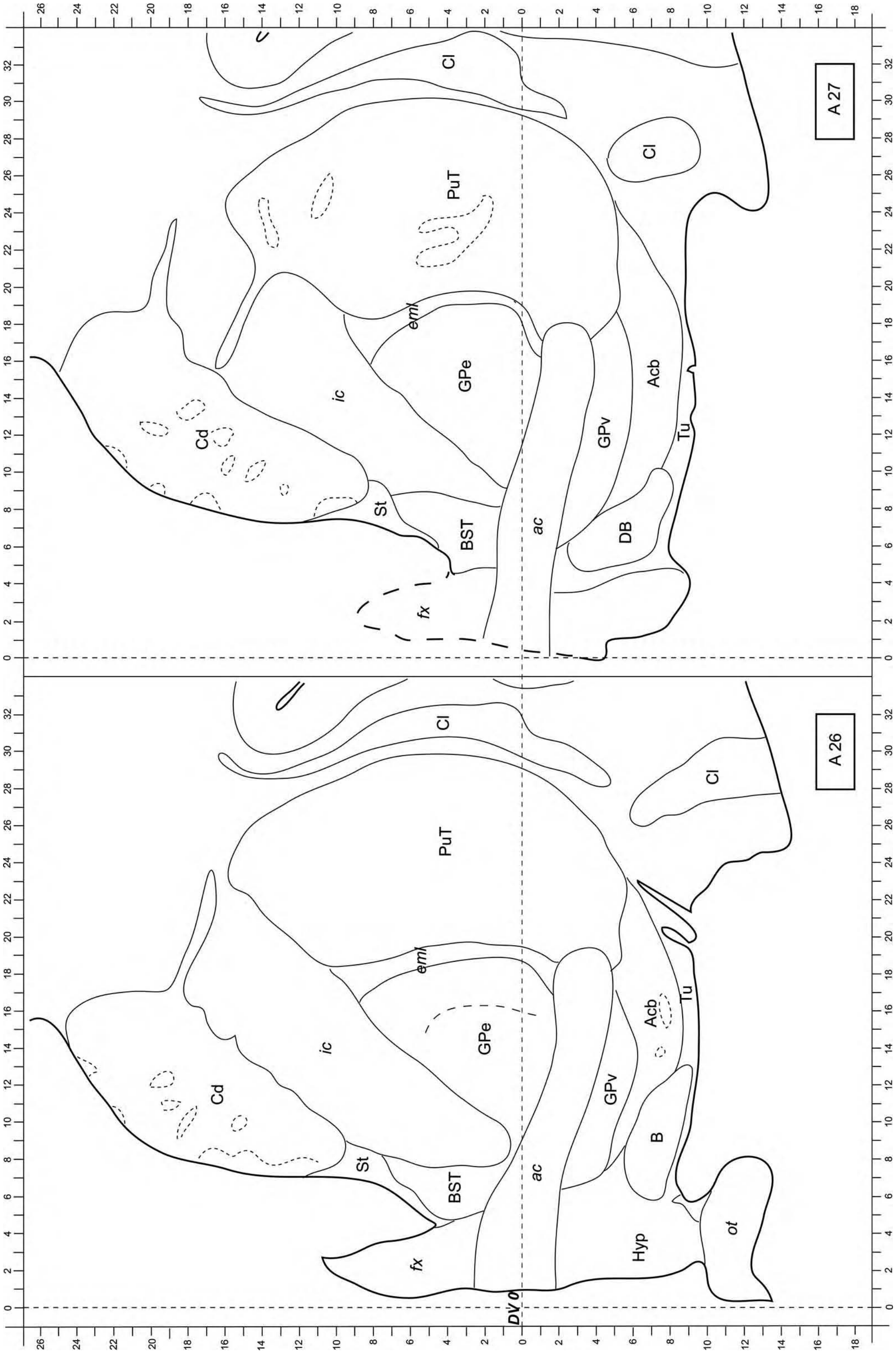
A 27
Cl
PuT
Cl
eml
GPe
ic
Cd
St
BST
ac
GPv
Acb
Tu
DB
fx
A 26
Cl
PuT
Cl
eml
GPe
ic
Cd
St
BST
ac
GPv
Acb
Tu
B
Hyp
ot
fx
DV 0
26
24
22
20
18
16
14
12
10
8
6
4
2
0
2
4
6
8
10
12
14
16
18
32
30
28
26
24
22
20
18
16
14
12
10
8
6
4
2
0

FIGURE 4.16

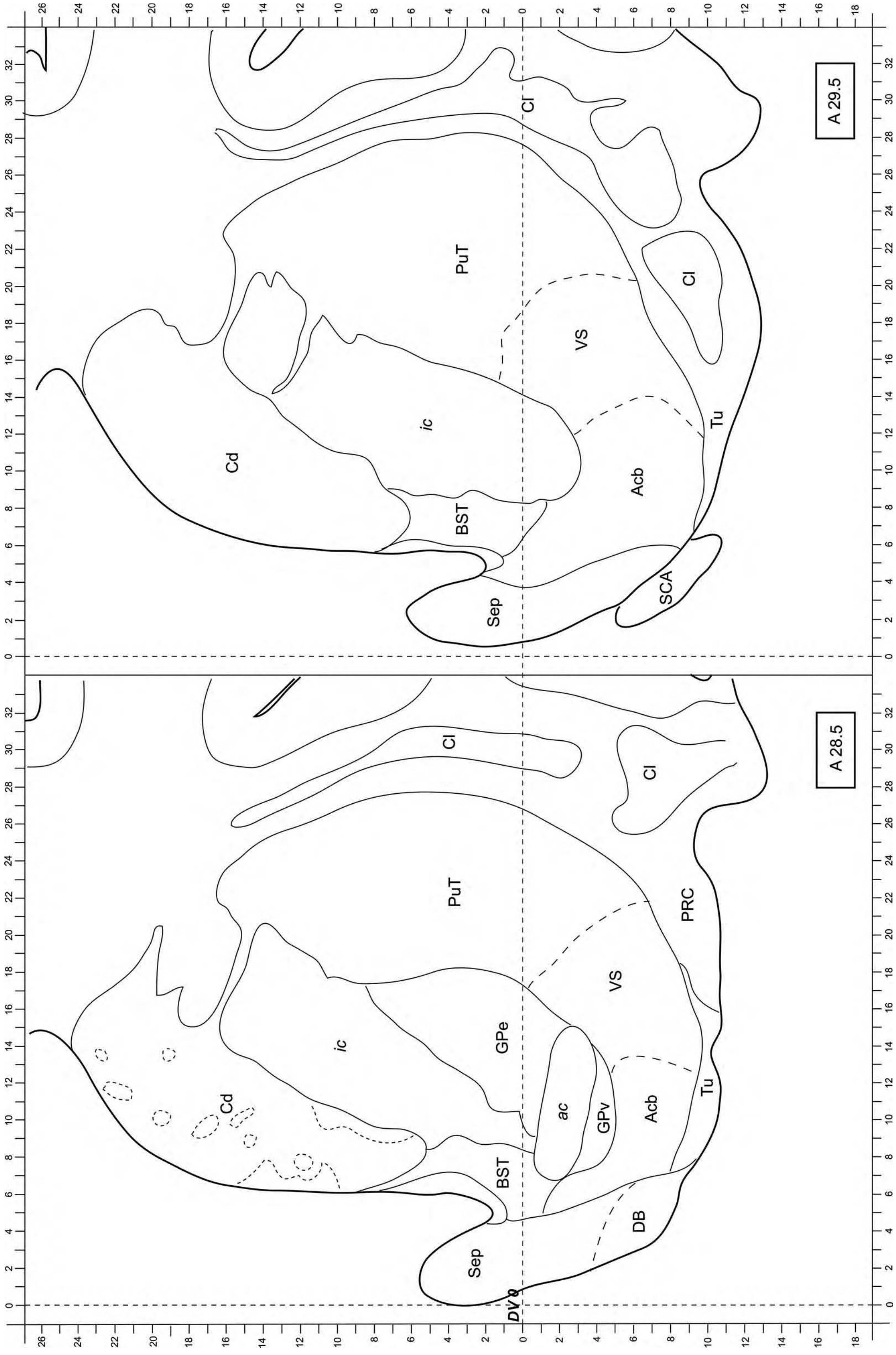
A 29.5
A 28.5
Cd
ic
PuT
Cl
Cl
VS
Tu
Acb
BST
Sep
SCA
Cd
ic
PuT
Cl
Cl
PRC
VS
GPe
ac
GPv
Acb
Tu
BST
DB
Sep
DV 0

FIGURE 4.17

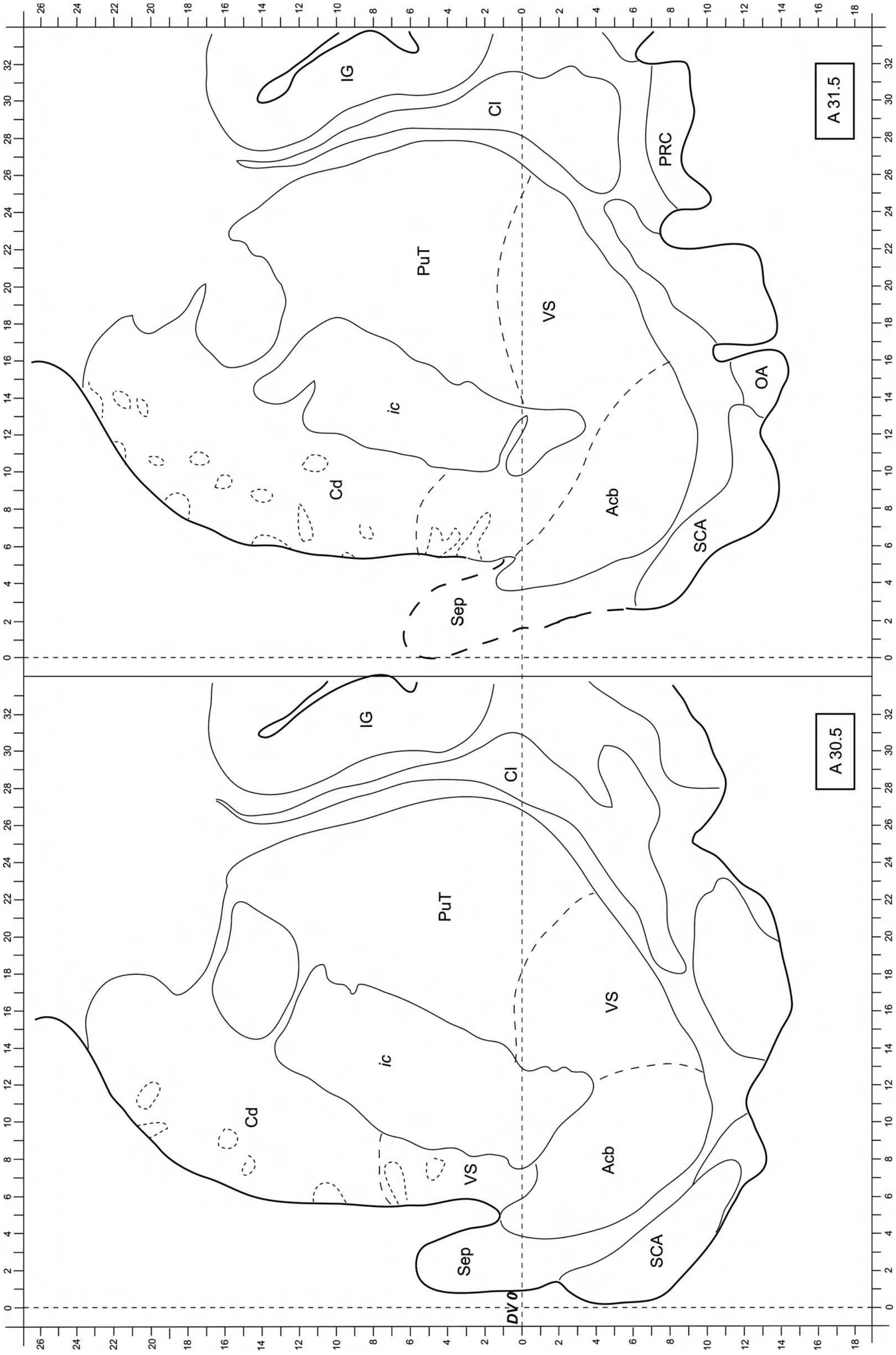
A 31.5
IG
Cl
PuT
VS
ic
Cd
Acb
SCA
Sep
PRC
OA
A 30.5
IG
Cl
PuT
VS
ic
Cd
VS
Acb
SCA
Sep
DV 0
26 24 22 20 18 16 14 12 10 8 6 4 2 0 2 4 6 8 10 12 14 16 18
32 30 28 26 24 22 20 18 16 14 12 10 8 6 4 2 0

FIGURE 4.18

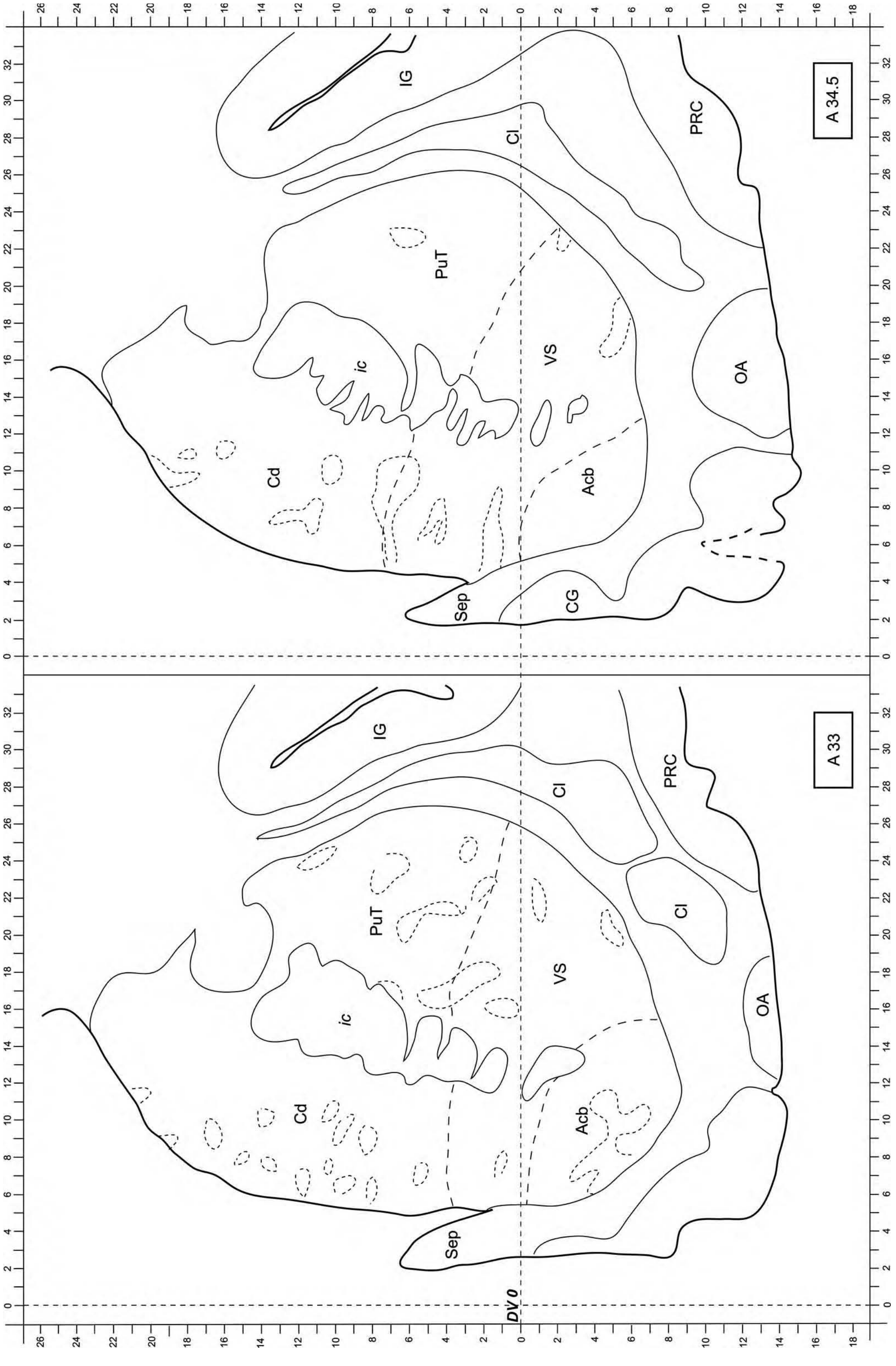
A 34.5
IG
Cl
PRC
PuT
VS
ic
OA
Cd
Acb
Sep
CG
A 33
IG
Cl
PRC
Cl
PuT
VS
ic
OA
Cd
Acb
Sep
DV 0
26 24 22 20 18 16 14 12 10 8 6 4 2 0 2 4 6 8 10 12 14 16 18
0 2 4 6 8 10 12 14 16 18 20 22 24 26 28 30 32

FIGURE 4.19


A 37
IG
CI
PRC
PuT
ic
Cd
GR
CG
A 35.5
IG
CI
PRC
PuT
ic
VS
Cd
Acb
GR
CG
DV 0

FIGURE 4.20

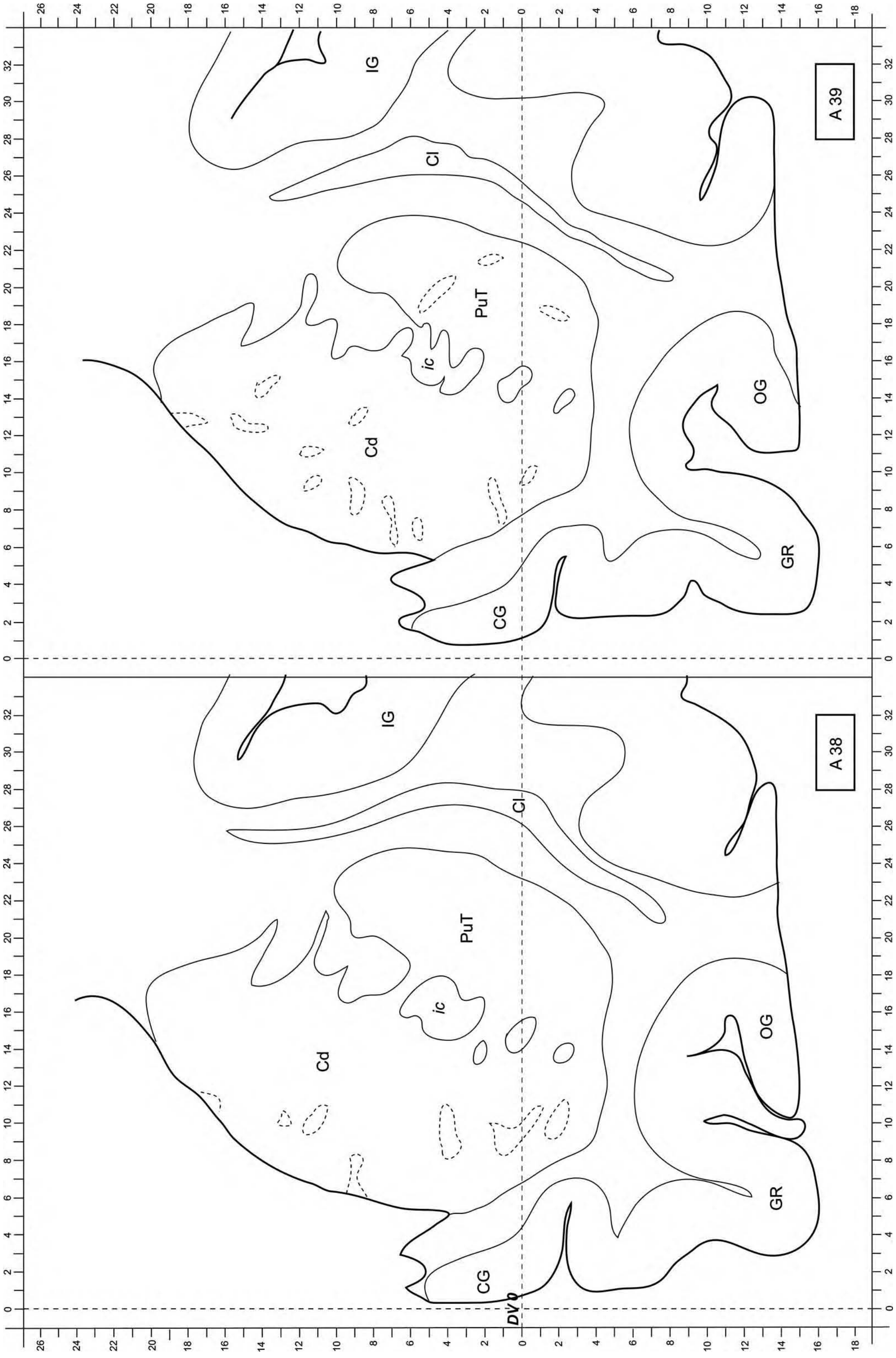

FIGURE 4.21

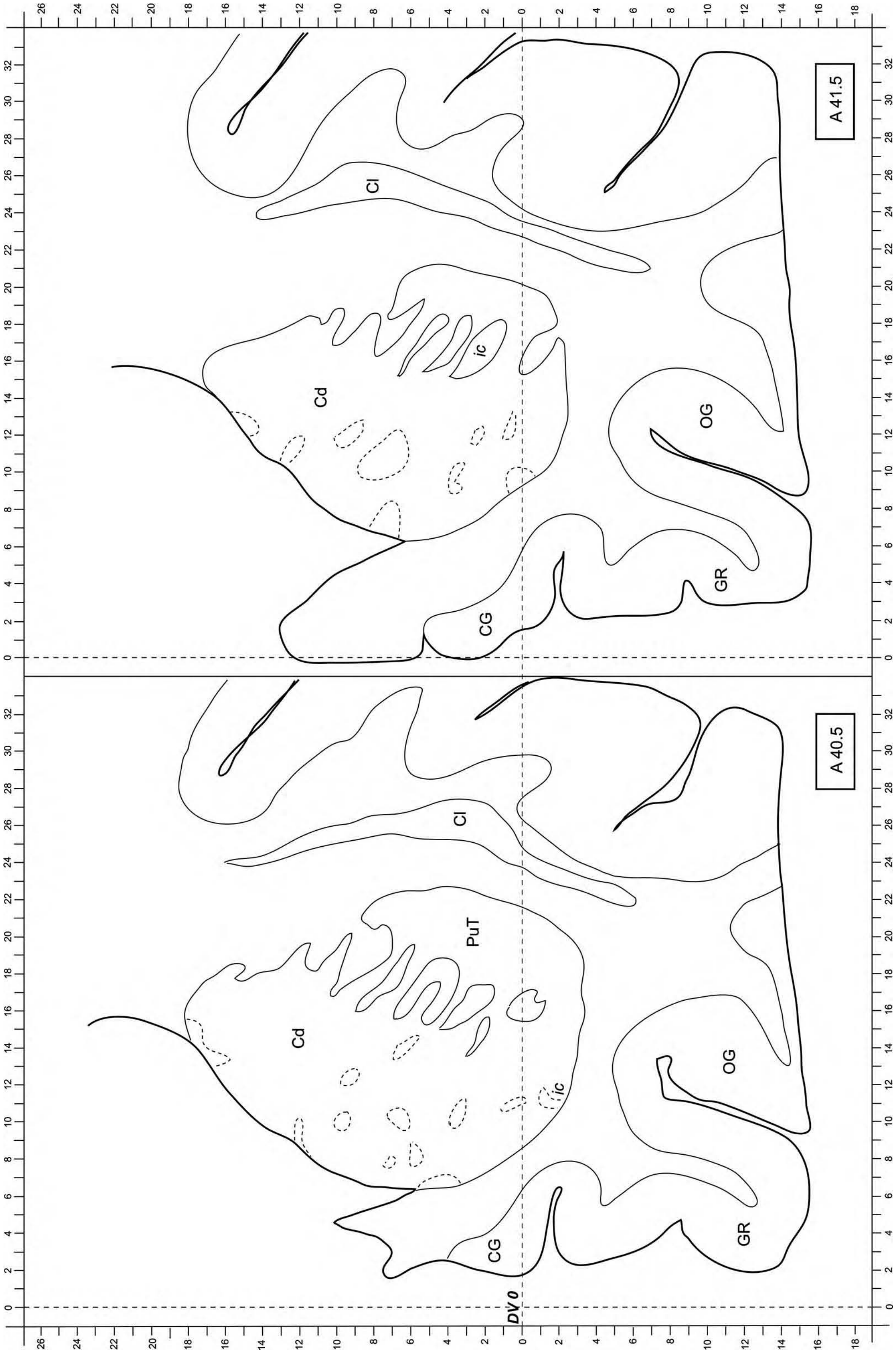
A 41.5
A 40.5
Cd
PuT
Cl
ic
OG
GR
CG
DV 0
26
24
22
20
18
16
14
12
10
8
6
4
2
0
2
4
6
8
10
12
14
16
18
32
30
28
26
24
22
20
18
16
14
12
10
8
6
4
2
0

FIGURE 4.22

FIGURES 4.23 to 4.47 Series of drawings of sagittal sections of the human thalamus and basal ganglia (right hemisphere of case Hb7; Table 2.1) arranged in a medial to lateral sequence. Mediolateral levels (in millimeters) relative to

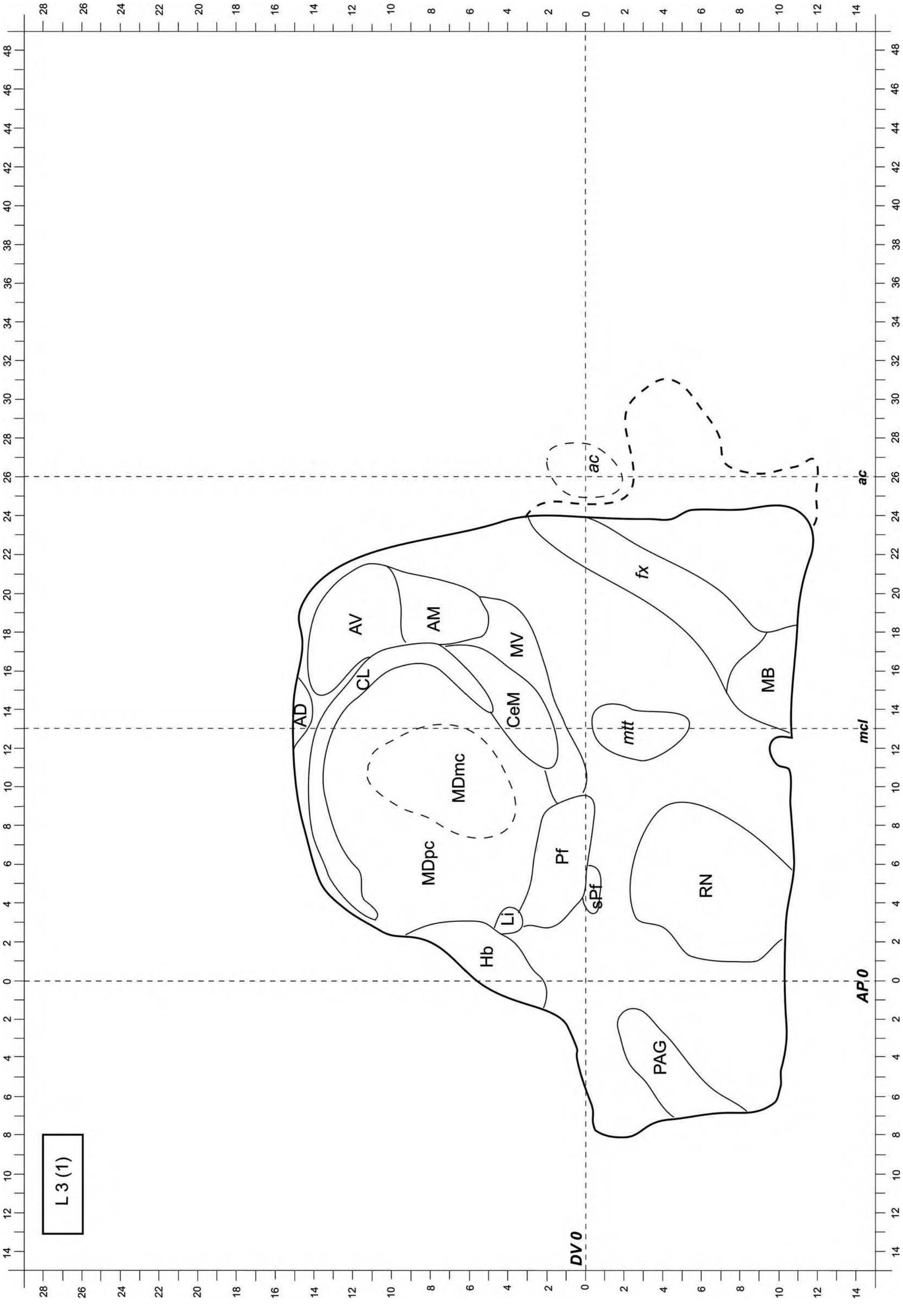

FIGURE 4.23

the interhemispheric plane or estimated thalamoventricular border (in parentheses) are indicated in the upper left of each drawing. Vertical interrupted lines indicate the posterior commissure (*AP 0*), midcommissural (*mcl*), and anterior commissure (*ac*) levels. The same conventions are used as in Figures 4.1 to 4.22.

FIGURE 4.24

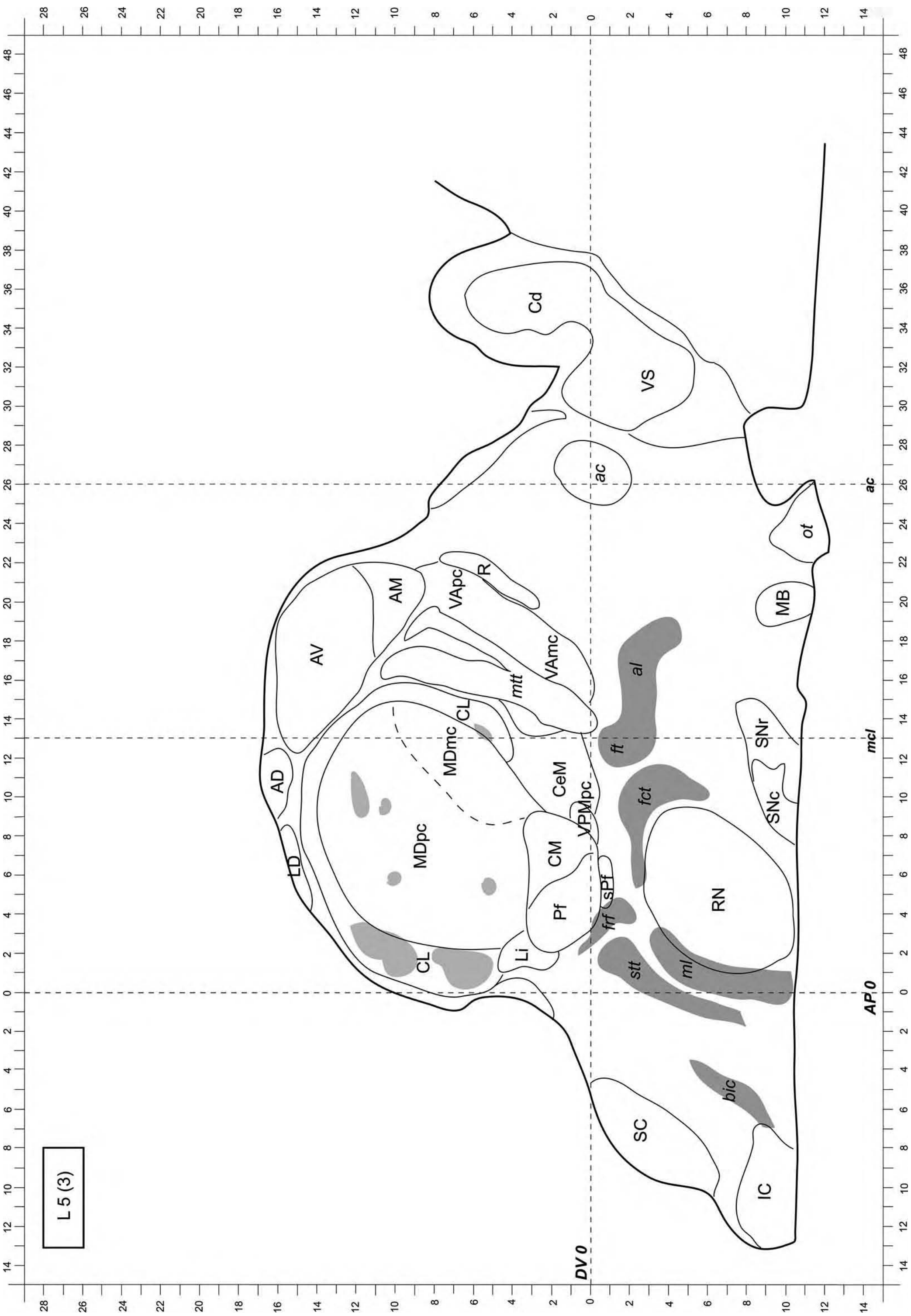
L 5 (3)
Cd
VS
ac
ot
MB
AM
AV
R
VApc
VAmc
mtt
CL
MDmc
CeM
AD
LD
MDpc
CM
VPMpc
sPf
Pf
Li
CL
frf
stt
ml
RN
al
ft
fct
SNr
SNc
SC
bic
IC
DV 0
AP 0
mcl
ac

FIGURE 4.25


L 6 (4)
Cd
Acb
ac
ot
ic
R
VApc
mtt
VLpl
AV
ZI
al
ft
ft
CL
LD
MDpc
VM
CM
VPMpc
fct
STh
SNr
SNc
RN
sPf
Pf
frf
sm
CL
Li
PuM
ml/stt
stt
SC
bic
IC
DV 0
AP 0
mcl
ac
28 26 24 22 20 18 16 14 12 10 8 6 4 2 0 2 4 6 8 10 12 14
48 46 44 42 40 38 36 34 32 30 28 26 24 22 20 18 16 14 12 10 8 6 4 2 0 2 4 6 8 10 12 14

FIGURE 4.26

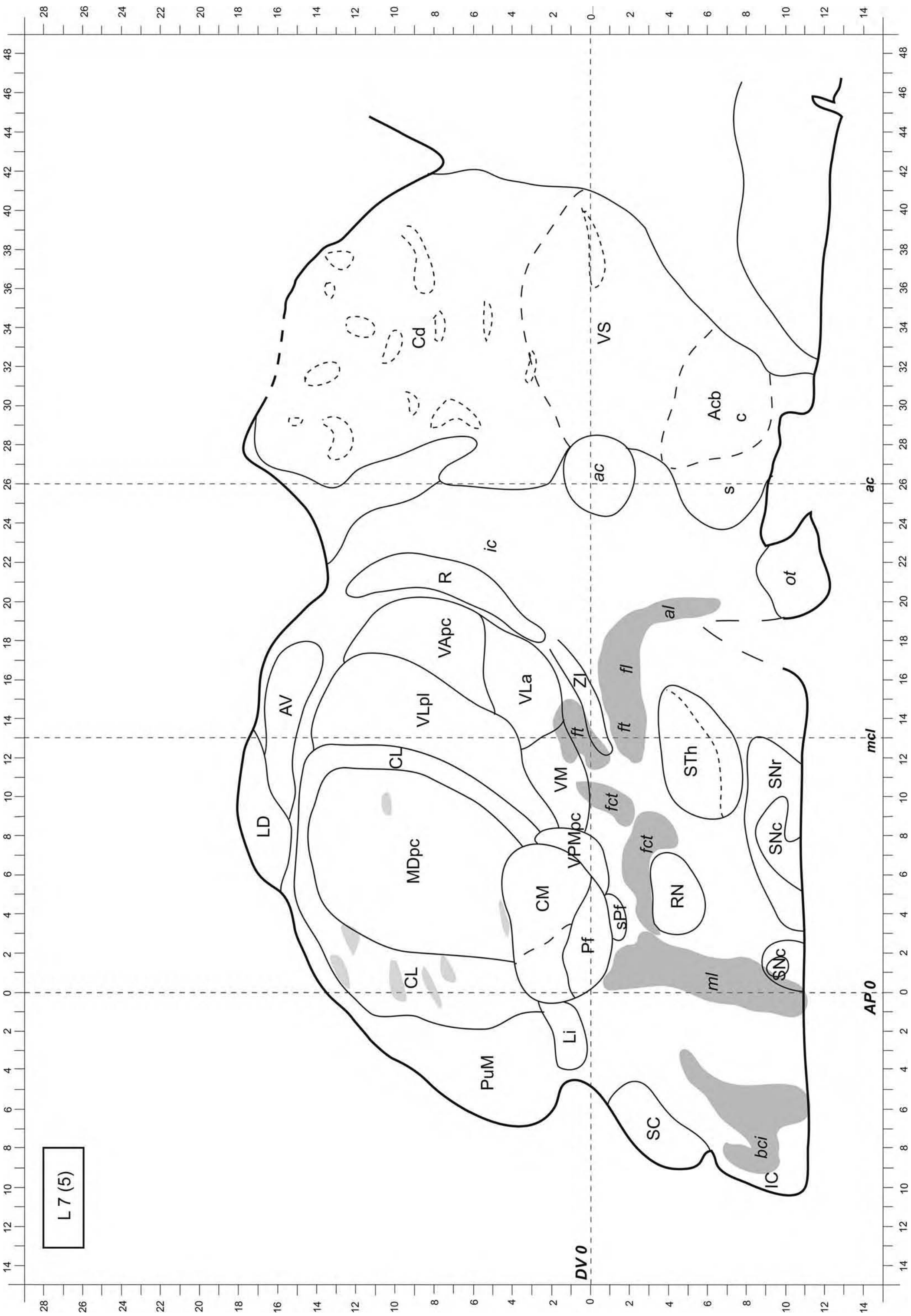
L 7 (5)
Cd
VS
Acb
c
s
ac
ot
ic
R
VApc
VLa
ZI
al
fl
ft
ft
AV
VLpl
CL
LD
MDpc
VM
fct
fct
VPMpc
CM
sPf
Pf
RN
STh
SNr
SNc
SNc
ml
CL
Li
PuM
SC
bci
IC
DV 0
AP 0
mcl
ac

FIGURE 4.27


L 8 (6)
Cd
VS
c
Acb
s
ac
St
ic
R
Hyp
VApc
al
ot
VLa
ZI
fl
VLpd
VM
STh
mcl
CL
VLpv
ft
SNr
LD
MDpl
VPM
fct
VPMpc
RN
SNc
MDpc
CM
sPf
Pf
ml
CL
AP 0
Li
PuM
bic
IC
DV 0
28 26 24 22 20 18 16 14 12 10 8 6 4 2 0 2 4 6 8 10 12 14
48 46 44 42 40 38 36 34 32 30 28 26 24 22 20 18 16 14 12 10 8 6 4 2 0 2 4 6 8 10 12 14

FIGURE 4.28

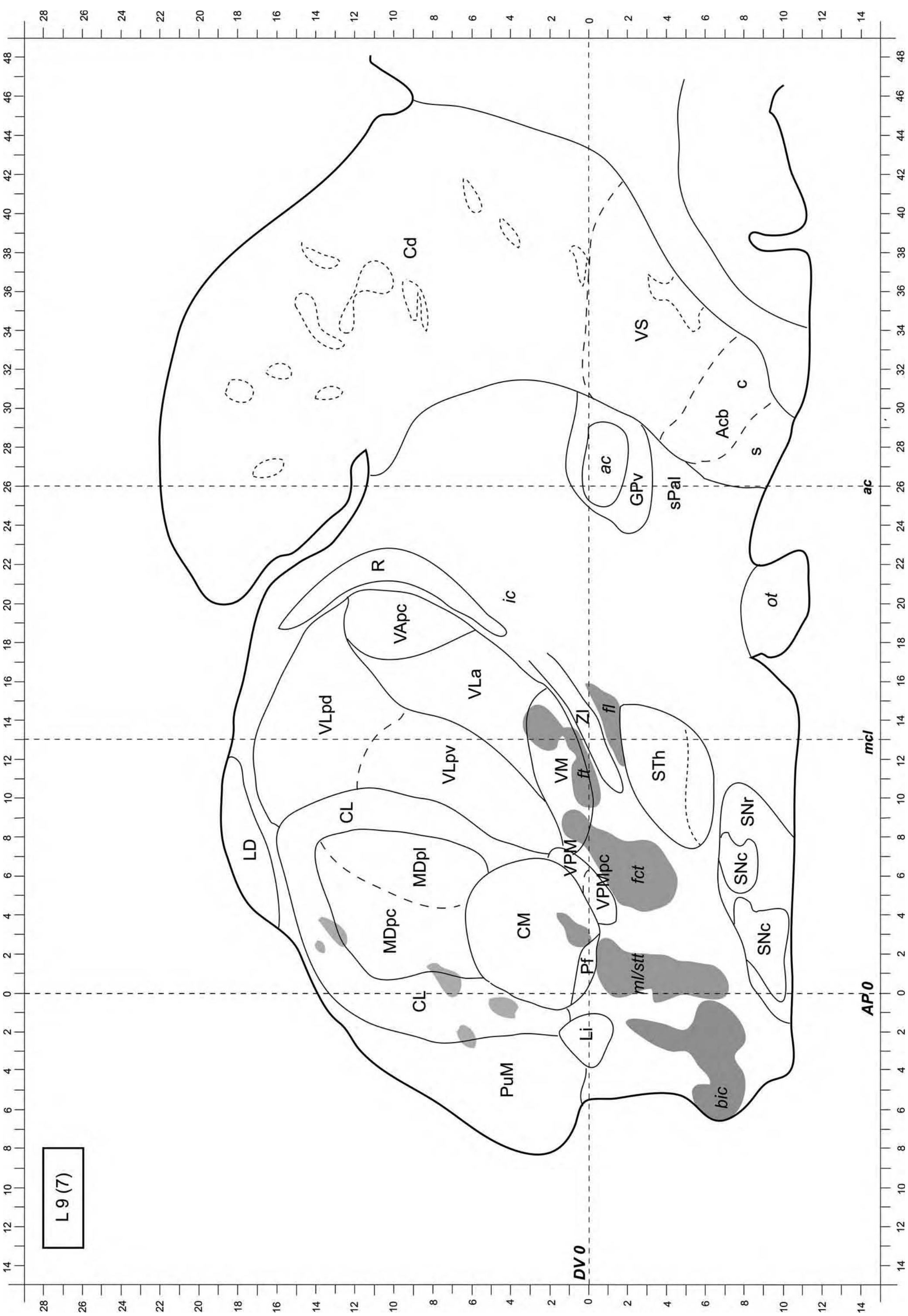
L 9 (7)
Cd
VS
c
Acb
s
ac
GPv
sPal
ot
R
ic
VApc
VLa
VLpd
VLpv
ZI
fl
VM
ft
STh
SNr
CL
LD
MDpl
VPM
fct
VPMpc
SNc
MDpc
CM
SNc
Pf
ml/stt
CL
Li
PuM
bic
DV 0
AP 0
ac
mcl

FIGURE 4.29

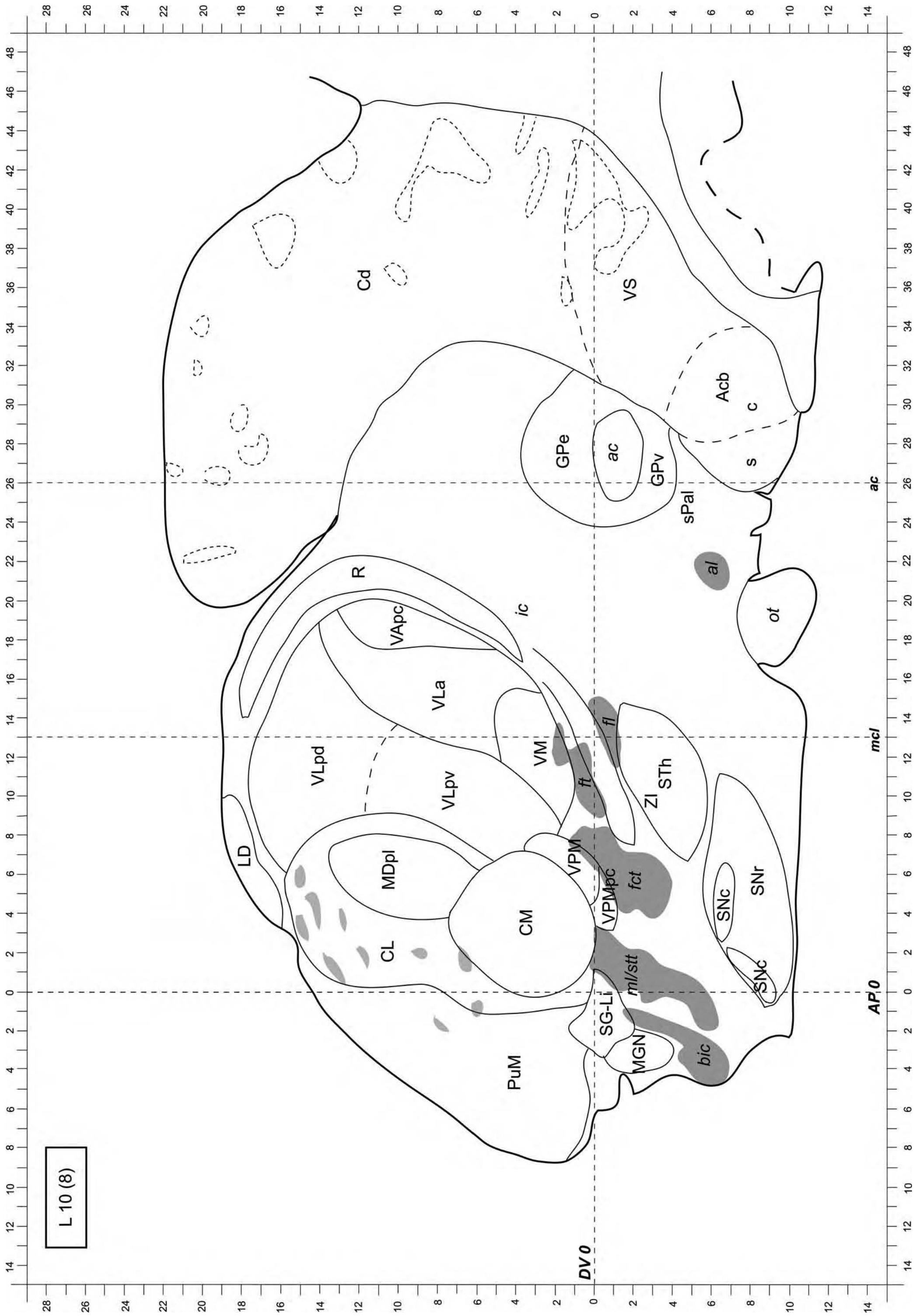
L 10 (8)
Cd
VS
Acb
c
s
GPe
ac
GPv
sPal
al
ot
R
ic
VApc
VLa
VLpd
VLpv
VM
ft
fl
STh
ZI
LD
MDpl
CM
VPM
VPMpc
fct
SNc
SNr
CL
ml/stt
SNc
SG-Li
MGN
bic
PuM
DV 0
AP 0
mcl
ac
28 26 24 22 20 18 16 14 12 10 8 6 4 2 0 2 4 6 8 10 12 14
48 46 44 42 40 38 36 34 32 30 28 26 24 22 20 18 16 14 12 10 8 6 4 2 0 2 4 6 8 10 12 14

FIGURE 4.30

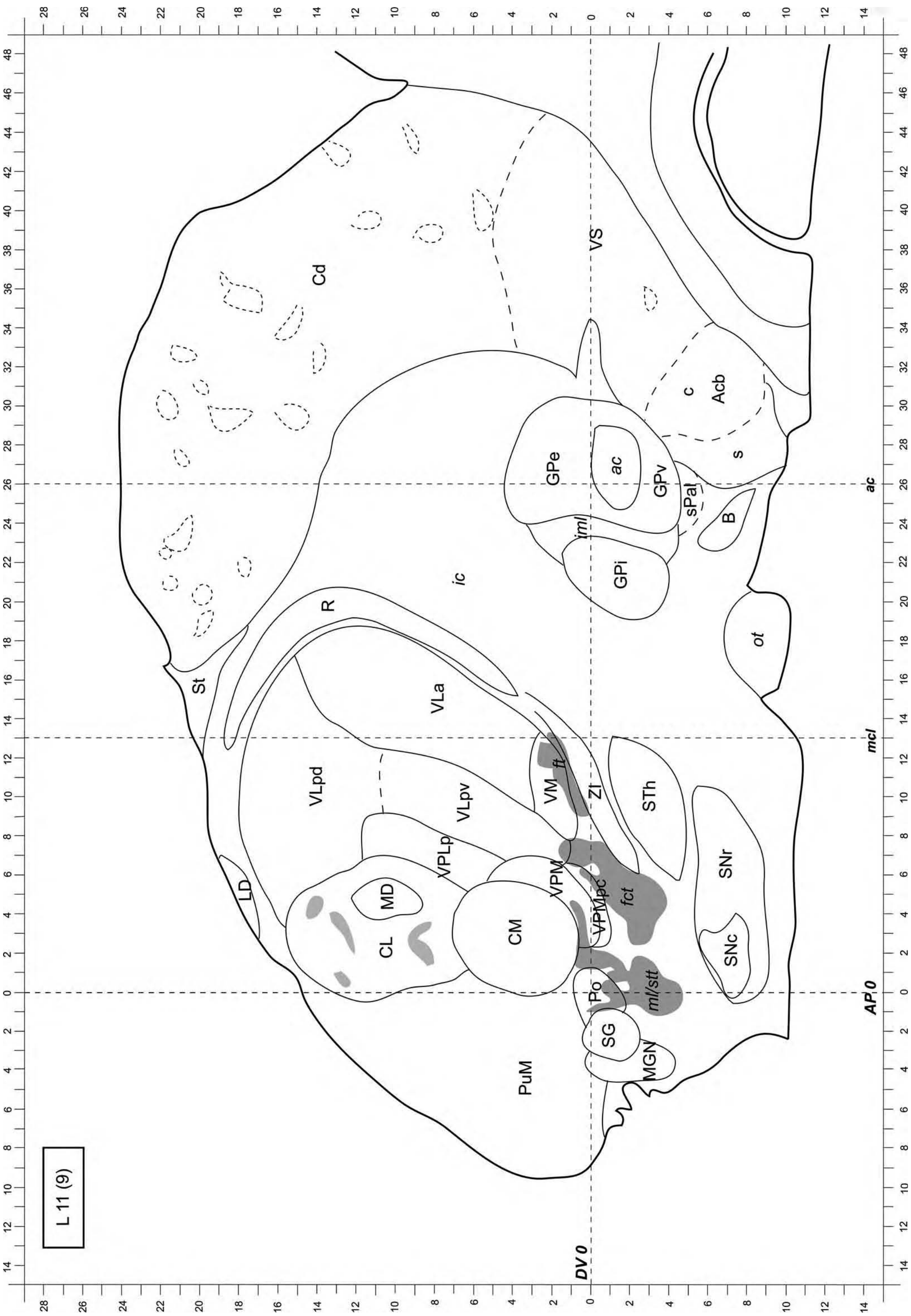
L 11 (9)
Cd
VS
c
Acb
s
GPe
ac
GPv
sPal
B
iml
GPi
ic
R
ot
St
VLa
VLpd
VLpv
VM
ft
ZI
STh
SNr
SNc
LD
MD
CL
VPLp
VPM
CM
VPMpc
fct
Po
ml/stt
SG
MGN
PuM
DV 0
AP 0
ac
mcl

FIGURE 4.31

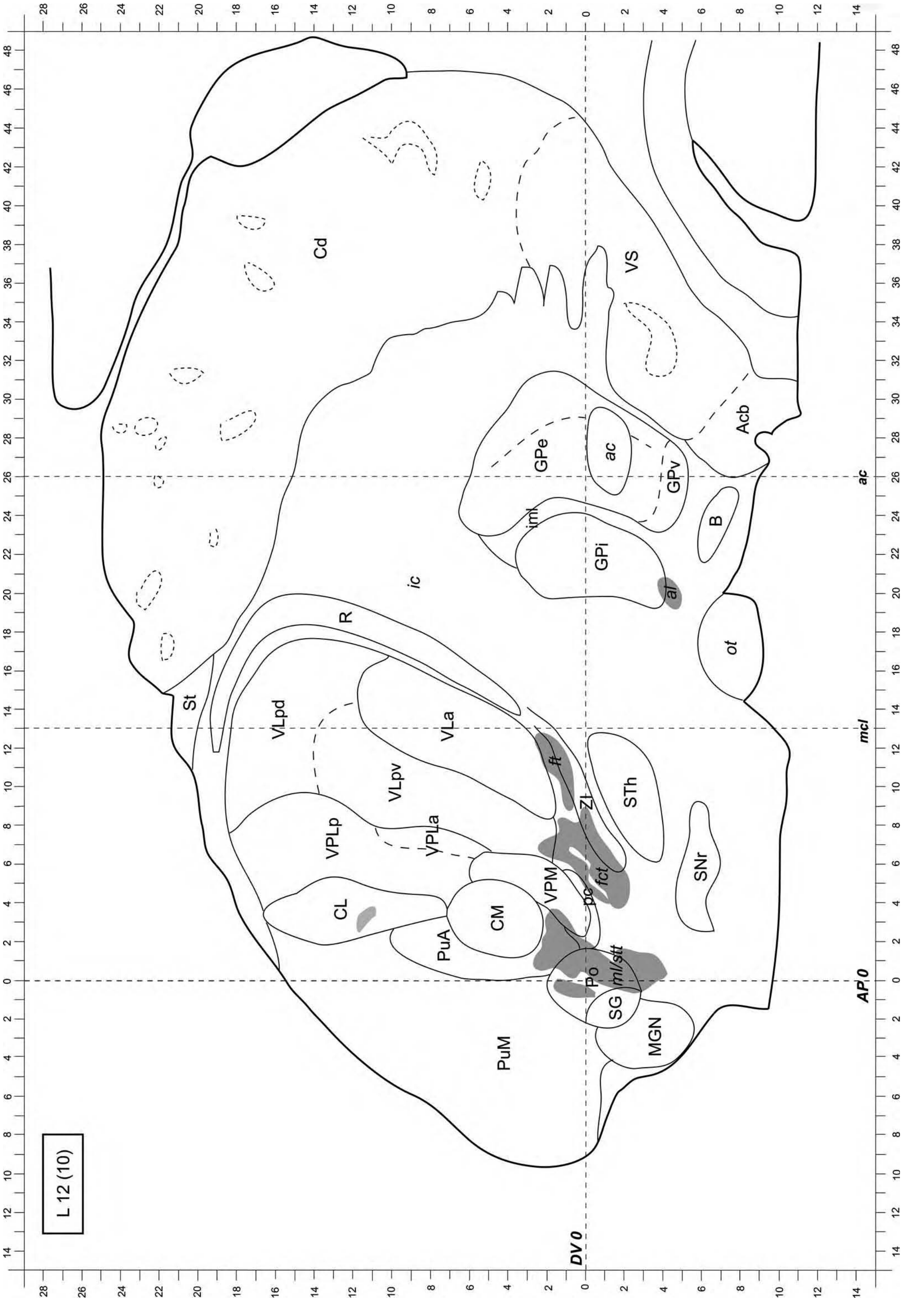
L 12 (10)
Cd
VS
Acb
GPe
ac
GPv
iml
GPi
B
al
ot
ic
R
St
VLpd
VLa
VLpv
VPLp
VPLa
ft
ZI
STh
SNr
fct
pc
VPM
CM
CL
PuA
ml/stt
Po
SG
MGN
PuM
DV 0
AP 0
mcl
ac

FIGURE 4.32

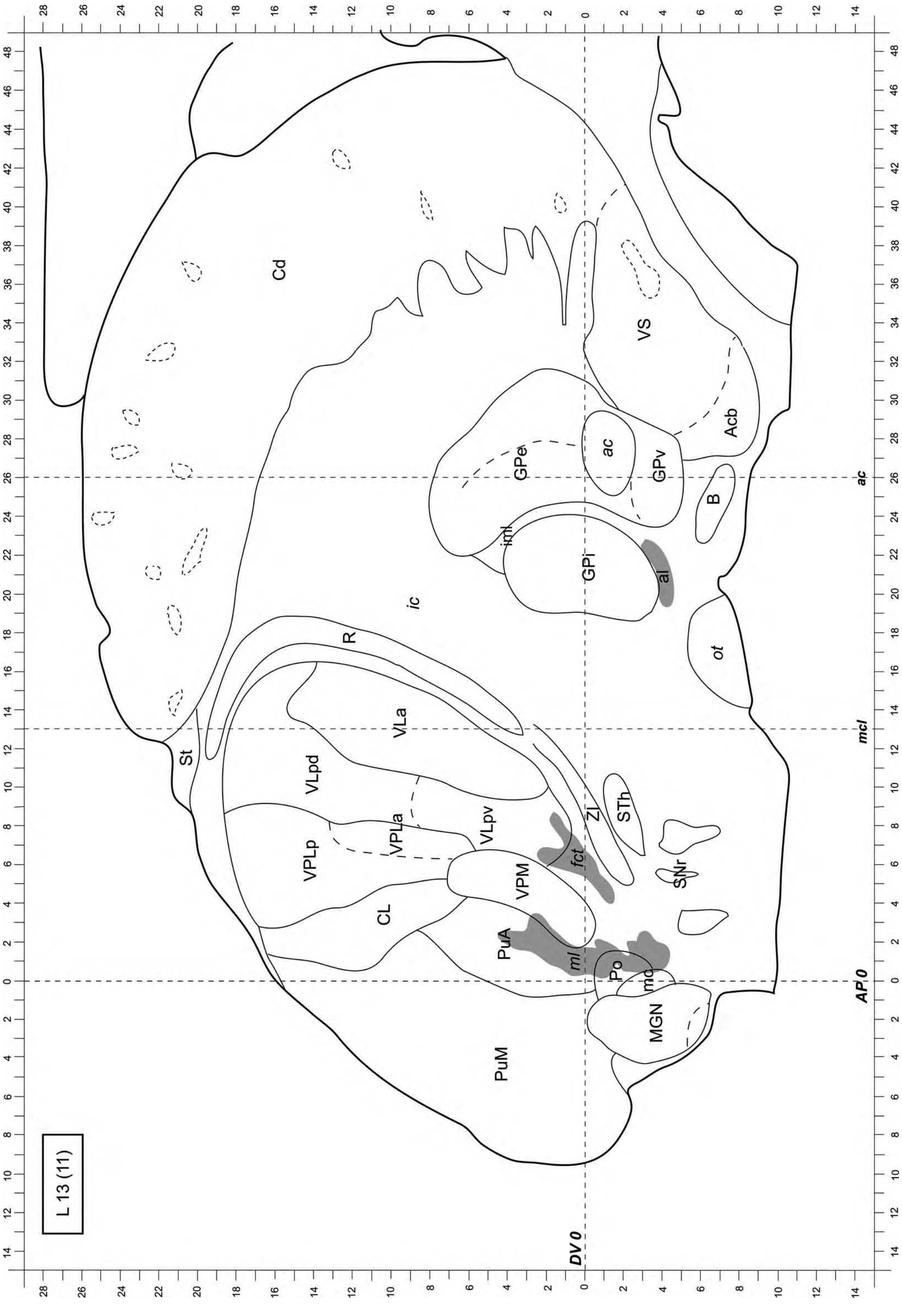
L 13 (11)
Cd
VS
Acb
ac
GPe
GPv
B
iml
GPi
al
ic
ot
R
VLa
St
VLpd
VLpv
VPLa
VPLp
ZI
STh
fct
SNr
VPM
CL
PuA
ml
Po
mc
MGN
PuM
DV 0
AP 0
mcl
ac

FIGURE 4.33

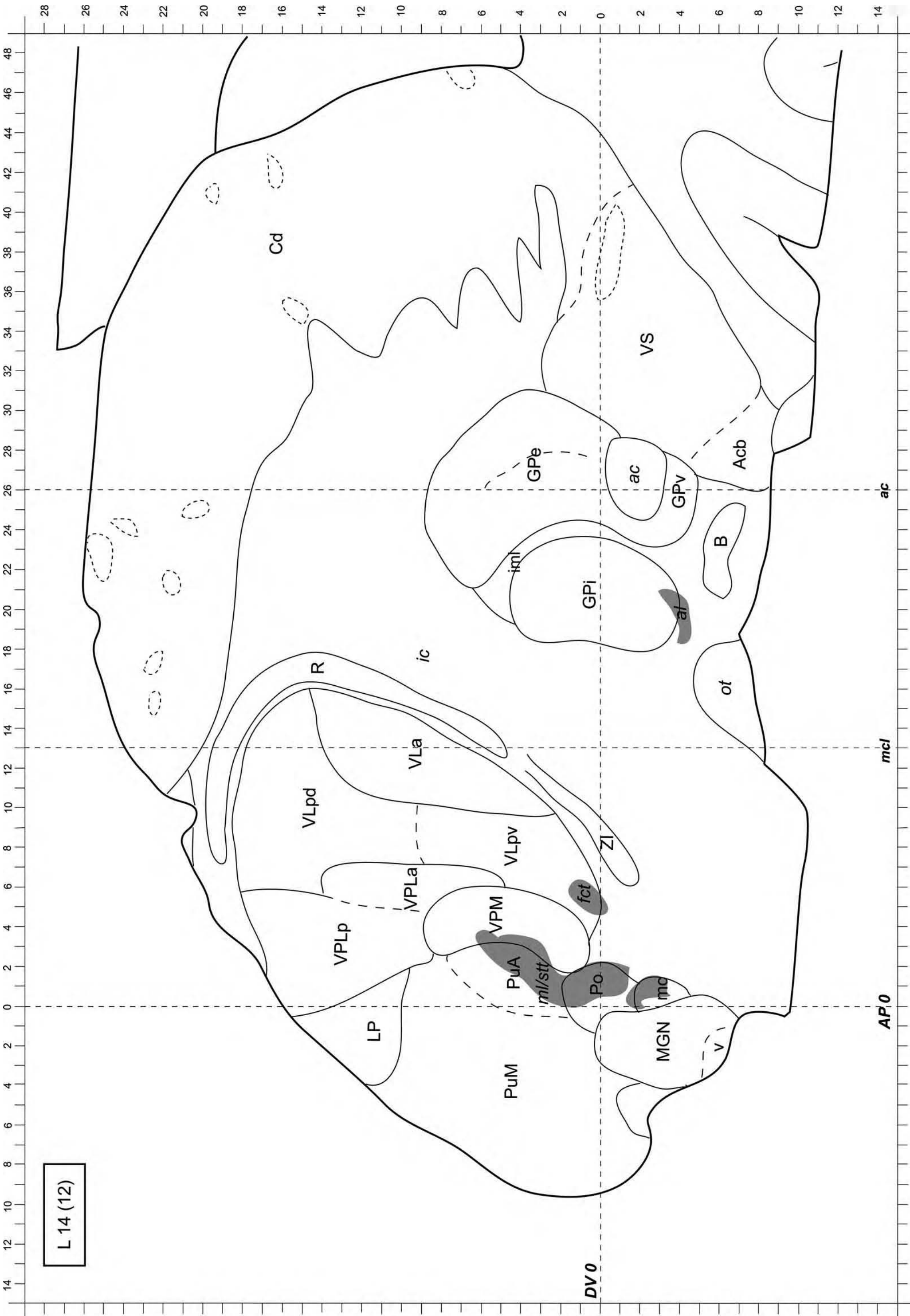
L 14 (12)
Cd
VS
GPe
ac
GPv
Acb
B
iml
GPi
al
ot
ic
R
VLa
VLpd
VLpv
ZI
fct
VPLa
VPM
VPLp
PuA
ml/stt
Po
mc
LP
MGN
v
PuM
DV 0
AP 0
mcl
ac

FIGURE 4.34

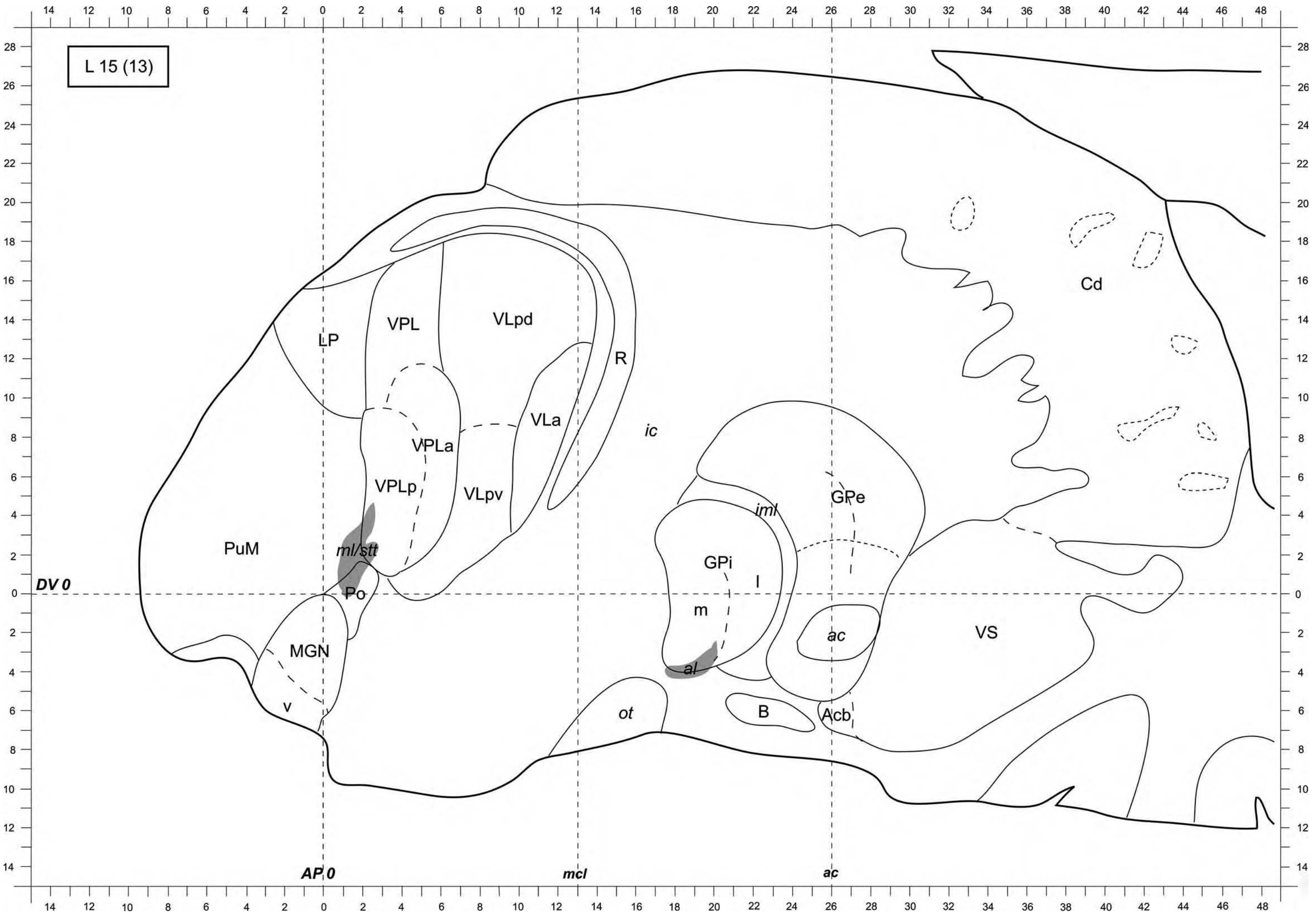
L 15 (13)
Cd
VS
GPe
GPi
iml
l
m
al
ac
Acb
B
ot
ic
R
VLa
VLpd
VLpv
VPL
VPLa
VPLp
LP
ml/stt
Po
MGN
v
PuM
DV 0
AP 0
mcl
ac

FIGURE 4.35

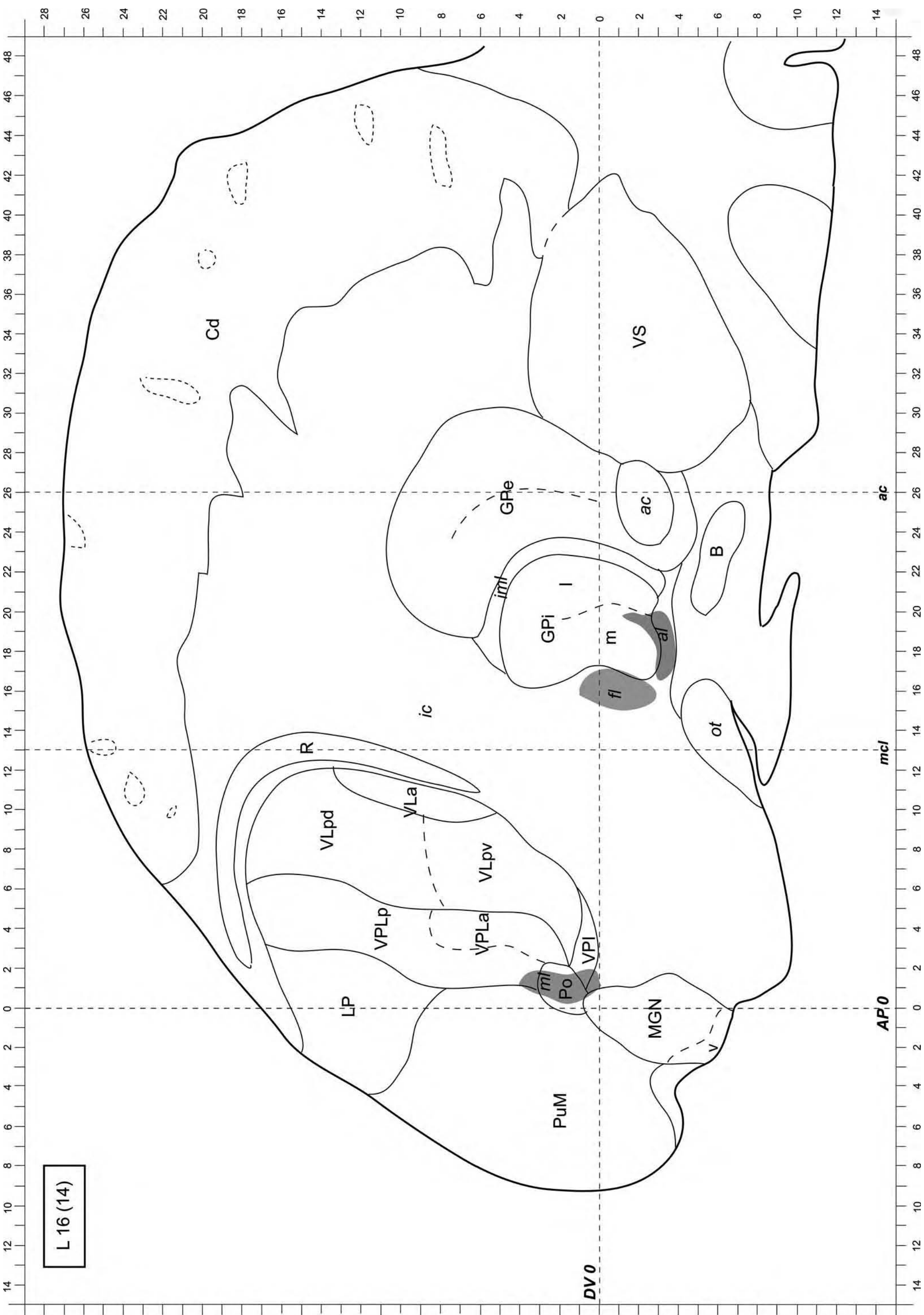
L 16 (14)
Cd
VS
GPe
ac
B
iml
I
GPi
m
al
fl
ic
ot
R
VLpd
VLa
VLpv
VPLp
VPLa
VPI
ml
Po
LP
MGN
PuM
ac
mcl
AP 0
DV 0

FIGURE 4.36

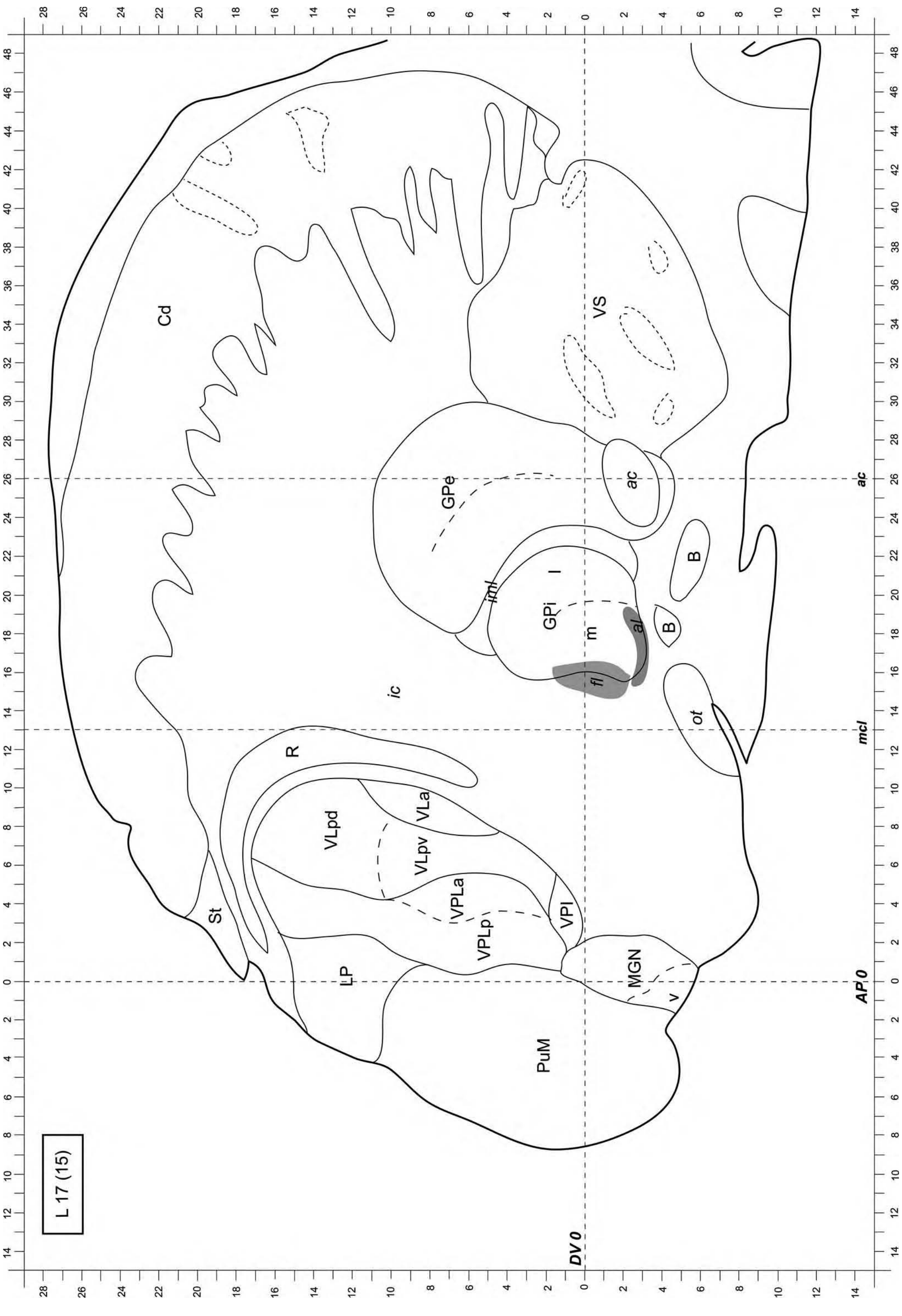
L 17 (15)
Cd
VS
GPe
ac
B
I
iml
GPi
m
al
B
fl
ic
ot
R
VLpd
VLa
VLpv
VPLa
VPLp
VPI
St
LP
MGN
v
PuM
DV 0
AP 0
mcl
ac

FIGURE 4.37

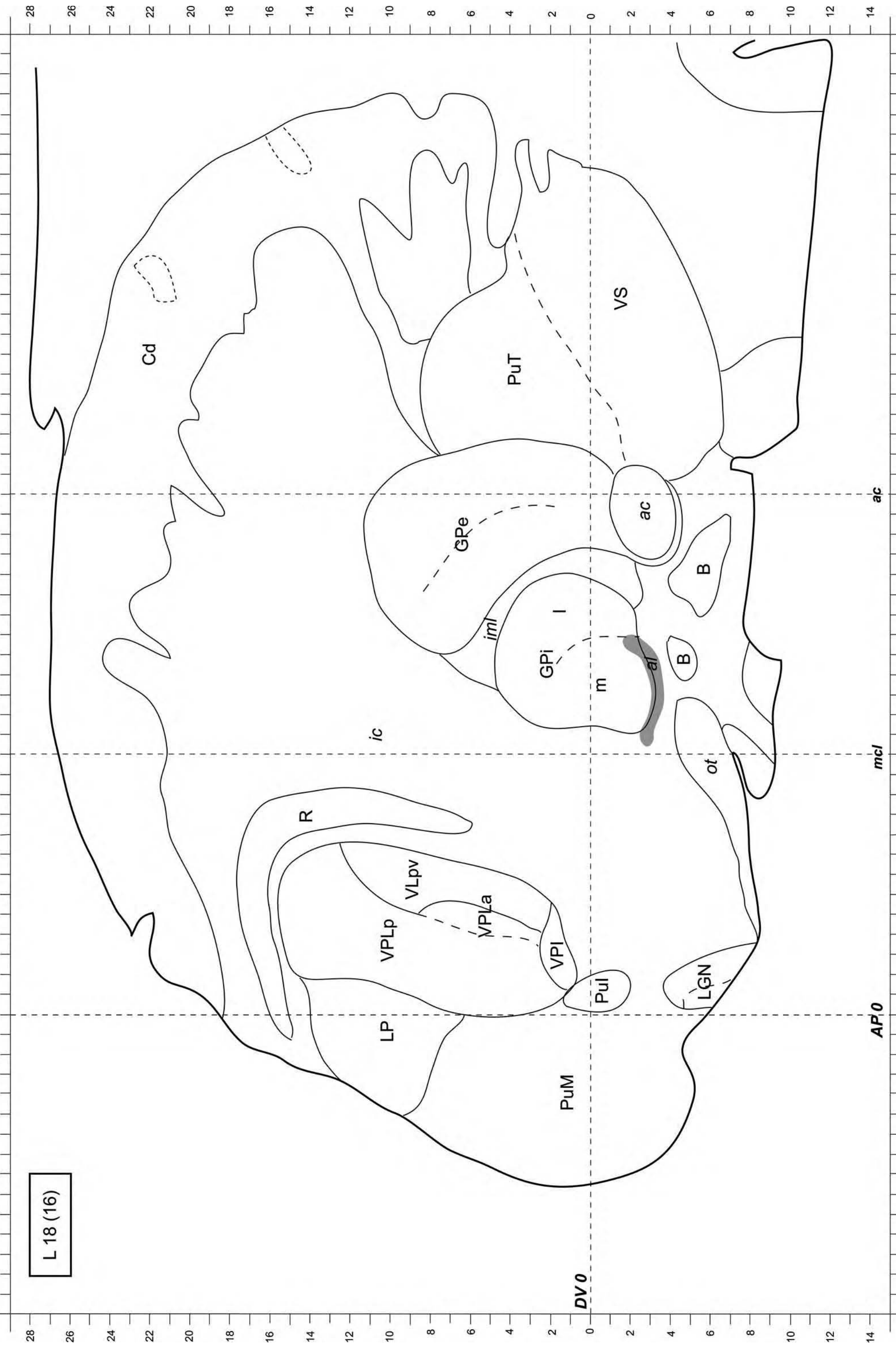
L 18 (16)
Cd
VS
PuT
GPe
ac
B
iml
I
GPi
m
al
B
ic
ot
R
VLpv
VPLa
VPLp
VPl
Pul
LGN
LP
PuM
ac
mcl
AP 0
DV 0

FIGURE 4.38

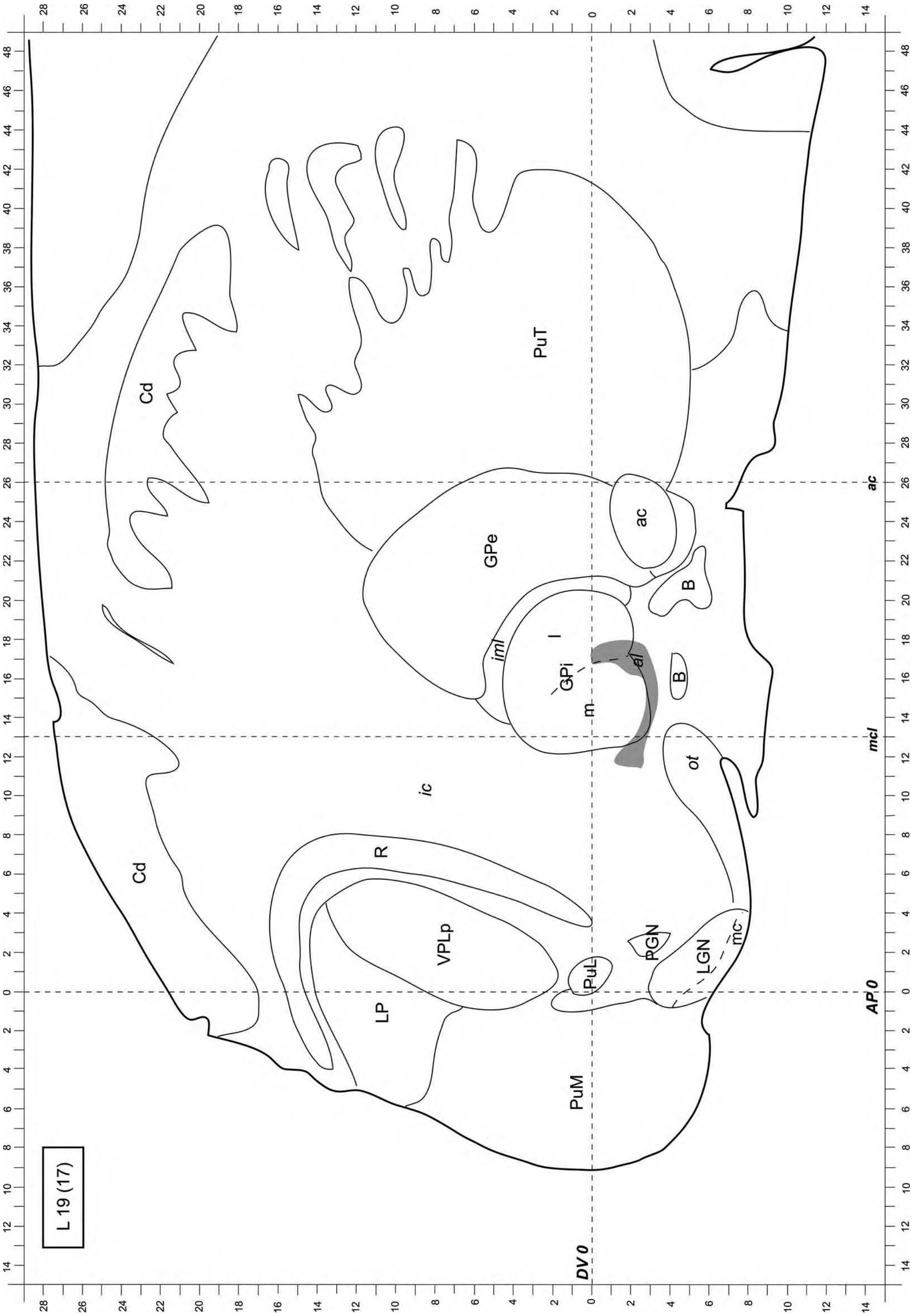
L 19 (17)
Cd
Cd
PuT
GPe
ac
B
B
I
iml
GPi
al
m
ot
ic
R
VPLp
LP
PuM
PuL
PGN
LGN
mc
ac
mcl
AP 0
DV 0
28 26 24 22 20 18 16 14 12 10 8 6 4 2 0 2 4 6 8 10 12 14
48 46 44 42 40 38 36 34 32 30 28 26 24 22 20 18 16 14 12 10 8 6 4 2 0 2 4 6 8 10 12 14

FIGURE 4.39


L 20 (18)
Cd
Cd
ic
PuT
eml
GPe
iml
GPi
al
ac
B
ot
R
LP
VPLp
PGN
LGN
mc
PuL
PuM
DV 0
AP 0
mcl
ac
28 26 24 22 20 18 16 14 12 10 8 6 4 2 0 2 4 6 8 10 12 14
48 46 44 42 40 38 36 34 32 30 28 26 24 22 20 18 16 14 12 10 8 6 4 2 0 2 4 6 8 10 12 14

FIGURE 4.40

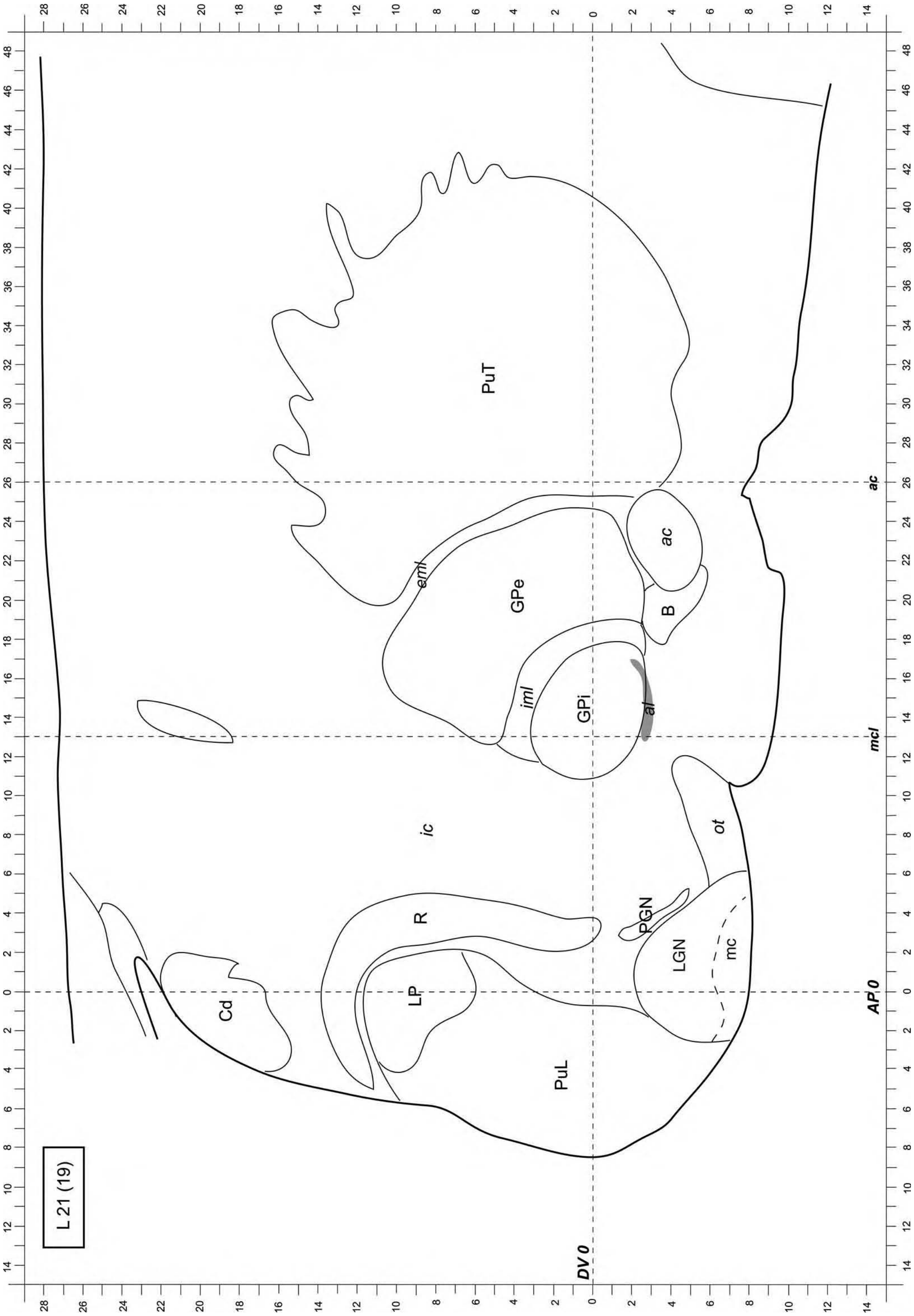
L 21 (19)
PuT
GPe
GPi
eml
iml
al
ac
B
ic
R
LP
PuL
Cd
PGN
LGN
mc
ot
DV 0
AP 0
mcl
ac
28
26
24
22
20
18
16
14
12
10
8
6
4
2
0
2
4
6
8
10
12
14
48
46
44
42
40
38
36
34
32
30
28
26
24
22
20
18
16
14
12
10
8
6
4
2
0
2
4
6
8
10
12
14

FIGURE 4.41

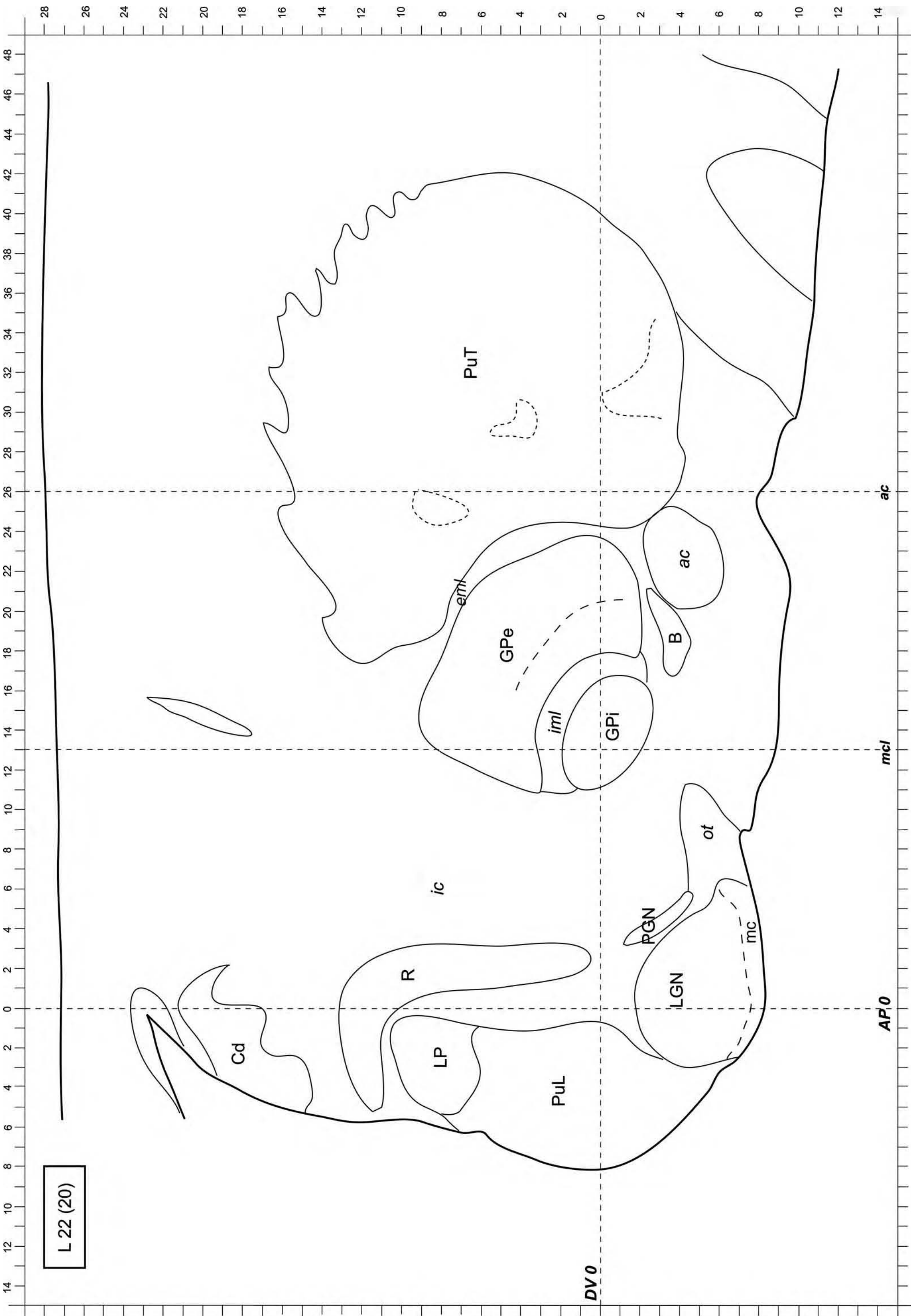
L 22 (20)
PuT
GPe
GPi
eml
iml
ac
B
ot
ic
PGN
LGN
mc
R
LP
PuL
Cd
DV 0
AP 0
mcl
ac

FIGURE 4.42

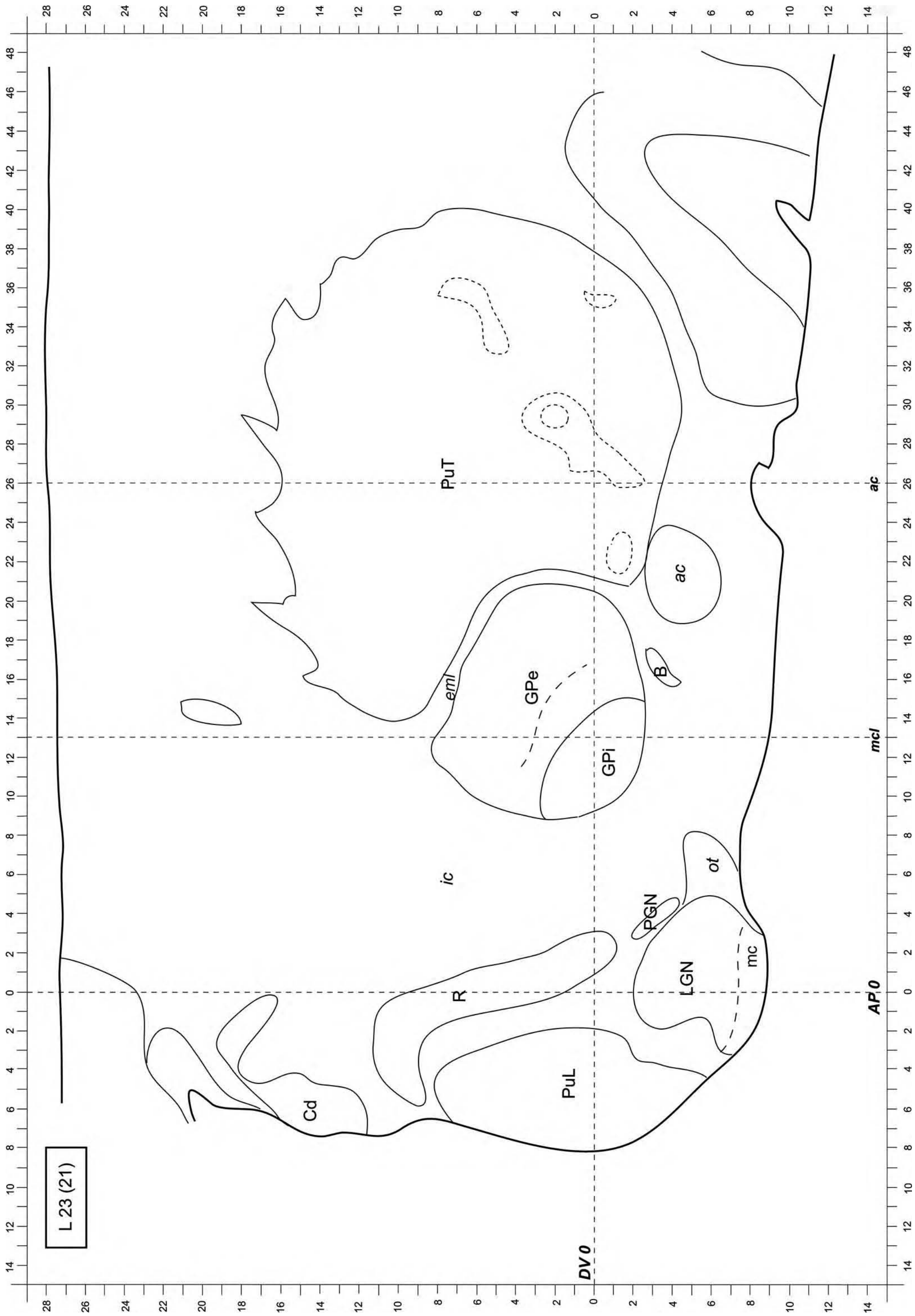
L 23 (21)
PuT
ac
GPe
GPi
eml
B
ic
ot
PGN
LGN
mc
R
PuL
Cd
DV 0
AP 0
mcl
ac
28
26
24
22
20
18
16
14
12
10
8
6
4
2
0
2
4
6
8
10
12
14
48
46
44
42
40
38
36
34
32
30
28
26
24
22
20
18
16
14
12
10
8
6
4
2
0
2
4
6
8
10
12
14

FIGURE 4.43

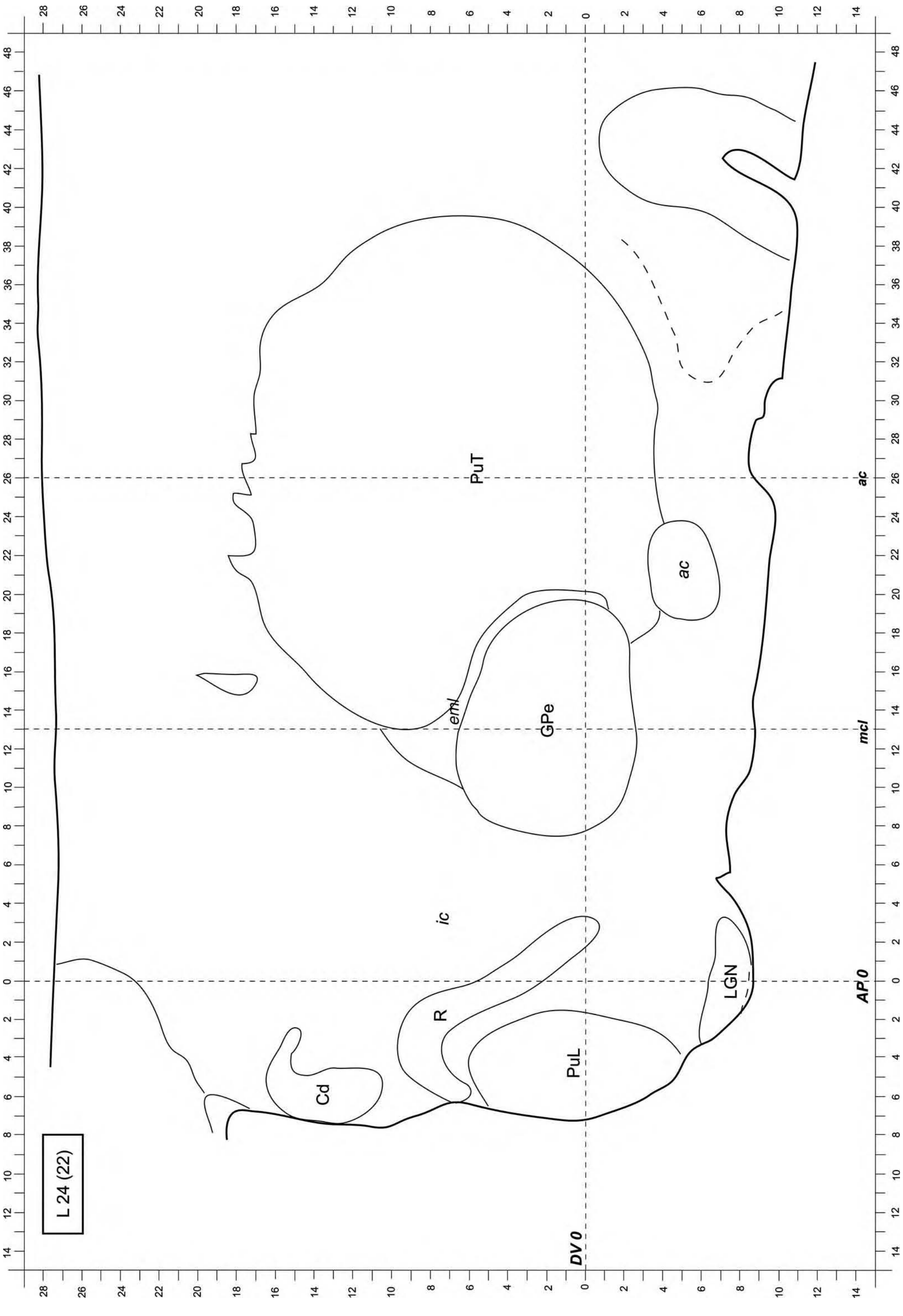

FIGURE 4.44

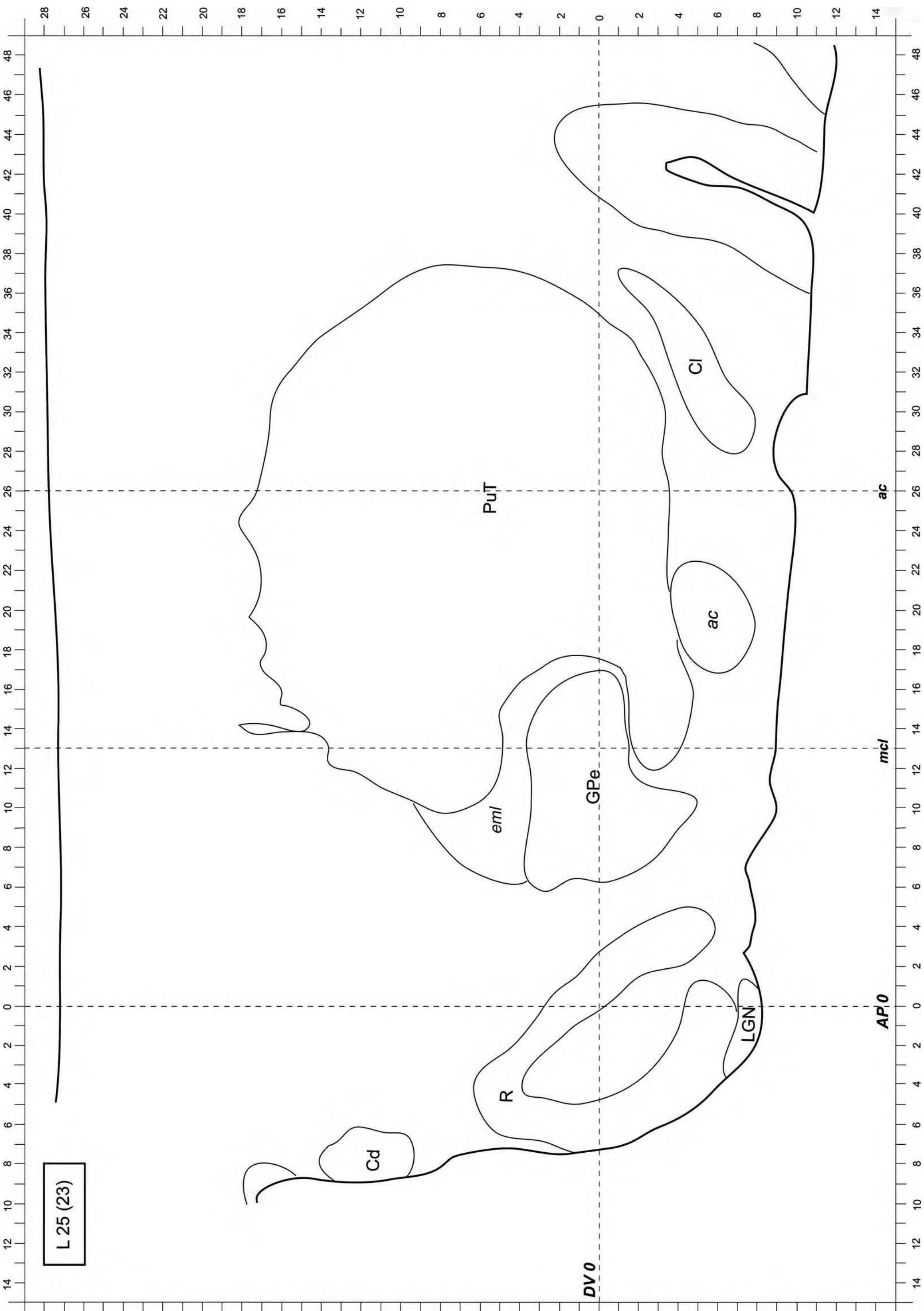

FIGURE 4.45

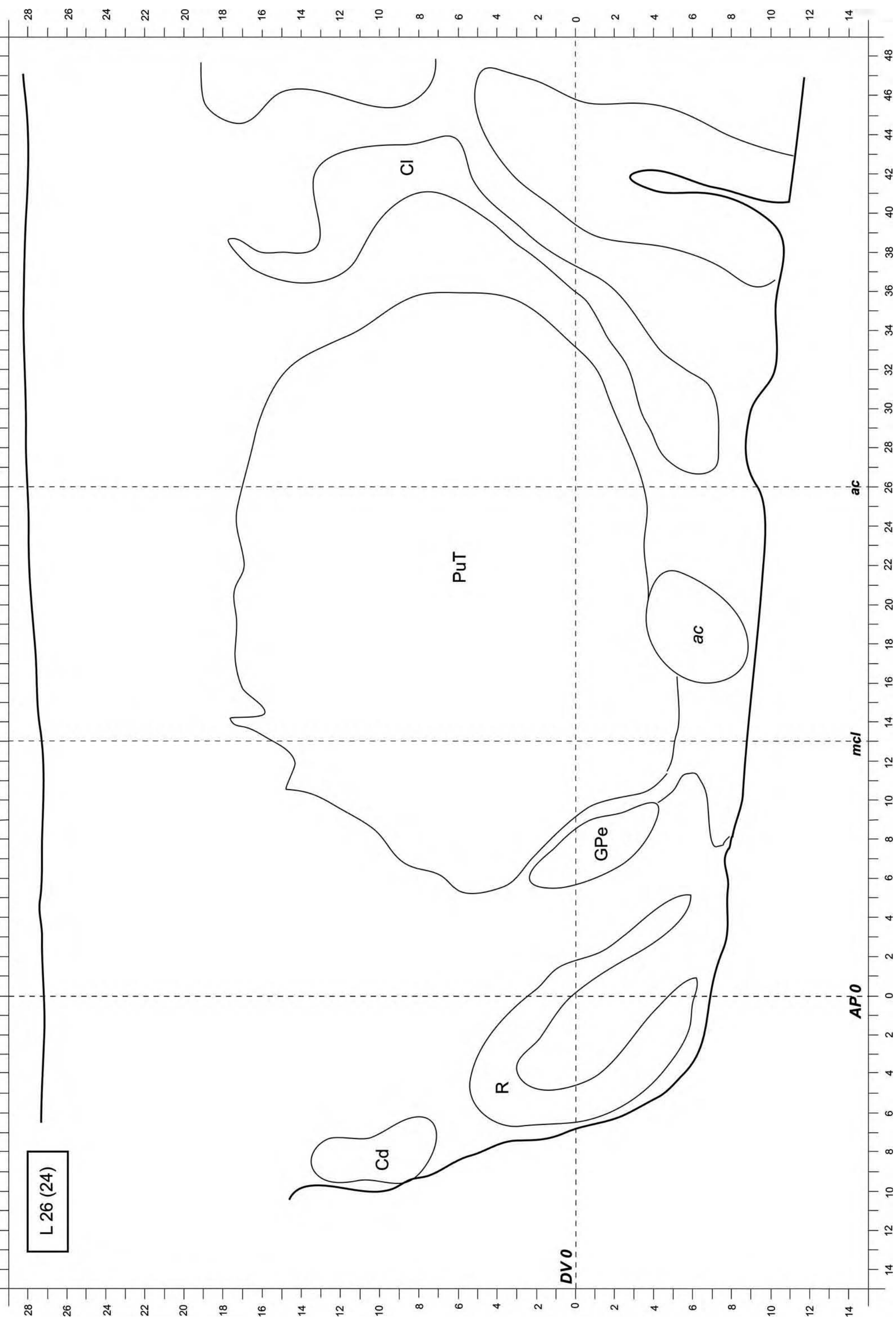

FIGURE 4.46

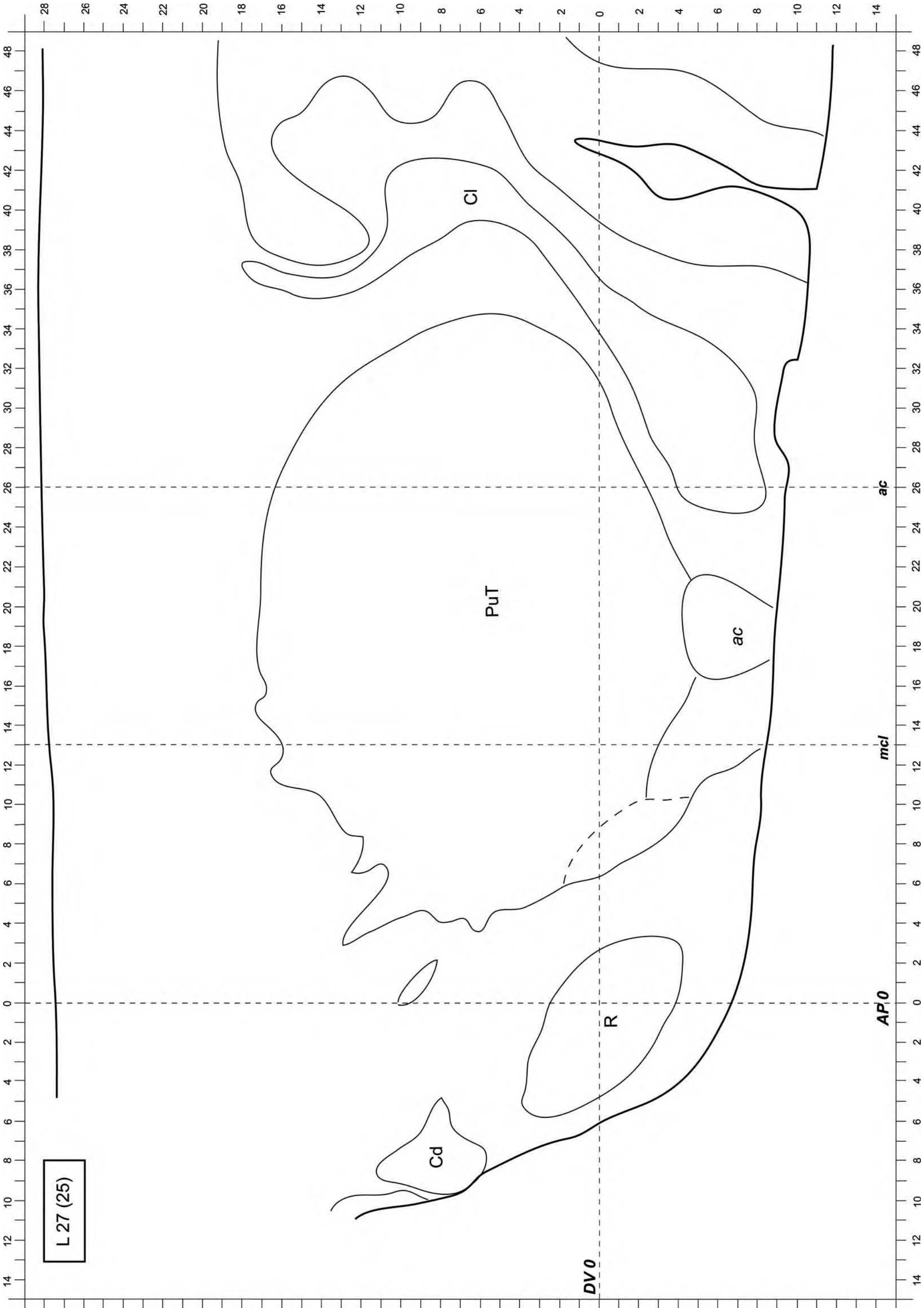
L 27 (25)
Cl
PuT
ac
R
Cd
ac
mcl
AP 0
DV 0
28 26 24 22 20 18 16 14 12 10 8 6 4 2 0 2 4 6 8 10 12 14
48 46 44 42 40 38 36 34 32 30 28 26 24 22 20 18 16 14 12 10 8 6 4 2 0 2 4 6 8 10 12 14

FIGURE 4.47

FIGURE 4.48 Postmortem MRI and photomicrographs of multiple stainings (AChE, myelin, CR-ir, and CB-ir) at the sagittal level 17 mm from the interhemispheric plane (case Hb7; Table 2.1). Notice the dense immunostaining for both CB and CR in the ventral striatum (VS) and ventral part of GPe, but more intense CR- than CB-ir staining in the subpallidal region comprising the basal nucleus of Meynert (**B**). This region corresponds to the extended amygdala defined by others and previously included in the substantia innominata. *Scale bars*: 5 mm.

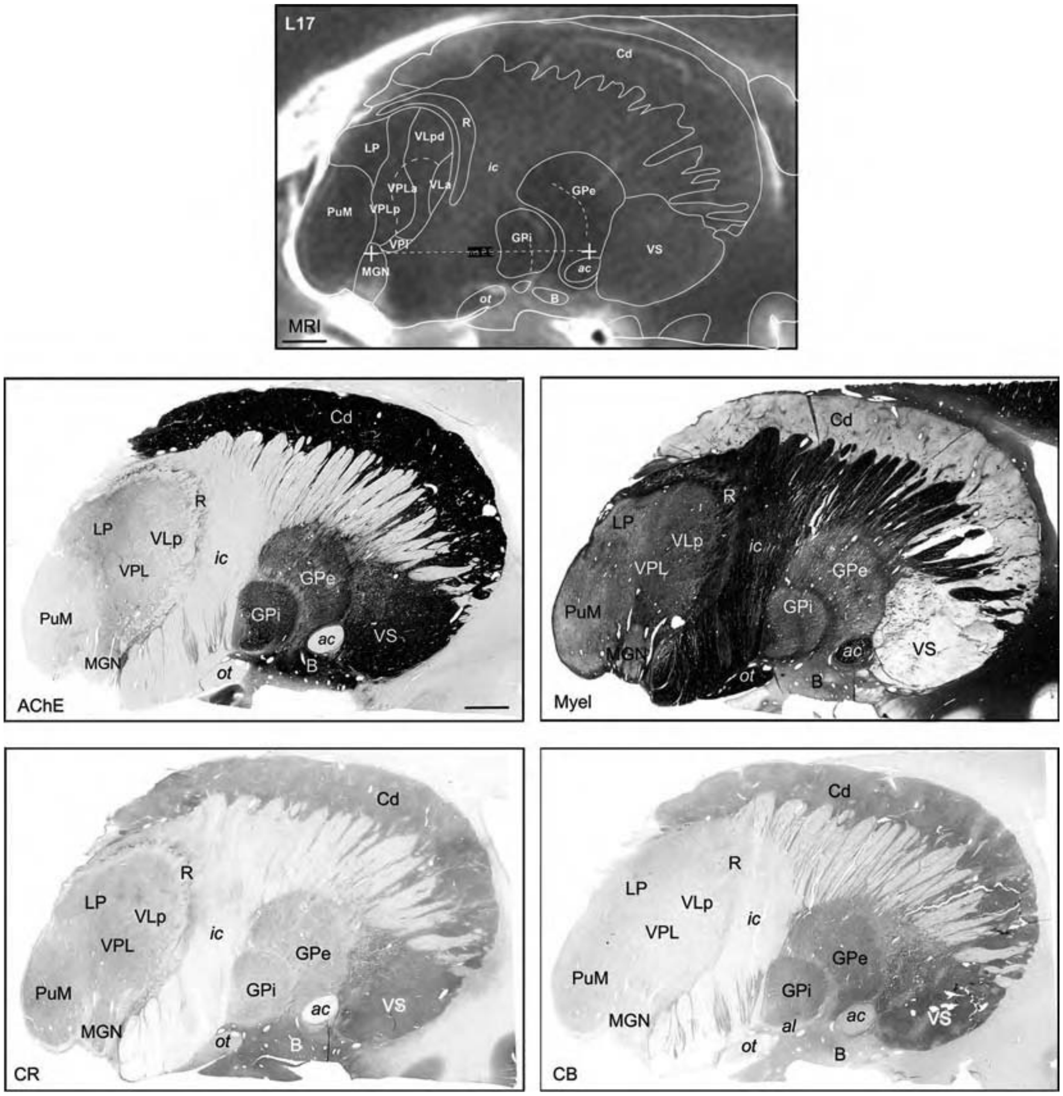

FIGURE 4.49 Photomicrographs of AChE (**A**), SMI-32 (**B**) and calcium-binding proteins CB (**C**) and CR (**D**) in sagittal sections of the striato-pallidal complex (case Hb6, Table 2.1). *Arrows* point to low AChE (**A**), SMI-32 (**B**), CB (**C**) and high CR patches (**D**). The patterns of CB- and CR-ir in GPv, subpallidal area and in the basal nucleus of Meynert (B) are similar to Figure 4.48. In the accumbens nucleus (Acb), the higher intensity of SMI-32- and CB-ir demarcates the core from the shell divisions. *Scale bar* in (**A**): 5 mm. *Source*: Adapted from Ref. 48.

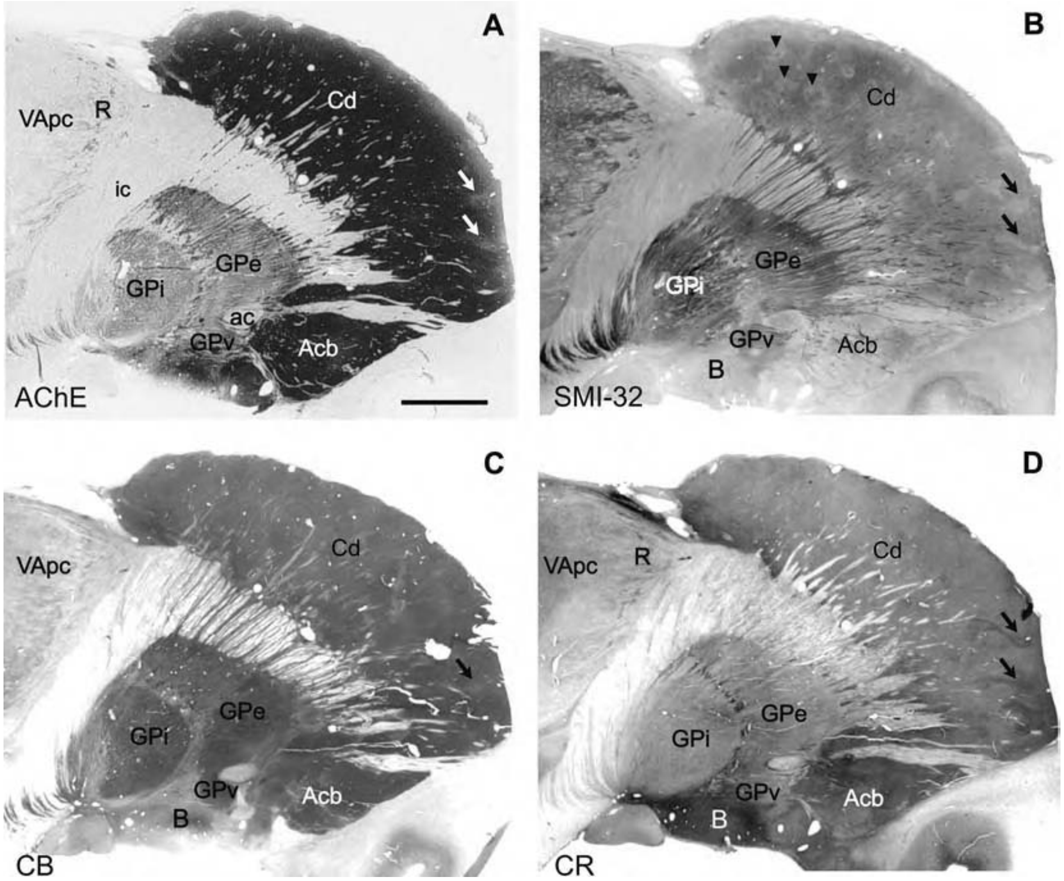

FIGURE 4.50 Postmortem MRI (**A**) and photomicrographs of staining for AChE (**B**), myelin (**D**) and immunoreactivity to the calcium-binding proteins CR (**C**) and CB (**E**) in frontal sections of the basal ganglia 22 mm anterior to pc (case Hb7, Table 2.1). The anterior GPi, as well as a ventral part of the putamen (PuT), are particularly enhanced in CB-ir (**E**), whereas the sublenticular area comprising the basal nucleus of Meynert (B) and the ansa peduncularis (*ap*) are strongly immunostained for CR. *Scale bars*: 5 mm.

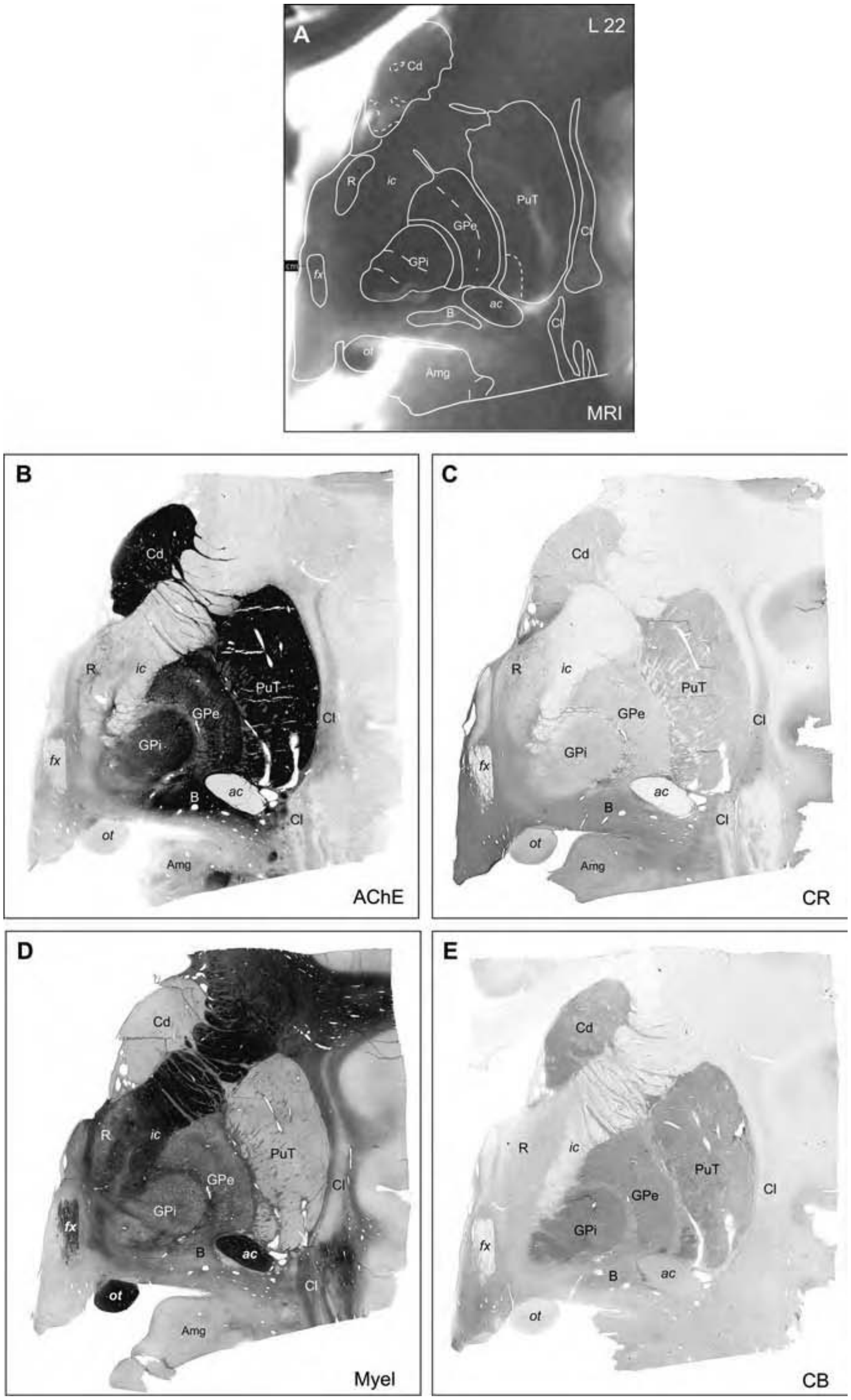

FIGURE 4.51 Photomicrographs of the patterns of CaBP immunostaining (**A, C, D**) in horizontal sections (2 mm ventral to ac-pc level) of the basal ganglia in relation to Nissl staining (**B**) (case Hb5, Table 2.1). The lower two panels show the complementarity of the distributions of PV (**C**) and CB (**D**) in the striatal and pallidal compartments, STh, RN and posteroventral thalamic nuclei. Immunostaining for CR (**A**) is most pronounced in the subcommissural and hypothalamic areas, as well as in the accessory laminae. *Scale bar* (**A**): 5 mm.

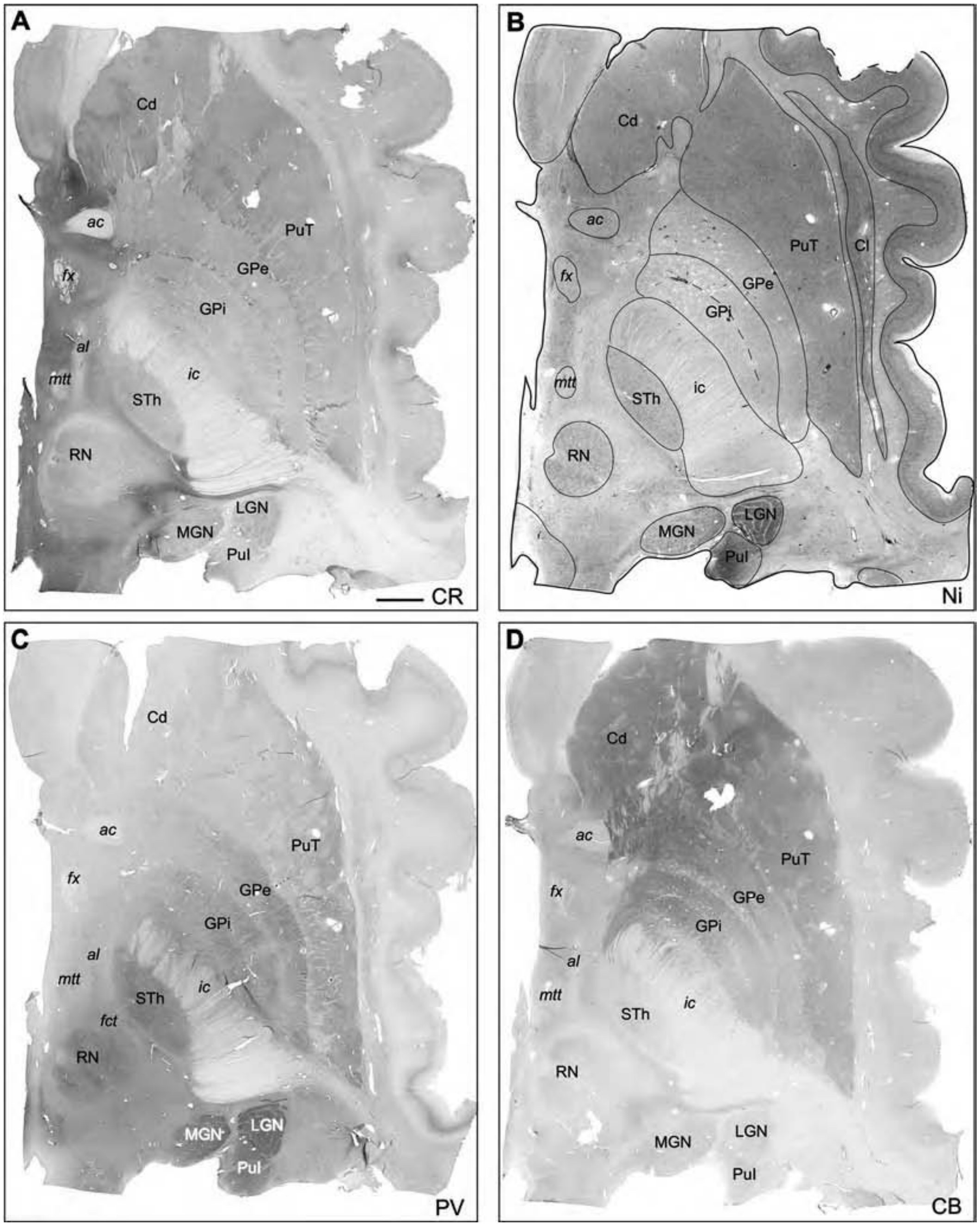

FIGURE 4.51

FIGURE 4.52 Photomicrographs of multiple stainings [Nissl (**A**), myelin (**B**), AChE (**C**), and CaBP-ir (**D–F**)] on horizontal sections of the striato-pallidal subdivisions and the substantia nigra (6 mm ventral to the intercommissural plane) (case Hb6; Table 2.1). Notice the largely complementary distributions of PV- and CB-ir (**E–F**) in the postero-ventral thalamus and striato-pallidal subdivisions. *Scale bar* (**A**): 5 mm.

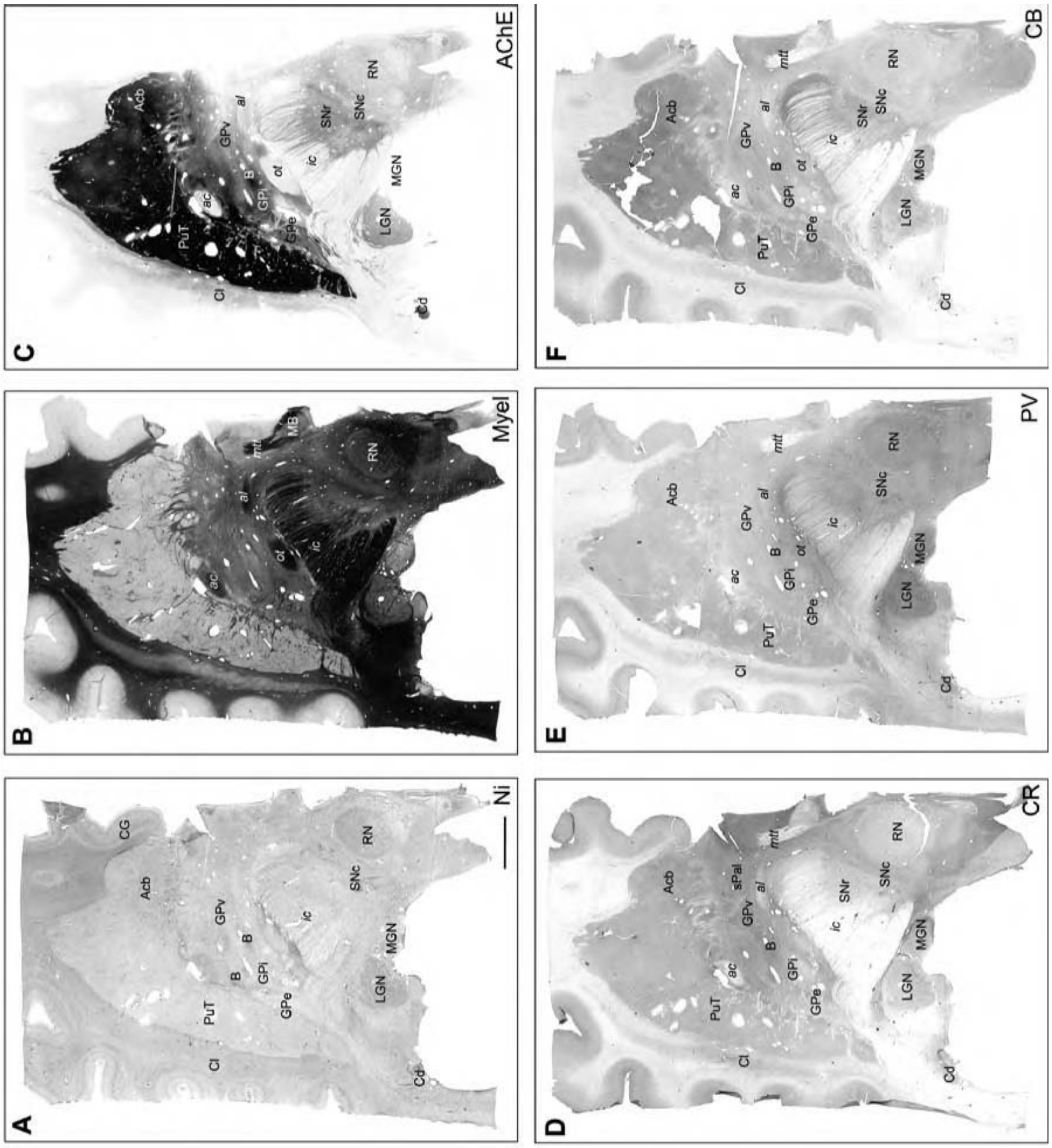

FIGURE 4.53 Photomicrographs showing complementary immunostainings of CB and CR in the pallidal and subpallidal areas (**A,B**) and in SN (**C,D**). Stars indicate corresponding locations in (**C**) and (**D**). *Scale bars*: 500 μm. *Source*: Adapted from Ref. 48.

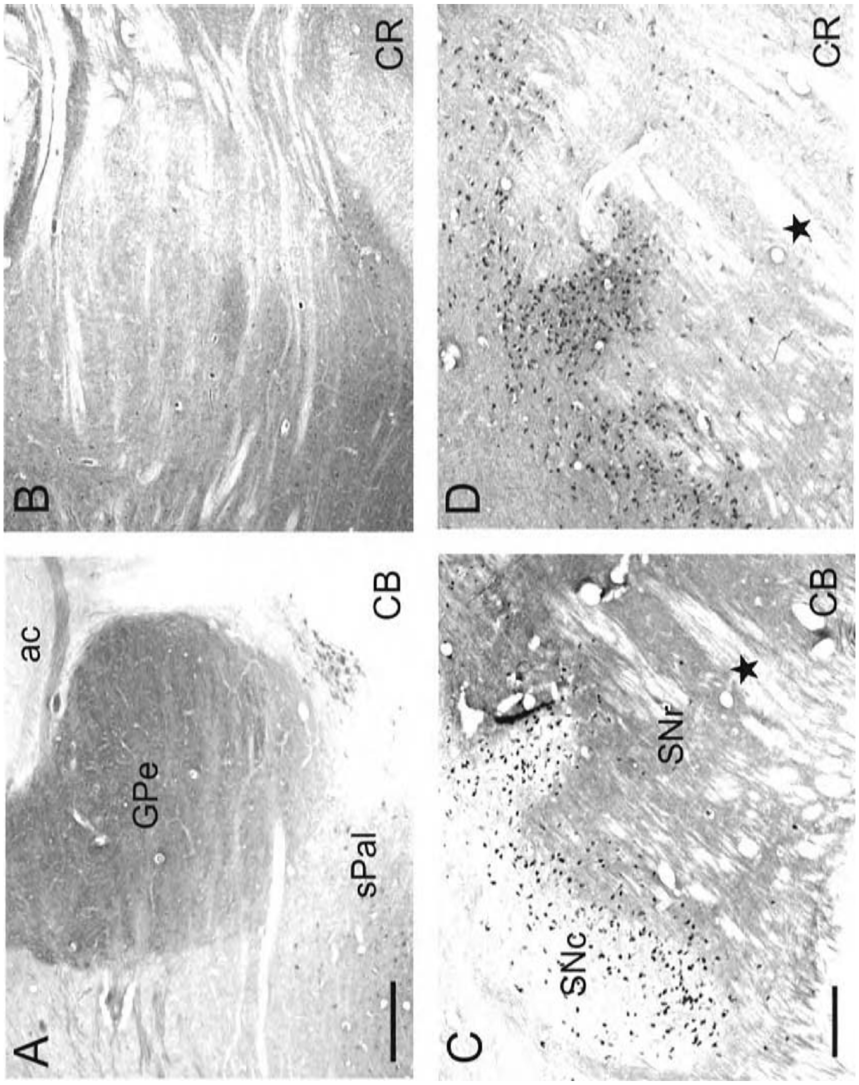

FIGURE 4.54 Combined photomicrographs and summary diagram of the striatopallidal anatomo-functional territories in frontal and horizontal sections of the human basal ganglia. The four territories (sensorimotor, *T1*; associative, *T2*; paralimbic, *T3*; and limbic, *T4*) are indicated in (**D**) by different grey areas and on horizontal section immunoreacted for CB (see *right panels*). *Source*: Adapted from Ref. 48.

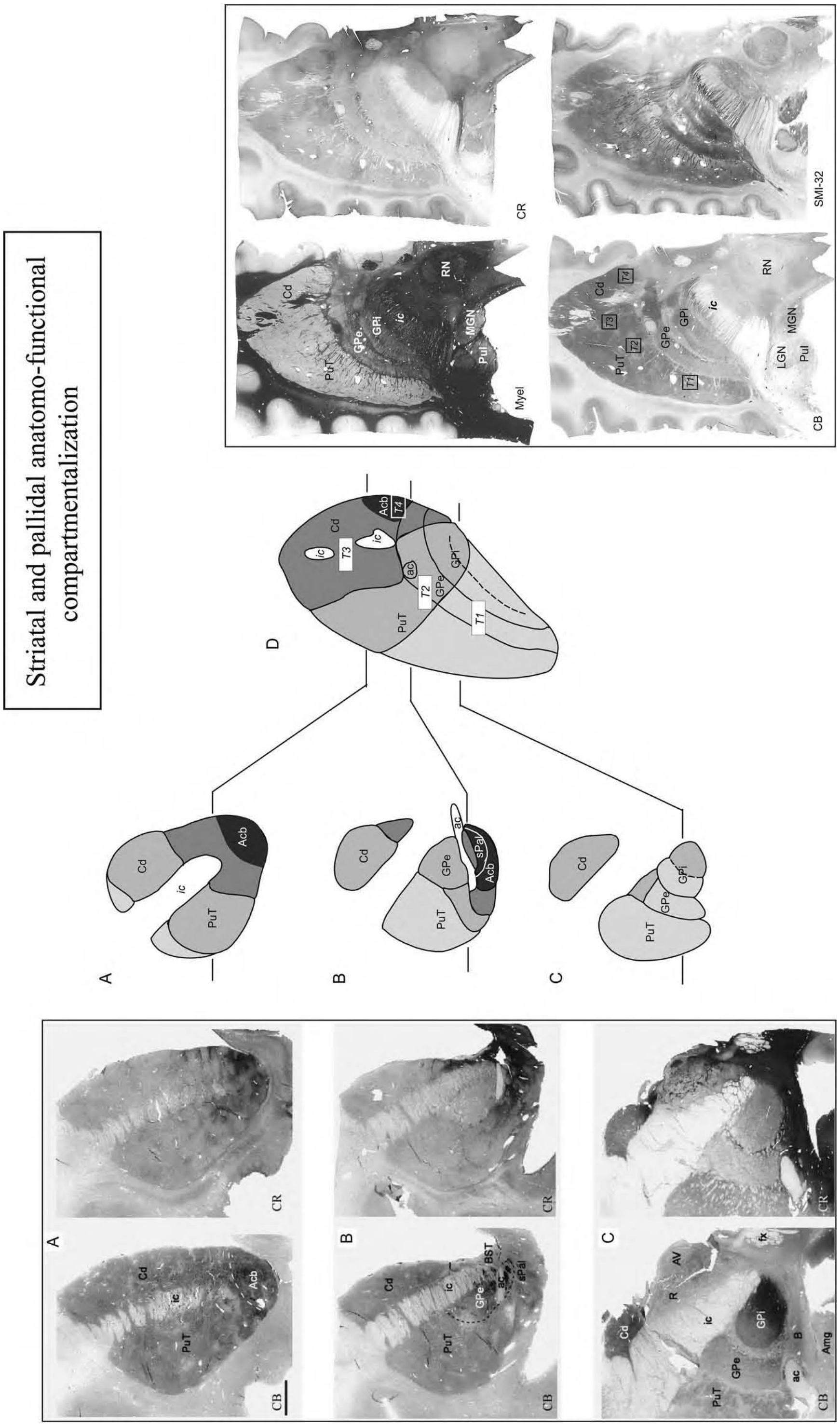

5 Subthalamic Fiber Tracts

The delineation of subthalamic fiber tracts, their stereotactic position, and correlation with high resolution postmortem MRIs represent an important addition to the previous atlas, as providing a basis for determination of prethalamic targets for the treatment of motor disorders (109). In the atlas of the human thalamus by Schaltenbrand and Wahren (26), drawings are superimposed on photomicrographs of the myeloarchitecture in the thalamus and adjoining areas. These are particularly helpful to identify different fiber tracts, but because of the drawbacks in terms of stereotactic precision, and uneven and often large intervals between sections, they are less than optimal for precise stereotactical targeting. In this atlas, we re-examined the myeloarchitecture of the thalamus, subthalamic, and pallidal areas and focused particularly on three major fiber tracts coming into the thalamus (medial lemniscus/spinothalamic tract, cerebello-, and pallidothalamic tracts). Comparison with immunostainings for calcium-binding proteins provides further insight into different anatomo-functional fiber sub-systems, also including other basal ganglia efferent pathways (pallido-subthalamic and striatonigral). The overall patterns of major sensory and motor fiber tracts coming into the thalamus are depicted in grey areas in the atlas maps and illustrated by photomicrographs in **Figures 5.1** to **5.6**. Other tracts are indicated by open areas (e.g., *ot*, *mtt, fx, scp*). The tracts are labeled for the parts where the fibers are the densest (the "bulks" of the tracts), but some cannot easily be separated, as discussed below for the somatosensory afferents. The spatial relationship between the different tracts and their thalamic territories are best seen on sagittal sections (**Fig. 5.1**).

CEREBELLOTHALAMIC AND PALLIDOTHALAMIC TRACTS

These two fiber tracts represent major motor afferent to the motor thalamus and are important surgical targets for the treatment of patients with essential tremor and Parkinson's disease, respectively (109,110) (see chap. 7 and **Fig. 7.1**).

The cerebellothalamic tract [or fasciculus cerebellothalamicus (*fct)*] is represented in the maps in Chapters 3 and 4, and in relation to the myeloarchitecture in sagittal and horizontal sections of **Figures 5.1** and **5.2**. It corresponds in large part to Hassler's prelemniscal radiations ("ra.prl") (26) and to the prerubral field or field H of Forel (56,111). The trajectory of the tract analysed in the three stereotactic planes is toward the posterior part of the ventral medial (VM) nucleus and the ventral lateral posterior nucleus (VLp), with possible extension into the VLa (e.g., **Fig. 5.1**). In some sections, part of the tract appears to take a posterior course toward the intralaminar nuclei. This would confirm an observation made in monkeys where cerebellar fibers taking a posterior course reach the CL nucleus (33). The tract is characterized by enhanced parvalbumin immunoreactivity, like the VLp and the RN (**Figs. 3.26** and **3.27**). The bulk of the fct is posterior and lateral to the pallidothalamic tract, and they come close together at some levels (**Fig. 5.1**), although still separated as reported earlier (112). The work by Nauta and Mehler (94) on striatal and pallidal connections in the monkey also gives an "historical" review on the early descriptions of the pallidothalamic pathways. From his early work (111), the fields bearing Forel name (H, H1, and H2) have been used to describe pallidothalamic fibers, though only H2 and H1 were later recognized to originate from the pallidum through the ansa and fasciculus lenticularis (al and fl, respectively). They were first noted by C. Vogt (113) to merge as H1 + H2 to form the fasciculus thalamicus (*ft*).

The course of pallidothalamic fibers has been re-examined recently in the monkey after tracer injections (114) or lesions in the internal pallidum (115,116). The two studies differ in terms of the origin of pallidal neurons giving rise to the al and fl: the first group suggests that both fascicules harbor pallidofugal axons originating from all sectors of GPi, while the second proposes a distinct origin for the two tracts, with fl arising from the sensorimotor part of GPi, and al from the anterior, associative, part of GPi. The present study cannot resolve the issue but following the course of fl and al in three planes, our data support that both arise from large parts of the GPi, though with al possibly not extending as far caudally as fl.

The multiarchitectonic analysis provides little information for the distinction between cerebello- and pallidothalamic tracts, except for enhanced PV-ir in fct and in postero-medial part of ft (**Fig. 5.3B**). The two tracts come close together but a small gap separates the two, as also seen in the sections stained for myelin or immunostained for CR. Most parts of the pallidothalamic fibers remain unstained, in contrast to adjacent subthalamic structures such as STh, RN, and ZI. The latter is characterized by high AChE, high CR-ir, and moderate CB-ir restricted to the ventral region (**Fig. 5.3**). The ZI has been divided anatomically and functionally into four regions, principally in rodents (117,118), and the present observations in the human brain may bear some similar properties. Nevertheless, the ZI as delimited here is relatively small and is only part of the region delimited as ZI in the Schaltenbrand and Wahren atlas (26).

The course of nigrothalamic afferents cannot be identified in the present study, but a recent study in monkeys suggests that at least part of the fibers reach the VM and VAmc nucleus medial to the STh nucleus (119).

MEDIAL LEMNISCUS/SPINOTHALAMIC TRACTS

The distinction between the medial lemniscus and spinothalamic tract in our material is difficult without additional criteria. Nevertheless, on the basis of evidence reported in the human brain (74,75) and comparison with tracings in the monkey, the tracts were labeled *ml*, *stt*, or *ml*/*stt* in the maps depending on their orientation and their thalamic targets. For example, at posterior levels of the thalamus (e.g., **Figs. 4.1–4.3**), the tract divides into two or three branches. One branch is oriented toward the posterior complex and CL which are associated with the *stt*, and another branch coursing laterally towards the VPI and VPL, may contain both *ml* and *stt*. In immunostained sections, some fibers associated with the *stt* are immunoreactive to CB and run medial and posterior to the PV-ir *ml* tract (**Figs. 3.26** and **3.34**).

CORRELATION WITH HIGH RESOLUTION POSTMORTEM MAGNETIC RESONANCE IMAGING

High resolution proton density MRIs were acquired in a 3-Tesla scanner (see protocol in Chapter 2). The images are illustrated in **Figures 5.5 and 5.6,** together with myelin stained sections of the same brain cut in the frontal and horizontal planes. Several anatomical features can be well recognized in the MRIs, in particular densely myelinated subthalamic fiber tracts such as the cerebello-thalamic (fct), pallidothalamic (fl and ft), and mammillothalamic (mtt) tracts. In the thalamus, several nuclei (AV, LD, MD) are clearly identifiable, as well as subdivisions within VLp (VLpv more intense than VLpd) and within MD (more intense signal in MDmc than in the rest of the nucleus). Other thalamic subdivisions are more difficult to distinguish, such as the borders between VM, VLa, and VA. In the basal ganglia, the striatopallidal compartments and SN are quite visible, but not the STh. The fuzzy border between STh and SN impedes direct targeting of the STh nucleus based on MR imaging only (120,121).

FIGURE 5.1 Subthalamic fiber tracts shown in photomicrographs of sagittal myelin stained sections (*right column*) and represented by grey areas in corresponding maps of the thalamus and subthalamic areas (case Hb1; Table 2.1). Distances to interhemispheric plane or thalamo-ventricular border (in parentheses) are indicated in the upper left corner of each drawing. The interrupted lines in the maps indicate the intercommissural level DV 0 (*horizontal lines*) and the levels of the pc and ac (*vertical lines*). *Scale bar*: 5 mm (*upper right panel*).

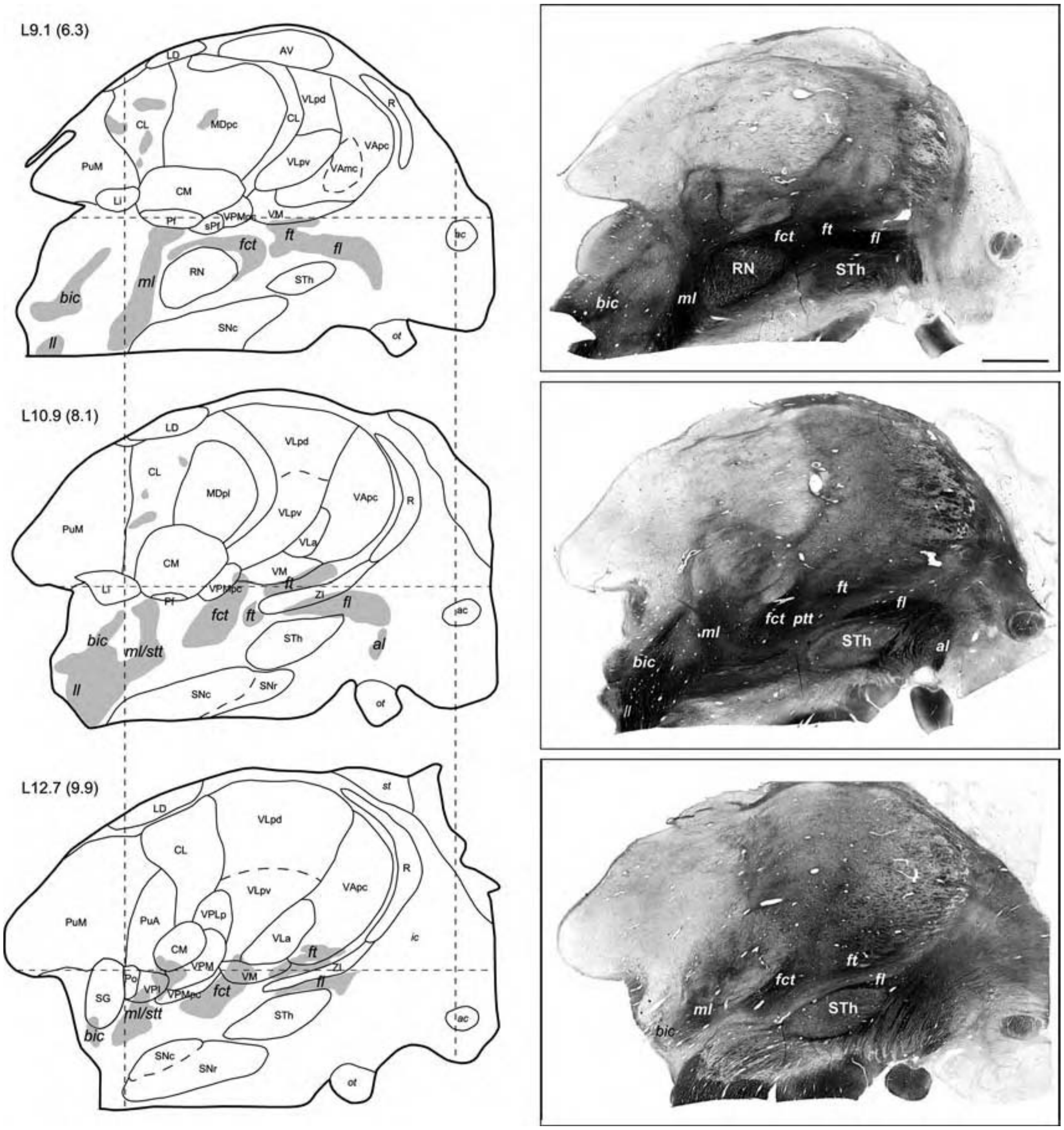

FIGURE 5.2 Horizontal atlas drawings of cerebello-thalamic (fct; *dark grey*) and pallidothalamic (ft, fl, al; *light grey*) fiber tracts (*upper panels*). Myelin sections at similar levels are represented in lower panels. The medial lemniscus (ml) and brachium of the inferior colliculus (bic) are also represented in the more ventral atlas maps (V2.7 and V3.6). Levels of sections are indicated in millimeters dorsal (D) or ventral (V) to the intercommissural plane (DV 0). Interrupted lines in the drawings indicate the posterior commissure (pc) and midcommissural (mcl) levels (case Hb1; Table 2.1). *Scale bars* (*upper and lower left panels*): 2 mm.

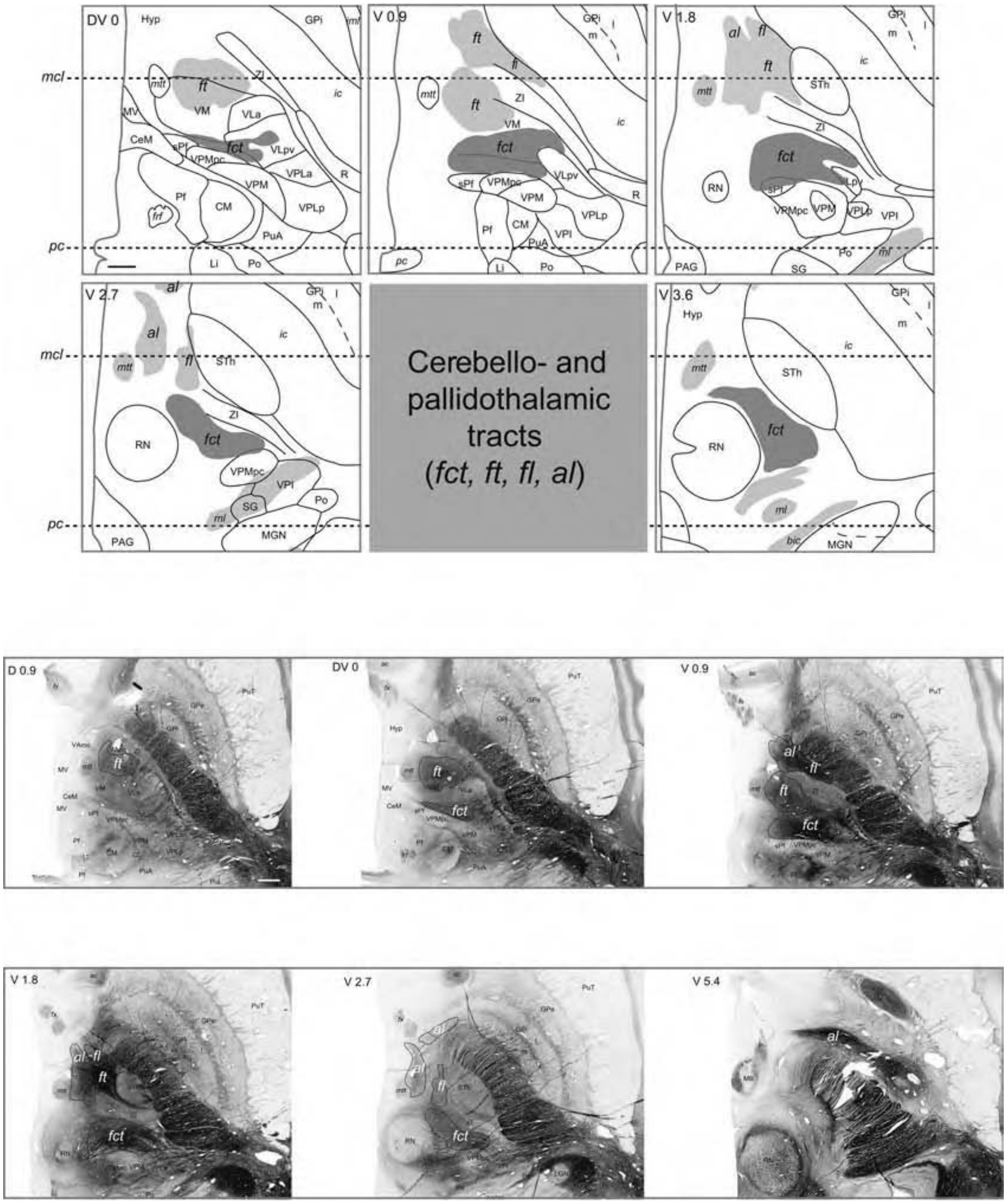

FIGURE 5.3 Multiarchitectonic characteristics of the “comb” system, pallidothalamic fibers (ft and fl) and neighboring areas. (**A**) Photomicrographs of the region comprised in the rectangle in the frontal section of the anterior tier of the thalamus (level A13, case Hb7; *right panel*). (**B**) Enlarged view of the fct, ft, and fl in sagittal atlas map and in sections stained for myelin and immunoreacted for the calcium-binding proteins PV and CR (from case Hb1; Table 2.1). *Scale bars*: 2 mm.

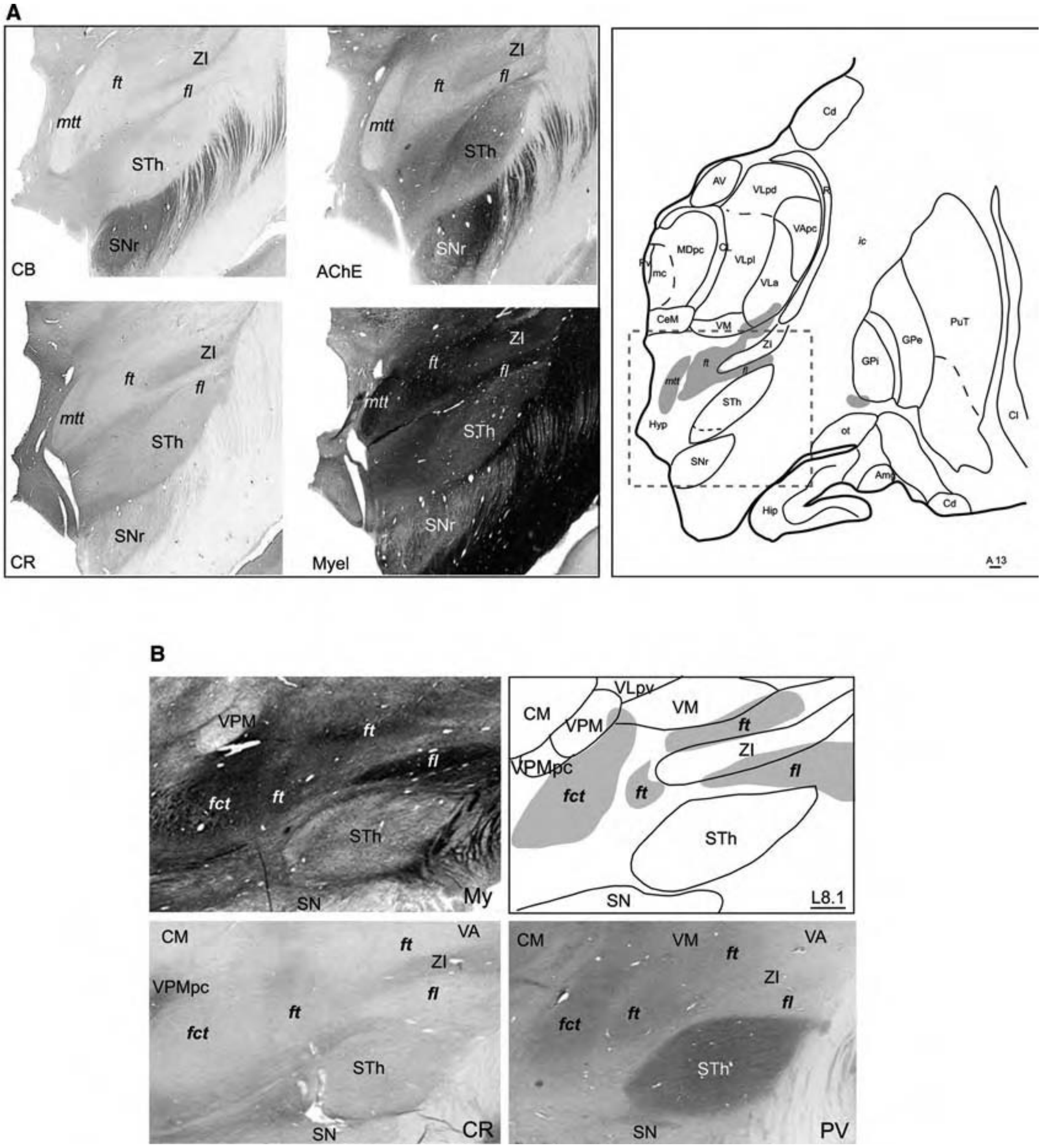

FIGURE 5.4 (A–F) Multiarchitectonic aspect of subthalamic fibers tracts and neighboring areas in adjacent sagittal sections 11 mm lateral to the interhemispheric plane (case Hb7; Table 2.1). The *arrows* in (**A**) and (**B**) point to the fasciculus subthalamicus and striatonigral fibers, respectively, which are part of the "comb" system. *Scale bar (**A**)*: 2 mm.

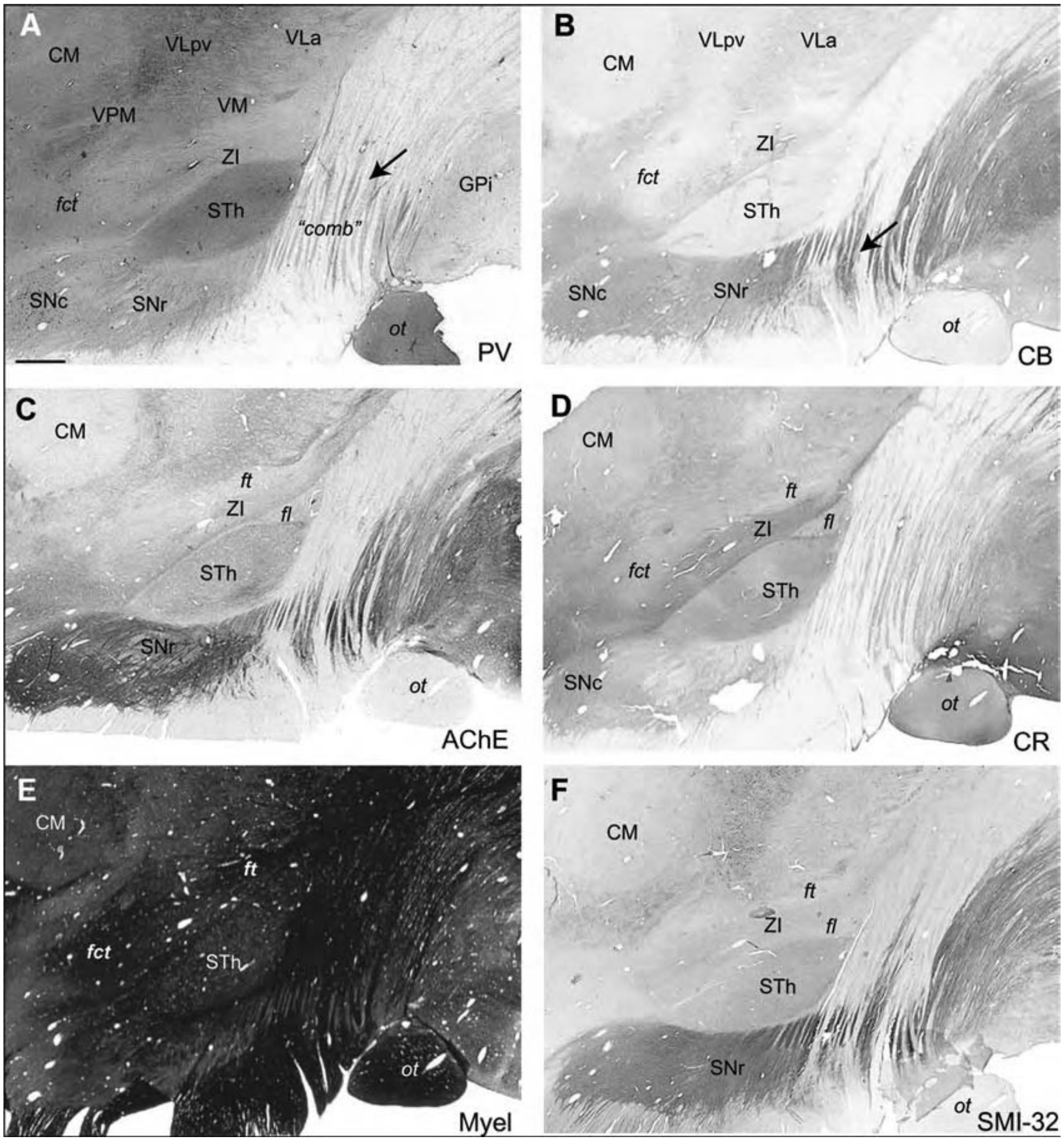

FIGURE 5.5 Comparison between frontal sections stained for myelin (**A** and **C**) and corresponding high resolution proton density MRI (**B** and **D**) of the same brain. The fiber tracts as well as some thalamic nuclei can be recognized in MRI, such as AV, LD, VLpv, MD (with more intense signal in MDmc), CM, and Pf. However, no clear limit is seen between STh and SN. *Scale bar* (***B***): 5 mm.

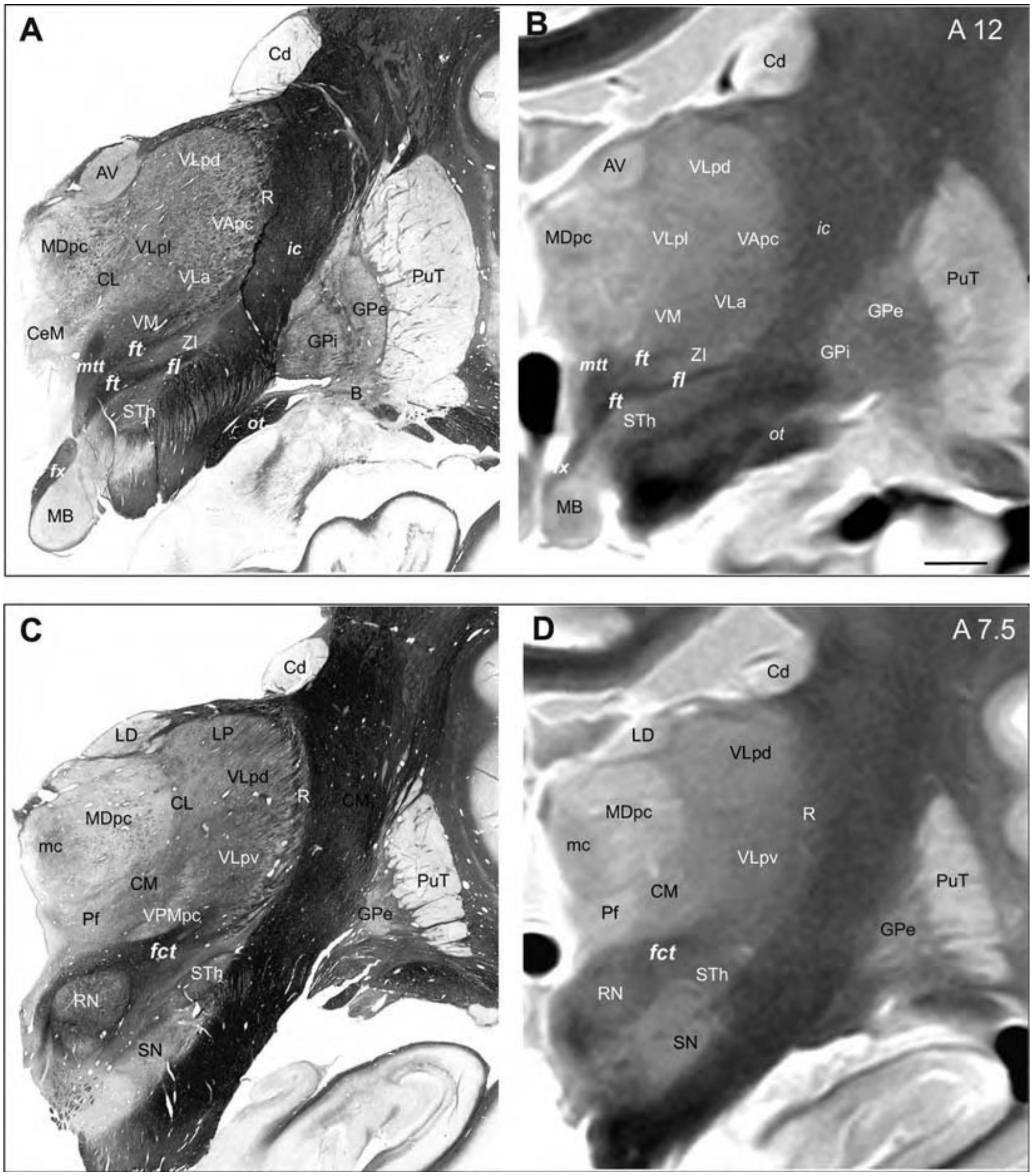

FIGURE 5.6 Correlation between myelin stained horizontal section (**A**) and proton density MRI (**B**) at levels close to the intercommissural (DV 0) plane. Besides fiber tracts, several thalamic nuclei can be distinguished in the MRI, such as VLpv, MGN, CM-Pf, and PuL. *Scale bar* (***A***): 5 mm.

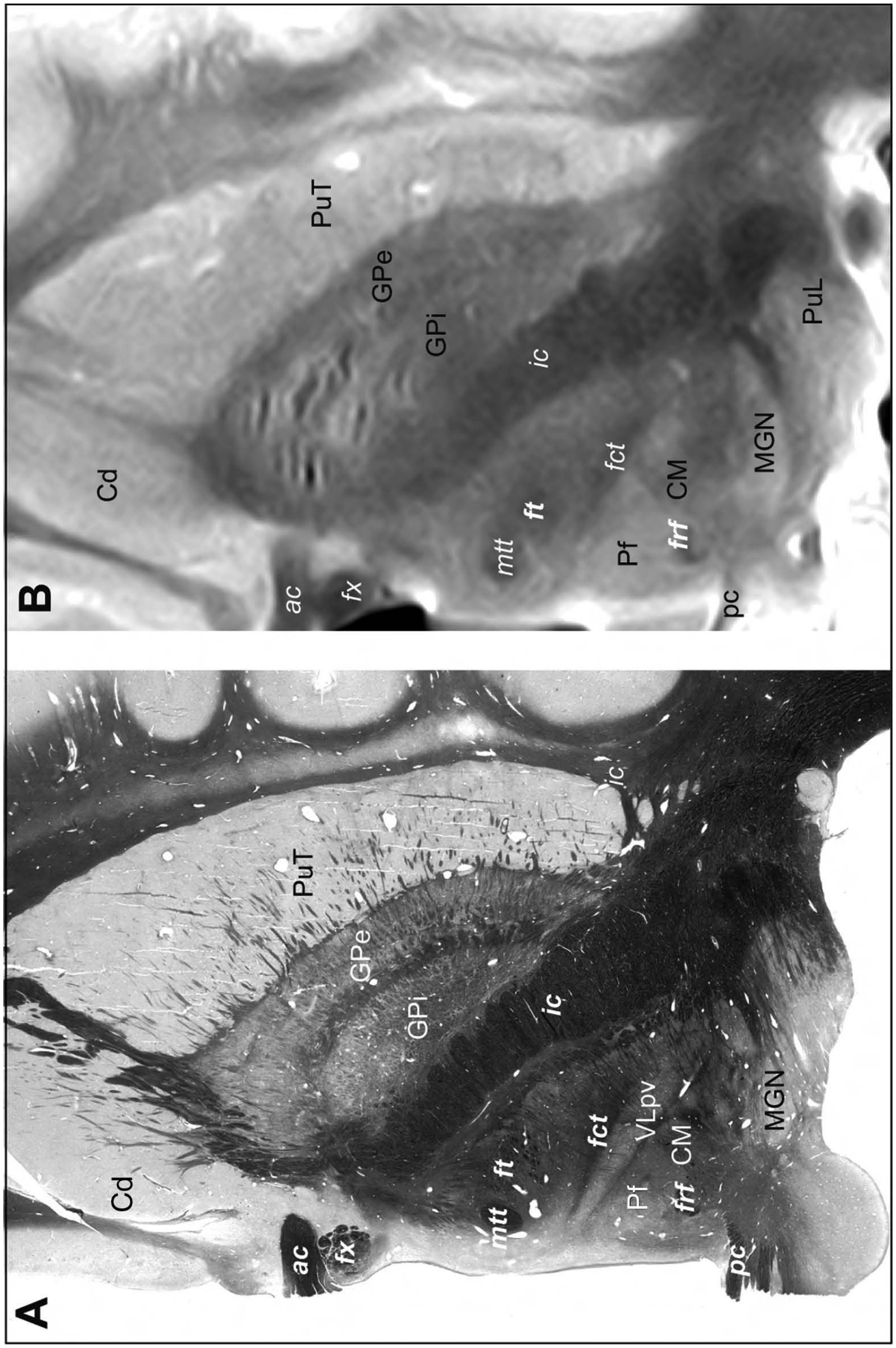

6 Interindividual Anatomical Variability

METHODOLOGICAL CONSIDERATIONS

Evaluation of how brains or specific structures (e.g., thalamus) in the brain differ from one subject to another is a difficult task. It has been investigated postmortem as well as "in vivo" with MRI visualization methods to construct probabilistic atlases (122–124) and also in the context of disease-related morphological changes (6,125). Postmortem brain examinations allow comparing detailed structures such as thalamic nuclei, whereas "in vivo" MRI provide relative crude estimates of such structures (126) but on a larger sample of brains.

In the present study, postmortem interindividual thalamic and basal ganglia variability was evaluated by comparing brain sections cut in the same stereotactic planes. The difficulty resides in cutting sections as close as possible to planes parallel (for horizontal sections) or perpendicular (for frontal and sagittal sections) to the ac–pc plane. Small deviations from these planes will result in differences depending on the direction of the deviation and thus not reflecting possible interindividual anatomical variability per se. Although great care has been given to fulfil these requirements, we cannot exclude some distortion factor from our material. Digitalization and 3D-rendered volumes can provide some correction by re-orienting the atlas model according to the reference system. Other "technical" factors include possible deformation of the brain during fixation. This could explain for example the greater difference observed in the dorsal thalamus, resulting in differences in dorsally located nuclei such as LD, AV, dorsal CL,VLpd. Nevertheless, brains that have been "suspended" in the fixative solution present similar differences in the dorso–ventral direction as the other. Moreover, MR images from patients show relatively large variations, some of the same magnitude seen in autopsy material (see below). In order to best estimate anatomical variability, sections cut in the horizontal or sagittal plane are more suitable than in the frontal plane where the ac and pc are not in the same plane. In the horizontal plane, the ac and pc centers may not lie *within* one section but *between* two, but the estimated difference is less than 500 μm.

DORSO-VENTRAL VARIATIONS

One major difference observed among brains is the dorsal limit of the thalamus as measured from the distance orthogonal to the ac–pc plane (**Fig. 6.5**). This "global" difference, which amounts to 3.5 mm, is reflected by similar difference in the dorsal extent of thalamic nuclei (e.g., PuM, CL, MD, VLpd) as illustrated in **Figures 6.1** and **6.2**, with a "shift" of the LD toward a more ventral and posterior position as if the brain had been "flattened." However, more ventrally located nuclei, such as CM, Li, VM, and positions of subthalamic fiber tracts are less affected. The differences in dorsal extent of the thalamus are similar to those evaluated in a 3D atlas-to-MRI registration study (62). In the basal ganglia, relatively large variations are observed in the dorso–ventral position of the pallidal subdivisions, as seen between cases Hb1 and Hb7 when compared on sagittal planes (e.g., **Figs. 3.18–3.25** and **4.30–4.45**). This variation is larger when considering the GPe and GPi. The level at which the ac–pc plane intersects GPe and GPi is more ventral in Hb7 than Hb1, as also seen in the frontal and sagittal series of the Schaltenbrand and Wahren atlas (26) and in frontal maps of the Mai et al. atlas (32). This difference could be related in part to deviation of the position of the ac–pc plane, with more impact on the pallidal than on thalamic level. However, the position and extent of GPi/GPe is similar in the other hemisphere of Hb1 cut horizontally with a more accurate position of the ac–pc plane (e.g., **Figs. 3.6–3.12**), suggesting that at least part of this variability is real.

LATERO-MEDIAL VARIATIONS

Our experience has been that the variations in lateral coordinates are less when referred to thalamoventricular border than to interhemispheric midsagittal plane. When measured in horizontal sections (**Fig. 6.5**), the distances vary up to 5 mm when measured from interhemispheric plane, and to 3 mm when measured from the thalamoventricular border. The difference in latero-medial extent of thalamic nuclei and subthalamic fiber tracts is illustrated in **Figure 6.1** in frontal sections of two different brains. This difference is particularly reflected in the most lateral thalamic nuclei (e.g., R), but less for more medial nuclei (CL, MD, CM). Smaller variations are also observed for the fct, RN, and SN. This variability tends to be independent from the length of the ac–pc line, as shown by the relatively small thalamic differences in two other brains with different intercommissural distances (**Fig. 6.3**).

Overall, variability in both dorso-ventral and latero-medial dimensions is not homogeneous but tends, at least for the thalamus and subthalamic area, to be smaller for structures closer to intercommissural plane, for dorsoventral position, and to the ventricular border, for latero-medial position.

ANTERO-POSTERIOR VARIATIONS

Antero-posterior positions of thalamic nuclei and basal ganglia structures tend to vary according to the intercommissural length. This variability can be taken into account by using different reference points for targeting, for example the posterior commissure (AP 0) level for targeting the posterior part of the CL nucleus, the midcommissural point (mcl) for the *fct*, *ft*, STh and posterior GPi, and the anterior commissure (*ac*) level for the anterior GPi. This is depicted in **Figures 6.3**, **6.4**, and **6.7** where drawings of sections from brains with same or different ac–pc distances are aligned on different reference points. The use of different landmarks provides thus a mean to reduce the variability of surgical targets by staying close to the reference points.

As pointed above, the latero-medial and dorso-ventral variations appear largely independent from the intercommissural distance. Because of this inhomogeneity, there is no available standardization procedure for adjusting data from different brains and correct fully for interindividual anatomical variability. This is illustrated in **Figure 6.7** (lower right panel) where adjusting brains with different ac–pc distances to a "standard" 26 mm distance results in latero-medial deviations of pallidal targets.

RELATION TO "IN VIVO" VARIABILITY

A number of structures within or adjacent to the thalamus and basal ganglia are visible in MRI, though with variable precision. This direct visualization, though not accurate enough for targeting (20,120,121), provides additional control for transferring atlas to MR target coordinates, as well as landmarks that are crucial for more accurate evaluation of overall thalamic and basal ganglia variability. Furthermore, this evaluation can be based on much larger number of cases, in both normal (control) conditions as well as in disease situations (patients undergoing stereotactic surgery). In the context of functional neurosurgery, the MRI resolution is limited by the time and protocol of peroperative MR acquisition. Nevertheless, in cases of patients undergoing surgery for PD or neuropsychiatric disorders, target placement in the internal pallidum is optimized by using 3D-IR MRI sequences allowing visualization of the striato-pallidal compartments. In a small group of patients, distances from the ac–pc plane to the maximal height of the thalamus and to the internal capsule were measured (**Fig. 6.5**). The variation of the dorsal height of the thalamus (D) was 2 mm, and that of the distance from thalamoventricular border to internal capsula (L) was 3 mm (up to 6 mm when measured from the interhemispheric plane). Both distances varied independently of the intercommissural length. Comparative measurements in three postmortem brains with similar intercommissural distances resulted in variations of the same magnitudes for the lateral distances when measured from the thalamo-ventricular border, but higher variation for the dorsal thalamic height. As discussed before, factors such as duration of fixation and positions of the brains in fixative may account for some of the differences observed in postmortem material. More quantitative analyses, on a larger number of cases, have to be conducted in the future.

ELECTROPHYSIOLOGICAL EVALUATION

During stereotactic neurosurgery, microelectrode recordings of multiple or single unit activity are used in many functional neurosurgery centers to assess proper target site for placement of therapeutic lesion or DBS electrode (14,16,121,127–134). The precision of this method, however, depends on the physiological characteristics of the structure to reach or serving as landmark along the penetration. In the thalamus, the presence of somatotopic maps and specific responses to motor or somatosensory stimulations, with relatively restricted receptive fields of the neurons in lateral nuclei (e.g., VPL) (128,135,136), provide criteria for adequate targeting in these nuclei. Changes in activity patterns in the pallidal segments or the STh in PD patients are means to localize borders of these structures (16–18,129,130,134,137), though these are not necessarily sufficient in large structures such as the pallidum. In our experience, the initial anatomo-radiological step of precise target coordinate determination and transfer onto MR images is the most critical for guiding the electrode penetration. Then, electrophysiological recordings allow the control of accurate depth of the target. This is particularly the case for targeting the pallidothalamic tract which passes on the dorsal surface of the STh and enters the thalamus just ventral to the motor thalamic nuclei VLa/VA/VM. The typical sequence of spontaneous activities encountered along the penetration are of sporadic or bursting activities in the thalamus, very low level of activity in the ZI area, sudden reappearance of multiple tonic, more or less regular, activities at the entrance into STh, and tonic regular single unit activities when coming into the SN. The variations in the depth of the dorsal border of STh (**Fig. 6.6**) are relatively small (±1.5 mm), although more variations are observed in the thickness of the nucleus. Anatomically, the STh is an elongated structure oriented obliquely, in an antero-medial to postero-lateral and dorso-lateral to ventro-medial axes. Small interindividual variations in this orientation relative to intercommissural or midsagittal planes, as well as slight variations in the position of intercommissural plane or interhemispheric plane, will result in differences in the depth at which the dorsal border of the STh is encountered. Physiological criteria are less clear for other targeted thalamic nuclei, such as the intralaminar CL nucleus for neurogenic pain. Nevertheless, the ventral limit of the CL and limitans (Li) nuclei (e.g., **Fig. 7.3D**) is often detected by a decrease of unit activity. Atlas reconstruction of MRI lesions taken three days postoperatively provide control of the correct position of the target, though with limited precision due to resolution of MR images, slice thickness, and possible slight errors in 3D stereotactic MRI slice orientations. The possible occurrence of a brain shift cannot be avoided in stereotactic interventions (138), but the use of a smaller, "pencil" shaped macroelectrode, as experienced in our operations for the last years, reduces significantly the problem. It is also important to note that more shift is likely to occur when the electrode has to pass through the ventricule before entering the thalamus as with medial thalamotomies, than without ventricular passage, such as with subthalamic or pallidal operations. In spite of these problems, the large majority of our penetrations in patients is localized close enough to the intended target so that only rarely (less than 1% of performed targets) was a second penetration for the same target necessary. Physiological criteria are also helpful to target the pallidum, in particular to determine its ventral limit and avoid the optic tract (129,130). In spite of their visualization in MRI (particularly with 3D-IR sequences), the contours of the pallidal segments are not very sharp, especially in ventral sections.

FIGURE 6.1 (***See color insert.***) Comparison of thalamic and basal ganglia subdivisions, and of cerebellothalamic tract (*fct*), in frontal maps of two different brains (Hb2, red contours; Hb7, white contours) at anteroposterior level 8 mm anterior to pc and aligned on the intercommissural (DV 0) and midsagittal (L 0) planes (interrupted horizontal and vertical lines, respectively). Selected structures are filled with colors to better illustrate the variability. Frontal sections from brain Hb2 were illustrated in the previous atlas (Figs. 6.24 to 6.29) (47). Intercommissural distances are 30 mm (Hb2) and 26 mm (Hb7). *Scale bar*: 5 mm.

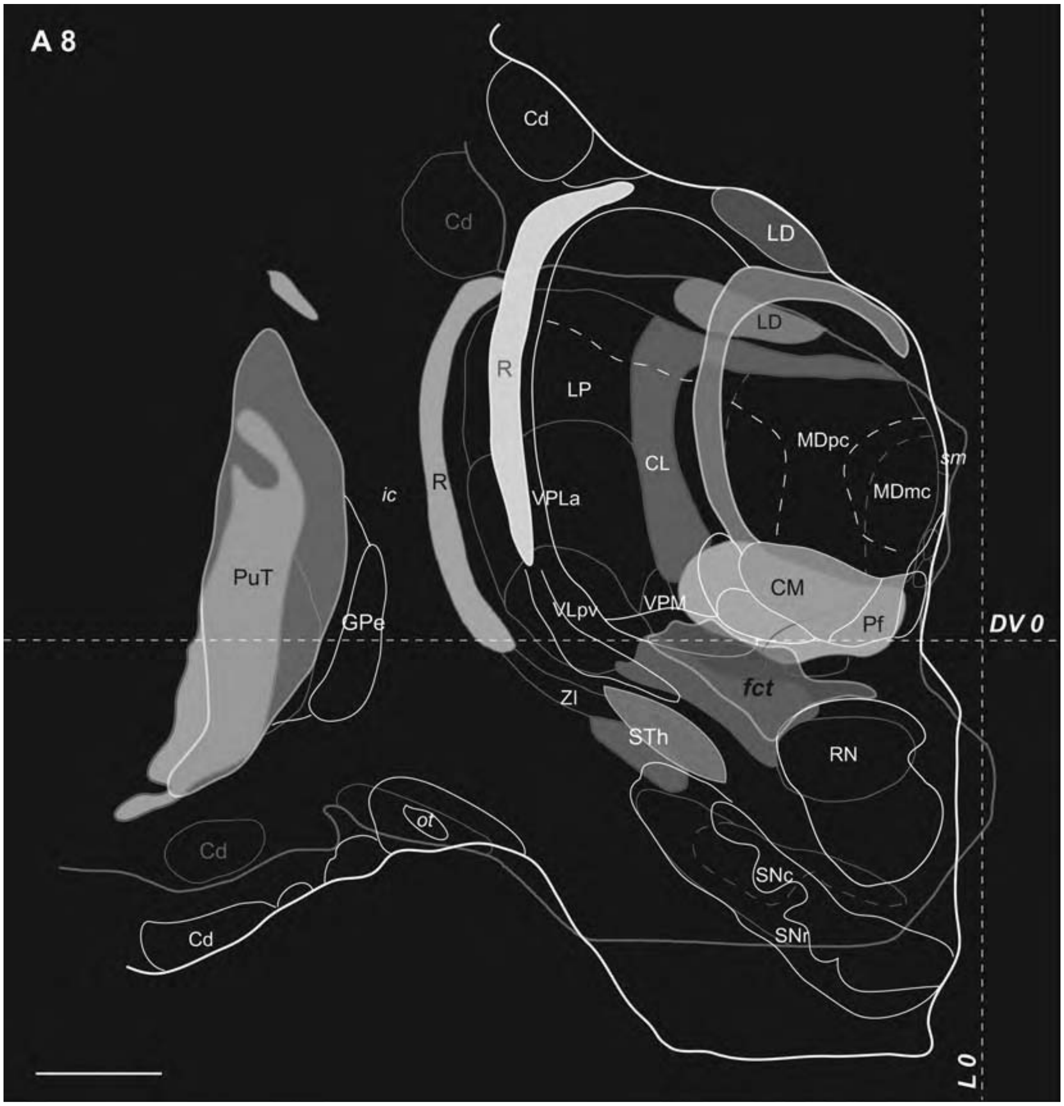

FIGURE 6.2 (***See color insert.***) Comparison of thalamic nuclei, subthalamic fiber tracts, STh and substantia nigra in sagittal maps of two different brains (Hb1, red contours; Hb7, white contours) adjusted to lateral planes L 7 and L8 of brain Hb7, and aligned on the intercommissural plane (DV 0). The intercommissural distances are 25 mm (Hb1) and 26 mm (Hb7).The variability is the lowest for structures close to the intercommissural (DV 0) plane. *Scale bar (upper panel)*: 5 mm.

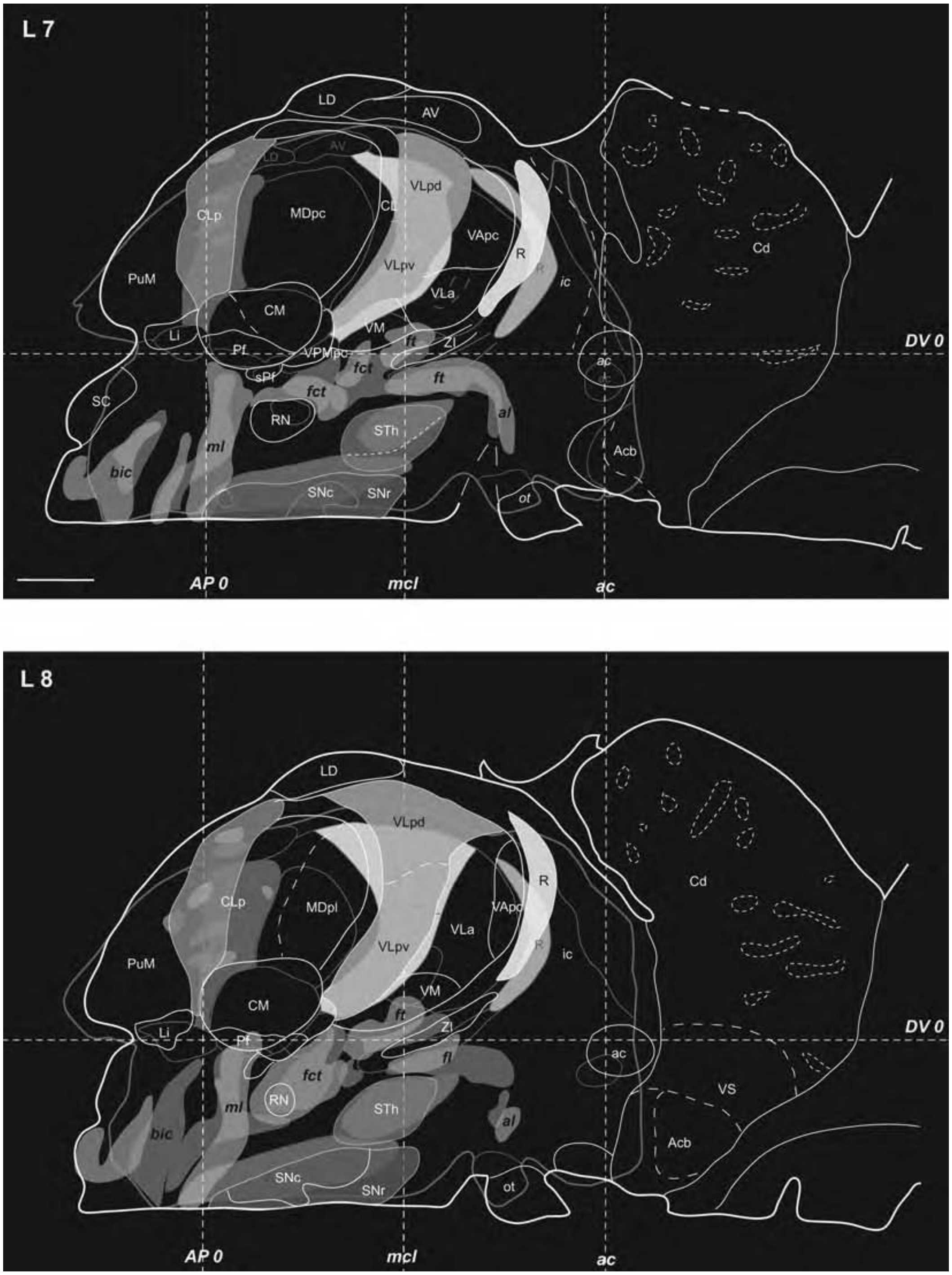

FIGURE 6.3 (***See color insert.***) Comparison of thalamic and striato-pallidal subdivisions in horizontal sections of two different brains (Hb2, red contours; Hb1, white contours) 3.6 mm dorsal to intercommissural plane and aligned on anteroposterior midcommissural (*mcl*) in (**A**) and posterior commissure level (*AP 0*) in (**B**). Same color codes for the CL, VLp, and R nuclei as in Figure 6.2. Intercommissural distances are 25 mm (Hb1) and 30 mm (Hb2). *Scale bar (**B**)*: 5 mm.

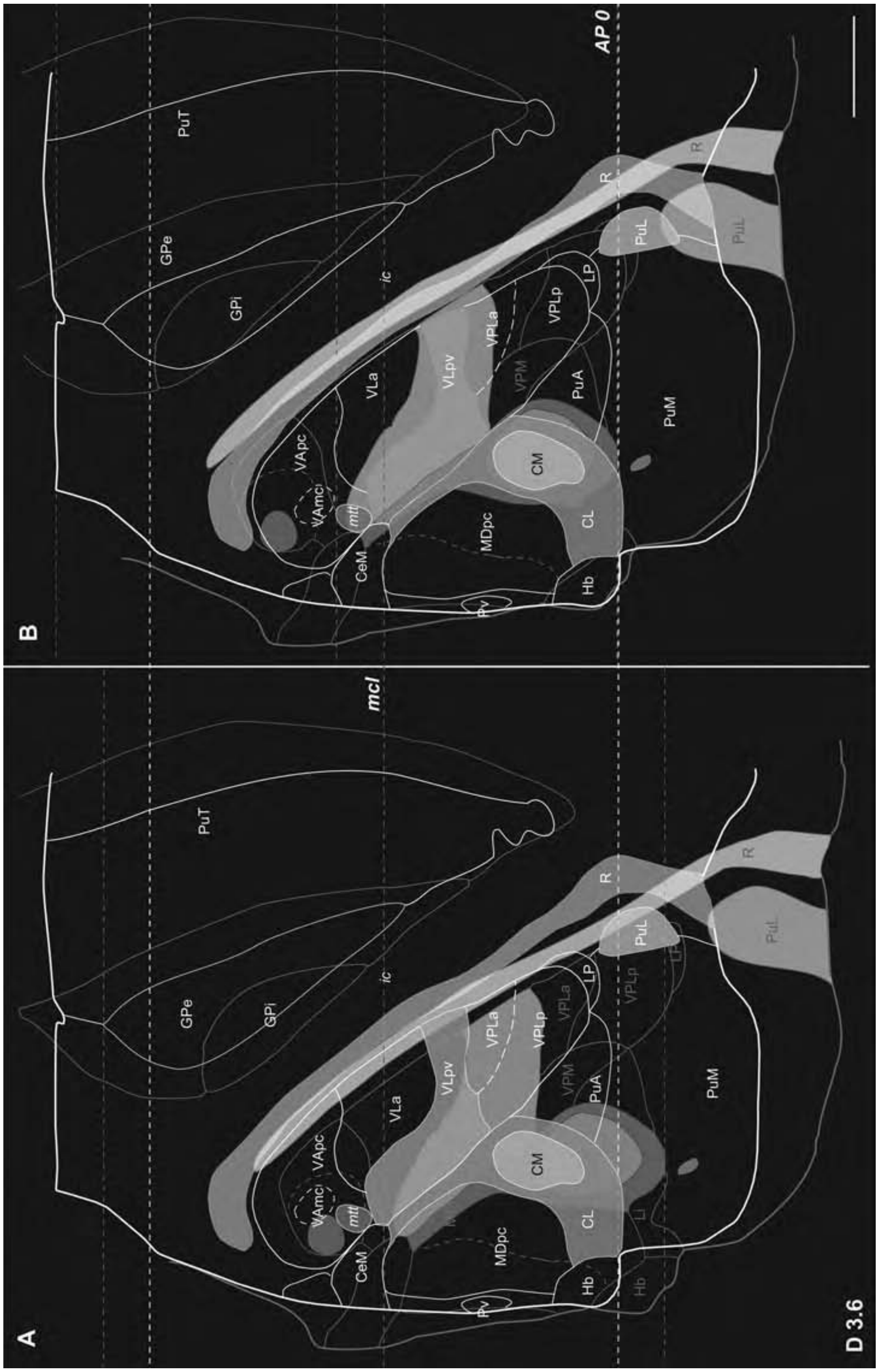

FIGURE 6.4 (***See color insert.***) Comparison of postero-inferior thalamus, subthalamic fiber tracts, STh and striato-pallidal subdivisions in horizontal sections of the brains illustrated in Figure 6.3 and 2 mm ventral to intercommissural plane. The maps are aligned on anteroposterior midcommissural (mcl) level in (**A**), posterior commissure level (AP 0) in (**B**), and anterior commissure (ac) level in (**C**). *Scale bar (**A**)*: 5 mm.

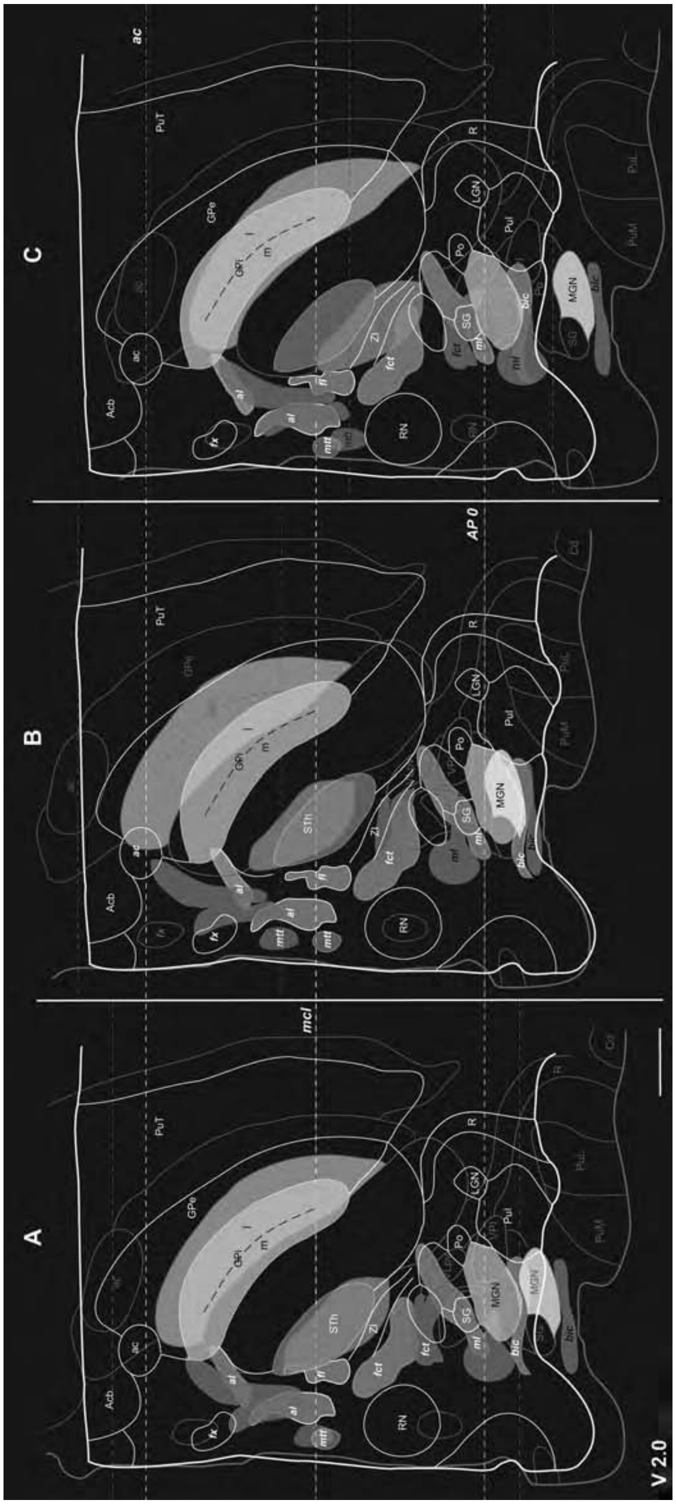

FIGURE 6.5 Measurements of thalamic dimensions "in vitro" (brain Hb1, *left panels*) and "in vivo" (T2-IR MRI, *right panels*). Distances from the pulvinar pole to pc, the thalamo-ventricular border to the internal capsule and from the ac–pc plane to dorsal thalamus are indicated in atlas sections and in MRIs. In horizontal and sagittal maps, interrupted lines indicate levels of the *pc*, *mcl*, and *ac* (*upper left panel*) and of the intercommissural plane (DV 0, *lower right panel*). *Scale bars:* 5 mm.

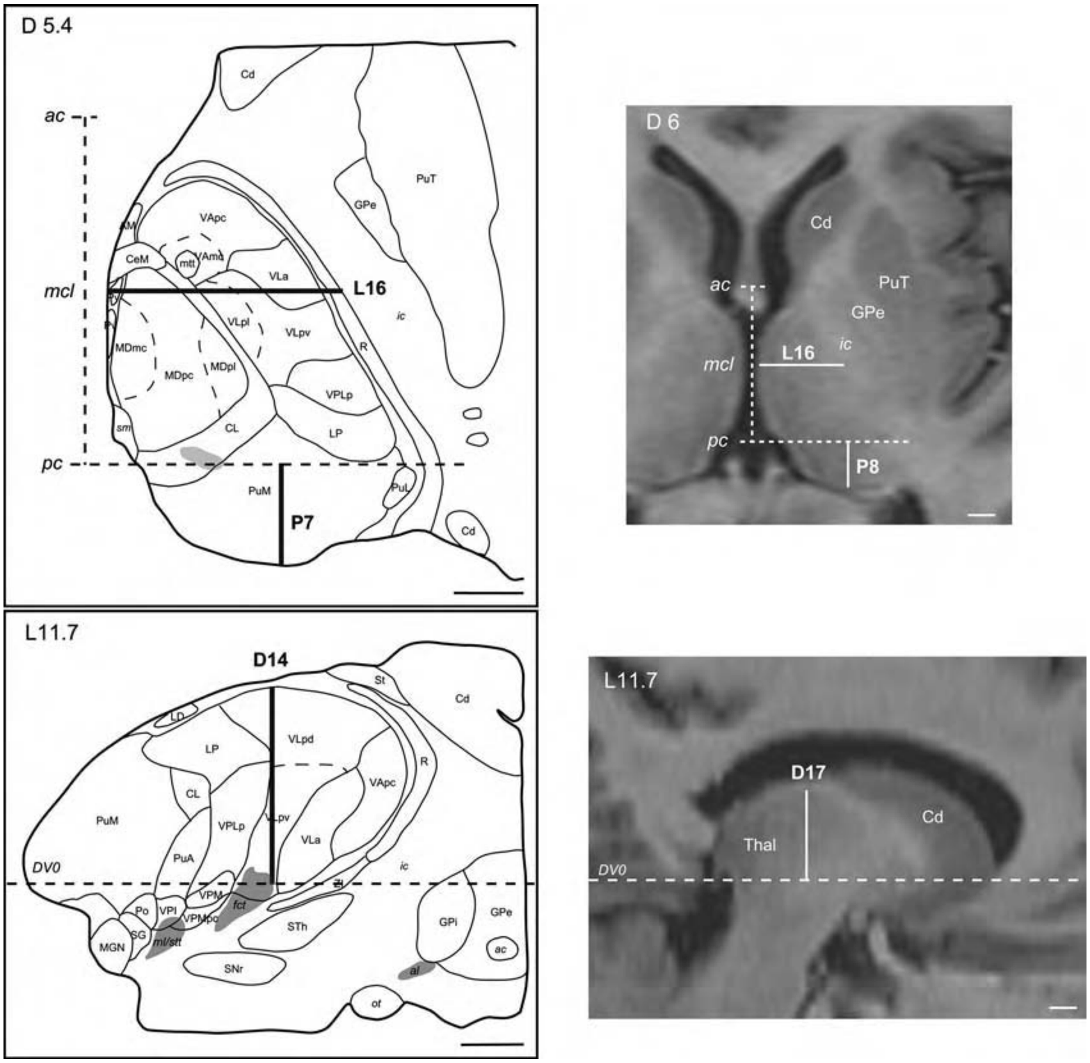

FIGURE 6.6 (***See color insert.***) Variability of subthalamic fiber tracts in the two different brains (Hb1 and Hb7) represented in Figure 6.2 and illustrated at sagittal levels 7.2 and 8.1 mm lateral to ventricular border (**A** and **B**, respectively). The electrode trajectories and positions of surgical lesions *CTT* (cerebellothalamic tractotomy) and *PTT* (pallidothalamic tractotomy) are represented by interrupted lines and open ovals. The myeloarchitecture at corresponding levels of case Hb 7 is illustrated by photomicrographs of sections adjacent to the graphical representations. The lower panels in (**C**) show the variation of the outlines of the STh at two sagittal levels [7.2 mm lateral to the thalamoventricular border (*open area*), and 0.9 mm more lateral (*filled green area*)], and in (**D**), the distribution of depth points where the dorsal limit of the STh nucleus was encountered electrophysiologically in the course of 35 penetrations in 20 patients. The depth variation of dorsal STh border between L7.2 and L8.1 is shown in green. *Scale bars (**A** and **C**)*: 2 mm.

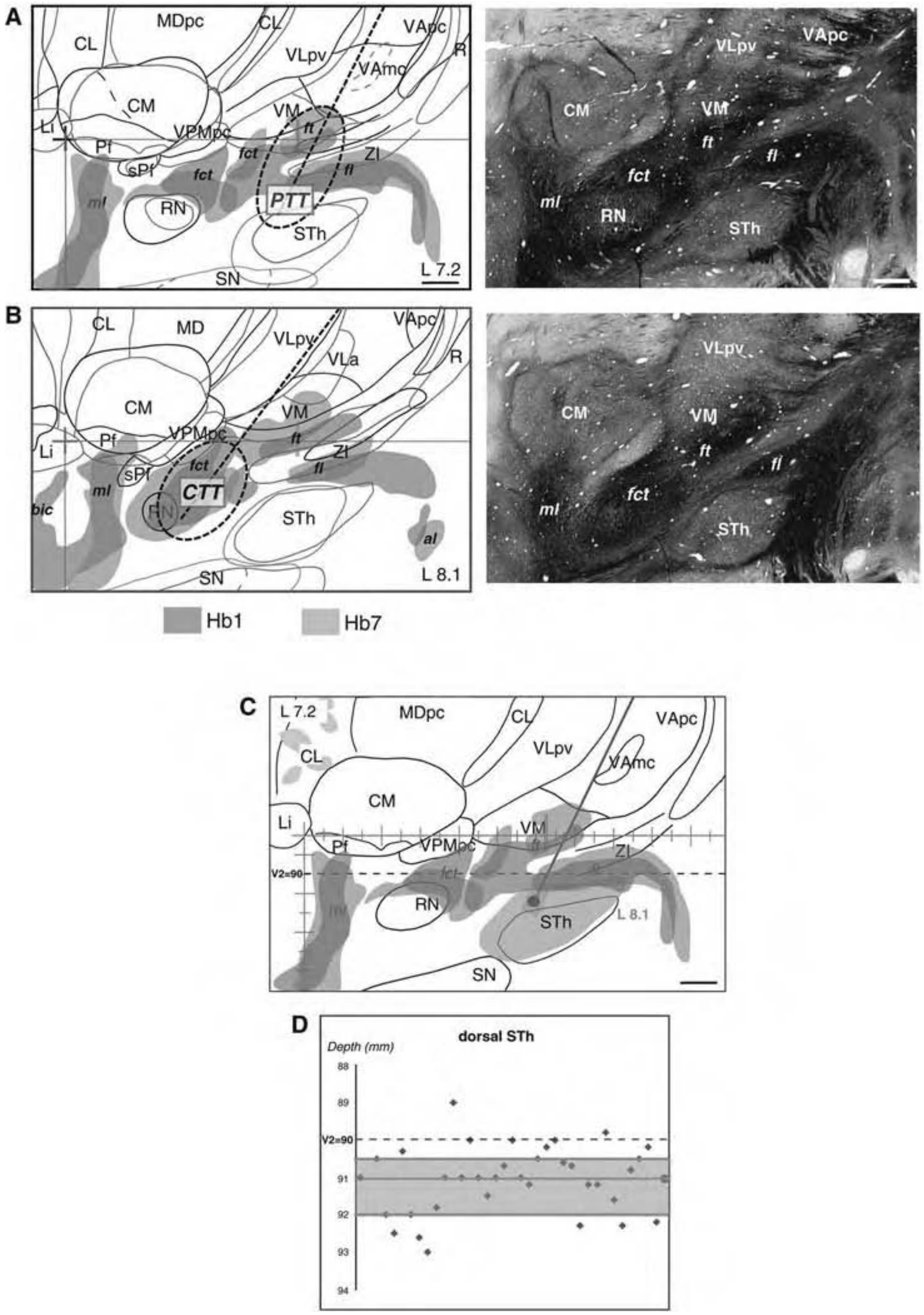

FIGURE 6.7 (***See color insert.***) *Upper panels*: Comparison of horizontal maps of subthalamic fiber tracts and striatopallidal compartments 2 mm ventral to the intercommissural plane from brains with same (**A** and **B**) or different (**C**) intercommissural distances (see Table 2.1). The sections are aligned according to midcommissural (*mcl*) point, which represents the reference anteroposterior level for *PTT*, *PMP* and *CTT* targets (lesions represented by filled grey or red circles). *Lower panels*: Horizontal maps from two brains with different intercommissural distances aligned on midcommissural (**D**), anterior commissure level (**E**) or adjusted (size reduced for Hb3 and enlarged for Hb6) to 26 mm intercommisural distance (**F**). *Scale bar (upper left panel)*: 5 mm.

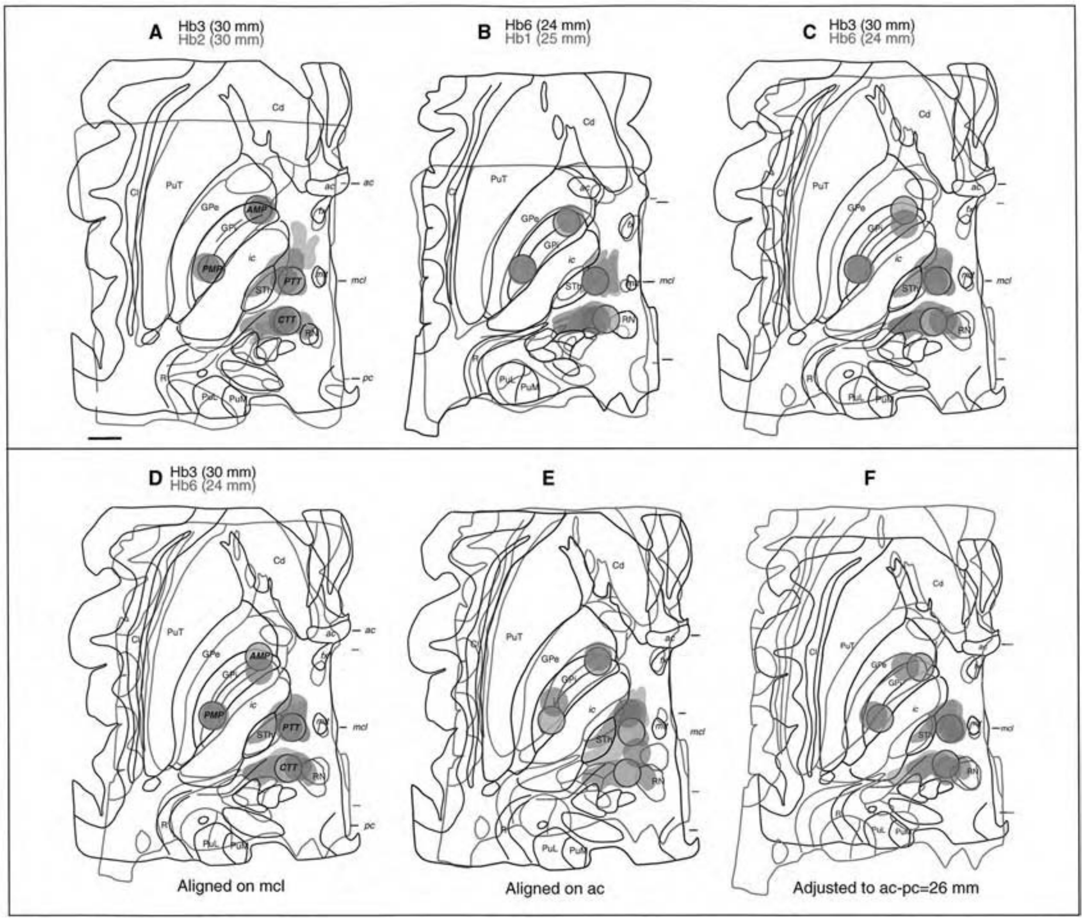

FIGURE 6.7

7 Atlas Applications

STEREOTACTIC FUNCTIONAL NEUROSURGERY

The primary application of this atlas is in the field of stereotactic functional surgery. From the start of our experience, it was clear that the most commonly used atlas of the human thalamus by Schaltenbrand and Wahren (26) was insufficient in terms of anatomical resolution and stereotactic precision to perform accurate and well-based stereotactic operations. Furthermore, a number of new staining procedures had been developed to reveal more details of the anatomy of both the thalamus and basal ganglia, in human as well as in nonhuman primates. This led to the development of our own atlas for the determination of surgical targets in several functional disorders, including Parkinson's disease, neurogenic pain, and neuropsychiatric disorders. A simplified diagram in **Figure 7.1** illustrates the principal surgical targets commonly used to treat patients with chronic, therapy-resistant motor disorders (essential tremor and Parkinson's disease), with either radiofrequency lesions (RFL) or high-frequency stimulations (HFS). We concentrate here on the targets that we have developed or updated from older surgical experiences, and refer to several publications from our group for the pathophysiological and clinical descriptions (13,17,109,131,139,140). The subthalamic nucleus target for the treatment of Parkinson's disease is also discussed below for its relation to the pallidothalamic tractotomy.

Our main surgical procedures are illustrated in **Figures 7.2** and **7.3**. In Parkinson's disease and essential tremor, the surgeries consist of small radiofrequency (RFL) lesions (3–4 mm diameter) selectively placed on the pallidothalamic or cerebellothalamic tracts (PTT and CTT, respectively; **Fig. 7.1**) at their entrance into the thalamus (109,131). Overlap of the RFL lesions with the fibers tracts (fct, fl, and ft) is illustrated in **Figure 7.2** where the lesions visualized on postoperative T1-weighted MRI are projected onto the atlas. The involvement of the pallido thalamic tract, at least of the fl in Forel field H2, is certainly significant for the clinical results obtained by dorsal subthalamotomy or chronic HFS at the dorsal border of the subthalamic nucleus, as recently reported by several groups (18,20,141–145). In neurogenic pain (**Fig. 7.3C–F**), RFLs are placed in the posterior part of the CL nucleus (CL thalamotomy, CLT) and the lesion extends 10 to 14 mm from the target to cover a large part of the nucleus (139,146). The lesion shown in **Figure 7.3A** and **B** is localized in the anterior part of the internal pallidum (AMP, for antero-medial pallidotomy), and alone or in combination with CLT represents the surgical intervention for the treatment of chronic, therapy-resistant neuropsychiatric disorders (140).

ELECTROPHYSIOLOGICAL MAPPING

As discussed in the previous chapter, the primary goal of peroperative physiological recordings is to assess target localization and eventually correct for possible brain shift and/or anatomical variability. A second goal is to better understand pathophysiological mechanisms underlying functional disorders [e.g., overactive GPi and STh in PD patients, overproduction of LTS bursts and local field potentials (LFP) low frequencies in the thalamus of patients suffering from different functional disorders (13,17,147–150)]. Our comprehension of these mechanisms, grounded in early experimental studies (151) and termed thalamocortical dysrhythmia (152), has also greatly benefited from pre- and postoperative analyses of surface electroencephalograms (EEG) (148,149) and magnetoencephalograms (MEG) (153,154). It is important to localize intraoperative subcortical recordings as accurately as possible. The possibility of identifying RFL lesions in MRIs (**Figs. 7.2** and **7.3**) and to reconstruct from there the position of recording or stimulation points provides more accurate localization than often possible with DBS stimulating electrodes and their problems of artifacts. The effects of macrostimulations were also analysed in different groups of patients, and in the lateral and medial thalamic nuclei (**Fig. 7.4**). The dominance of somatosensory responses in neurogenic pain patients, of motor effects in parkinsonian patients, and of limbic responses among a neuropsychiatric group in the same thalamic region provides evidence for significant plastic changes occurring during the evolution of the disease.

FUNCTIONAL NEUROIMAGING

The recent advances in brain imaging techniques have increased significantly the possibilities to explore in vivo morphological and functional aspects of the human brain, in normal and pathological conditions. Nevertheless, the proper identification of regions of interest still depends on the use of fine-grained histological atlases (23,24,155). For example, interpretations of clinical consequences after vascular insults limited to the thalamus were possible after integrating the atlas (21,22).The application of high-resolution MRI to directly visualize finer morphological features, such as thalamic nuclei, fiber tracts, cortical layers is still limited to postmortem brains (156,157; see also Figs. 5.5–5.6) and not to patients undergoing stereotactic functional neurosurgery.

3D ATLAS MODEL

The scope of computerized atlases has greatly expanded, from postmortem brain atlases for neuronavigation systems, to “in vivo” probabilistic atlases (e.g., 158–160). The former are based on one or two brains only but benefit from high anatomical resolution; the latter involve analyses of large numbers of brains from living subjects to take into account interindividual variability, but are limited in anatomical precision. Digitalization of the atlas of the human thalamus (47) provided an internally consistent 3D model and its coregistration with MRI for neuronavigation (62). Illustration of the model and example of “on line” visualization of the electrode trajectory in CL are given in **Figure 7.5**. The goal now is to amass data from additional postmortem brains to computerize a 3D statistical atlas and evaluate quantitatively interindividual anatomical variability.

FIGURE 7.1 (***See color insert.***) Simplified diagram of the cortico-basal ganglia/cerebello-thalamo-cortical networks and most frequently used surgical targets to treat patients with Parkinson's disease and essential tremor. Surgeries consist of either therapeutic radiofrequency lesions or high frequency stimulations (HFS). Both procedures target the same structures (e.g., VL-thalamotomy or HFS), except for the pallidothalamic tract which is not per se targeted by neurosurgeons using HFS.

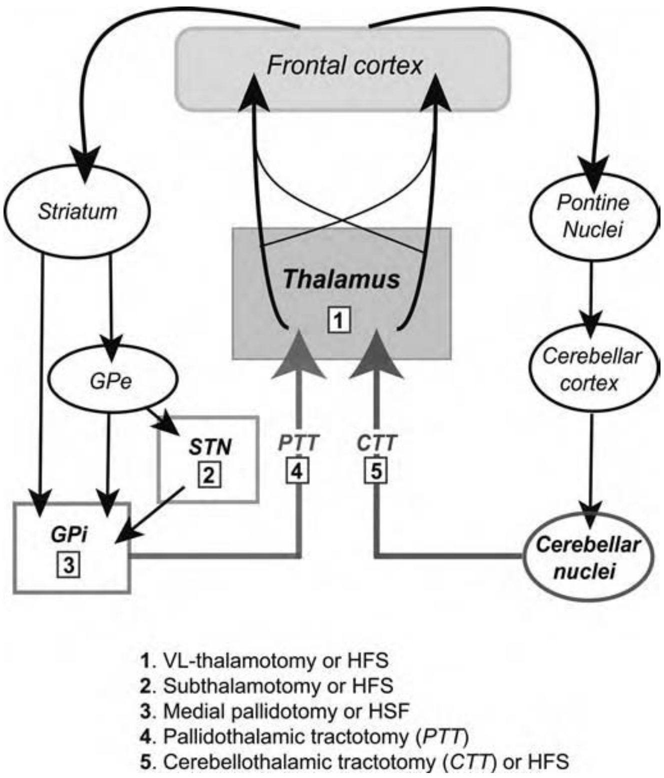

FIGURE 7.2 Sagittal atlas projection of a *PTT* lesion (**B**) as reconstructed from two-days postoperative sagittal T1-weighted MRI (**A**). The same *PTT* lesion and a *CTT* lesion in a patient with essential tremor are shown on a horizontal postoperative MRI 2 mm ventral to the intercommissural plane (**C** and **D**) and projected onto the atlas in (**E**). The edemas seen in MRI are not included in the graphic reconstructions.The pallidothalamic (*fl* and *ft*), cerebellothalamic (*fct*), and medial lemniscus (*ml*) are represented in light grey areas in (**B**) and (**E)**. *Scale bars*: 5 mm (**A,C,D**) and 2 mm (**B** and **E**).

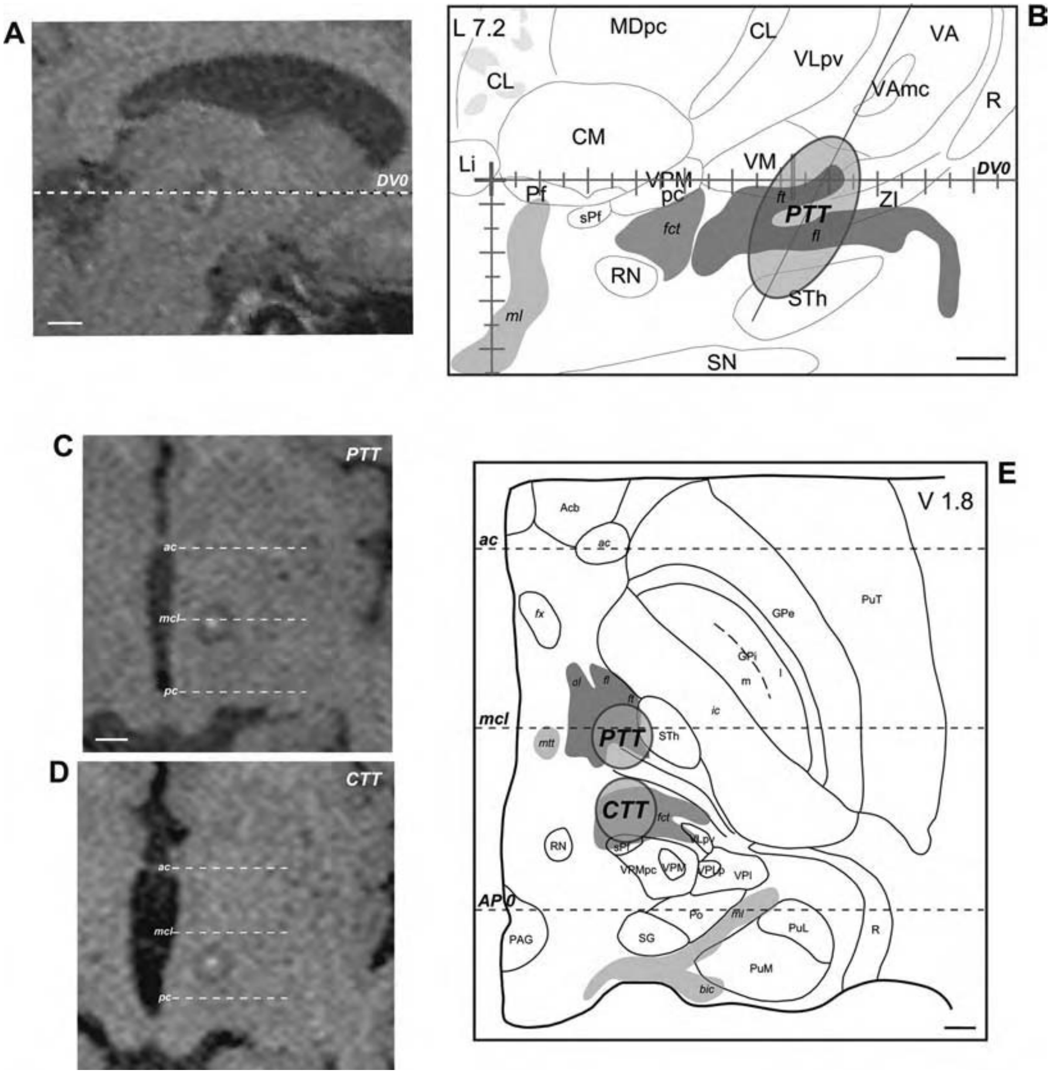

FIGURE 7.3 Postoperative T1-weighted MRI (**A,C,E**) and atlas projections (**B,D,F**) of therapeutic RFL lesions centred in the anteromedial pallidum (AMP) and posterior part of the central lateral nucleus (CLT). The CLT is represented on sagittal (**C** and **D**) and horizontal (**E–F**) planes to show the overlap with the posterior, enlarged part of the CL characterized by dense cellular clusters (small light grey areas). The same conventions for fiber tracts were used as in Figure 7.2. *Scale bars*: 5 mm (**A,C,E**), and 2 mm (**B,D,F**).

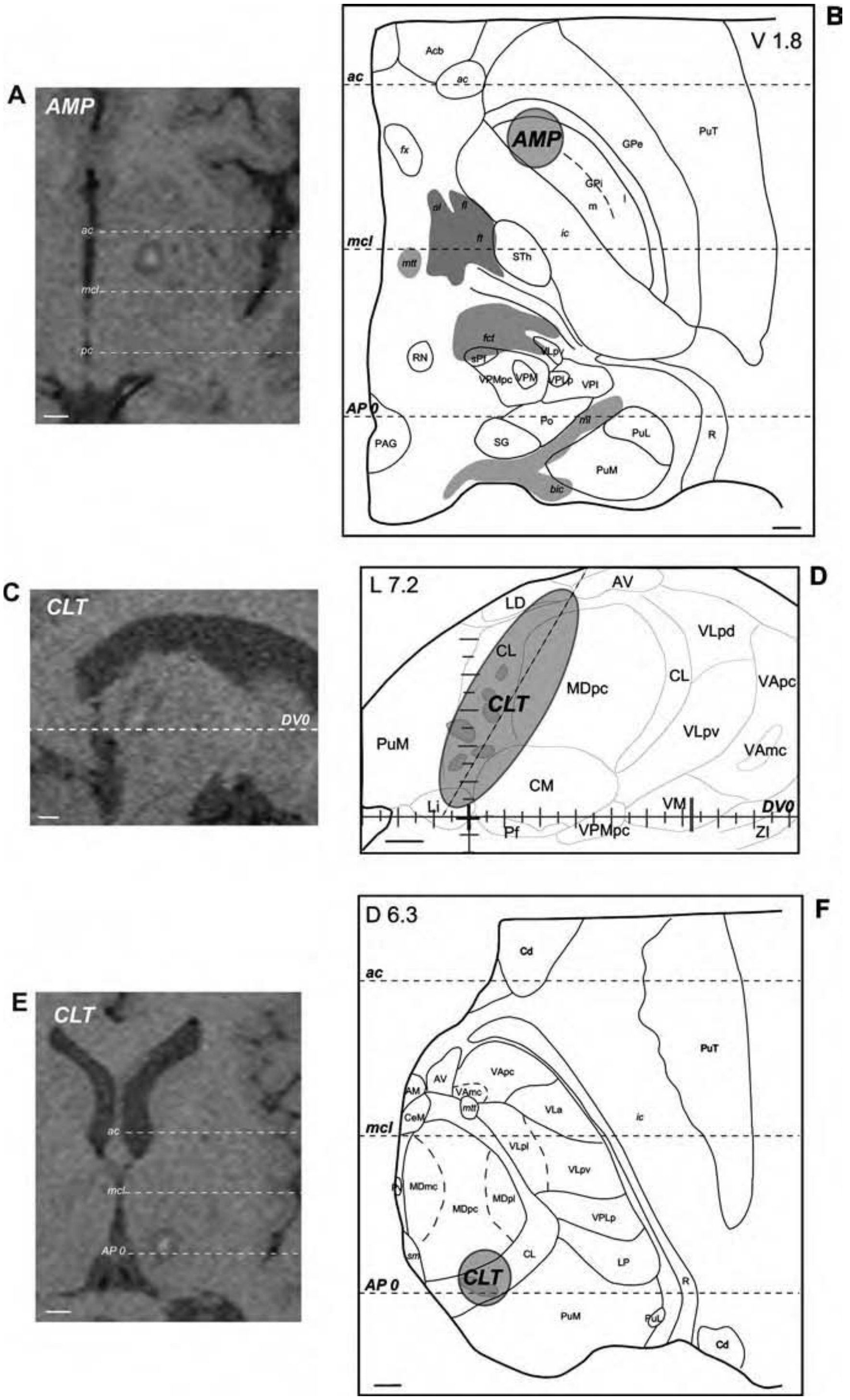

FIGURE 7.4 (***See color insert.***) Sagittal atlas projections of *CLT* and *PTT* lesions (**A** and **B**) and projections of response modalities to intraoperative thalamic stimulations in four neurogenic pain (NP), five parkinsonian (PD), and four neuropsychiatric (Npsy) patients obtained between sagittal levels L7 and L8 (**C**–**E**). Symbols correspond to different patients and color indicates somatosensory (*red*), motor (*green*), limbic (*blue*), or bimodal (e.g., *red/green*) responses. *Scale bars*: 2 mm (A and C).

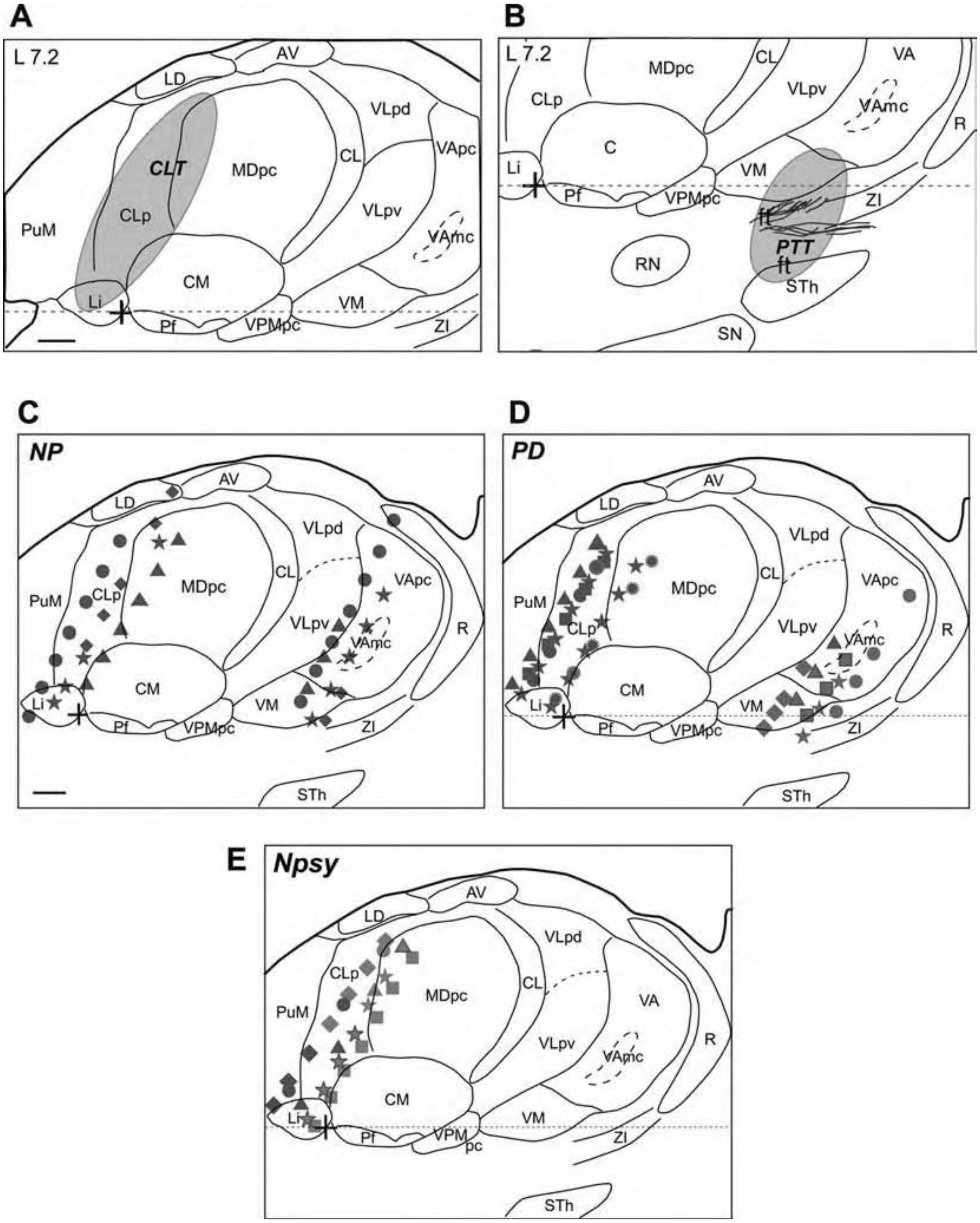

FIGURE 7.5 (***See color insert.***) (**A**) Three-dimensional model of the human thalamus with representation of two sections parallel to electrode penetrations aiming at CLT and PTT, respectively, and crossing the posterior part of CL (CLp) and the motor nuclei VA, VLA, and VM. Left is posterior. The anterior section is also represented in (**C**) with projections of 1 mm distant parallel electrode trajectories aiming at PTT. (**B**) 3D to 2D projection of the CLT trajectory onto a horizontal IR-MRI slice dorsal to the target. The large arrow points to the region of the CL nucleus (*yellow contour*) pierced by the electrode. *Source*: Adapted from Ref. 62.

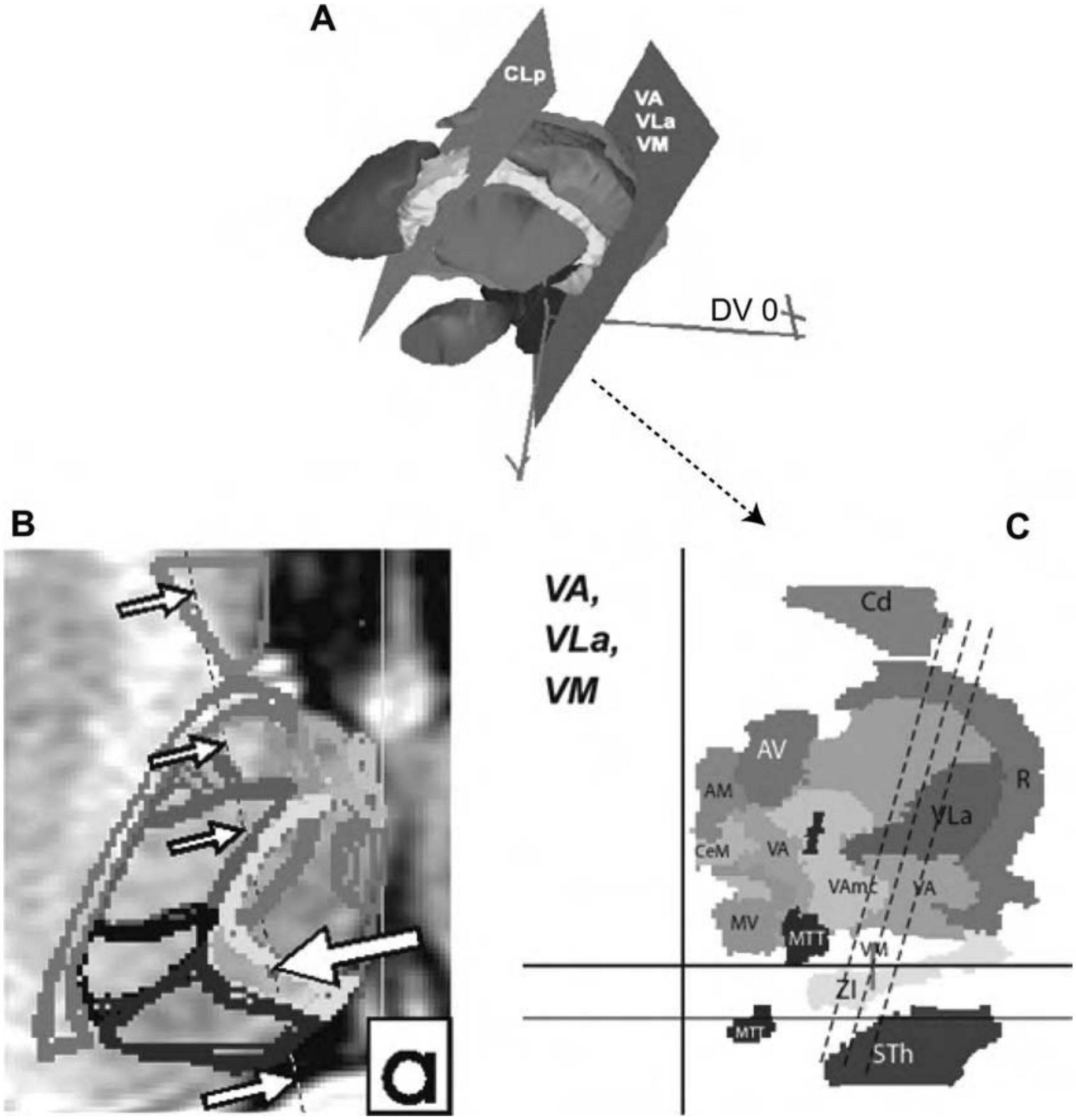

References

1. Patel NK, Plaha P, O'Sullivan K, McCarter R, Heywood P, Gill SS. MRI directed bilateral stimulation of the subthalamic nucleus in patients with Parkinson's disease. J Neurol Neurosurg Psychiatry 2003; 74(12):1631–1637.
2. Richter EO, Hoque T, Halliday W, Lozano AM, Saint-Cyr JA. Determining the position and size of the subthalamic nucleus based on magnetic resonance imaging results in patients with advanced Parkinson disease. J Neurosurg 2004; 100(3):541–546.
3. Holtzheimer PE, III, Roberts DW, Darcey TM. Magnetic resonance imaging versus computed tomography for target localization in functional stereotactic neurosurgery. Neurosurgery 1999; 45(2):290–297; discussion 7–8.
4. Starr PA, Vitek JL, DeLong M, Bakay RA. Magnetic resonance imaging-based stereotactic localization of the globus pallidus and subthalamic nucleus. Neurosurgery 1999; 44(2):303–313; discussion 13-4.
5. Spinks R, Magnotta VA, Andreasen NC, et al. Manual and automated measurement of the whole thalamus and mediodorsal nucleus using magnetic resonance imaging. Neuroimage 2002; 17(2):631–642.
6. Kemether EM, Buchsbaum MS, Byne W, et al. Magnetic resonance imaging of mediodorsal, pulvinar, and centromedian nuclei of the thalamus in patients with schizophrenia. Arch Gen Psychiatry 2003; 60(10):983–991.
7. Hazlett EA, Buchsbaum MS, Byne W, et al. Three-dimensional analysis with MRI and PET of the size, shape, and function of the thalamus in the schizophrenia spectrum. Am J Psychiatry 1999; 156(8):1190–1199.
8. Ohye C, Shibazaki T, Sato S. Gamma knife thalamotomy for movement disorders: evaluation of the thalamic lesion and clinical results. J Neurosurg 2005;102 (suppl):234–240.
9. Keep MF, Mastrofrancesco L, Erdman D, Murphy B, Ashby LS. Gamma knife subthalamotomy for Parkinson disease: the subthalamic nucleus as a new radiosurgical target. Case report. J Neurosurg 2002; 97(suppl 5):592–599.
10. Friedman DP, Goldman HW, Flanders AE, Gollomp SM, Curran WJ Jr. Stereotactic radiosurgical pallidotomy and thalamotomy with the gamma knife: MR imaging findings with clinical correlation—preliminary experience. Radiology 1999; 212(1):143–150.
11. Young RF. Gamma knife radiosurgery as an alternative form of therapy for movement disorders. Arch Neurol 2002; 59(10):1660–1662; author reply 2–4.
12. Hutchison WD, Lozano AM, Davis KD, Saint-Cyr JA, Lang AE, Dostrovsky JO. Differential neuronal activity in segments of globus pallidus in Parkinson's disease patients. Neuroreport 1994; 5(12):1533–1537.
13. Jeanmonod D, Magnin M, Morel A. Low-threshold calcium spike bursts in the human thalamus. Common physiopathology for sensory, motor and limbic positive symptoms. Brain 1996; 119(Pt 2): 363–375.
14. Lenz FA, Dougherty PM. Neurons in the human thalamic somatosensory nucleus (Ventralis caudalis) respond to innocuous cool and mechanical stimuli. J Neurophysiol 1998; 79(4):2227–2230.
15. Lenz FA, Gracely RH, Baker FH, Richardson RT, Dougherty PM. Reorganization of sensory modalities evoked by microstimulation in region of the thalamic principal sensory nucleus in patients with pain due to nervous system injury. J Comp Neurol 1998; 399(1):125–138.
16. Lozano AM, Hutchison WD. Microelectrode recordings in the pallidum. Mov Disord 2002; 17(suppl 3): S150-S154.
17. Magnin M, Morel A, Jeanmonod D. Single-unit analysis of the pallidum, thalamus and subthalamic nucleus in parkinsonian patients. Neuroscience 2000; 96(3):549–564.
18. Breit S, LeBas JF, Koudsie A, et al. Pretargeting for the implantation of stimulation electrodes into the subthalamic nucleus: a comparative study of magnetic resonance imaging and ventriculography. Neurosurgery 2006; 58(suppl 1):ONS83–ONS95.
19. Gross RE, Lombardi WJ, Lang AE, et al. Relationship of lesion location to clinical outcome following microelectrode-guided pallidotomy for Parkinson's disease. Brain 1999; 122(Pt 3):405–416.
20. Zonenshayn M, Sterio D, Kelly PJ, Rezai AR, Beric A. Location of the active contact within the subthalamic nucleus (STN) in the treatment of idiopathic Parkinson's disease. Surg Neurol 2004; 62(3):216–225; discussion 25–26.

21. Van der Werf YD, Scheltens P, Lindeboom J, Witter MP, Uylings HB, Jolles J. Deficits of memory, executive functioning and attention following infarction in the thalamus; a study of 22 cases with localised lesions. Neuropsychologia 2003; 41(10):1330–1344.
22. Montes C, Magnin M, Maarrawi J, et al. Thalamic thermo-algesic transmission: ventral posterior (VP) complex versus VMpo in the light of a thalamic infarct with central pain. Pain 2005; 113(1–2):223–232.
23. Behrens TE, Johansen-Berg H, Woolrich MW, et al. Non-invasive mapping of connections between human thalamus and cortex using diffusion imaging. Nat Neurosci 2003; 6(7):750–757.
24. Wiegell MR, Tuch DS, Larsson HB, Wedeen VJ. Automatic segmentation of thalamic nuclei from diffusion tensor magnetic resonance imaging. Neuroimage 2003; 19(2 pt 1):391–401.
25. Schaltenbrand G, Bailey P. Introduction to Stereotaxis with an Atlas of the Human Brain. Stuttgart: Thieme, 1959.
26. Schaltenbrand G, Wahren W. Atlas for Stereotaxy of the Human Brain. Stuttgart: Thieme, 1977.
27. Dewulf A. Anatomy of the Normal Human Thalamus: Topometry and Standardized Nomenclature. Amsterdam-London-New York: Elsevier, 1971.
28. Van Buren JM, Maccubbin DA. An outline atlas of the human basal ganglia with estimation of anatomical variants. J Neurosurg 1962; 19:811–839.
29. Percheron G. Thalamus. In: Paxinos G, Mai JK, eds. The Human Nervous System. 2nd ed. San Diego: Elsevier Academic Press, 2004:592–675.
30. Hassler R. Architectonic organization of the thalamic nuclei. In: Schaltenbrand G, Walker AE, eds. Stereotaxy of the Human Brain Anatomical, Physiological and Clinical Applications. Stuttgart: G. Thieme, 1982:140–180.
31. Niemann K, Naujokat C, Pohl G, Wollner C, von Keyserlingk D. Verification of the Schaltenbrand and Wahren stereotactic atlas. Acta Neurochir (Wien) 1994:129(1-2):72–81.
32. Mai JK, Assheuer J, Paxinos G. Atlas of the Human Brain. 2nd ed. San Diego: Elsevier Academic Press, 2004.
33. Calzavara R, Zappala A, Rozzi S, Matelli M, Luppino G. Neurochemical characterization of the cerebellar-recipient motor thalamic territory in the macaque monkey. Eur J Neurosci 2005; 21(7):1869–1894.
34. Cavada C, Company T, Hernandez-Gonzalez A, Reinoso-Suarez F. Acetylcholinesterase histochemistry in the macaque thalamus reveals territories selectively connected to frontal, parietal and temporal association cortices. J Chem Neuroanat 1995; 8(4):245–257.
35. Cote PY, Sadikot AF, Parent A. Complementary distribution of calbindin D-28k and parvalbumin in the basal forebrain and midbrain of the squirrel monkey. Eur J Neurosci 1991; 3(12):1316–1329.
36. Craig AD, Zhang ET, Blomqvist A. Association of spinothalamic lamina I neurons and their ascending axons with calbindin-immunoreactivity in monkey and human. Pain 2002; 97(1–2):105–115.
37. Jones EG, Hendry SH. Differential calcium binding protein immunoreactivity distinguishes classes of relay neurons in monkey thalamic nuclei. Eur J Neurosci 1989;1(3):222–246.
38. Karachi C, Francois C, Parain K, et al. Three-dimensional cartography of functional territories in the human striatopallidal complex by using calbindin immunoreactivity. J Comp Neurol 2002; 450(2):122–134.
39. Meredith GE, Pattiselanno A, Groenewegen HJ, Haber SN. Shell and core in monkey and human nucleus accumbens identified with antibodies to calbindin-D28k. J Comp Neurol 1996; 365(4): 628–639.
40. Molinari M, Dell'Anna ME, Rausell E, Leggio MG, Hashikawa T, Jones EG. Auditory thalamocortical pathways defined in monkeys by calcium-binding protein immunoreactivity. J Comp Neurol 1995; 362(2):171–194.
41. Parent A, Cote PY, Lavoie B. Chemical anatomy of primate basal ganglia. Prog Neurobiol 1995; 46(2–3):131–197.
42. Parent A, Fortin M, Cote PY, Cicchetti F. Calcium-binding proteins in primate basal ganglia. Neurosci Res 1996; 25(4):309–334.
43. Rausell E, Bae CS, Vinuela A, Huntley GW, Jones EG. Calbindin and parvalbumin cells in monkey VPL thalamic nucleus: distribution, laminar cortical projections, and relations to spinothalamic terminations. J Neurosci 1992; 12(10):4088–4111.
44. Jones EG. Correlation and revised nomenclature of ventral nuclei in the thalamus of human and monkey. Stereotact Funct Neurosurg 1990; 54–55:1–20.
45. Macchi G, Jones EG. Toward an agreement on terminology of nuclear and subnuclear divisions of the motor thalamus. J Neurosurg 1997; 86(4):670–685.
46. Hirai T, Jones EG. A new parcellation of the human thalamus on the basis of histochemical staining. Brain Res Brain Res Rev 1989; 14(1):1–34.
47. Morel A, Magnin M, Jeanmonod D. Multiarchitectonic and stereotactic atlas of the human thalamus. J Comp Neurol 1997; 387(4):588–630.
48. Morel A, Loup F, Magnin M, Jeanmonod D. Neurochemical organization of the human basal ganglia: anatomofunctional territories defined by the distributions of calcium-binding proteins and SMI-32. J Comp Neurol 2002; 443(1):86–103.

49. Talairach J, Tournoux P. Co-planar Stereotactic Atlas of the Human Brain. 3-D proportioned system: an approach to cerebral imaging. Stuttgart: G. Thieme, 1988.
50. Burgel U, Mecklenburg I, Blohm U, Zilles K. Histological visualization of long fiber tracts in the white matter of adult human brains. J Hirnforsch 1997; 38(3):397–404.
51. Hutchins B, Weber JT. A rapid myelin stain for frozen sections: modification of the Heidenhain procedure. J Neurosci Methods 1983; 7(3):289–294.
52. Koelle GB, Friedenwald JS. A histochemical method for localizing cholinesterase activity. Proc Soc Exp Biol Med 1949; 70:617–622.
53. Mesulam MM, Geula C. Chemoarchitectonics of axonal and perikaryal acetylcholinesterase along information processing systems of the human cerebral cortex. Brain Res Bull 1994; 33(2):137–153.
54. Evers P, Uylings HB. Effects of microwave pretreatment on immunocytochemical staining of vibratome sections and tissue blocks of human cerebral cortex stored in formaldehyde fixative for long periods. J Neurosci Methods 1994; 55(2):163–172.
55. Walker AE. The Primate Thalamus. Chicago: Chicago Press, 1938.
56. Papez J, Stotler, W. Connections of the red nucleus. AMA Arch Neurol Psychiat 1940; 44:776–791.
57. Ranson S, Ranson, M. Pallidofugal fibers in the monkey. AMA Arch Neurol Psychiat 1939; 42:1059–1067.
58. Alheid GF, Heimer L, Switzer RC. Basal ganglia. In: Paxinos G, ed. The Human Nervous System. New York: Academic Press, 1990:483–582.
59. Heimer L. A new anatomical framework for neuropsychiatric disorders and drug abuse. Am J Psychiatry 2003; 160(10):1726–1739.
60. Parent A, Hazrati LN. Functional anatomy of the basal ganglia. I. The cortico-basal ganglia-thalamo-cortical loop. Brain Res Brain Res Rev 1995; 20(1):91–127.
61. Parent A, Hazrati LN. Functional anatomy of the basal ganglia. II. The place of subthalamic nucleus and external pallidum in basal ganglia circuitry. Brain Res Brain Res Rev 1995; 20(1):128–154.
62. Niemann K, Mennicken VR, Jeanmonod D, Morel A. The Morel stereotactic atlas of the human thalamus: atlas-to-MR registration of internally consistent canonical model. Neuroimage 2000; 12(6):601–616.
63. Jones EG. A description of the human thalamus. In: Steriade M, Jones EG, McCormick DA, eds. Thalamus. Oxford: Elsevier, 1997:425–499.
64. Munkle MC, Waldvogel HJ, Faull RL. Calcium-binding protein immunoreactivity delineates the intralaminar nuclei of the thalamus in the human brain. Neuroscience 1999; 90(2):485–491.
65. Munkle MC, Waldvogel HJ, Faull RL. The distribution of calbindin, calretinin and parvalbumin immunoreactivity in the human thalamus. J Chem Neuroanat 2000; 19(3):155–173.
66. Fortin M, Asselin MC, Gould PV, Parent A. Calretinin-immunoreactive neurons in the human thalamus. Neuroscience 1998; 84(2):537–548.
67. Hirai T, Jones EG. Distribution of tachykinin- and enkephalin-immunoreactive fibers in the human thalamus. Brain Res Brain Res Rev 1989; 14(1):35–52.
68. Stepniewska I, Preuss TM, Kaas JH. Architectonic subdivisions of the motor thalamus of owl monkeys: Nissl, acetylcholinesterase, and cytochrome oxidase patterns. J Comp Neurol 1994; 349(4):536–557.
69. Graziano A, Jones EG. Widespread thalamic terminations of fibers arising in the superficial medullary dorsal horn of monkeys and their relation to calbindin immunoreactivity. J Neurosci 2004; 24(1):248–256.
70. Rausell E, Jones EG. Chemically distinct compartments of the thalamic VPM nucleus in monkeys relay principal and spinal trigeminal pathways to different layers of the somatosensory cortex. J Neurosci 1991; 11(1):226–237.
71. Jones EG. A pain in the thalamus. J Pain 2002; 3(2):102–104; discussion 13–14.
72. Blomqvist A, Zhang ET, Craig AD. Cytoarchitectonic and immunohistochemical characterization of a specific pain and temperature relay, the posterior portion of the ventral medial nucleus, in the human thalamus. Brain 2000;123(Pt 3):601–619.
73. Craig AD, Bushnell MC, Zhang ET, Blomqvist A. A thalamic nucleus specific for pain and temperature sensation. Nature 1994; 372(6508):770–773.
74. Mehler WR. The posterior thalamic region in man. Confin Neurol 1966; 27(1):18–29.
75. Mehler WR. Central pain and the spinothalamic tract. Adv Neurol 1974; 4:127–145.
76. Jones EG. A new view of specific and nonspecific thalamocortical connections. Adv Neurol 1998; 77:49–71; discussion 2–3.
77. Jones EG. Viewpoint: the core and matrix of thalamic organization. Neuroscience 1998; 85(2):331–345.
78. Jones EG. Chemically defined parallel pathways in the monkey auditory system. Ann NY Acad Sci 2003; 999:218–233.
79. Hashikawa T, Rausell E, Molinari M, Jones EG. Parvalbumin- and calbindin-containing neurons in the monkey medial geniculate complex: differential distribution and cortical layer specific projections. Brain Res 1991; 544(2):335–341.

80. Hackett TA, Stepniewska I, Kaas JH. Thalamocortical connections of the parabelt auditory cortex in macaque monkeys. J Comp Neurol 1998; 400(2):271–286.
81. Morel A, Garraghty PE, Kaas JH. Tonotopic organization, architectonic fields, and connections of auditory cortex in macaque monkeys. J Comp Neurol 1993; 335(3):437–459.
82. Leuba G, Saini K. Calcium-binding proteins immunoreactivity in the human subcortical and cortical visual structures. Vis Neurosci 1996; 13(6):997–1009.
83. Percheron G, Francois C, Talbi B, Yelnik J, Fenelon G. The primate motor thalamus. Brain Res Brain Res Rev 1996; 22(2):93–181.
84. Morel A, Liu J, Wannier T, Jeanmonod D, Rouiller EM. Divergence and convergence of thalamocortical projections to premotor and supplementary motor cortex: a multiple tracing study in the macaque monkey. Eur J Neurosci 2005; 21(4):1007–1029.
85. Sidibe M, Bevan MD, Bolam JP, Smith Y. Efferent connections of the internal globus pallidus in the squirrel monkey: I. Topography and synaptic organization of the pallidothalamic projection. J Comp Neurol 1997; 382(3):323–347.
86. Sidibe M, Pare JF, Smith Y. Nigral and pallidal inputs to functionally segregated thalamostriatal neurons in the centromedian/parafascicular intralaminar nuclear complex in monkey. J Comp Neurol 2002; 447(3):286–299.
87. Alheid GF. Extended amygdala and basal forebrain. Ann NY Acad Sci 2003; 985:185–205.
88. DeLong MR. Primate models of movement disorders of basal ganglia origin. Trends Neurosci 1990; 13(7):281–285.
89. Garcia-Rill E. The pedunculopontine nucleus. Prog Neurobiol 1991; 36(5):363–389.
90. Haber SN. The primate basal ganglia: parallel and integrative networks. J Chem Neuroanat 2003; 26(4):317–330.
91. Heimer L, Van Hoesen GW. The limbic lobe and its output channels: implications for emotional functions and adaptive behavior. Neurosci Biobehav Rev 2006; 30(2):126–147.
92. Holt DJ, Graybiel AM, Saper CB. Neurochemical architecture of the human striatum. J Comp Neurol 1997; 384(1):1–25.
93. McFarland NR, Haber SN. Thalamic relay nuclei of the basal ganglia form both reciprocal and nonreciprocal cortical connections, linking multiple frontal cortical areas. J Neurosci 2002; 22(18):8117–8132.
94. Nauta WJ, Mehler WR. Projections of the lentiform nucleus in the monkey. Brain Res 1966; 1(1):3–42.
95. Obeso JA, Rodriguez-Oroz MC, Rodriguez M, et al. Pathophysiology of the basal ganglia in Parkinson's disease. Trends Neurosci 2000; 23(suppl 10):S8–S19.
96. Wichmann T, DeLong MR. Models of basal ganglia function and pathophysiology of movement disorders. Neurosurg Clin N Am 1998; 9(2):223–236.
97. de Olmos JS, Heimer L. The concepts of the ventral striatopallidal system and extended amygdala. Ann NY Acad Sci 1999; 877:1–32.
98. Shink E, Sidibe M, Smith Y. Efferent connections of the internal globus pallidus in the squirrel monkey: II. Topography and synaptic organization of pallidal efferents to the pedunculopontine nucleus. J Comp Neurol 1997; 382(3):348–363.
99. Pahapill PA, Lozano AM. The pedunculopontine nucleus and Parkinson's disease. Brain 2000; 123(Pt 9):1767–1783.
100. Lavoie B, Parent A. Pedunculopontine nucleus in the squirrel monkey: distribution of cholinergic and monoaminergic neurons in the mesopontine tegmentum with evidence for the presence of glutamate in cholinergic neurons. J Comp Neurol 1994; 344(2):190–209.
101. Haber SN, Kunishio K, Mizobuchi M, Lynd-Balta E. The orbital and medial prefrontal circuit through the primate basal ganglia. J Neurosci 1995; 15(7 Pt 1):4851–4867.
102. Haber SN, McFarland NR. The concept of the ventral striatum in nonhuman primates. Ann NY Acad Sci 1999; 877:33–48.
103. Heimer L. Basal forebrain in the context of schizophrenia. Brain Res Brain Res Rev 2000; 31(2–3):205–235.
104. Heimer L, Alheid GF, de Olmos JS, et al. The accumbens: beyond the core-shell dichotomy. J Neuropsychiatry Clin Neurosci 1997; 9(3):354–381.
105. Damier P, Hirsch EC, Agid Y, Graybiel AM. The substantia nigra of the human brain. I. Nigrosomes and the nigral matrix, a compartmental organization based on calbindin D(28K) immunohistochemistry. Brain 1999; 122(Pt 8):1421–1436.
106. Fortin M, Parent A. Calretinin as a marker of specific neuronal subsets in primate substantia nigra and subthalamic nucleus. Brain Res 1996; 708(1–2):201–204.
107. McRitchie DA, Halliday GM. Calbindin D28k-containing neurons are restricted to the medial substantia nigra in humans. Neuroscience 1995; 65(1):87–91.
108. McRitchie DA, Hardman CD, Halliday GM. Cytoarchitectural distribution of calcium binding proteins in midbrain dopaminergic regions of rats and humans. J Comp Neurol 1996; 364(1):121–150.
109. Magnin M, Jeanmonod D, Morel A, Siegemund M. Surgical control of the human thalamocortical dysrhythmia: II. Pallidothalamic tractotomy in Parkinson's disease. Thalamus and Related Systems 2001; 1:81–89.

110. Velasco F, Jimenez F, Perez ML, et al. Electrical stimulation of the prelemniscal radiation in the treatment of Parkinson's disease: an old target revised with new techniques. Neurosurgery 2001; 49(2):293–306; discussion 8.
111. Forel A. Untersuchungen über die Haubenregion und ihre oberen Verknüpfungen im Gehirne des Menschen und einiger Säugethiere, mit Beiträgen zu den Methoden der Gehirnuntersuchung. Arch Psychiat Nervenkr 1877; 7:393–495.
112. Verhaart W. A comparison between the corpus striatum and the red nucleus a subcortical centra of the cerebral motor system. Psychiat Neurol BI (Amst) 1938; 32:676–737.
113. Vogt C. La myéloarchitecture du thalamus du cercopithèque. J Psychol Neurol 1909; 12:285–324.
114. Parent M, Parent A. The pallidofigal motor fiber system in primates. Parkinsinism and Related Disorders 2004; 10:203–211.
115. Baron MS, Noonan JB, Mewes K. Restricted ablative lesions in motor portions of GPi in primates produce extensive loss of motor-related neurons and degeneration of the lenticular fasciculus. Exp Neurol 2006; 202:67–75.
116. Baron MS, Sidibe M, DeLong MR, Smith Y. Course of motor and associative pallidothalamic projections in monkeys. J Comp Neurol 2001; 429(3):490–501.
117. Mitrofanis J. Some certainty for the "zone of uncertainty"? Exploring the function of the zona incerta. Neuroscience 2005; 130(1):1–15.
118. Mitrofanis J, Ashkan K, Wallace BA, Benabid AL. Chemoarchitectonic heterogeneities in the primate zona incerta: Clinical and functional implications. J Neurocytol 2004; 33(4):429–440.
119. Francois C, Tande D, Yelnik J, Hirsch EC. Distribution and morphology of nigral axons projecting to the thalamus in primates. J Comp Neurol 2002; 447(3):249–260.
120. Cuny E, Guehl D, Burbaud P, Gross C, Dousset V, Rougier A. Lack of agreement between direct magnetic resonance imaging and statistical determination of a subthalamic target: the role of electrophysiological guidance. J Neurosurg 2002; 97(3):591–597.
121. Zonenshayn M, Rezai AR, Mogilner AY, Beric A, Sterio D, Kelly PJ. Comparison of anatomic and neurophysiological methods for subthalamic nucleus targeting. Neurosurgery 2000; 47(2):282–292; discussion 92–94.
122. Collins DL, Neelin P, Peters TM, Evans AC. Automatic 3D intersubject registration of MR volumetric data in standardized Talairach space. J Comput Assist Tomogr 1994; 18(2):192–205.
123. Mazziotta J, Toga A, Evans A, et al. A probabilistic atlas and reference system for the human brain: International Consortium for Brain Mapping (ICBM). Philos Trans R Soc Lond B Biol Sci 2001; 356(1412):1293–322.
124. Uylings HB, Rajkowska G, Sanz-Arigita E, Amunts K, Zilles K. Consequences of large interindividual variability for human brain atlases: converging macroscopical imaging and microscopical neuroanatomy. Anat Embryol (Berl) 2005; 210(5–6):423–431.
125. Byne W, Buchsbaum MS, Mattiace LA, et al. Postmortem assessment of thalamic nuclear volumes in subjects with schizophrenia. Am J Psychiatry 2002; 159(1):59–65.
126. Deoni SC, Josseau MJ, Rutt BK, Peters TM. Visualization of thalamic nuclei on high resolution, multi-averaged T1 and T2 maps acquired at 1.5 T. Hum Brain Mapp 2005; 25(3):353–359.
127. Hutchison WD, Allan RJ, Opitz H, et al. Neurophysiological identification of the subthalamic nucleus in surgery for Parkinson's disease. Ann Neurol 1998; 44(4):622–628.
128. Lenz FA, Kwan HC, Martin RL, Tasker RR, Dostrovsky JO, Lenz YE. Single unit analysis of the human ventral thalamic nuclear group. Tremor-related activity in functionally identified cells. Brain 1994; 117(Pt 3):531–543.
129. Lozano AM, Hutchison WD, Tasker RR, Lang AE, Junn F, Dostrovsky JO. Microelectrode recordings define the ventral posteromedial pallidotomy target. Stereotact Funct Neurosurg 1998; 71(4):153–163.
130. Lozano AM, Lang AE, Hutchison WD, Dostrovsky JO. Microelectrode recording-guided posteroventral pallidotomy in patients with Parkinson's disease. Adv Neurol 1997; 74:167–174.
131. Magnin M, Jetzer U, Morel A, Jeanmonod D. Microelectrode recording and macrostimulation in thalamic and subthalamic MRI guided stereotactic surgery. Neurophysiol Clin 2001; 31(4):230–238.
132. Mandir AS, Rowland LH, Dougherty PM, Lenz FA. Microelectrode recording and stimulation techniques during stereotactic procedures in the thalamus and pallidum. Adv Neurol 1997; 74:159–165.
133. Tasker RR, Lenz F, Yamashiro K, Gorecki J, Hirayama T, Dostrovsky JO. Microelectrode techniques in localization of stereotactic targets. Neurol Res 1987; 9(2):105–112.
134. Vitek JL, Bakay RA, Hashimoto T, et al. Microelectrode-guided pallidotomy: technical approach and its application in medically intractable Parkinson's disease. J Neurosurg 1998; 88(6):1027–1043.
135. Lenz FA, Kwan HC, Martin R, Tasker R, Richardson RT, Dostrovsky JO. Characteristics of somatotopic organization and spontaneous neuronal activity in the region of the thalamic principal sensory nucleus in patients with spinal cord transection. J Neurophysiol 1994; 72(4):1570–1587.
136. Lenz FA, Seike M, Lin YC, et al. Neurons in the area of human thalamic nucleus ventralis caudalis respond to painful heat stimuli. Brain Res 1993; 623(2):235–240.
137. Lopez-Flores G, Miguel-Morales J, Teijeiro-Amador J, et al. Anatomic and neurophysiological methods for the targeting and lesioning of the subthalamic nucleus: Cuban experience and review. Neurosurgery 2003; 52(4):817–830; discussion 31.

138. Bourgeois G, Magnin M, Morel A, et al. Accuracy of MRI-guided stereotactic thalamic functional neurosurgery. Neuroradiology 1999; 41(9):636–645.
139. Jeanmonod D, Magnin M, Morel A, et al. Surgical control of the human thalamocortical dysrhytmia: I. Central lateral thalamotomy in neurogenic pain. Thalamus and Related Systems 2001; 1:71–79.
140. Jeanmonod D, Schulman J, Ramirez R, et al. Neuropsychiatric thalamocortical dysrhythmia: surgical implications. Neurosurg Clin N Am 2003; 14(2):251–265.
141. Patel NK, Heywood P, O'Sullivan K, McCarter R, Love S, Gill SS. Unilateral subthalamotomy in the treatment of Parkinson's disease. Brain 2003;126(Pt 5):1136–1145.
142. Godinho F, Thobois S, Magnin M, et al. Subthalamic nucleus stimulation in Parkinson's disease: anatomical and electrophysiological localization of active contacts. J Neurol 2006; 253:1347–1355.
143. Plaha P, Ben-Shlomo Y, Patel NK, Gill SS. Stimulation of the caudal zona incerta is superior to stimulation of the subthalamic nucleus in improving contralateral parkinsonism. Brain 2006; 129(Pt 7):1732–1747.
144. Voges J, Volkmann J, Allert N, et al. Bilateral high-frequency stimulation in the subthalamic nucleus for the treatment of Parkinson disease: correlation of therapeutic effect with anatomical electrode position. J Neurosurg 2002; 96(2):269–279.
145. Hamel W, Fietzek U, Morsnowski A, et al. Deep brain stimulation of the subthalamic nucleus in Parkinson's disease: evaluation of active electrode contacts. J Neurol Neurosurg Psychiatry 2003; 74(8):1036–1046.
146. Jeanmonod D, Magnin M, Morel A, et al. Thalamocortical dysrhythmia II. Clinical and surgical aspects. Thalamus and Related Systems 2001; 1:245–254.
147. Sarnthein J, Morel A, von Stein A, Jeanmonod D. Thalamocortical theta coherence in neurological patients at rest and during a working memory task. Int J Psychophysiol 2005; 57(2):87–96.
148. Sarnthein J, Stern J, Aufenberg C, Rousson V, Jeanmonod D. Increased EEG power and slowed dominant frequency in patients with neurogenic pain. Brain 2006; 129(Pt 1):55–64.
149. Stern J, Jeanmonod D, Sarnthein J. Persistent EEG overactivation in the cortical pain matrix of neurogenic pain patients. Neuroimage 2006; 31(2):721–731.
150. Hodaie M, Cordella R, Lozano AM, Wennberg R, Dostrovsky JO. Bursting activity of neurons in the human anterior thalamic nucleus. Brain Res 2006; 1115(1):1–8.
151. Llinas R, Jahnsen H. Electrophysiology of mammalian thalamic neurones in vitro. Nature 1982; 297(5865):406–408.
152. Llinas R, Ribary U, Contreras D, Pedroarena C. The neuronal basis for consciousness. Philos Trans R Soc Lond B Biol Sci 1998; 353(1377):1841–1849.
153. Llinas RR, Ribary U, Jeanmonod D, Kronberg E, Mitra PP. Thalamocortical dysrhythmia: A neurological and neuropsychiatric syndrome characterized by magnetoencephalography. Proc Natl Acad Sci USA 1999; 96(26):15222–15227.
154. Llinas R, Ribary U, Jeanmonod D, et al. Thalamocortical dysrhythmia I. Functional and imaging aspects. Thalamus and Related Systems 2001; 1:237–244.
155. Johansen-Berg H, Behrens TE, Sillery E, et al. Functional-anatomical validation and individual variation of diffusion tractography-based segmentation of the human thalamus. Cereb Cortex 2005; 15(1):31–39.
156. Pfefferbaum A, Sullivan EV, Adalsteinsson E, Garrick T, Harper C. Postmortem MR imaging of formalin-fixed human brain. Neuroimage 2004; 21(4):1585–1595.
157. Fatterpekar GM, Delman BN, Boonn WW, et al. MR microscopy of normal human brain. Magn Reson Imaging Clin N Am 2003;11(4):641–653.
158. Niemann K, van Nieuwenhofen I. One atlas—three anatomies: relationships of the Schaltenbrand and Wahren microscopic data. Acta Neurochir (Wien) 1999;141(10):1025–1038.
159. Nowinski WL, Yang GL, Yeo TT. Computer-aided stereotactic functional neurosurgery enhanced by the use of the multiple brain atlas database. IEEE Trans Med Imaging 2000;19(1):62–69.
160. Uylings HB, Sanz Arigita E, de Vos K, et al. The importance of a human 3D database and atlas for studies of prefrontal and thalamic functions. Prog Brain Res 2000;126:357–368.

List of Abbreviations

ac	Anterior commissure
al	Ansa lenticularis
Acb(l, m)	Accumbens nucleus (lateral and medial)
AChE	Acethylcholinesterase
AD	Anterodorsal nucleus
AMP	Anteromedial pallidotomy
AM	Anteromedial nucleus
Amg	Amygdala
ap	Ansa peduncularis
B	Basal nucleus of Meynert
bic	Brachium of the inferior colliculus
BST	Bed nucleus of the stria terminalis
CaBP	Calcium-binding proteins
cc	Corpus callosum
Cd	Caudate nucleus
CeM	Central medial nucleus
CB	Calbindin D-28K
CG	Cingulate gyrus
CR	Calretinin
CL(p)	Central lateral nucleus (posterior part)
CLT	Central lateral thalamotomy
Cl	Claustrum
CM	Centre médian nucleus (or centromedian)
CP	Cerebral peduncle
CTT	Cerebellothalamic tractotomy
DG	Dentate gyrus
DB	Diagonal band of Broca
EC	Entorhinal cortex
eml	External medullary lamina
fct	Fasciculus cerebello-thalamicus
fl	Fasciculus lenticularis
frf	Fasciculus retroflexus
ft	Fasciculus thalamicus
fx	Fornix
GPi	Globus pallidus, internal segment
GPe	Globus pallidus, external segment
GPv	Globus pallidus, ventral subcommissural part
GR	Gyrus rectus
Hb (l,m)	Habenular nucleus (lateral and medial subdivisions)
Hip	Hippocampus
Hyp	Hypothalamus
ic	Internal capsule
IC	Inferior colliculus
IG	Insular gyrus
iml	Internal medullary lamina
LD	Lateral dorsal nucleus
LGN (mc)	Lateral geniculate nucleus (magnocellular layers)
Li	Limitans nucleus

ll	Lateral lemniscus
LP	Lateral posterior nucleus
MB	Mammillary body
MD (pc, mc, pl)	Mediodorsal nucleus (parvocellular, magnocellular, and paralamellar divisions)
MGN	Medial geniculate nucleus
MGm	Medial geniculate nucleus, medial division
MGv	Medial geniculate nucleus, ventral division
MGd	Medial geniculate nucleus, dorsal division
ml	Medial lemniscus
mtt	Mammillothalamic tract
MV	Medioventral nucleus
OG	Orbital gyrus
OA	Olfactory area
ot	Optic tract
PAG	Periaqueductal grey area
pc	Posterior commissure
Pf	Parafascicular nucleus
PMP	Posteromedial pallidotomy
Po	Posterior nucleus
PRC	Piriform cortex
PTT	Pallidothalamic tractotomy
PuA	Anterior pulvinar
PuI	Inferior pulvinar
PuL	Lateral pulvinar
PuM	Medial pulvinar
PuT	Putamen
Pv	Paraventricular nuclei
PV	Parvalbumin
R	Reticular thalamic nucleus
RN	Red nucleus
SC	Superior colliculus
SCA	Subcallosal area
scp	Superior cerebellar peduncle
Sep	Septal area
SG	Suprageniculate nucleus
sm	Stria medullaris
SNc	Substantia nigra, pars compacta
SNr	Substantia nigra, pars reticulata
sPal	Subpallidal area
sPf	Subparafascicular nucleus
STh	Subthalamic nucleus
stt	Spinothalamic tract
Tu	Olfactory tubercule
VA(pc, mc)	Ventral anterior nucleus (parvocellular and magnocellular divisions)
VLa	Ventral lateral anterior nucleus
VLp(d, v)	Ventral lateral posterior nucleus (dorsal and ventral divisions)
VM	Ventral medial nucleus
VPI	Ventral posterior inferior nucleus
VPL(p, a)	Ventral posterior lateral nucleus (posterior and anterior divisions)
VPM	Ventral posterior medial nucleus
VPMpc	Ventral posterior medial nucleus, parvocellular division
VS	Ventral striatum
VTA	Ventral tegmental area
ZI	Zona incerta

Index

Ac. *See* Anterior commissure (ac)
Accumbens nucleus (Acb), 26–29, 87–88
  AChE, CB, CR photomicrographs, 104
  anatomofunctional compartmentalization, 53–55
  photomicrographs, 45
Acetylcholinesterase (AChE), 15, 104
  photomicrographs, 50–51
AD. *See* Anterodorsal nucleus (AD)
AM. *See* Anteromedial nucleus (AM)
Anatomofunctional compartmentalization, 53–55
Anterior commissure (ac), 26–29
Anterior commissure level
  thalamus and basal ganglia, 17
Anterior group of thalamic nuclei, 14
Anterior pulvinar (PuA), 36–38, 87–88
  thalamic nuclei
Anterodorsal nucleus (AD), 19, 78–80
  anatomical variability, 6
  thalamic nuclei, 14
Anteromedial nucleus (AM), 20, 30–35, 78–80
Antero-posterior variations, 120
Anteroventral (AV), 14
Autopsy material, 3
AV. *See* Anteroventral (AV)

B. *See* Basal nucleus of Meynert (B)
Basal ganglia
  anatomo-functional compartmentalization, 53
  atlas maps, 53
  block preparation, 10
  frontal sections, 7, 11, 52, 104, 122
  horizontal sections, 17–29
  MRI, 11
  pallidum, 54–55
  sagittal sections, 30–41
  stereotactic functional neurosurgery and neuroimaging, 53–110
  striatum, 53–54
  substantia nigra, 55
  subthalamic nucleus, 55
Basal nucleus of Meynert (B), 39–41, 90–102
  extended amygdala
  photomicrographs, 103
Block preparation, 3–4
  basal ganglia atlas, 10
  thalamic atlas, 3, 9, 53
Brachium of the inferior colliculus (bic), 114

CaBP. *See* Calcium-binding proteins (CaBP)
Calbindin (CB), 16, 104
Calcium-binding proteins (CaBP), 14–15
  pallidal and cerebellar territories, 5, 54
  striato-pallidal compartmentalization, 6, 53, 106
  subthalamic fiber tracts, 6, 13, 17, 111
  subthalamus, 52
  thalamus, 52
Calretinin (CR), 104
  limbic territory
Caudate nucleus (Cd), 17–29, 36–38, 39–41, 56–77, 90–102
  AChE, 104, 105
  CaBP, 104–106
  CB, CR, 104, 105
  MRI, 117
  myelin, 105, 117, 118
  Nissl, 46–47
  pallidothalamic fibers, 115
  photomicrographs, 45
postmortem MRI and photomicrographs, 49, 103
  striatal and pallidal anatomo-functional compartmentalization, 109
  subthalamic fibers and striato-pallidal compartments, 128
  thalamus and basal ganglia, 122
CB. *See* Calbindin (CB)
Cd. *See* Caudate nucleus (Cd)
CeM. *See* Central medial nucleus (CeM)
Central lateral nucleus (CL), 19, 30–35, 78–80, 81–86, 87–88
  AChE, 48
  CaBP, 104–106
  myelin, 42
  Nissl, 42, 43, 46–47, 48
  Nissl, myelin and AChE, 50–51
  postmortem MRI and photomicrographs, 44
  subthalamic fiber tracts, 113, 127
  thalamus and basal ganglia, 122
  in vivo and in vitro thalamus, 126
Central lateral thalamotomy (CLT)
  neurogenic pain, 130
  postoperative MRI, 134
  sagittal atlas projections, 134
  surgical target, 130
Central medial nucleus (CeM), 19–25, 30–35, 78–80
  myelin, 42, 48
  Nissl, 42
  thalamic nuclei, 13
Centre median nucleus (CM), 13, 15–16, 43, 44, 51, 117, 119
  AChE, 4–6, 10, 13–16
Cerebellothalamic and pallidothalamic tracts, 111–112
  atlas maps, 113–118
Cerebellothalamic tractotomy (CTT)
  motor disorders, 130–131
  postoperative MRI, 127, 128, 132
  sagittal atlas projection, 132
Cerebral peduncle (CP)
  postmortem MRI and photomicrographs, 49
Chronic functional disorders, 1
CL. *See* Central lateral (CL)
CLT. *See* Central lateral thalamotomy (CLT)
CM. *See* Centre median (CM)

Comb system, 115
CP. *See* Cerebral peduncle (CP)
CR. *See* Calretinin (CR)
CTT. *See* Cerebellothalamic tractotomy (CTT)

Data analysis, 5–6
Diffusion tensor imaging (DTI), 2
Dorsoventral level
  thalamus and basal ganglia, 17
  variations, 119
DTI. *See* Diffusion tensor imaging (DTI)

Electrophysiological evaluation, 120–121
Electrophysiological mapping, 129–130

Functional neuroimaging, 130
Functional neurosurgery, 120, 130

Globus pallidus, external segment (GPe), 19–25, 26–29, 36–38, 39–41, 87–88, 90–102
  AChE, 104, 105
  CaBP, 104–105, 108
  CaBP photomicrographs, 106
  CB, 104, 105, 108
  CR, 104, 105, 108
  MRI, 117
  myelin, 105, 117, 118
  photomicrographs, 45
  postmortem MRI and photomicrographs, 103
  striatal and pallidal anatomo-functional compartmentalization, 109
  subthalamic fibers and striato-pallidal compartments, 128
  thalamic and striato-pallidal subdivisions, 124
Globus pallidus, internal segment (GPi), 19–25, 26–29, 36–38, 39–41, 87–88, 90–102
  AChE, 104, 105
  CaBP, 104–105
  CaBP photomicrographs, 106
  CB, CR, PV,104, 105
  MRI, 117
  myelin, 117, 118
  photomicrographs, 45
  postmortem MRI and photomicrographs, 103
  striatal and pallidal anatomo-functional compartmentalization, 109
  subthalamic fibers, 116
  subthalamic fibers and striato-pallidal compartments, 128
  thalamic and striato-pallidal subdivisions, 124
Globus pallidus, ventral subcommissural part (GPv), 87–88
  AChE, 104, 107
  CaBP, 104, 107
  CB, 104
  CR, 104
  Nissl, 107
GPe. *See* Globus pallidus, external segment (GPe)
GPi. *See* Globus pallidus, internal segment (GPi)
GPv. *See* Globus pallidus, ventral subcommissural part (GPv)
Graphic representations, 6–7
Guillotine knife, 9

Habenula (Hb), 30–35, 78–80
  AChE, 48
  myelin, 48
  thalamic nuclei, 13
High frequency stimulation (HFS), 1–2, 129
High resolution postmortem magnetic resonance imaging, 112
Hippocampus (Hip), 111
  postmortem MRI and photomicrographs, 49
Hypothalamus (Hyp), 53, 54, 106

Immunocytochemistry, 5
Inferior colliculus (IC), 30–35, 81–86
  CaBP, 104–106
  myelin, 42
  Nissl, 42
Interindividual variability, 130
  in vivo variability, 120
  postmortem variability, 130–131

Lateral dorsal nucleus (LD), 18, 81–86
  CaBP, 16
  myelin, 43
  Nissl, 43, 46–47
  photomicrographs, 45
  postmortem MRI and photomicrographs, 44, 49
  PV-ir, 16
  thalamus and basal ganglia, 122
  thalamic nuclei, 14
Lateral geniculate nucleus (LGN), 16, 39–41
  CaBP, 14
  CaBP photomicrographs, 106
  postmortem MRI and photomicrographs, 49
  PV-ir, 14
Lateral posterior nucleus (LP), 18, 36–38, 90–102
  AChE, 48
  myelin, 48
  Nissl staining photographs, 46–47
  postmortem MRI and photomicrographs, 49, 103
  thalamus and basal ganglia, 122
  thalamic nuclei, 14
Lateral pulvinar (PuL), 19–25, 26–29, 39–41, 56–77
  myelin and MRI, 118
  subthalamic fibers and striato-pallidal compartments, 128
Latero-medial variations, 119–120
LD. *See* Lateral dorsal nucleus (LD)
LFP. *See* Local field potentials (LFP)
LGN. *See* Lateral geniculate nucleus (LGN)
Limitans nucleus (Li), 19–25, 30–35, 78–80, 81–86
  cerebello- and pallidothalamic tracts, 114
  myelin, 42, 43
  Nissl, 42
  postmortem MRI and photomicrographs, 49
  subthalamic fiber tracts, 113, 127
Local field potentials (LFP), 129
LP. *See* Lateral posterior nucleus (LP)

Magnetic resonance images, sources of, 7–8
Magnetoencephalogram (MEG), 129
Mammillary body (MB), 30–35, 78–80
  myelin and MRI, 117
MD. *See* Mediodorsal nucleus (MD)
Medial geniculate nucleus (MGN), 36–38, 87–88, 90–102
  AChE, 50–51, 107
  CaBP, 14, 16, 107
  CaBP photomicrographs, 106
  CB-ir, 16
  functional considerations, 13–14
  myelin, 50–51
  myelin and MRI, 118

[Medial geniculate nucleus (MGN)]
  Nissl, 50–51, 107
  postmortem MRI and photomicrographs, 103
  PV-ir, 14, 16
Medial geniculate nucleus, medial division (MGm)
  CaBP, 16
  PV-ir, 16
Medial geniculate nucleus, ventral division (MGv)
  CaBP, 16
  functional considerations, 14
Medial lemniscus/spinothalamic tracts, 112
  CaBP, 16
  pain processing, 16
  subthalamic fiber tracts
Mediodorsal nucleus (MD), 19, 20, 30–35, 78–80, 81–86
  AChE, 48
  MRI, 117
  myelin, 42, 43, 48, 117
  Nissl, 42, 43, 46–47, 48, 117
  pallidothalamic fibers, 115
  photomicrographs, 45
  postmortem MRI and photomicrographs, 44
  subthalamic fiber tracts, 127
  thalamic nuclei, 13
  thalamic and striato-pallidal subdivisions, 124
  thalamus and basal ganglia, 122
Medioventral nucleus (MV), 19–25, 78–80
  thalamic nuclei, 13
MEG. *See* Magnetoencephalogram (MEG)
MGm. *See* Medial geniculate nucleus, medial division (MGm)
MGN. *See* Medial geniculate nucleus (MGN)
MGv. *See* Medial geniculate nucleus, ventral division (MGv)
Midcommissural level
  thalamus and basal ganglia, 17
Multiarchitectonic parcellation, 6
MV. *See* Medioventral nucleus (MV)
Myelin
  photomicrographs, 42, 45, 49, 50–51
  postmortem MRI, 49
  subthalamic fiber tracts, 6, 13, 16, 111–112

Neuroimaging, 1–2, 130–131
Neurosurgery, 1, 53, 120, 130–131
  cerebellothalamic tractotomy, 126
  pallidotomy, 130
  pallidothalamic tractotomy, 126, 130
  thalamotomy, 6, 130
Nissl stainings
  photomicrographs, 42–43, 46–47, 47, 48, 50–51

PAG. *See* Periaqueductal grey area (PAG)
Pallidothalamic tractotomy (PTT)
  Parkinson’s disease, 6, 111, 130–131, 132, 134
  sagittal atlas projection, 132, 134
  subthalamic fiber tracts, 127
Parafascicular nucleus (Pf), 19–25, 30–35, 78–80
  cerebello- and pallidothalamic tracts, 114
  thalamic nuclei, 13
Paraventricular nuclei (Pv)
  myelin and AChE photomicrographs, 48
  thalamic nuclei, 13
Periaqueductal grey area (PAG), 26–29, 30–35, 56–77, 78–80
Pf. *See* Parafascicular nucleus (Pf)
Po. *See* Posterior nucleus (Po)
Posterior commissure
  thalamus and basal ganglia, 17
Posterior nucleus (Po), 19–25, 26–29, 36–38, 87–88, 90–102
  cerebello- and pallidothalamic tracts, 114
  thalamic nuclei, 14
Postmortem, 3, 7, 11, 44, 49, 112, 119–121
PTT. *See* Pallidothalamic tractotomy (PTT)
PuA. *See* Anterior pulvinar (PuA)
PuL. *See* Lateral pulvinar (PuL)
Pulvinar nuclei, 19–25, 20, 26–29, 36–38, 56–77, 81–86, 87–88, 90–102
  AChE, 48, 50–51
  myelin, 48, 50–51
  myelin and Nissl stainings, 42, 43
  Nissl, 50–51
  photomicrographs, 45
  postmortem MRI and photomicrographs, 44, 49, 103
  thalamic nuclei, 14
  in vivo and in vitro thalamus, 126
Putamen (PuT), 19–25, 26–29, 39–41
  CaBP photomicrographs, 106
  myelin and MRI, 118
  Nissl staining photographs, 46–47
  striatal and pallidal anatomo-functional compartmentalization, 109
  subthalamic fibers and striato-pallidal compartments, 128
  thalamic and striato-pallidal subdivisions, 124
  thalamus and basal ganglia, 122
  in vivo and in vitro thalamus, 126
Pv. *See* Paraventricular nuclei (Pv)
PV immunoreactivity (PV-ir), 14

R. *See* Reticular thalamic nucleus (R)
Radiofrequency lesions (RFL), 129
  MRI, 133
Red nucleus (RN), 26–29, 30–35, 78–80, 81–86
  CaBP photomicrographs, 106
  cerebello- and pallidothalamic tracts, 114
  myelin and Nissl stainings, 42
  Nissl, myelin, AChE, CaBP-ir photomicrographs, 107
  postmortem MRI and photomicrographs, 44
  subthalamic fiber tracts, 113, 127
  thalamus and basal ganglia, 122
Reference coordinate system, 7
Reticular nucleus, 14
Reticular thalamic nucleus (R), 17, 19–25, 26–29, 39–41, 56–77, 81–86, 90–102
  AChE, 104, 105
  CaBP, 104, 105
  CB, 104, 105
  CR, 104, 105
  PV, 13–16, 54, 112
  myelin, 43, 105
  Nissl, 43
  postmortem MRI and photomicrographs, 44, 103
  subthalamic fiber tracts, 113, 127
  thalamic nuclei, subthalamic fiber tracts, 123
  thalamus and basal ganglia, 122
  in vivo and in vitro thalamus, 126
RFL. *See* Radiofrequency lesions (RFL)
RN. *See* Red nucleus (RN)

SC. *See* Superior colliculus (SC)
SG. *See* Suprageniculate nucleus (SG)
SG/Li. *See* Suprageniculate/limitans (SG/Li)

SN. *See* Substantia nigra (SN)
SNc. *See* Substantia nigra, pars compacta (SNc)
SNr. *See* Substantia nigra, pars reticulata (SNr)
sPAL. *See* Subpallidal area (sPAL)
sPf. *See* Subparafascicular (sPf)
Stereotactic atlases, 1
Stereotactic functional neurosurgery and neuroimaging,129–136
  abbreviations, 143–144
  atlas, 129–136
  basal ganglia, 53–110
  interindividual anatomical variability, 119–136
  material and methods, 3–12
  MRI, 1
  new anatomical framework, 1–2
  subthalamic fiber tracts, 111–118
  thalamus, 13–52
Stereotactic precision, 2
STh. *See* Subthalamic nucleus (STh)
Stimulations, 122, 132–133
Subpallidal area (sPAL)
  CB and CR photomicrographs, 108
Subparafascicular (sPf)
  thalamic nuclei, 13
Substantia nigra (SN), 30–35
Substantia nigra, pars compacta (SNc), 81–86
  CaBP photomicrographs, 108
  CB and CR photomicrographs, 108
  myelin and Nissl stainings, 42, 43
  photomicrographs, 45
  postmortem MRI and photomicrographs, 49
  subthalamic fiber tracts, 113
  thalamic nuclei, subthalamic fiber tracts, 123
Substantia nigra, pars reticulata (SNr), 81–86, 87–88
  CaBP photomicrographs, 108
  CB and CR photomicrographs, 108
  comb system, 54, 114, 116
  Nissl, myelin, AChE, CaBP-ir photomicrographs, 107
  photomicrographs, 45
  postmortem MRI and photomicrographs, 49
  thalamic nuclei, subthalamic fiber tracts, 123
Subthalamic fiber tracts
  multiarchitectonic characteristics, 14, 53, 112, 114
  myelin, 45–50, 112
  stereotactic functional neurosurgery and neuroimaging, 111–118
Subthalamic nucleus (STh), 1, 18–20, 26–29, 36–38, 36–41, 56–77, 81–88
  AChE photomicrographs, 48
  myelin and MRI, 117
  myelin and Nissl stainings, 43
  Nissl staining photographs, 46–47
  pallidothalamic fibers, 115
  photomicrographs, 45
  postmortem MRI and photomicrographs, 44
  subthalamic fiber tracts, 113
  subthalamic fibers and striato-pallidal compartments, 128
  thalamic nuclei, subthalamic fiber tracts, 123
  thalamus and basal ganglia, 122
Subthalamic pallidothalamic tract, 13
Superior colliculus (SC), 30–35, 56–77, 81–86
  myelin and Nissl stainings, 42
  Suprageniculate/limitans (SG/Li)
  thalamic nuclei, 14
Suprageniculate nucleus (SG), 26–29, 36–38
  Nissl, myelin and AChE, 50–51
Surgical targets, 131
Thalamic atlas
  bloc preparation, 9
  guillotine procedure, 9
Thalamic nuclei
  anterior group, 14
  lateral group, 11
  medial group, 12
  posterior group, 12–13
Thalamus
  atlas, 2
  frontal sections, 7, 11, 54, 56, 104
  functional considerations, 15–16
  horizontal sections, 17
  MRI, 11
  multiarchitectonic characteristics, 14–15
  nomenclature, 6
  sagittal sections, 30–41
  stereotactic functional neurosurgery and neuroimaging, 13–52
  three-dimensional model, 135
Three dimensional model
  atlas, 130

Ventral anterior (VA)
  thalamic nuclei, 13
Ventral anterior nucleus (VA)
  CaBP, 16
  CB-ir, 16
  PV-ir, 16
  three-dimensional model, 135
Ventral anterior nucleus, magnocellular divisions (VAmc), 30–35
  myelin, and AChE photomicrographs, 48
  myelin and Nissl stainings, 42, 43
  subthalamic fiber tracts, 113, 127
Ventral anterior nucleus, parvocellular divisions (VApc), 18, 19, 36–38, 81–86
  AChE, CB, CR photomicrographs, 104
  myelin and AChE photomicrographs, 48
  myelin and MRI, 117
  myelin and Nissl stainings, 42, 43
  Nissl staining photographs, 46–47
  photomicrographs, 45
  subthalamic fiber tracts, 113, 127
  in vivo and in vitro thalamus, 126
Ventral lateral anterior nucleus (VLa), 19–25, 20, 36–38, 90–102
  CaBP, 16
  CB-ir, 16
  cerebello- and pallidothalamic tracts, 114
  myelin and AChE photomicrographs, 48
  photomicrographs, 45
  postmortem MRI and photomicrographs, 44
  PV-ir, 16
  subthalamic fibers, 116
  thalamic nuclei, 13
  three-dimensional model, 135
  in vivo and in vitro thalamus, 126
Ventral lateral posterior nucleus (VLp), 17, 18, 19–25, 20, 36–38, 81–86, 87–88, 90–102
  cerebello- and pallidothalamic tracts, 114
  myelin and MRI, 117
  myelin and Nissl stainings, 43
  Nissl staining photographs, 46–47
  pallidothalamic fibers, 115
  photomicrographs, 45
  postmortem MRI and photomicrographs, 103
  PV-ir, 14

[Ventral lateral posterior nucleus (VLp)]
  subthalamic fiber tracts, 113
  subthalamic fibers, 113, 116, 127
  thalamic nuclei, 13
  thalamic nuclei, subthalamic fiber tracts, 123
  thalamus and basal ganglia, 122
Ventral medial nucleus (VM), 81–86
  CaBP, 16
  CB-ir, 16
  cerebello- and pallidothalamic tracts, 114
  myelin and Nissl stainings, 43
  subthalamic fibers, 116, 127
  thalamic nuclei, 13
  three-dimensional model, 135
Ventral posterior inferior nucleus (VPI), 13–16
Ventral posterior lateral nucleus (VPL), 13–15, 112, 120
  CaBP, 14
  subthalamic fiber tracts, 116,127
Ventral posterior medial nucleus (VPM), 19–25, 26–29, 36–38, 87–88
  photomicrographs, 45
  PV-ir, 14
  thalamus and basal ganglia, 122
Ventral striatum (VS), 90–102
  anatomofunctional compartmentalization, 53
  postmortem MRI and photomicrographs, 103
Ventroposterior complex (VP), 19–25, 20, 26–29, 36–38, 87–88, 90–102
  cerebello- and pallidothalamic tracts, 114
  myelin and AChE photomicrographs, 48
  Nissl, myelin and AChE, 50–51
  postmortem MRI and photomicrographs, 103
  thalamic nuclei, 13
  in vivo and in vitro thalamus, 126
VLa. *See* Ventral lateral anterior nucleus (VLa)
VLp. *See* Ventral lateral posterior nucleus (VLp)
VM. *See* Ventral medial nucleus (VM)
VPL. *See* Ventroposterior complex (VPL)
VPM. *See* Ventral posterior medial nucleus (VPM)
VS. *See* Ventral striatum (VS)

Zona incerta (ZI), 26–29
  pallidothalamic fibers, 115
  photomicrographs, 45
  subthalamic fibers, 116, 127
  thalamus, 13
  thalamus and basal ganglia, 122

Neurosurgery

Stereotactic Atlas of the Human Thalamus and Basal Ganglia

about the book . . .

This reference presents a new collection of diagrams of the human thalamus, basal ganglia, and adjoining structures for accurate targeting in stereotactic functional neurosurgery. This guide consists of a series of maps in the three stereotactic planes and comparisons between brains with similar and differing intercommissural distances to help specialists pinpoint precise targets, map through anatomic variations, and develop computerized models for stereotactic functional neurosurgery. Paired with a CD that allows for the enlargement and reader-friendly analysis of maps and illustrations found within the text, this source stands as the first atlas of the human thalamus and basal ganglia to focus on combined high stereotactic precision and anatomical resolution.

With a variety of pictomicrographs and summary diagrams, this source examines the distribution of different neurochemical markers in the thalamus and basal ganglia for comparison with non-human primate data...provides a detailed description of fiber tracts leading to the thalamus, with particular focus on those targeted in stereotactic functional neurosurgery...correlates histological maps with MR images from the same autopsy brains...provides an evaluation of interindividual anatomical variability by comparing 3D stereotactic representations of the thalamus and basal ganglia in different brains with the same or different intercommissural distances...examines functional aspects of the thalamus and basal ganglia...and considers current applications of the atlas including target determination, evaluation of surgical strategies, and functional data projections.

about the author . . .

ANNE MOREL leads a neuroanatomy laboratory in the Department of Functional Neurosurgery, Neurosurgical Clinic, University Hospital Zurich, Switzerland. Dr. Morel received the Ph.D. degree from the University of Lausanne, studying the functional organization of the cat's auditory thalamus. During her postgraduate studies, she acquired knowledge of the organization of the thalamocortical and corticocortical connections in auditory and visual systems. This experience greatly contributed to her current research on the anatomy of the human thalamus and basal ganglia.

Printed in the United States of America

DK3579

ISBN 0-8247-2894-7
90000
9 780824 728946

informa
healthcare
www.informahealthcare.com

270 Madison Avenue
New York, NY 10016

2 Park Square, Milton Park
Abingdon, Oxon OX14 4RN, UK